NMR Investigations of Assembly Proteins

Inaugural-Dissertation
to obtain the academic degree
Doctor rerum naturalium (Dr. rer. nat.)
submitted to the Department of Biology, Chemistry and Pharmacy
of Freie Universität Berlin

by
Arndt Wallmann
from Celle, Germany

February 2019

This work was completed in the period from December 2014 to February 2019 at the Department of NMR-Supported Structural Biology of the Leibniz-Forschungsinstitut für Molekulare Pharmakologie (FMP) in Berlin.

1. Reviewer: Prof. Dr. Hartmut Oschkinat
2. Reviewer: Prof. Dr. Oliver Daumke

Date of defence: 3rd June 2019

Summary

Protein assemblies adopt both transient and permanent complex structures that can vary strongly in overall architecture. Complexes that adopt open helical symmetries often switch dynamically between assembly and disassembly and thus require factors that regulate complex formation. Structural studies on such systems benefit from an integrated methodological approach to gain insights into the relevant mechanistic and physiological features of the complex. This thesis focuses on two proteins: one directly modulates and regulates the assembly of microtubules in plant cells, while the other assembles to functional filaments that are involved in a signalosome pathway of the human innate immune response.

Microtubules are protein assemblies that are essential for cell proliferation, growth and transport of cargo in eukaryotic cells. In plants, the cortical microtubule network directs the synthesis of cellulose, a fundamental component of the cell wall, which provides the bulk of plant biomass. Microtubule-associated proteins (MAPs) play an important role in maintaining the organization, structure and dynamics of the microtubule array. The MAP companion of cellulose synthase (CC) supports cellulose synthesis during salt stress by promoting the formation of a microtubule array with increased stress tolerance and by regulating cellulose synthase localization in *Arabidopsis thaliana*. Strikingly, the cytosolic N-terminus of CC1 (CC1ΔC223) is sufficient to facilitate both microtubule reassembly and cellulose synthesis during salt stress. This thesis outlines the molecular mechanism for how CC1ΔC223 binds to and bundles microtubules to sustain cellulose synthesis under conditions of high salinity. Solution-state nuclear magnetic resonance (NMR) spectroscopy was employed to characterize the structural features of CC1ΔC223 and its interaction with microtubules. Chemical shifts of backbone carbon, nitrogen and protons were assigned by combining 3D and 4D triple-resonance NMR experiments with non-uniform sampling (NUS). Free CC1ΔC223 in solution is intrinsically disordered but the carbon chemical shifts hint at several regions with enhanced propensity for β-strand secondary structure.

The addition of microtubules to isotopically-enriched CC1ΔC223 resulted in reversible and residue-specific line broadening effects, stemming from the reversible association of CC1ΔC223 to the microtubule surface, where it experiences fast transverse relaxation due

to the long rotational correlation time of the complex. Interestingly, the results showed that CC1ΔC223 binds with four hydrophobic and conserved linear motifs that are connected by flexible linker regions. Peptides that each contained one microtubule-binding motif retained microtubule-binding activity and STD-NMR experiments indicated strong contributions of aromatic side chains to the overall binding. The mutation of two key tyrosine residues in the N-terminal binding region reduced the binding affinity *in vitro* and resulted in a salt-sensitive phenotype *in vivo*.

Electron microscopy analysis showed that CC1ΔC223 induces bundling of microtubules in a concentration-dependent manner, and fluorescence microscopy revealed that CC1ΔC223 can diffuse on microtubules bidirectionally. Cross-linking of CC1ΔC223 and tubulin dimers combined with mass spectrometry analysis suggested binding of the protein at the protomer interfaces along the microtubule lattice and the hydrophobic pocket longitudinally between tubulin dimers.

The microtubule-binding behaviour of CC1ΔC223 is reminiscent of that of the neuropathology-related and non-homologous protein Tau, which also bundles and diffuses on microtubules in a highly dynamic manner. The microtubule-binding motifs of CC1ΔC223 share some remarkable similarities in hydrophobicity, size, sequence and spacing with the microtubule-binding regions of Tau. Hence, CC1 sustains microtubule organization and cellulose synthase localization during salt stress *via* a Tau-like mechanism that may have evolved independently.

Signalosomes are higher-order intracellular protein assemblies that play important roles in several signalling cascades of the innate immune system. The filamentous core of signalosomes typically consists of proteins containing death domains like CARD, PYD or DD that, through assembly of the filament, link the upstream danger signal to the downstream enzyme-driven pathway. The second part of the thesis focuses on assemblies formed by the CARD domain of the adaptor protein RIP2 that are initiated by the cytosolic receptor NOD2. Since RIP2 forms insoluble filaments *via* its CARD domain, solid-state NMR spectroscopy was employed to study the structure of the RIP2CARD assembly. To obtain the backbone resonance assignments, proton-detected experiments on ^{2}H, ^{13}C, ^{15}N-labelled and 100 % back-exchanged RIP2CARD samples were acquired at 60 kHz magic angle spinning (MAS). These data were evaluated together with carbon-detected ^{13}C-^{13}C DARR correlations on protonated samples that were either uniformly ^{13}C-labelled or selectively [2-^{13}C]- or [1,3-^{13}C]-glycerol labelled, yielding the assignment of backbone and side-chain resonances.

The chemical shifts of the assigned residues of filamentous RIP2CARD closely matched the chemical shifts of monomeric RIP2CARD in solution, showing that the overall conformation is maintained upon filament formation. The solid-state MAS NMR data yielded no signals from the C-terminal segment of the protein, which typically contains a helix in the CARD fold. This result corroborates the lack of ordered structure in this region reported already by the structure of the monomeric RIP2CARD domain and indicates that the local disorder is retained in filamentous RIP2CARD.

The structure of the RIP2CARD filament, solved by cryogenic electron microscopy (cryo-EM), has a helical configuration that is similar to other CARD filaments of the innate immune system. The most significant chemical shift differences between RIP2CARD in solution and within the filament map to the subunit interfaces of the assembly structure. These chemical shift differences report on local conformational changes due to packing effects in the filament and therefore independently confirm the overall architecture of the assembly structure.

The results give important structural insights into the NOD2-RIP2 pathway and highlight the importance of RIP2 polymerization for the signalling mechanism. Moreover, the work paves the way for future research on the structural aspects of the NOD2CARDs-RIP2CARD interface and the regulation of filament formation.

Zusammenfassung

Komplex-bildende Proteine sind an vielen biologische Prozessen in der Zelle beteiligt und können sich stark in Struktur und Funktionalität unterscheiden. Viele Proteinkomplexe mit offener helikaler Symmetrie können ihre Struktur durch dynamischen Auf- und Abbau umgestalten und benötigen folglich Faktoren, welche die Bildung der Komplexe regulieren. Die Erforschung von solchen Systemen profitiert von einem breiten methodischen Ansatz, mit dem die relevanten strukturellen und funktionellen Eigenschaften des Komplexes charakterisieren werden können. In der vorliegenden Arbeit wurden zwei Proteine untersucht. Eines reguliert die Struktur des Mikrotubulinetzwerks in Pflanzenzellen und das andere bildet funktionelle Filamente im Rahmen der angeborenen menschlichen Immunabwehr.

Mikrotubuli sind röhrenförmige Proteinkomplexe, die essentiell für die Zellteilung, die Zellstabilität und den Transport von Fracht innerhalb von eukaryotischen Zellen sind. In Pflanzen bilden sie ein Netzwerk unterhalb der Zellmembran, welches die Synthese von Zellulose unterstützt. Zellulose ist ein Hauptbestandteil der pflanzlichen Zellwand, die wiederum einen Großteil der Biomasse der Pflanze ausmacht. Die Struktur und Dynamik von Mikrotubulinetzwerken werden von Mikrotubuli-assoziierten Proteinen (MAP) organisiert und reguliert. In *Arabidopsis thaliana* unterstützt das MAP companion of cellulose synthase 1 (CC1) die Zellulosesynthese unter Salzstress, indem es den Aufbau eines stresstoleranten Mikrotubulinetzwerkes befördert und die Lokalisierung des Zellulose Synthase Komplexes vermittelt. Der zytosolische N-terminus von CC1 (CC1ΔC223) ist dabei ausreichend, um die Restrukturierung des Mikrotubulinetzwerkes und die Aufrechterhaltung der Zellulosesynthese zu bewirken. Diese Arbeit beschreibt erstmals den molekularen Mechanismus, mit dem CC1 Mikrotubuli bindet und bündelt, was die Restrukturierung des Mikrotubulinetzwerkes ermöglicht und somit die Zellulosesynthese unterstützt.

Mittels Lösungs-Kernspinresonanz (NMR) Spektroskopie konnten die strukturellen Eigenschaften von CC1 und seine Interaktion mit Mikrotubuli untersucht werden. Die chemischen Verschiebungen des Kohlenstoffs, Wasserstoffs und Stickstoffs im Proteinrückgrats wurden mithilfe von 3D und 4D dreifach-Resonanz NMR Experimenten mit nichtuniformen Aufnahmeverfahren sequenzspezifisch zugeordnet. Freies CC1ΔC223 nimmt keine feste Struktur

an, enthält jedoch isolierte Regionen deren chemische Verschiebungen auf eine Tendenz zur Ausbildung von β-Strang Sekundärstruktur hindeuten.
Die Hinzugabe von Mikrotubuli zu isotopenangereicherten CC1ΔC223 führte zu einer reversiblen und sequenzspezifischen Linienverbreiterung, die aufgrund der reversiblen Assoziation von CC1ΔC223 an die Mikrotubulusoberfläche entsteht. Hier erfährt das Protein eine schnelle transversale Relaxation aufgrund der langen Rotationskorrelationszeit des Komplexes. Die Ergebnisse zeigen, dass CC1ΔC223 mit vier konservierten, hydrophoben und linearen Motiven Mikrotubuli bindet, welche durch flexible Regionen verbunden sind. Peptide, die jeweils ein Bindemotiv tragen, zeigen Mikrotubuli-Bindeaktivität und STD-NMR Experimente deuten auf eine starke Beteiligung von aromatischen Seitengruppen an der Bindung hin. Die Mutation von zwei wichtigen Tyrosinresten des N-terminalen Bindemotivs reduzierte die Bindeaktivität der Region *in vitro* und führte zu einer Störung der CC1-Proteinfunktion und damit zu einem salzsensitiven Pflanzenphänotyp *in vivo*.
Mithilfe von fluoreszenz- und elektronenmikroskopischen Aufnahmen konnte gezeigt werden, dass CC1ΔC223 konzentrationsabhängig Mikrotubuli bündelt und bidirektional an Mikrotubuli entlang diffundieren kann. Chemische Cross-Linking und Massenspektrometrie Experimente zwischen CC1ΔC223 und Mikrotubuli detektierten Bindestellen von CC1 entlang der Protomer Schnittstelle und nahe der hydrophoben Tasche zwischen Tubulin Dimeren.
Das dynamische Bindeverhalten von CC1ΔC223 gleicht dem des Tau Proteins, welches keine evolutionäre Verwandtschaft mit CC1 teilt und mit der Pathologie mehrerer neurologischer Erkrankungen des Menschen in Verbindung gebracht wird. Ähnlich wie CC1ΔC223 kann auch Tau Mikrotubuli bündeln und an ihnen entlang diffundieren. Die Mikrotubulibindenen Motive von CC1 und Tau ähneln sich stark in Hydrophobizität, Größe, Sequenz und Verteilung. Somit weist der Mechanismus mit dem CC1 die Mikrotubuli Organisation reguliert und damit die Zellulosesynthese unter Salzstress unterstützt starke Parallelen zur Funktionsweise von Tau auf und hat sich wahrscheinlich unabhängig in der Evolution entwickelt.

Signalosome sind intrazelluläre Proteinkomplexe mit helikaler Struktur, die wichtige Funktionen in vielen Signalkaskaden des angeborenen Immunsystems übernehmen. Der filamentöse Kern der Signalosome wird meist aus CARD, PYD oder DD Domänen gebildet, die durch Formation des Filaments das aktivierende Signal an den enzymabhängigen Signalweg weiterleiten. Im Rahmen dieser Arbeit wurde die CARD Domäne des Adapterproteins RIP2, welches von dem zytosolischen Rezeptor NOD2 aktiviert wird, näher untersucht.
Da das RIP2CARD Protein unlösliche Filamente bildet, wurde die strukturelle Analyse des

Proteins mithilfe der Festkörper-NMR-Spektroskopie untersucht. Für die sequenzspezifische Zuordnung der chemischen Verschiebungen des Proteinrückgrats wurden Protonendetektierte Spektren an ^{2}H, ^{13}C, ^{15}N-markierten und 100 % rückgetauschten RIP2CARD Proben bei 60 kHz magic angle spinning (MAS) aufgenommen. Diese Daten wurden zusammen mit Kohlenstoff-detektierten ^{13}C-^{13}C DARR Korrelationen ausgewertet, die an protonierten Proben mit uniformer ^{13}C-Markierung oder selektiver [2-^{13}C]- oder [1,3-^{13}C]-Glycerol-Markierung aufgenommen wurden. Mit diesen Experimenten konnte die Zuordnung der chemischen Verschiebungen der Aminosäurenseitenketten durchgeführt werden.

Die chemischen Verschiebungen der zugeordneten Reste der RIP2CARD Filamente stimmen größtenteils mit denen des monomeren RIP2CARD in Lösung überein. Dies zeigt, dass das Protein im Filament seine Konformation überwiegend beibehält. Es konnten keine Signale aus dem C-terminalen Segment des Proteins detektiert werden. Dies deutet darauf hin, dass diese Region auch innerhalb des Filaments unstrukturiert bleibt, wie in der Struktur des monomeren RIP2CARD in Lösung.

Die durch Kryoelektronenmikroskopie (Cryo-EM) gelöste Filamentstruktur von RIP2CARD zeigt den klassischen helikalen Aufbau anderer CARD Komplexe des Immunsystems. Die größten Unterschiede zwischen den chemischen Verschiebungen des monomeren und filamentösen RIP2CARD sind an den Grenzflächen der Untereinheiten des Proteinkomplexes zu finden. Diese Unterschiede gehen aus den lokalen Veränderungen der chemischen Umgebung hervor, die durch das Binden der Untereinheit entstehen und bestätigen somit die Struktur des Filaments.

Die Ergebnisse geben wichtige strukturelle Einblicke in den NOD2-RIP2 Signalweg und unterstreichen die Bedeutung der Filamentbildung für den Mechanismus. Ausserdem schaffen sie eine Grundlage, um weiterführende Strukturanalysen der NOD2CARDs-RIP2CARD Interaktion und der zugrundeliegenden Regulation der Filamentbildung durchzuführen.

Table of contents

List of figures

Nomenclature

Acronyms / Abbreviations

ATP	Adenosine triphosphate
BEST	Band-selective Excitation Short-Transient
CARD	Caspase Recruitment Domain
CC1	Companion of Cellulose Synthase 1
CL-MS	Cross-linking Mass Spectrometry
CP	Cross Polarization
CPMG	Carr-Purcell-Meiboom-Gill
CSA	Chemical Shift Anisotropy
CSC	Cellulose Synthase Complex
DARR	Dipolar Assisted Rotational Resonance
DD	Death Fold Domains
GDP	Guanosine Diphosphate
GFP	Green Fluorescent Protein
GTP	Guanosine Triphosphate
HMQC	Heteronuclear Multiple Quantum Coherence
HSQC	Heteronuclear Single Quantum Coherence
IDP	Intrinsically Disordered Protein

INEPT	Insensitive Nuclei Enhanced by Polarization Transfer
MAP	Microtubule-associated Protein
MASC	Microtubule-associated CesA Compartment
MAS	Magic Angle Spinning
MBP	Maltose-binding protein
MDP	Muramyl Dipeptide
MTBD	Microtubule-binding Domain
MT	Microtubule
NLR	NOD-like Receptors
NMR	Nuclear Magnetic Resonance
NOD	Nucleotide Oligomerization Domain
NOE	Nuclear Overhauser Effect
NUS	Non-uniformly Sampling
PABP	Polyanion-binding Proteins
PAMP	Pathogen-associated Molecular Pattern
PRR	Pattern Recognition Receptors
RF	Radio Frequency
RIP	Receptor-interacting Protein
STD	Saturation Transfer Difference
TEM	Transmission Electron Microscopy
TM	Transmembrane
WT	Wild-Type

Chapter 1

Introduction

1.1 Assembly proteins

Networks of interacting proteins form the molecular frameworks that underpin all fundamental processes of the cell. As the majority of proteins are organized in quaternary structures, ordered protein assembly is a universal biological principle guiding a multitude of molecular mechanisms [1]. Transient or permanent complex structures can perform large-scale coordinated and cooperative processes in the cell. On a genome-wide scale, the evolution of assembly pathways has been shown to be closely entangled with the complexes' quaternary structure resulting from gene fusion events and subsequent evolutionary selection [2]. Modification of the assembly pathways through mutation can increase their susceptibility to misassembly or aggregation, which can have severe biological consequences, as seen in the pathology of various diseases including neurodegenerative disorders such as Alzheimer's and Parkinson's disease [3, 4].

Higher-order protein assemblies adopt a wide variety of quaternary structures, which can be composed of repeated copies of either a single subunit (homomeric) or of multiple distinct protein subunits (heteromeric). Upon complex formation, the interaction between subunits can induce conformational changes between the structures in the free and bound state. The overall flexibility of the monomer has been reported as an important indicator for the extent of conformational change in the complex [5]. Most assembly proteins form symmetric structures adopting dimeric, cyclic, cubic or helical topologies [1]. However, while the first three exemplify symmetries with a finite number of subunits, a helical symmetry allows, in principle, an indefinite assembly of an open-ended filament. Proteins of this type can dynamically and specifically assemble to complex structures and have important roles in processes like force generation, structural support and information transmission [6, 7].

The collective properties of many helical assemblies are modified through continuous cycles of assembly and disassembly. Their open symmetry requires factors that can impact the assembly kinetics and regulate complex formation in a location- or signal-dependent manner. The relevant factors typically include subunit concentration, steric restrictions, compartmentalization and the binding of regulatory proteins. An example of such a regulatory protein is presented in the first part of this thesis: the work describes the molecular mechanism by which the plant protein CC1 regulates the assembly of microtubules under salt stress conditions.

Helical assembly proteins also play an important role in many signalling cascades of the cell. Their open symmetry and highly cooperative formation allow for unique mechanisms of signal transmission and signal amplification and can facilitate a rapid threshold response [6]. The dynamic assembly and disassembly of these signalling proteins mediate their temporal and spatial control and can reduce biological noise in the signal transduction. An example of such a protein is presented in the second part of this thesis, which focuses on an investigation into the filament-forming protein RIP2CARD and its activator NOD2 from the human innate immune system.

1.1.1 Structural biology on assembly proteins

In the last years, solid-state magic-angle spinning (MAS) nuclear magnetic resonance (NMR) and cryogenic electron microscopy (cryo-EM) have emerged as powerful methods for studying the structure of protein assemblies. New technological developments in methodology and technology of MAS NMR have widened the range of potential target systems [8]. These include innovations in the radio frequency console technologies, increased access to high-field NMR instruments, the use of hyperpolarization methods and fast-spinning probes [9–11]. Given an appropriate set of equipment, MAS NMR is now routinely used to study membrane proteins, sedimented soluble proteins, amyloid fibrils, whole tissue and also helical assemblies [12, 13, 4, 14, 15]. Using classical carbon-carbon through-space correlations, structural studies were successfully conducted on assembly proteins such as the prion-forming domain of Het-s, the type III secretion system and the human immunodeficiency virus 1 (HIV-1) capsid [16–18]. More recently, the structure of the AP205 nucleocapsid assembly was determined with fully protonated samples, employing proton detection and proton-proton distance restraints for structure calculation [11].

Assembly structures are, in principle, also amenable to structural characterization by more traditional methods such as X-ray crystallography and solution-state NMR. However, assemblies with non-crystallographic symmetries, such as most helical symmetries, are challenging targets for these methods due to their high molecular weight and the lack of any long-range order. In many cases, solution-state NMR and X-ray can provide the structures of the monomeric subunits, but typically not the fully assembled filament. However, the structure determination of homomeric helical filaments by MAS NMR can also be particularly demanding due to the ambiguities between inter- and intrasubunit restraints and the often complex and diverse symmetry, which has to be determined from a large conformational space [15, 19].

Recently, the proportion of structures determined by cryo-EM significantly increased as a result of the development of new sensor technology for direct electron detection [20]. Although cryo-EM is well-suited for very large and well-ordered structures with multiple distinct subunits, cryo-EM density maps often achieve only near-atomic resolution and do not recover disordered or dynamic regions. Solid-state MAS NMR can supply data from both the rigid and dynamic regions and can further probe for protein–protein interfaces, solvent exposure or enzymatic reactions. Hence, as both techniques can deliver complementary information, an integrated approach can be advantageous for a comprehensive characterization of assembly structures. In a commonly used combined structural approach, lower-resolution cryo-EM can provide information on the symmetry of the complex, while MAS NMR adds the atomic-level structural details. This approach has been successfully utilized in studying the structure of amyloid-β(1–42) fibrils, the *Shigella* type-III secretion needle and the ASC inflammasome [21–23].

1.2 NMR spectroscopy

NMR spectroscopy is a widely used technique in a number of scientific fields including physics, chemistry, biology and medicine. Besides being a standard method for the analysis of small chemical compounds, NMR allows for a robust and non-invasive structural analysis of biological macromolecules at atomic resolution. In the field of structural biology, NMR represents a powerful method for analysing the structure, dynamics and interactions of proteins under near-physiological conditions.

1.2.1 Physical principles of NMR

NMR experiments are performed in a large static magnetic field B_0 that is conventionally aligned along the z-axis. NMR-active nuclei have at least two quantized energy levels, also called spin states. The number of allowed spin states depends on the nuclear spin quantum number I, which is determined by the ratio of protons and neutrons of the respective nucleus. Most nuclei that are relevant for biomolecular NMR such as ^{13}C, ^{15}N and ^{1}H have a $I = \frac{1}{2}$ nuclear spin. Atoms with nuclear spin $I = \frac{1}{2}$ adopt two spin states whose degeneracy is broken by the magnetic field (Zeeman effect). The two spin states α and β have energy levels of $+\frac{1}{2}$ and $-\frac{1}{2}$. The energy difference (ΔE) between the two states is given by:

$$\Delta E = h\nu_0 = h\gamma B_0/2\pi \tag{1.1}$$

where h is Planck's constant and γ the isotope-dependent gyromagnetic ratio. The resonance frequency ν_0 is in the radio frequency (RF) range and is defined as the free precession frequency of the nucleus (Larmor frequency). Transitions between the two energy levels can be induced by the absorption of electromagnetic radiation at this resonance frequency.

At equilibrium, the population of the two different spin states is described by the Boltzmann distribution, which gives the ratio of the occupation number N as follows:

$$\frac{N_\alpha}{N_\beta} = \exp(\frac{\Delta E}{kT}) = \exp(\frac{h\gamma B_0/2\pi}{kT}) \tag{1.2}$$

where k is the Boltzmann constant and T the thermodynamic temperature. The equilibrium population difference is proportional to the energy difference between the α and β states and therefore to the strength of the applied magnetic field and inversely proportional to the temperature. The NMR signal intensity is directly determined by the population difference. However, even in large fields the difference remains very small (< 0.01 %), making NMR a relatively insensitive analytical method.

The equilibrium population is shifted towards the low energy α-state resulting in the macroscopic net magnetization M_0. This net magnetization vector precesses around B_0 at the Larmor frequency. The application of a 90° on resonance RF field B_1 rotates the net magnetization into the xy plane, perpendicular to B_0. This rotation creates an oscillating magnetic field that induces a current in the detection coil of the spectrometer that surrounds the sample. Due to relaxation processes the magnetization returns to the state of equilibrium and the signal decays over time. This free induction decay (FID) describes the precession of the nuclear spin about the magnetic field and can be Fourier-transformed to obtain the frequency spectrum of the signal.

For each type of spin in a molecule, the Larmor frequency is perturbed by the local magnetic field that is determined by the surrounding electrons and the local chemical environment of the nucleus. Due to these screening effects, chemically distinct nuclei experience different local magnetic fields, which causes a shift in their resonance frequencies relative to the ideal

Larmor value. This so-called chemical shift (δ) is given relative to a standard in the magnetic field (ν_{ref}) and is reported in parts per million (ppm):

$$\delta = 10^6 \frac{\nu - \nu_{ref}}{\nu_{ref}} \tag{1.3}$$

Since large molecules produce complex chemical landscapes, this gives rise to a multitude of different resonance frequencies of the involved nuclei, providing insight into the local chemical environment. The size of the molecule with its repeating chemical moieties, e.g. in proteins, and the resolution of the experiment determines how clearly chemical shifts are discernible from each other.

The NMR signal decays over time as relaxation causes the transverse magnetization to decay and the system returns to the equilibrium state. There are two principle relaxation parameters in NMR: the spin-lattice relaxation (T_1) and the spin-spin relaxation (T_2). T_1 relaxation is a longitudinal relaxation process in which the magnetization vector returns to its equilibrium position. In the T_1-time the longitudinal magnetization recovers ~ 63 % of its initial value, determining the ideal frequency of repetition of an NMR experiment:

$$M_z(t) = M_0(1 - e^{-\frac{t}{T_1}}) \tag{1.4}$$

T_2 relaxation is a transverse relaxation process that caused by the loss of phase coherence due to short-lived interactions of the spins. In the T_2-time the transverse magnetization irreversibly decays to ~ 37 % of its initial value, primarily determining NMR linewidth ($\Delta\nu$):

$$M_{xy}(t) = M_0(e^{-\frac{t}{T_2}}) \tag{1.5}$$

$$\Delta\nu = \frac{1}{\pi T_2} + \gamma \Delta B_0 = \frac{1}{\pi T_2^*} \tag{1.6}$$

The effective transverse relaxation time T_2^* includes magnetic field inhomogeneities (ΔB_0) that add to the homogeneous T_2 relaxation time. While T_1-times are in the order of seconds, T_2-times are typically in the range of milliseconds.

1.2.2 Relaxation and molecular exchange in solution

Conventional solution-state NMR requires that the molecular complex experiences all possible orientations over the time span of an experiment by rapid molecular tumbling. The size of the complex increases the correlation time τ_c, the time it takes for a spherical molecule to rotate by one radian. Since T_2 depends on the accumulation of dipole-dipole (DD) and chemical shift anisotropy (CSA) effects, it continues to decrease as the particle size increases, while T_1 has its minimum where the reciprocal of the correlation time is similar to the Larmor frequency of the detected nucleus ($\omega_0\tau_c \sim 1$).

Chemical exchange can also contribute to T_2 relaxation. Considering a two-site exchange reaction:

$$\mathrm{A} \underset{\mathrm{k_{-1}}}{\overset{\mathrm{k_1}}{\rightleftharpoons}} \mathrm{B} \tag{1.7}$$

in which the exchange rate k_{ex} is defined as:

$$k_{ex} = k_1 + k_{-1} = \frac{k_1}{p_b} = \frac{k_{-1}}{p_a} \tag{1.8}$$

with p_a and p_b being the equilibrium population of sites A and B, respectively. The sites are assumed to exhibit distinct chemical shifts ω_a and ω_b, with $\Delta\omega$ being the frequency difference between the two chemical shifts. k_1 is the forward first-order kinetic rate constant and k_{-1} is the reverse first-order kinetic rate constant. The contribution to the transverse relaxation rate and linewidth critically depends on how fast the exchange process is on the NMR chemical shift time scale. The kinetics of the exchange can be slow ($\frac{k_{ex}}{\Delta\omega} < 1$), intermediate ($\frac{k_{ex}}{\Delta\omega} \approx 1$) or fast ($\frac{k_{ex}}{\Delta\omega} > 1$). In the slow exchange regime two resonances with frequencies ω_a and ω_b are resolved if the populations of the two sites are similar. In contrast, fast exchange leads to a single averaged resonance with a population-weighted frequency $p_a\omega_a + p_b\omega_b$. In the intermediate exchange regime, a single population-weighted signal or two resonances close to the original frequency can be detected. The linewidth of these peaks is broadened due to the exchange-induced interference during the NMR acquisition period. This intermediate exchange relaxation rate R_{ex} adds to the transverse relaxation rate R_2:

$$R_{ex} = \frac{p_a p_b \Delta\omega^2}{k_{ex}} \tag{1.9}$$

Unlike R_2, R_{ex} is heavily dependent on B_0, because it is proportional to $\Delta\omega^2$ and sensitive to changes in parameters that alter the kinetics of the exchange reaction (e.g. temperature), which are typically in the microsecond to millisecond regime. Importantly, exchange-induced broadening can also stem from a strongly increased correlation time τ_c upon complex formation as when a small NMR-detectable molecule is immobilized on a surface or binds to a high-molecular weight object. This contribution is independent of B_0 and is commonly referred to as lifetime broadening with $\Delta R_{2,A} = k_1$ and $\Delta R_{2,B} = k_{-1}$. Therefore it is possible to monitor these reactions *via* readily observable changes in the NMR spectra.

1.2.3 Solid-state MAS NMR

The local magnetic field experienced by a given nucleus will differ between molecules in a sample depending on a molecule's spatial orientation to the applied static magnetic field. As discussed previously, in solution-state NMR rapid molecular tumbling averages out anisotropic interactions such that chemical shifts average to their isotropic values and dipolar coupling is cancelled out. In static solid samples, molecules are more rigid and thus these anisotropic interactions are not averaged to zero, resulting in extremely broad signals. MAS NMR mechanically averages these interactions by rotating the sample about an axis oriented at a defined angle, which increases the resolution of the spectrum. At the magic-angle (θ_{magic}) of 54.74° the following term describing the expected value of the orientation dependence becomes zero:

$$3cos^2\theta_{magic} - 1 = 0 \tag{1.10}$$

As the hetero- and homonuclear dipolar coupling and CSA interactions all contain orientation-dependent terms, these factors become time-averaged to zero if the sample is spun around the magic angle. While CSA averages to a non-zero value, the quadrupolar interaction is partially averaged leaving a residual secondary quadrupolar interaction. Nuclear dipole-dipole (DD) interaction are time averaged to their isotropic value assuming that the MAS rate is greater or equal to the magnitude of the anisotropic interaction. While this results in narrow signals, the loss of the orientational dependence also means loss of valuable information on structure and dynamics. Depending on the studied system, partial and complete averaging are utilized in NMR experiments. Residual CSA produces spinning sidebands at multiples of the MAS frequency in the spectrum with their intensities depending on the MAS rate relative to the CSA of the nuclear spin.

Due to the large homonuclear dipolar couplings of protons, only the recent development of fast MAS methodology made high-resolution proton detection routinely feasible for protein solid-state NMR. Using rotors with small diameters, samples are now spun at MAS rates of 111 kHz and beyond. Proton-detected NMR is inherently more sensitive than the commonly used carbon detection because of the higher gyromagnetic ratio of ^{1}H nuclei facilitating experiments on protein samples in the sub-mg range and reducing the need for expensive and sometimes impractical ^{2}H-labelling.

As described above, the relaxation properties of a molecule are heavily influenced by its motion in solution, which limits the application of solution-state NMR to fast-tumbling proteins with relatively short correlation times. This requirement for rapid tumbling places an upper limit on the size of target proteins. Since solid-state MAS NMR is not limited by long correlation times, increasing particle size is not accompanied by changes in relaxation parameters and linewidth.

1.2.4 Application of NMR to large molecular systems

Due to the relationship between molecule size and T_2 relaxation, classical solution-state NMR methods are limited to protein complexes up to a molecular weight of $\sim$ 40 kDa. Using more advanced methods like the Transverse Relaxation Optimized Spectroscopy (TROSY), complexes beyond 500 kDa can be studied by solution-state NMR [24–26]. Another approach to reduce T_2 relaxation is to dilute the proton spins through uniform deuteration [27]. Using metabolic precursors, selective protonation of specific groups (e.g. methyls) can be achieved to probe for structural changes of macrocomplexes [28, 29]. In very large systems, it is not possible to obtain full sequence-specific assignment of the protein's backbone chemical shifts. Hence, assignment of the methyl-containing residues is often mutation-guided and therefore very laborious [30].

Intrinsically disordered proteins (IDPs) do not have a well-defined secondary or tertiary structure under physiological conditions. Thus, IDPs do not tumble like globular proteins but rather retain a high degree of local flexibility. These intramolecular motions cause slower relaxation rates and allow for the acquisition of spectra with narrow linewidths even for large proteins. The lack of an ordered structure, however, results in a low dispersion of proton resonances and severe signal-overlap that can complicate data analysis. On the other hand, the significantly decreased transverse relaxation rates also enable the application of long pulse sequences that produce multidimensional spectra to resolve the signals for assignment. In the last years, NMR researchers have developed a diverse methodological toolkit for studying the structural propensities, fast dynamics and conformational plasticity of IDPs *in vitro* and *in vivo* [31–33]. Moreover, various solution-state NMR studies of disordered proteins and peptides have successfully exploited chemical exchange effects to investigate their interactions with large molecular complexes and assemblies [34, 35]. In particular, the investigation of MAP interaction with microtubules and tubulin benefited from the use of relaxation-based and exchange-transferred NMR methods like transferred nuclear Overhauser effect (trNOE) or saturation transfer difference (STD) NMR [36–40].

Although there are no theoretical size and solubility limitations for MAS NMR, challenges regarding sensitivity and spectral crowding can arise with increasing molecular weight. To resolve highly crowded spectra, the acquisition of higher-dimensional spectra combined with the application of sparse-sampling techniques have proven useful [41]. The spectral quality is also affected by protein dynamics and overall sample heterogeneity. Hence, the preparation of reproducible homogeneous isotopically-labelled samples is crucial for performing structural studies by MAS NMR.

Higher-order helical homomeric assemblies containing multiple copies of the same subunit are well-suited for study by MAS NMR because they share the same chemical environment and therefore produce only one set of chemical shifts. To reduce assignment ambiguities, sparse ^{13}C-labelling relying on mixed samples with different isotopic labelling represents a good strategy to distinguish between intra- and inter-subunit cross-peaks. In addition to inter-atomic distance restraints, measuring the subunits accessibility to water with soluble paramagnetic relaxation enhancement (PRE) agents can aid with the validation of the overall assembly architecture. Furthermore, as chemical shifts are directly comparable between solution- and solid-state NMR, the integration of the two methods allows for a detailed analysis of structural and dynamical changes that accompany the formation of an assembly.

Chapter 2

Microtubules and CC1

2.1 Microtubules and the cytoskeleton

The cytoskeleton of the eukaryotic cell consists of an intricate network of interlinking filamentous protein assemblies [7]. Primarily, it is essential for regulating the mechanical support and properties of the cell and, through association with extracellular fibres, the whole tissue [42]. The cytoskeletal framework provides the means for cell movement and processes that require structural reorganization like endocytosis, cell division, or the formation of specialized structures like flagella and cilia [7]. Beyond that, the cytoskeleton coordinates the spatial and temporal organization of the contents of the cell underlying intracellular transport processes and cell signalling pathways [43].

There are three major types of cytoskeletal protein assemblies: actin filaments, microtubules and the diverse intermediate filament protein family. All types resist mechanical deformation and build networks that guide the arrangement and maintenance of cellular compartments. Upon external mechanical force or intracellular signalling, the polymers can quickly reorganize to adjust to the respective stimulus [44]. The principles that determine the different properties of the three cytoskeletal networks are the dynamics of the polymer assembly, their polarity and stiffness, and the type of regulatory factors that calibrate the organization of the networks. Unlike intermediate filaments, both actin filaments and microtubules consist of asymmetrical subunit structures, which form polarized assemblies. This directionality is utilized by molecular motors that are specialized to move towards a particular end of the respective filament. Motors are crucial for the overall organization of the network and have essential roles in transporting cargo within the cell. Intermediate filaments, microtubules and actin filaments do not represent isolated frameworks, but rather are directly and indirectly interconnected through continuous mechanical coupling and specific cross-linking proteins [7].

2.1.1 Microtubule structure

Microtubules are present in all eukaryotic cells and the FtsZ protein family represents an ancient homologue in prokaryotes [45]. Of all cytoskeleton assemblies, microtubules display the highest stiffness and are able to span the length of an animal cell in an almost linear fashion [46]. The assembly is a tube-like structure with an outside diameter of 24 nm and an inner diameter of 17 nm (Fig. 2.1) [47]. The hollow tubulus is constructed from laterally aligned protofilaments, which are composed of repeating α- and β-tubulin dimers that are 8 nm in length. Tubulins are globular proteins with a molecular weight of 55 kilodaltons (kDa) each and high sequence homology sharing $\sim$ 40 % amino acid sequence identity. The longitudinal end-to-end interaction of the dimers defines the distinct polarity of microtubules and the interprotofilament interactions define the stability and mechanical properties of the assembly [48]. In the fully assembled tubulus, the β-tubulin exposing end is called the plus-end and the α-tubulin exposing end is called the minus-end (Fig. 2.1). Although most of the cellular microtubules are typically build from 13 protofilaments, other symmetry architectures have been observed *in vitro* and *in vivo* [49]. The 13-protofilament microtubule commonly has a monomer pitch of three per helical turn resulting in a seam interface due to discontinuity arising from the odd start number. Here, the lateral interprotofilament interactions differ from the rest of the tubulus: instead of the lateral α-α and β-β interface, the seam contains heterologous α-β and β-α contacts that have been shown to be less stable [50].

2.1.2 Microtubule dynamics

Microtubules are highly dynamic structures that can rapidly change in size *via* cycles of polymerization and depolymerization. In mammalian cells, microtubules are typically nucleated by microtubule-organizing centres (MTOCs) that can form γ-tubulin ring complexes (γ-TURC) which act as template structures for the initial microtubule formation [52]. After the nucleation event, the microtubule grows by the addition of tubulin dimers to the ends, with the plus-end growing much more rapidly than the minus-end (Fig. 2.2). The rate of growth is mainly determined by temperature and the local concentration of available tubulin. The depolymerization rate occurs in a stochastic manner, does not directly depend on the subunit concentration and is several times faster than the growth rate. While α- and β-tubulin can both bind GTP, only β-tubulin exhibits GTPase activity, carrying an exchangeable nucleotide binding site and hydrolising GTP to GDP. The binding site on α-tubulin is non-exchangeable and GTP is not hydrolysed. GTP-bound tubulin dimers are incorporated into the growing end of the microtubule, thus establishing and maintaining a stabilizing GTP-cap [50]. The

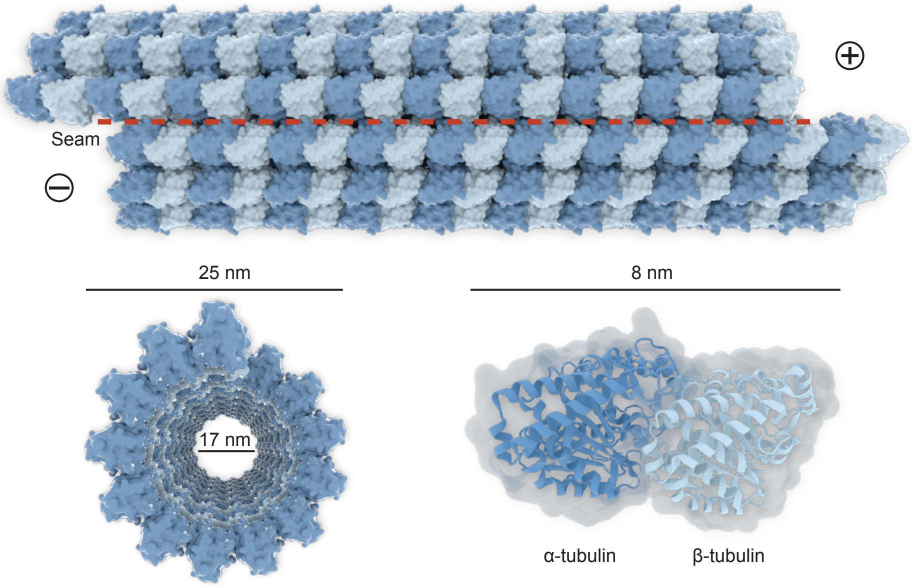

Figure 2.1 **The architecture of microtubules.** Side and top view on a 13-protofilament microtubule with a monomer pitch of three tubulins per helical turn. Atomic model of the tubulin dimer was taken from [51] (PDB code: 1TUB). Image by Barth van Rossum.

hydrolysis of GTP to GDP occurs after a delay and can lead to the loss of the protecting GTP-cap and subsequent rapid depolymerization and shrinkage of the microtubule (catastrophe). Conversely, GTP-islands and specific molecular factors can cause the reformation of the GTP-cap and recovery of microtubule growth (rescue). Hence, the cycle of assembly and disassembly is controlled by the GTPase activity of β-tubulin. Structurally, the growing plus-end of the microtubule often exhibits a slightly curved and flattened sheet-like appearance, while the shrinking plus-end shows highly curved individual protofilaments that seem to 'peel off' from the tubulus [53]. Upon GTP hydrolysis tubulin dimers undergo a straight-to-curved conformational change in the microtubule, leading to weakened lateral interactions between the protofilaments [54]. This results in an outward curvature of the protofilament and microtubule disassembly. The property of microtubule networks switching dynamically between these assembly and disassembly processes is commonly referred to as dynamic instability [55]. To characterize the overall dynamics of a microtubule array, their growth and shrinkage rate and the frequency of catastrophe and rescue events are often-used parameters.

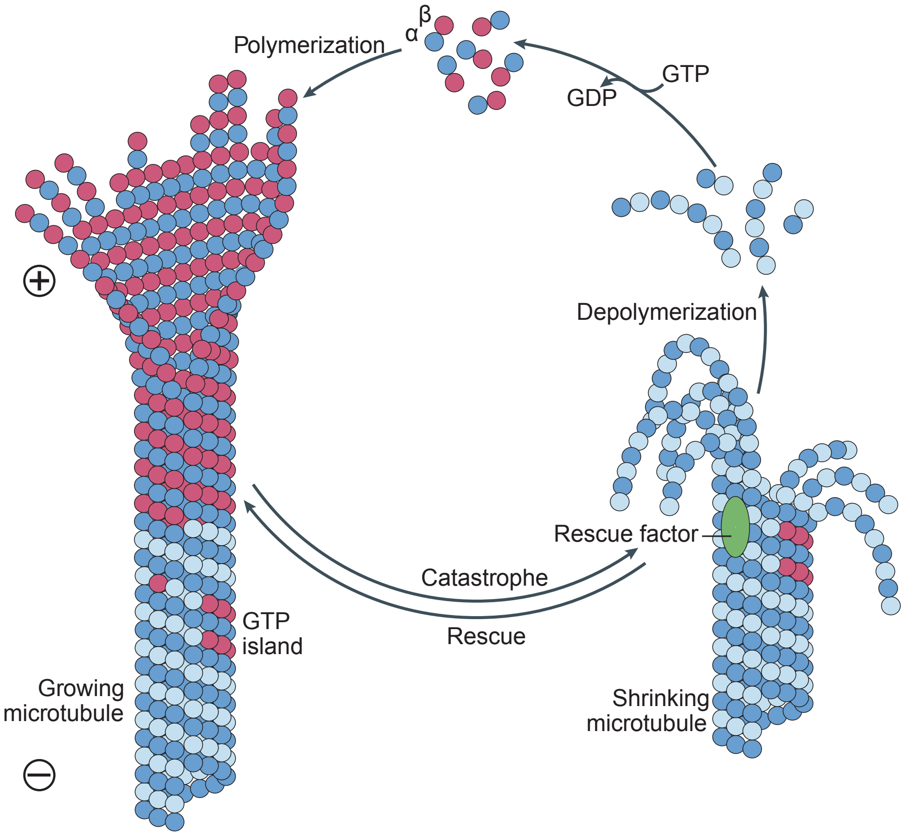

Figure 2.2 **The microtubule assembly cycle.** Microtubules switch between polymerization and depolymerization in cycles of catastrophes and rescues depending on the nucleotide-state of the bound GTP/GDP nucleotide. GTP-β-tubulin is shown in magenta, GDP-β-tubulin in light-blue and α-tubulin in dark-blue. GTP-bound tubulin dimers are incorporated into the growing microtubule plus-ends, building a stabilizing GTP cap. Hydrolysis of the GTP-cap leads to rapid depolymerization and catastrophe, while GTP-islands on the microtubule and molecular rescue factors can induce prolonged polymerization and rescue. Image adapted and modified from [56].

2.1.3 Microtubule-associated proteins

Although dynamic instability is also present *in vitro* and represents a structural property of tubulin itself, *in vivo* microtubule stability is modulated by a variety of additional cellular effectors called microtubule associated proteins (MAPs) [56–58]. All eukaryotic cells contain diverse sets of MAPs that modulate and regulate the dynamics and the structure of the microtubule network (Fig. 2.3). MAP function is of vital importance in a number of cellular events that require finely-tuned cytoskeletal organization like mitosis, cell motility and differentiation [56, 59]. Beyond the mere maintenance of cytoskeletal organization and integrity, MAP function also plays a role in controlling and mediating interactions with other elements of the cell, such as membranes [60].

The motor proteins of the kinesin and dynein families belong to a prominent group of MAPs and use microtubules as tracks for anterograde (plus-end) and retrograde (minus-end) cellular transport, respectively [61]. They are ATPases that power the movement on the microtubules and can transport large cargoes (e.g. secretory vesicles) in the direction of the nucleus or the cell periphery. Moreover, motor proteins are involved in the mediation of microtubule-to-microtubule contacts, e.g. in the separation of sister chromatids during cell division [62]. Intriguingly, some members of the kinesin family (kinesin 8, 13 and 14) are microtubule depolymerases that regulate microtubule disassembly by removing terminal subunits or target the GTP-cap in an ATP-dependent manner [63]. Kinesin-13 is known to diffuse along the microtubule lattice, stabilizing the curved protofilaments of disassembling microtubules [64]. The structurally and functionally diverse group of plus-end-tracking proteins (+TIPs) also localizes to the growing end of the microtubules [65]. Here, they can act as microtubule polymerases, like the XMAP215 family of proteins, which recruit tubulin dimers and promote rapid and processive polymerization of the plus-end [66]. Another group of +TIPs, known as end-binding proteins (EBs), restructure microtubule ends resulting in increased rates of polymerization and catastrophe *in vitro* [67]. EB-proteins contain multiple binding sites for additional +TIP partners and are thus considered to be essential regulators of +TIP networks, recruiting a variety of factors to microtubule growing ends. Moreover, the EB1 homologue Mal3p has been reported to preferentially bind the seam of microtubules potentially stabilizing the tubular assembly [68]. Another well-studied group of +TIP proteins are the cytoplasmic linker proteins (CLIP)-associated proteins (CLASPs) that can suppress catastrophes and promote rescues [69, 70]. Here, the cytoskeleton-associated protein-glycine-rich domain (CAP-Gly) has a central function as a tubulin-binding module conserved in organisms from yeast to human [71]. Acting as a connecting element in the dynein-dynactin pathway, defects in the CAP-Gly domain of CLIP170 interfere with the proper recruitment of dynactin to the growing ends of microtubules [72].

Examples of minus-end-tracking proteins (-TIPs) are the above mentioned γ-TURC, which can nucleate and stabilize microtubules. When recruited to the microtubule lattice by augmin, γ-TURC can initiate the formation of 'branched' microtubule arrays [73]. The invertebrate -TIP Patronin stabilizes microtubule minus-ends by protecting them from kinesin-13-induced depolymerization during mitosis [74]. Loss of this activity affects the maintenance of non-centrosomal microtubules in cell migration and morphology. In mammals, the calmodulin-regulated spectrin-associated proteins (CAMSAP) have only recently emerged as γ-tubulin-independent minus-end regulators that stabilize non-centrosomal microtubules [75, 76].

The ring-forming enzyme katanin can sever microtubules into small fragments employing an ATP-dependent power stroke and can also depolymerize microtubules from their ends [77, 78]. This mechanism allows for rapid disassembly and reorganization of microtubule networks and has been reported to be essential in biological processes like chromosome segregation, spindle scaling and phototropism [79, 80].

Historically, many early studies on MAPs investigated proteins that had been isolated from animal brain tissue, since it is a very accessible and abundant source of microtubules. The members of the so-called structural MAPs are mainly of neuronal origin, lack any enzymatic activity and bind to microtubules with rather low affinities [57]. Typically, they contain several repeating domains that allow for a single MAP to bind several tubulin dimers independently. This molecular architecture enables them to promote tubulin polymerization and the formation of microtubule bundles in neurons. The structural MAPs include members of the MAP1, MAP2, MAP4 family and Tau. While MAP1, MAP2 and Tau are all exclusively found in the axons and dendrites of nerve cells, MAP4 is also present in many other types of tissue [81, 82]. Due to differences in the molecular topology and the microtubule interaction motifs, the MAP1 family does not belong to the same MAP class of Tau, MAP2 and MAP4 [82, 83]. The latter three proteins all contain an N-terminal projection domain and a C-terminal microtubule binding domain which carries a proline-rich sequence and, depending on protein and splice variant, three or four pseudorepeats. In these $\sim$ 30-residue spanning repeats the Tau/MAP2/MAP4 family shares significant sequence homology, while the N-terminal projection domain varies considerably in size and sequence among the proteins.

All structural MAPs have been proposed to serve as primary targets of phosphorylation-mediated regulation of microtubules involving a number of protein kinases [84]. Hence, upstream regulation of MAP activity through phosphorylation appears to be a crucial regulatory pathway to control microtubule organization in the cell. While the complexity of the MAP regulatory network has yet to be unravelled, several studies report, although to a varying degree, that phosphorylation can directly impede microtubule association of structural MAPs [85–87]. One example is the microtubule-affinity-regulating kinase (MARK) that has been shown to destabilize microtubules by phosphorylating MAPs when overexpressed in neuronal cells [88]. Under physiological conditions, this mechanism is thought to facilitate vesicle transport by stripping MAPs off the microtubule tracks and paving the way for the respective motor proteins [89]. Furthermore, the observation of differentially phosphorylated MAPs during early cellular morphogenesis suggests that the regulation of MAP networks plays an important role in major developmental processes like the generation and maintenance of cell polarity [90, 91].

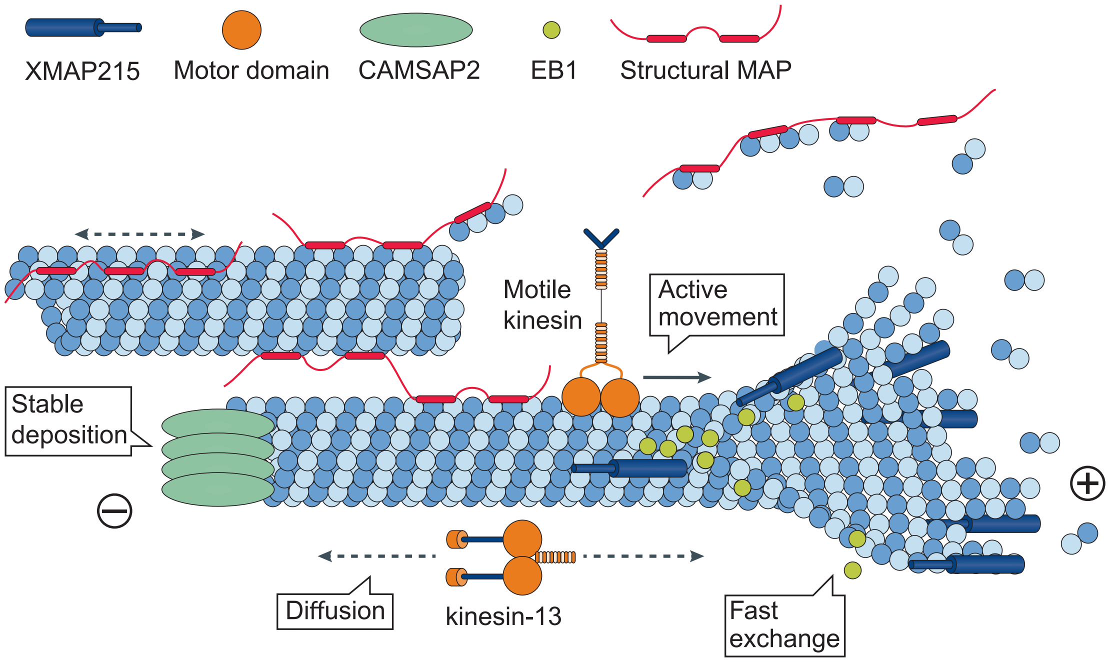

Figure 2.3 **Overview of MAPs in the cell.** Illustration of several types of MAPs on the microtubule. While XMAP215 localizes to distal growing microtubule plus-ends, EB1 forms a comet-like accumulation tens of nanometres away from the tip that exhibits rapid turn-over. In contrast, CAMSAP dissociates slowly at growing microtubule minus-ends forming stable depositions. Motile members of the kinesin family (e.g. kinesin-4) processively move to the microtubule plus-end in an ATP-driven manner powered by their motor domains. Kinesin-13 diffuses on the microtubule lattice towards the microtubule ends, where it acts as an ATP-dependent depolymerase. Structural MAPs are composed of repeating modular domains that can bind, polymerize or bundle microtubules in a non-enzymatic way. Their movement on the microtubule lattice might also be realized *via* bi-directional diffusion. Image adapted and modified from [56].

2.1.4 Tau and tauopathies

Among the mammalian Tau/MAP2/MAP4 family, Tau is the most-studied member due to its importance in the pathology of several neurodegenerative diseases, commonly referred to as tauopathies [92].

In healthy brains, Tau is located at the axons of neurons, where it contributes to the assembly and stabilization of microtubules that drive neurite outgrowth [93, 94]. Beyond this, Tau is a multifunctional protein that plays a role in cell signal transduction and enhancement, heat shock cell protection and long-term potentiation [95, 96]. Tau has numerous binding partners including membrane-lipids, SH3-containing proteins and other cytoskeletal proteins like actin. [97–99]

In adult human brains, six Tau isoforms, ranging from 352 to 441 residues, are expressed and constitute ~ 80 % of all neuronal MAPs [100, 101]. Depending on the inclusion of exon 10, isoforms contain a microtubule-binding domain (MTBD) with either three (3R) or four (4R) of the above-mentioned ~ 30-amino-acid microtubule-binding repeats (4R Tau in Fig. 2.4 **A**). NMR studies on Tau revealed its overall intrinsic disorder in solution and short stretches of residues with β-strand propensity [102]. The MTBD contains several hydrophobic binding regions that interact rather transiently with tubulin and microtubules [103, 36]. These motifs are interspersed by linker regions that remain flexible in the complex. Recent cryo-EM data suggests a model in which the repeats bind longitudinally along a microtubule protofilament (Fig. 2.4 **B** and **C**) [104]. However, this data also reports some highly conserved Tau regions that seem to remain flexible in the complex, suggesting that proper tubulin and microtubule interaction might require high conformational plasticity of the protein. This dynamic mode of interaction is reinforced by the observation that Tau can form liquid-like droplets that nucleate microtubules and can freely diffuse along the microtubule lattice [105–107]. Early *in vitro* analysis had shown that Tau promotes tubulin polymerization and also stabilizes assembled microtubules [108]. Furthermore, Tau can bundle microtubules with a spacing of 25 to 41 nm both *in vitro* and *in vivo* [109, 110]. This distance is regulated *via* its N-terminal projection domain and truncations of this domain modulate the microtubule spacing within the bundle. Interestingly, disease-related mutations in the Tau MTBD can cause distinct defects in microtubule organization that may have a deleterious impact during neurodegeneration by misregulating the dynamic and bundling properties of microtubules [111]. While Tau expression in non-neuronal cells resulted in microtubule stabilization and bundling, Tau depletion in primary cerebellar neurons inhibited neurite polarity and outgrowth [112, 113]. Curiously, Tau knockout (KO) mouse lines are viable and show no overt phenotype, but the animals develop motor deficits and cognitive impairments during older age [114]. This is possibly explained by the compensatory expression of other MAP proteins like MAP1A, but the mechanism remains elusive [115]. Studies on the effect of stress on Tau KO mice show that Tau is an important mediator in stress-driven neuropathology [116]. More recently, Tau emerged as a key regulator of the cell's compensatory mechanisms upon oxidative stress, which might have physiological significance in the early stages of neurodegenerative disorders [117].

Neurodegenerative diseases classified as tauopathies include Alzheimer's disease, Parkinson's disease, corticobasal degeneration, progressive supranuclear palsy and chronic traumatic encephalopathy [92]. The defining characteristic of these neurological disorders is the aggregation and accumulation of Tau in neurons and glia of the affected patients. The clinical symptoms can vary strongly among the conditions, but often include cognitive, behavioural and motor impairments, combined with a characteristic neuropathological pattern of brain atrophy. The most prevalent and best-known tauopathy is Alzheimer's disease, in which β-amyloid plaques and Tau inclusions called neurofibrillary tangles (NFTs) form and propagate in the course of the disease. Ultrastructurally, NFTs contain paired helical filaments (PHFs) and straight filaments (SFs) that are morphologically discernible by negative-stain electron microscopy but are both formed by 3R and 4R Tau isoforms (Fig. 2.4 **D**) [118, 119]. In the brain, hyperphosphorylation or mutation of Tau is thought to induce its dissociation from the microtubules and subsequent self-aggregation resulting in the formation of the cytotoxic fibrils [95]. Due to the small number of hydrophobic residues, Tau shows little tendency to form filaments *in vitro*. Tau aggregation can only be reproduced by polyanionic agents such as RNA, polyglutamate and heparin [120]. Due to this limitation, much of the structural research on Tau filaments had to rely on artificially induced or seeded filaments that are highly heterogeneous and might lack physiological relevance [121]. Only recently, an investigation by cryo-EM resolved the atomic structures of PHFs and SFs derived directly from an Alzheimer's patient, revealing similar protofilaments but differences in the protofilament packing (Fig. 2.4 **E**) [3]. The observation that the structure of Tau filaments from Pick's disease adopt a different fold when compared to the Alzheimer filaments suggests that aggregated Tau may adopt disease-specific molecular conformations [122].

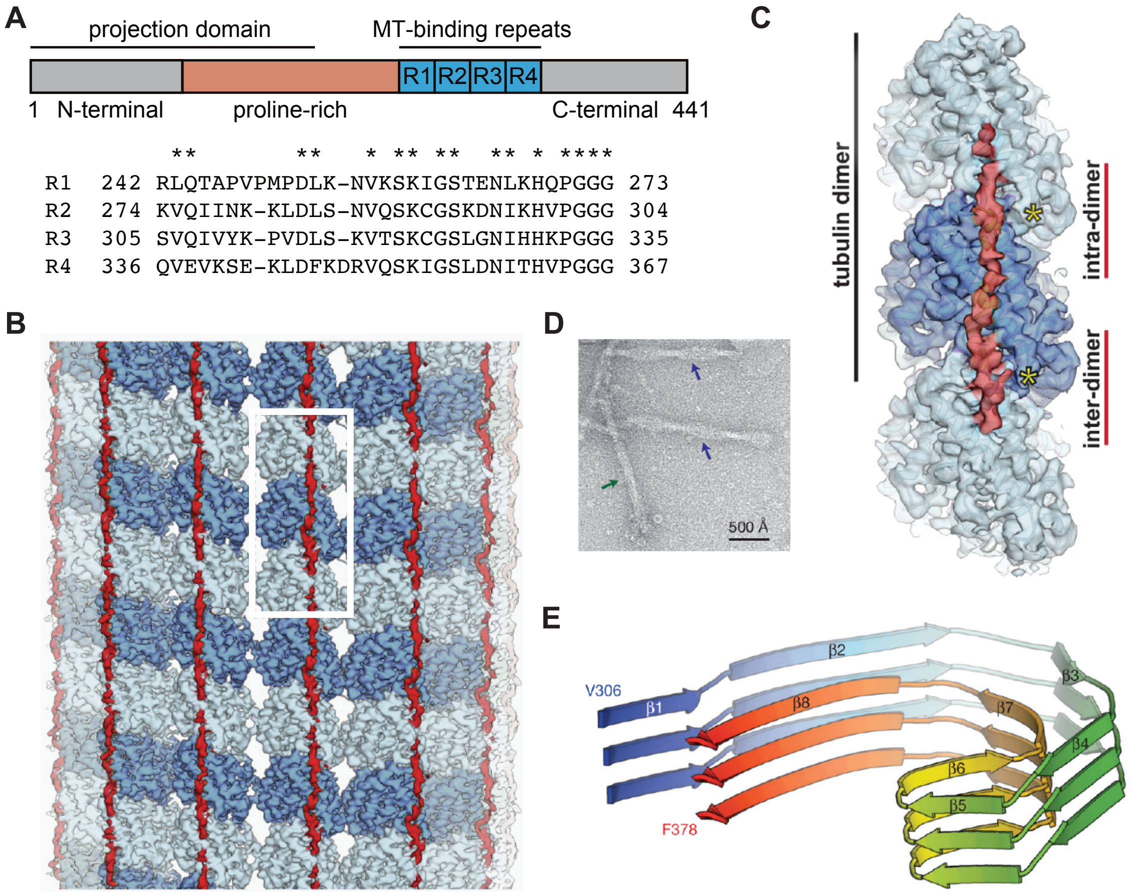

Figure 2.4 **The MAP Tau and its role in disease.** **A** The domain architecture of the 441-residue 4R-Tau contains four MT-binding domains (R1-R4) and a projection domain that includes the N-terminal region and a part of the proline-rich region. The sequence alignment of the repeats is shown below with conserved residues marked with an asterisk. **B** Cryo-EM density map at 4.1 Å resolution of a Tau-decorated microtubule (Tau in red, α-tubulin in dark-blue, β-tubulin in light-blue). White frame see blow-up in **C**. Tau spans over three tubulin monomers binding across intra-and inter tubulin interfaces. The tubulin C-termini are marked with yellow asterisks. **D** Negative-stain electron micrograph of Tau filaments showing distinguishable PHFs (blue arrows) and SFs (green arrow). **E** Rendered cartoon structure of Tau fibrils adopting the Alzheimer fold. The structure includes eight β-strand regions spanning R3 and R4 (306-378). Images **B**, **C** adapted and modified from [104] and **D**, **E** from [3].

2.2 Microtubule organization and cell stress in plants

The plant microtubule array plays a vital role in growth, development and the maintenance of homeostasis in plants [123]. With tubulin being one of the most conserved proteins among eukaryotes, the sequence and overall structure do not show significant differences between animals and plants (e.g. Human and Arabidopsis share ~ 80 % sequence identity). In contrast to animals, higher plants may carry a large number of different tubulin genes (e.g. six α-tubulin genes in Arabidopsis) due to their increased gene redundancy and genome plasticity in events of polyploidization [124]. Although some tubulin isotypes have been reported to be exclusively expressed in specific plant tissues, the extent of how tubulin heterogeneity impacts microtubule function remains unclear.

Like in most eukaryotes, the common plant microtubule consists of 13 protofilaments with a pitch of 3 tubulin dimers associated in a head-to-tail fashion. Plant microtubules display the characteristic metastable behaviour, resulting from the above described direct link between GTP hydrolysis and polymerization activity. Although the overall mechanism of dynamic instability is conserved between animals and plants, there are subtle differences in microtubule dynamics: for example, while animal microtubule plus-ends frequently undergo neither growth nor shrinkage in so-called pause states, this state only rarely occurs in Arabidopsis cells [125]. In contrast to animal cells, free microtubule minus-ends that show no association with any nucleation complexes and exhibit slow depolymerization are very common in plant cells. In higher plants, the fundamental organization of nucleation complexes is similar to that of animals, carrying homologous structures to the γ-TURC [126]. In Arabidopsis cells, the microtubule-associated atypical proteins kinase (PHS1) can inhibit microtubule polymerization directly through phosphorylation of a threonine residue that resides at the longitudinal interdimer interface [127]. Lacking a homologous kinase, animal and fungal organisms do not possess a similar mechanism.

Microtubule arrays in plant cells manifest in multiple distinct organizations [123]. During mitosis, microtubules radiate from the nuclear envelope, forming a dense and narrow structure called the preprophase band that marks the division plane of the cell [128]. After the separation of the chromosomes by the mitotic spindle, microtubules form the phragmoplast that guides the separation of the two daughter cells in late cytokinesis by providing a framework for the transport of cell wall components from the Golgi to the cell plate [129]. In interphase cells microtubules commonly form a dense network beneath the plasma membrane in a quasi-2D sheet [130]. These non-centrosomal cortical microtubules nucleate mostly at the plasma membrane in parallel to or branching from a pre-existing microtubule. The cortical array regulates cell stability, shape and growth in plants [123].

2.2.1 Cellulose synthesis and the plant cell wall

The cortical microtubule array guides cellulose synthesis by steering the membrane-embedded cellulose synthase complexes (CSCs) [131]. This hexameric rosette-like complex is mainly composed of cellulose synthase (CesA) subunits that synthesize β-1,4-glucan chains which assemble to para-crystalline cellulose microfibrils through extensive hydrogen-bonding [132]. The CSC structure, approximately 20 - 30 nm in diameter, is proposed to comprise 36 CesAs that can each synthesize an individual glucan chain into the apoplast. In Arabidopsis, there are 10 CesA genes (CesA1-10) that encode for proteins that are involved in either primary or secondary wall cellulose synthesis [133]. While some CesAs were assigned to either or the other, the role of some CesA family members and the exact stoichiometry of the respective complexes remain unknown. Visualization of the CSCs in transgenic Arabidopsis plants revealed that they move on tracks of cortical microtubules with an approximate speed of 250 - 300 nm/min [131]. This movement occurs as nascent cellulose fibres become entangled in the cell wall, which results in a repulsion and thus displacement of the CSCs by its own catalytic activity. Hence, mutants with reduced cellulose synthesis also show decreased speed of the CSC [134, 135]. The interaction between microtubules and CSCs is mediated by the Cellulose Synthase Interacting 1 (CSI1)/POM2 protein [136]. This leads cellulose microfibrils and cortical microtubules to coalign in non-dividing interphase cells [137]. In etiolated Arabidopsis hypocotyls, cellulose fibrils are mostly oriented transverse to the growth axis. In response to internal or external stimuli, such as light or hormone application, the microtubule network can dynamically reorientate to inhibit cell expansion [80, 138]. This process is tightly regulated and relies heavily on the composition and the mechanistic properties of the cell wall.

Besides supporting directed plant growth and thus determining plant morphology, the cell wall provides mechanical rigidity and stability to the plant body and protection against its environment [139]. The primary and secondary wall differ in composition, thickness and function. While the flexible and thin primary cell walls form during cell division and are reinforced during cell growth, the more rigid and thick secondary cell walls form later and are deposited underneath the primary walls of specialized cells like tracheary elements and fibres [140]. Cellulose is the major constituent of both cell wall types and acts as a framework for deposition of other wall components. In contrast to cellulose, other water-soluble carbohydrate-based cell wall polymers like hemicellulose and pectin are synthesized in the Golgi and subsequently transported to the apoplast by exocytosis [141]. The primary cell wall also contains a number of structural glycoproteins that are involved in processes like cell-cell interaction, cell wall remodelling and defence response [142].

2.2.2 MAPs in plant cells

Resulting from the direct functional link between cortical microtubules and cellulose synthesis, regulation and maintenance of the microtubule network is of vital importance for the plant's ability to coordinate tissue growth, which is strictly controlled by the cellulose deposition patterns [143]. Hence, there are numerous plant MAPs that structure and restructure the cortical microtubule array under specific developmental or environmental conditions [144, 145]. While plants do contain many MAPs common to most eukaryotes, they also produce several plant-specific MAPs with no clear homologues in species outside the plant kingdom. These include the above-mentioned POM2/CSI1 that tethers the CSC to microtubules and the MAP70 protein family that affects microtubule dynamics and secondary cell wall patterning [136, 146]. While the +TIP family members EB1, CLASP and XMAP215 are evolutionarily conserved between animals and plants, SPIRAL1 represents an example of a plant-specific +TIP [147]. By accumulating at the microtubule growing plus-end, it promotes microtubule polymerization and controls anisotropic cell expansion. The -TIP SPIRAL2 stabilizes free microtubule minus-ends promoting polymerization of acentrosomal cortical microtubules in Arabidopsis [148].

Compared to other eukaryotes, higher plants contain a diverse set of kinesins [149]. While the function of some subfamilies (e.g. kinesin-5 and kinesin-14) are similar to those in animals and fungi, others are more specialized or unique to plants (kinesin-7 and kinesin-14). Notably, plants lack dynein as the major minus-end-directed motor protein but employ minus-end-directed kinesins for vesicle transport [150].

The biological roles of katanin in plants are well-studied and include a diverse set of plant developmental processes [151]. One of the most prominent functions of katanin is the fragmentation and reorientation of cortical microtubules in response to the perception of blue light [80]. The severing activity of katanin is regulated by hormones like gibberellic acid (GA), ethylene and auxin [152].

The members of the MAP65 family are evolutionarily conserved across eukaryotes, but are most-extensively studied *in planta* [153–155]. They induce antiparallel microtubule bundling in kinetochore fibres and in parts of the cortical array. Although the 25 - 30 nm MAP65-induced spacing of the microtubules is comparable to the spacing produced by brain-derived MAPs like Tau, the proteins are not homologous.

2.2.3 The cellular stress response

Abiotic stresses, such as soil salinity, substantially impact plant growth and thus dramatically curtail global agricultural productivity ($\sim$ 50 - 80 % loss in yield) [156, 157]. Most abiotic stresses affect the water equilibrium within the plant cell. Under normal conditions, high turgor pressure pushes the plasma membrane of the protoplast against the rigid cell wall. Under conditions of extreme osmotic stress, the protoplast can shrink and the interface between membrane and cell wall is lost (plasmolysis), disrupting cellulose synthesis and plant growth. Mild osmotic stress leads to the rapid displacement of the CSCs from the plasma membrane to microtubule-associated CesA compartments (MASCs), also known as small CesA compartments (SmaCCs) [158, 159]. Hence, cellulose production is halted until the CSC pool can repopulate the plasma membrane.

To maintain the osmotic pressure, plant cells respond to salt through elaborate signalling pathways, which involve the propagation of intra- and intercellular Ca^{2+} signals and the production of reactive oxygen species (ROS) and abscisic acid (ABA) [156]. This framework activates the salt overly sensitive (SOS) pathway that attempts to remove Na^{+} from the cell's cytoplasm [160].

Cortical microtubules have been proposed to serve as sensors of environmental stress in interphase cells. Salt stress and other osmotic stresses result in rapid depolymerization of the microtubule array [161]. However, under prolonged salt exposure the microtubules are re-assembled into a stress-tolerant microtubule array. Intriguingly, degradation of the above-mentioned SPIRAL1 by the 26S proteasome was shown to be essential for the fast depolymerization of the microtubule array upon salt stress in Arabidopsis [162]. Moreover, upon acute hyperosmotic stress, the intrinsic phosphatase activity of PHS1 is suppressed, leading to direct phosphorylation of α-tubulin further aiding with depolymerization [127].

While there are many molecular factors known that induce and promote the depolymerization of the microtubule array under stress-conditions, far less is known about the factors that establish and organize the stress-tolerant microtubule array.

2.2.4 The companion of cellulose synthase proteins

The companion of cellulose synthase (CC) proteins are a novel class of plant-specific proteins that co-express with multiple CesA genes and associate with CSCs in the plasma membrane [163]. Based on phylogenetic estimates, the CC protein family has four members in Arabidopsis (CC1-4), all lacking clear homology to proteins of known function. Each member is composed of a cytosolic N-terminus, a transmembrane (TM) domain and an apoplastic C-terminus (Fig. 2.5 **A**).

The double knockout plants of CC1 and its closest homologue CC2 (*cc1cc2*) display no phenotypic deviations from the wild-type (WT) when grown under regular conditions. However, on high salt-containing media (75 and 100 mM NaCl), the mutant seedlings show clear growth defects, including cell swelling, reduced hypocotyl elongation and contain significantly lower levels of cellulose (Fig. 2.5 **B** and **C**). Treatment with the cellulose synthesis inhibitors isoxaben, dichlobenil (DCB) and the microtubule depolymerizing agent oryzalin, each leads to similar growth defects. In contrast, applying sorbitol to mimic the NaCl-induced osmotic pressure does not reduce hypocotyl growth compared to the WT, indicating that CC1 functions in response to ionic rather than osmotic stress.

Live cell imaging of fluorescently labelled GFP-CC1 revealed that GFP-CC1 is co-delivered with CesA proteins to the plasma membrane, where it tracks together with the CSCs. Upon salt stress, CC1 is depleted from the plasma membrane and co-localizes to MASCs/SmaCCs together with the CSCs. When salt stress is applied, the cortical microtubule array of WT-cells disintegrates after 2 h and then reassembles after 8 h to a stable stress-tolerant array. Intriguingly, the *cc1cc2* array disassembles very rapidly after 30 min and reassembles after 4 h, only to gradually disappear again around the 8 h mark, remaining virtually absent during the rest of the experiment (50 h) (Fig. 2.5 **D**). Furthermore, while the frequency of catastrophe and rescue events is increased during the recovery phase in WT-cells, indicating structural reorganization of the microtubule network, the *cc1cc2* mutant cells undergo no such change in microtubule dynamics. These findings suggest that CC proteins play an essential role in safeguarding and restructuring the microtubule array under salt stress conditions. Indeed, microtubule co-sedimentation and turbidity assays showed that the cytosolic N-terminus (residues 1-120, CC1ΔC223) binds microtubules ($K_D = 9.5 \pm 2.0\,\mu\text{M}$) and promotes their polymerization *in vitro* (Fig. 2.5 **E** and **F**). Notably, expression of CC1ΔC223 is sufficient to restore microtubule reassembly, cellulose synthesis and seedling growth in *cc1cc2* mutant seedlings grown on salty media (Fig. 2.5 **G**). Lacking the transmembrane domain, CC1ΔC223 is freely localized in the cytosol, mainly near microtubules at the cell cortex. In contrast, the C-terminal truncation (residues 121-342, CC1ΔN120) still tracks together with CSCs at the plasma membrane, but expression does not restore *cc1cc2* growth on salt-containing media. Still, expression of CC1ΔN120 is able to partially rescue the reduced and swollen cells of the *cc1cc2* growth phenotype caused by cellulose synthase inhibition through isoxaben and DCB treatment. Hence, the N- and C-terminus of CC1 appear to have distinct cellular functions: while the C-terminus may support cellulose synthesis under adverse conditions directly at the CSC, the N-terminus is involved in reorganizing the cortical microtubule array under salt stress conditions. The observation that only CC1ΔC223 is essential for the cell's recovery after salt-exposure revealed that the reduced growth arises mainly due to the defects of the microtubule array. Although the research by Endler et al. revealed the importance of the CC proteins during salt stress, the molecular mechanism by which CC1 binds and reorganizes microtubule networks to render them stress-tolerant is not yet understood.

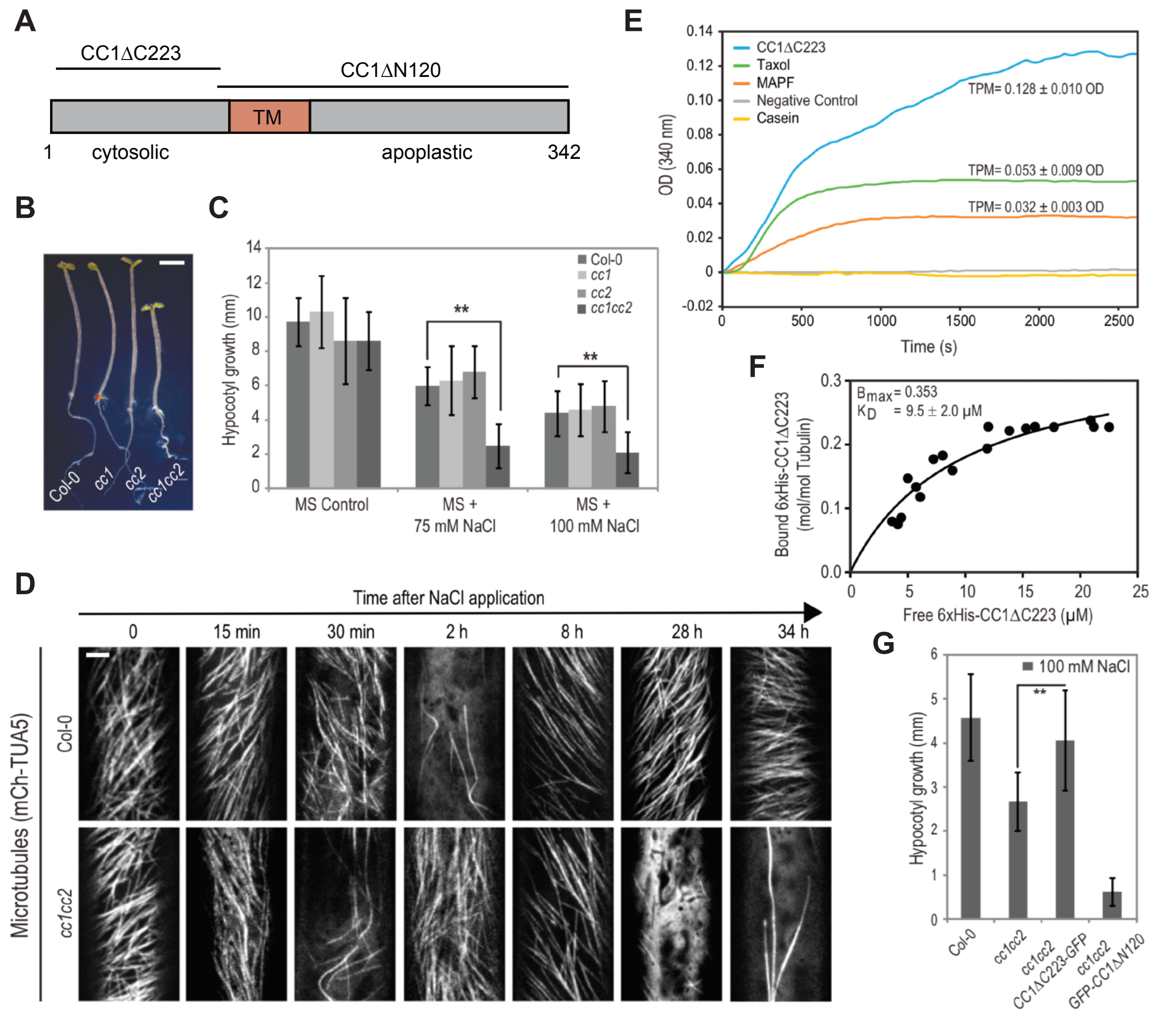

Figure 2.5 **The MAP CC1 sustains cellulose synthesis during salt stress.** **A** The domain architecture of CC1 contains a cytosolic N-terminus, a transmembrane domain (TM) and an apoplastic C-terminus. The protein truncations CC1ΔC223 and CC1ΔN120 are indicated. **B** Hypocotyl growth of seedlings carrying single (*cc1*, *cc2*) and double (*cc1cc2*) knockout mutations on salt-supplemented media compared to the WT control (Col-0). Quantification shown in **C** with two different salt concentrations. **D** Cortical microtubule coverage of Col-0 and *cc1cc2* cells after exposure to salt over time. Scale bar = 2.5 mm. **E** Microtubule turbidity assay showing that CC1ΔC223 promotes microtubule formation *in vitro* (positive control: Taxol and MAPF, negative control: buffer and casein). **F** Binding constant determination of CC1ΔC223 to MTs by spin down assay. **F** The hypocotyl growth of *cc1cc2* plants on salt is restored by CC1ΔC223-GFP but not by GFP-CC1ΔN120. Images adapted from [163].

2.3 Aim and scope of this project

Plant biomass is largely comprised of polysaccharide-based cell walls, of which cellulose is the main constituent. The cell walls make up the bulk of plant biomass, with a total annual production rate of approximately 40 billion tonnes representing the major carbon sink on Earth [164, 139]. Understanding how cellulose synthesis is regulated is therefore of immense importance to plant biology in general and agricultural activity in particular. Despite the importance of the cell wall and cellulose synthesis for plant growth, very little is known about how these processes respond to abiotic stress such as salt exposure, or how cellulose synthesis, and thus plant growth, may be improved to enhance stress-tolerance [165]. The organization and regulation of the cortical microtubule array are essential to maintain cellulose synthesis under salt stress conditions [166]. The CC proteins, which are integral components of the CSC, can bind to microtubules and support their re-assembly to a stress tolerant array after salt exposure [163]. However, the molecular mechanism and structural characteristics of this interaction remain unknown. A detailed molecular description of the mechanism by which CC1 organizes microtubule networks is largely lacking and the general properties that render a microtubule array stress resistant are poorly understood.

The aim of this project was to investigate the CC1 structure and its interaction with microtubules by solution-state NMR spectroscopy. Three main questions are addressed in this thesis: How does CC1 structure relate to its microtubule-binding function? What are the effects of CC1-interaction on the microtubule organization? What are the essential structural and functional features of CC1 and how do they compare with other known MAPs? To gain a complete picture of the mechanism, the *in vitro* approach was combined with extensive *in vivo* experiments designed to complement and validate the results. The effects of mutation and fragmentation on protein function help to identify the essential determinants of the interaction developing a functional classification of the MAP CC1.

Understanding the mechanisms that govern the polymerization, stabilization and reorganization of cortical microtubules under salt stress will offer valuable new insights on how plants maintain growth on saline soil and might reveal paths to the development of salt-tolerant cultivars.

Chapter 3

Material and Methods

3.1 Materials

The following tables list

- chemical compounds (Tab. 3.1)
- buffer and media (Tab. 3.2)
- equipment (Tab. 3.3)
- software (Tab. 3.4)

which were used in this project. Further customary chemicals not mentioned in the list were provided by the vendors Roth, Merck or Sigma-Aldrich.

3.2 Sample preparation

Cloning, expression and purification of CC1ΔC223, CC1ΔC223YYAA and AtSH3 were performed by Dr. Anne Diehl, Martina Leidert and Natalja Erdmann at the FMP. Peptides were synthesized by Ines Kretzschmar at the FMP peptide chemistry core facility.

3.2.1 Expression of CC1ΔC223

For heterologous protein production of CC1ΔC223, pETM11-HisCC1ΔC223 (KanaR) and the helper plasmid pBAD-σ32(I54N) (AmpR) were co-transformed into the *Escherichia coli* strain BL21(DE3) star. At an OD of 0.6, σ32-I54N expression was induced by 0.2 % L-arabinose for 2 h on LB medium, followed by the induction of His-CC1ΔC223 with 1 mM

Table 3.1 Chemicals

Chemical	Manufacturer
^{15}N-Ammonium chloride	Cambridge Isotopes
^{13}C-Glucose	Cambridge Isotopes
2-Mercaptoethanol	Sigma-Aldrich
ATP	Roth
BSA	Roth
Colchicine	Cytoskeleton, Inc
Complete protease inhibitor (EDTA-free)	Roche Diagnostics
Coomassie Brilliant Blue G-250	Serva
Deuteriumoxide (D_2O) 99.9 %	Deutero GmbH
Dithiothreitol (DTT)	Roth
Dimethyl sulfoxide (DMSO)	Cytoskeleton, Inc
EDTA	Roth
EGTA	Roth
Ficoll PM 70	Sigma-Aldrich
GppCp	Jena Biosciences
GTP	Roth
Imidazole	Roth
Isopropyl β-D-1-thiogalactopyranoside (IPTG)	Roth
Glucose	Roth
Glycerol 99.5 %	Sigma-Aldrich
Heparin sodium salt	Roth
HRV-3C PreScission Protease	Sigma-Aldrich
Kanamycin sulfate	Roth
Sodium azide	Roth
Sodium dodecyl sulfate (SDS)	Roth
Taxol	Cytoskeleton, Inc
Tetramethylethylenediamine (TEMED)	Roth
Vinblastine	Cytoskeleton, Inc

Table 3.2 Buffer and Media

Buffer/Medium	Composition
SDS-running buffer	25 mM Tris-HCl, 190 mM Glycin, 0.01 % SDS
SDS-sample buffer (6x)	375 mM Tris-HCl , 12 % SDS, 60% Glycerol, 0,02 % Bromophenol blue, 600 mM DTT (pH 6.8)
Tris sample buffer	20 mM Tris-HCl, 200 mM NaCl (pH 7.4)
PEM	100 mM Na-Pipes, 1 mM EGTA, 1 mM $MgSO_4$, 1 mM GTP and 1 mM DTT (pH 6.9)
hPEM	1 M Na-Pipes, 1 mM EGTA, 1 mM $MgSO_4$, 1 mM GTP and 1 mM DTT (pH 6.9)
PBS	10 mM $NaHPO_4$, 1.8 mM $KH2PO_4$, 137 mM NaCl, 2.7 mM KCl (pH 6.9)
LB-medium	10 g/l Trypton, 10 g/l NaCl, 5 g/l yeast extract
Trace elements	5 g/l EDTA, 0.5 g/l $FeSO_4$, 50 mg/l $ZnCl_2$, 10 mg/l $CuSO_4$ (pH 7.6)
M9 salts	8 g/l Na_2HPO_4 x $2H_2O$, 2 g/l $FeSO_4$, 0.5 g/l NaCl (pH 7.2)
M9 medium	1 mM $MgSO_4$, 0.3 mM $CaCl_2$, 0.01 mM Thiamin HCl, 0.01 mM Biotin, M9 Salts 2x, Trace Elements 1x, 4 g/l glucose and 1 g/l NH_4Cl (labelled/unlabelled)

Table 3.3 Equipment

Equipment	Usage	Developer
Avance III 600 MHz	NMR	Bruker Biospin
Avance III 750 MHz	NMR	Bruker Biospin
Syro	Peptide Synthesizer	Multisyntech
NanoDrop 2000c	UV/Vis-Photometer	Thermo Fisher
Safire	Microplate reader	TECAN
Amicon Ultra	Centrifugation filter	Merck Millipore
Optima XL-I	Analytical ultracentrifuge	Beckman
Optima LE-80K	Ultracentrifuge	Beckman
MAX-XR	Ultracentrifuge	Beckman
Sorvall MTX 150	Ultracentrifuge	Thermo Scientific
Type 45 Ti	Rotor	Beckman
Type 70 Ti	Rotor	Beckman
TLA 110	Rotor	Beckman
TLA 55	Rotor	Beckman
Delta 350	pH-Meter	Mettler
AT21 Comparator	Microscale	Mettler
Multitron	Incubator	Infors HT
Microfluidizer LM10	Shear Fluid Homogenizer	Microfluidics Corp.
SE250 MightySmall	SDS-PAGE	Hoefer

Table 3.4 Software

Software	Version	Developer	Usage
TopSpin	3.1, 3.2	Bruker	Data acquisition and processing
Analysis	2.4.1	CCPN	Assignment
R	3.2.2	R Foundation	Statistics and plotting
RStudio	1.1.456	RStudio, Inc	Statistics and plotting
Pymol	1.7	Schrödinger	Visualization
NMRPipe	8.1	F. Delaglio	Data processing
NMRDraw	8.1	F. Delaglio	Data visualization
Inkscape	0.92	Open source	Graphics editing
Illustrator CC	17.0.0	Adobe	Graphics editing

IPTG on M9 minimal medium with ^{15}N-ammonium chloride and/or ^{13}C glucose for uniform isotope labelling ([u-^{13}C/^{15}N]). After additional 5 h at 37 °C the cells were harvested by centrifugation and stored at -80 °C.

3.2.2 Purification of CC1ΔC223

After thawing, the cells were lysed by a shear fluid homogenizer in 5 cycles at 13,000 psi. The cellular debris was spun down and the supernatant was collected. Subsequent protein purification was achieved by metal chelate affinity chromatography. Fractions enriched with the target protein were pooled and the His-tag was cleaved off overnight at 10 °C using a 3C/PreScission Protease. The cleaved tag and the protein were separated by gel filtration chromatography and the buffer was exchanged to the Tris sample buffer. The collected fractions were concentrated at 12 °C and 3,000 x g with a 3 kDa cut-off centrifugal filter. Final concentrations were in the range of 1 to 6 mg/ml (70 - 500 µM) and supplemented with 0.02 % sodium azide and complete protease inhibitor. Extinction coefficients of proteins were determined with ProtParam [167]. The protein samples were snap frozen and stored at -80 °C until further use. DTT was added immediately before use. Expression and purification of the mutant CC1ΔC223YYAA followed the same protocol.

3.2.3 Peptide synthesis

Table 3.5 lists all synthetic peptides used in this project. Peptide production was based on the standard Fmoc-solid-phase peptide synthesis method. Peptides were synthesized with acetyl- and amide protection groups at the N- and C-termini, respectively. Peptides were further purified by reversed-phase HPLC and the pure product was lyophilized. The synthesis was validated using mass spectrometry (MS). Peptides were not isotopically labelled and yields varied between the different peptides.

3.2.4 Microtubule purification and assembly

Since nerve cells contain a high density of microtubules, brain tissue is the most abundant natural source for tubulin. Porcine brain tubulin was purified following the protocol described in [168]. The porcine brain tissue was transported in ice-cold PBS buffer directly from the slaughterhouse to the laboratory. After homogenization of the tissue, tubulin was purified from the crude-brain extract by a series of alternate depolymerizing and polymerizing steps. Polymerization was performed at 37 °C for 45 min in PEM buffer with added glycerol (33 %), 2-Mercaptoethanol (0.2 %) and protease inhibitor (0.1 %). After microtubule recovery by

Table 3.5 Peptides

Peptide	Sequence
CC1(3-38)	AKTDSEVTSLAASSPARSPRRPVYYVQSPSRDSHDG
CC1(16-38)	SPARSPRRPVYYVQSPSRDSHDG
CC1(41-64)	TATSFHSTPVLSPMGSPPHSHSSM
CC1(50-85)	VLSPMGSPPHSHSSMGRHSRESSSSRFSGSLKPGSR
CC1(65-85)	GRHSRESSSSRFSGSLKPGSR
CC1(83-103)	GSRKVNPNDGSKRKGHGGEKQ
CC1(86-120)	KVNPNDGSKRKGHGGEKQWKECAVIEEEGLLDDGD
CC1(100-114)	GEKQWKECAVIEEEG
CC1YYAA(16-38)	SPARSPRRPVAAVQSPSRDSHDG
CC1(258-291)	LPPAPPAPLPKPKKKKGAPVPIPDPPAPPAPVPM
Tau(211-242)	RTPSLPTPPTREPKKVAVVRTPPKSPSSAKSR

centrifugation at 100,000 x g for 1 h, the pellet was resuspended in PEM buffer devoid of GTP and the solution was incubated on ice for 40 minutes to allow for complete depolymerization. After ultracentrifugation, the tubulin-containing supernatant was repeatedly polymerized as described above. After three polymerization/depolymerization cycles, the last cycle was performed in hPEM buffer to remove residual MAPs from the microtubules. For storage, the tubulin samples were snap frozen and stocked at -80 °C.

For experimental use, stock-tubulin was polymerized in PEM buffer. During polymerization the tubulin concentration ranged from 10 - 40 µM and Taxol was added in equimolar concentration. The sample was incubated at 37 °C for 45 min. The microtubules were pelleted by ultracentrifugation at 100,000 x g for 1 h. These Taxol-stabilized microtubules were diluted to the required concentration in the desired buffer. For NMR experiments, the microtubule pellet was resuspended in a 1:1 mixture of the PEM buffer and Tris sample buffer.

3.3 Sample analysis

Electron microscopy was performed at the FMP core facility for transmission electron microscopy (TEM). Grid preparation and image acquisition were carried out by Dr. Dmytro Puchkov and Svea Hohensee. Analytical ultracentrifugation (AUC) and protein stability assay was performed by Nils Cremer at the FMP and circular dichroism (CD) spectroscopy by Dr. Christopher Kesten at the Max Planck Institute of Molecular Plant Physiology. The turbidity assay was established by Jean-Marc Gensch.

3.3.1 Electron microscopy

Electron microscopy was employed to test the stability of microtubules over the course of the experiments. The Taxol-stabilized microtubules were applied to copper grids coated with 0.3 % formvar and incubated for 30 s, washed once with dH_2O, then stained with 1 % aqueous uranyl acetate solution, rinsed with dH_2O, and dried. The samples were examined on a Zeiss 900 transmission electron microscope.

3.3.2 Analytical ultracentrifugation

For sedimentation velocity (SV) experiments, two-channel centrepieces were loaded with 400 µL samples of CC1ΔC223 in dialysis buffer at concentrations ranging from 15 to 60 µM. The runs were carried out at 35,000 rpm and 20 °C. The absorbance detector collected scans at 280 nm every 5 min for $\sim$ 12 h. Sedimentation coefficient distributions c(s) were determined using the program Sedfit and the partial-specific volume of CC1ΔC223 was based on its amino acid sequence using a prediction by Sednterp [169].

3.3.3 Circular dichroism spectroscopy

6xHis-CC1ΔC223 was dialysed against pure water overnight at 4 °C. The sample was cleaned from any protein aggregation by centrifugation (20,000 x g for 10 min) and the supernatant was diluted to $\sim$ 8 µM and transferred to a 0.1 mm path length cuvette. Each spectrum was subtracted by a water baseline spectrum. CD spectra were recorded at room temperature on a N_2-purged spectropolarimeter. Four spectra were accumulated for each measurement with a response time of 4 s, 1 nm data pitch and a 1 nm bandwidth from 260 to 186 nm. The mean residue ellipticity ($[\Theta]_{MRW}$) was calculated using the equation:

$$[\Theta]_{MRW} = \frac{\Theta(\lambda) \times 0.1}{n \times c \times d} \tag{3.1}$$

with n being the number of peptide bonds, c the concentration of the protein in mol/l, and d the pathlength in cm.

3.3.4 Turbidity assay

To determine microtubule assembly rates the protein's light scattering was monitored in a bulk phase turbidity assay. The measurement was performed in the above-noted buffer ratio with 1 mM GTP and the plates were incubated at 37 °C for 2 min. 40 µM of tubulin were incubated with varying amounts of the respective analyte. The final CC1 concentration was 30 µM and peptide concentrations ranged from 10 - 100 µM. The positive control was 10 µM of Taxol and buffer was used as a negative control. Polymerization was monitored at 37 ºC in 20 s intervals for 45 min in a photospectrometry plate reader detecting at 340 nm. OD-values of each timepoint were plotted as a line graph against time and the samples were checked for microtubules by TEM afterwards.

3.4 Sequence analysis and phylogeny

Sequence-based analysis of predicted intrinsically disorder in proteins was conducted with the meta-predictor PONDR-FIT and the algorithms VSL2 and VL3. PONDR-FIT employs a consensus artificial neural network (ANN) prediction method that analyses the output of multiple disorder predictors [170]. Pairwise sequence alignments were created using the EMBOSS Needle and EMBOSS Matcher tools for global and local alignments, respectively [171]. General amino-acid similarity scoring was guided by the BLOSUM62 matrix. Phylogenetic analysis was conducted by selectively identifying CC1 homologues in plant model organisms using BLAST [172]. Multiple sequence alignments were produced by the Constraint-based Multiple Alignment Tool (COBALT) and phylogenetic trees were created using the fast minimum evolution method implemented in COBALT [173]. Tau and CC1 evolutionary sequence conservation was calculated by CONSURF on approximately 300 closest homologous sequences identified by BLAST for each protein [174]. The multiple sequence alignment was created using the Clustal Omega alignment program [175].

3.5 NMR spectroscopy

All experiments were performed at 20 °C at 600 and 750 MHz narrow-bore Bruker Avance AVIII spectrometers equipped with cryogenically cooled triple resonance TCI probe heads. Protein and peptide samples were measured in the above-mentioned buffer ratio supplemented with 10 % D_2O in standard 5 mm NMR tubes. The raw NMR data was collected and processed using TopSpin. All data was apodized with 90 °-shifted sine functions and zero-filled to yield appropriate data matrices and the chemical shifts were referenced using DSS. A summary of the NMR experiments employed is given below.

3.5.1 Backbone assignment

Initial 2D ^{1}H-^{15}N Heteronuclear Single Quantum Coherence (HSQC) experiments were recorded on ^{15}N-labelled CC1ΔC223 for peak counting and secondary structure estimation (Fig. 3.1 **A**). As one of the most frequently used experiments in solution-state NMR spectroscopy, the HSQC provides the correlation between the nitrogen and amide proton, giving one peak per pair of coupled nuclei at their respective chemical shift positions. The transfer of magnetization from the proton to the nitrogen is achieved *via* the J-coupling-based Insensitive Nuclei Enhanced by Polarization Transfer (INEPT) and limited to one bond. After a second INEPT module, the signal is detected on the amide-protons.
SOFAST-HMQC experiments were employed on samples with low concentration of proteins (10 - 50 µM). In contrast to the HSQC, the Heteronuclear Multiple Quantum Coherence (HMQC) experiment lets both ^{1}H and ^{15}N evolve during evolution time (Fig. 3.1 **B**). This leads to homonuclear ^{1}H-J-coupling that broadens the linewidth in the ^{15}N-dimension. The Band-Selective Optimized-Flip-Angle Short-Transient (SOFAST) scheme allows for very short recycle delays and therefore high sensitivity with high signal-to-noise ratio (S/N) per unit experimental time [176]. The reduction of T_1 is achieved by using band-selective proton pulses that excite the nuclei at optimized flip-angles with only a small number of RF pulses, thereby minimizing signal loss due to B_1 inhomogeneity.
HSQC and HMQC spectra were typically acquired with 512 x 128 complex data points resulting in 51 ms (^{1}H) and 42 ms (^{15}N) of acquisition time. During acquisition, nitrogen decoupling was achieved using a WALTZ-16 decoupling scheme. The HSQC pulse sequence contained a 3-9-19 WATERGATE block for water suppression and recycle delay was 1.3 s (Fig. 3.1 **C**). The nitrogen carrier frequency was set to 119 ppm and the spectral width was 32 ppm. The proton carrier was set to the respective water resonance frequency. The number of scans was chosen according to the protein concentration in the sample. In the SOFAST-HMQC, the variable-flip-angle pulse had a PC9 shape, and band-selective ^{1}H refocusing was realized using a REBURP shape [177, 178]. The recycle delay was set to 100 ms.

A number of backbone assignment strategies are available for protein with uniform ^{13}C and ^{15}N labelling employing multi-dimensional triple-resonance experiments. Along with the two-dimensional (2D) HSQC, the 3D HNCACB and 3D HN(CO)CACB experiments form the standard set of spectra commonly used for the backbone assignment (Fig. 3.1 **D**). Following the classical naming convention, the involved nuclei define the name of an experiment, while spins, whose chemical shifts are not evolved are put in parentheses. The HNCACB experiment correlates the HN and the ^{15}N resonances of each amino acid with ^{13}CA/CB

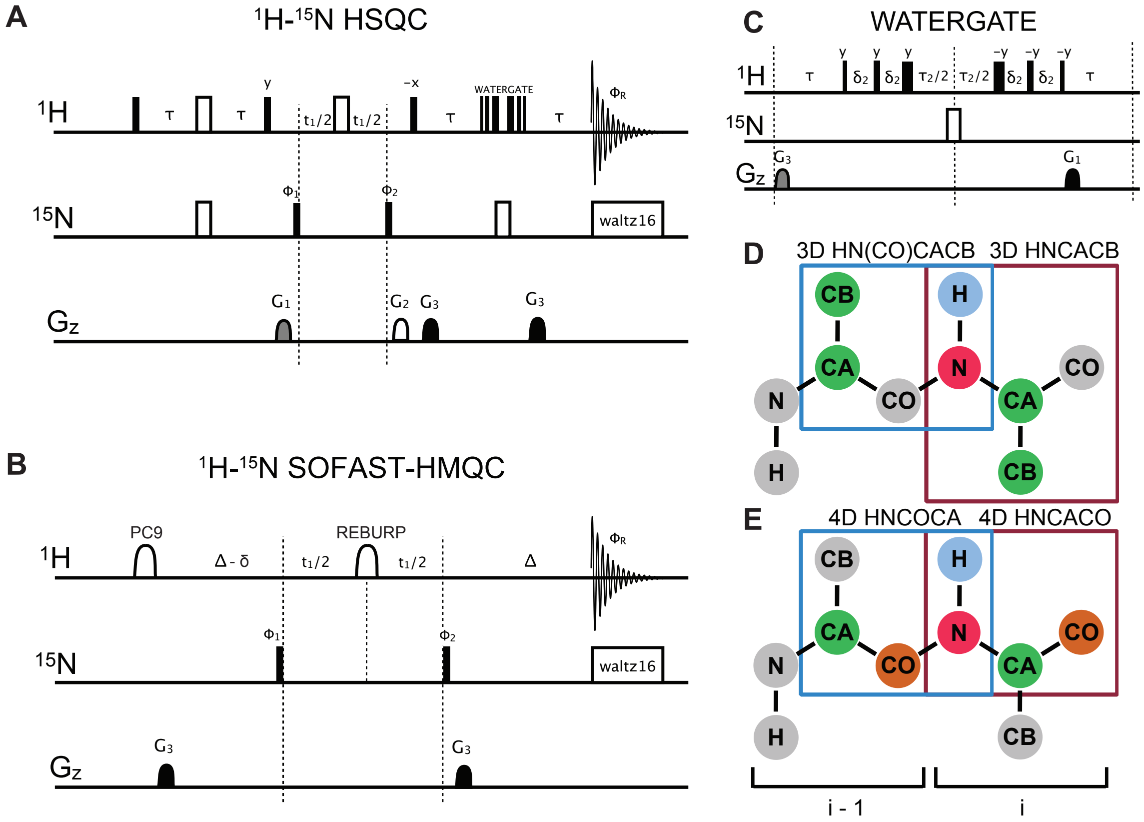

Figure 3.1 **HSQC, SOFAST-HMQC and assignment strategy. A** and **B** Schematic representation of the HSQC and SOFAST-HMQC pulse sequence. Filled and open pulse symbols indicate 90° and 180° RF pulses, respectively. Gradients G_z have a sinus shape and a duration of 1 ms. Pulses are x-direction if not labelled otherwise. ϕ_1 = x, -x; ϕ_2 = x, x, -x, -x; ϕ_R = x, -x, -x, x. Delay $\tau = \Delta = 1/4J_{HN}$. In **B**, the delay δ accounts for spin evolution during the PC9 pulse. **C** WATERGATE pulse sequence employed in **A**. The ^{1}H-pulses are calculated based on the 90° pulse (factor of 0.231, 0.692 and 1.4621). δ_2 is the delay for binomial water suppression and $\tau_2 = \delta_2 - \tau_{p180}(N)$. **D** and **E** Cartoon representation of the protein backbone along with 3D and 4D experiments, respectively. Coloured nuclei are evolved in the respective experiment. The assignment of intra-residual (i) chemical shifts and those of the preceding residue ($i-1$) allow the connection of sequential residues along the protein backbone.

aliphatic carbon resonances of both the same (i) and, to a lesser extent, the preceding residue ($i-1$). The HN(CO)CACB experiment correlates HN_i and $^{15}N_i$ resonances only with the $^{13}CA/CB_{i-1}$. The magnetization transfer of HNCACB (Eq. 3.2) and HN(CO)CACB (Eq. 3.3) can be summarized by the following pathways:

$$\begin{aligned} HN_{\mathrm{i}} \xrightarrow{J_{HN}} {}^{15}N_{\mathrm{i}} \xrightarrow{J_{NCA}} {}^{13}CA_{\mathrm{i-1,i}} \xrightarrow{J_{CACB}} {}^{13}CA/CB_{\mathrm{i-1,i}}[t_1] \\ \xrightarrow{J_{CACB}} {}^{13}CA_{\mathrm{i-1,i}} \xrightarrow{J_{NCA}} {}^{15}N_{\mathrm{i}}[t_2] \xrightarrow{J_{HN}} HN_{\mathrm{i}}[t_3] \end{aligned} \tag{3.2}$$

$$\begin{aligned} HN_{\mathrm{i}} \xrightarrow{J_{HN}} {}^{15}N_{\mathrm{i}} \xrightarrow{J_{NCO}} {}^{13}CO_{\mathrm{i-1}} \xrightarrow{J_{COCA}} {}^{13}CA_{\mathrm{i-1}} \xrightarrow{J_{CACB}} {}^{13}CA/CB_{\mathrm{i-1}}[t_1] \\ \xrightarrow{J_{CACB}} {}^{13}CA_{\mathrm{i-1}} \xrightarrow{J_{COCA}} {}^{13}CO_{\mathrm{i-1}} \xrightarrow{J_{NCO}} {}^{15}N_{\mathrm{i}}[t_2] \xrightarrow{J_{HN}} HN_{\mathrm{i}}[t_3] \end{aligned} \tag{3.3}$$

Common to these experiments is the initial INEPT transfer of magnetization from protons to nitrogen, where chemical shift evolution is recorded. The magnetization is then transferred *via* J-coupling to carbon atoms using another INEPT pulse train. While the HNCACB evolves directly on the CA and CB atoms of the *i* residue, the HN(CO)CACB spectrum includes a transfer over the backbone carbonyl to the preceding $i-1$ residue. The chemical shifts of CA and CB are evolved simultaneously and appear in one dimension. Then, magnetization follows an equivalent path in the reverse direction to the amide protons, where the signal is finally detected (out-and-back transfer).

Applying the approach of the above-mentioned SOFAST method, Band-selective Excitation Short-Transient (BEST) experiments yield an increased sensitivity for high repetition rates by promoting efficient T_1 relaxation between consecutive scans in multidimensional NMR experiments [179]. Backbone amide protons are selectively excited by band-selective pulses. Thus, the remaining proton spins allow for improved cross-relaxation. The overall efficiency of the experiment therefore depends critically on the choice of pulse shapes.

4D HNCOCA and 4D HNCACO experiments add a second carbon-dimension by evolving on the backbone carbonyl (Fig. 3.1 **E**). The magnetization transfer of HNCOCA (Eq. 3.4) and HNCACO (Eq. 3.5) can be summarized by the following pathways:

$$\begin{aligned} HN_{\mathrm{i}} \xrightarrow{J_{HN}} {}^{15}N_{\mathrm{i}} \xrightarrow{J_{NCO}} {}^{13}CO_{\mathrm{i-1}}[t_1] \xrightarrow{J_{COCA}} \\ {}^{13}CA_{\mathrm{i-1}}[t_2] \xrightarrow{J_{COCA}} {}^{13}CO_{\mathrm{i-1}} \xrightarrow{J_{NCO}} {}^{15}N_{\mathrm{i}}[t_3] \xrightarrow{J_{HN}} HN_{\mathrm{i}}[t_4] \end{aligned} \tag{3.4}$$

$$\begin{aligned} \mathrm{HN_i} &\xrightarrow{\mathrm{J_{HN}}} {}^{15}\mathrm{N_i} \xrightarrow{\mathrm{J_{NCA}}} {}^{13}\mathrm{CA_{i-1,i}[t_1]} \xrightarrow{\mathrm{J_{COCA}}} \\ {}^{13}\mathrm{CO_{i-1,i}[t_2]} &\xrightarrow{\mathrm{J_{COCA}}} {}^{13}\mathrm{CA_{i-1,i}} \xrightarrow{\mathrm{J_{NCA}}} {}^{15}\mathrm{N_i[t_3]} \xrightarrow{\mathrm{J_{HN}}} \mathrm{HN_i[t_4]} \end{aligned} \tag{3.5}$$

Overall measurement time directly depends on the number of increments measured in the indirect dimensions. Due to the high number of points in the indirect dimensions, measurement times of 4D experiments with traditional uniform acquisition schedules are impractically long. Conventional multidimensional experiments are based on standard on-grid sampling, where discrete Fourier transform (DFT) processing is applied to data that is regularly spaced in all grid dimensions. As a result, the spacing between points defines the maximum frequency that can be sampled causing longer measurement time with increasing resolution. Sparse sampling exploits the high redundancy present in NMR data by omitting points in the indirect dimension in an optimized way determined by the respective sampling scheme [180]. The spectrum is then reconstructed by non-Fourier methods. This results in a radically reduced measurement time without affecting resolution even for high-dimensional experiments. Hence, most experiments beyond three dimensions are recorded in a non-uniformly sampled (NUS) fashion.

Free ^{13}C,^{15}N-labelled CC1ΔC223 was assigned using 3D HNCACB, HN(CO)CACB and 4D HNCOCA and HNCACO experiments. The two 3D experiments were acquired each with 512 x 44 x 64 complex data points in the direct F_3 (^{1}H) and the two indirect F_2 (^{15}N), F_1 (^{13}C) dimensions resulting in 51 ms, 22 ms and 6.4 ms of acquisition time, respectively. The 4D data was acquired using non-uniform-sampling with 22 % sparse sampling and reconstructed with the MDD routine implemented in the Bruker TopSpin processing software. All spectra were recorded as BEST-type experiments on a sample with 250 µM CC1ΔC223.

After the chemical shift assignment, secondary structure propensity was analysed by employing the neighbour-corrected Structural Propensity Calculator (ncSPC) tool using the ncIDP reference library for the data analysis [181, 182]. The ncIDP library was specifically compiled for disordered proteins and the ncSPC tool employs a refined version of the SSP score, which has been shown to detect meaningful structural propensities in IDPs. The chemical shifts were automatically referenced using the method described by Marsh et al. [183].

3.5.2 Relaxation and dynamics

Beyond the overall tumbling in solution, proteins exhibit internal motions between conformational states on defined time-scales. The investigation of these dynamic properties adds detail to the structural characterization of the studied protein and can provide mechanistic insights into function. In solution state NMR, the ^{15}N-R$_1$ and ^{15}N-R$_2$ relaxation rates and ^{1}H-^{15}N hetero nuclear Overhauser effect (hetNOE) experiments are often used to characterize protein backbone dynamics in the picosecond to nanosecond regime [184].

The ^{15}N-R$_1$ and ^{15}N-R$_2$ relaxation experiments employ a series of relaxation delays over the appropriate time regime. To determine the overall relaxation time, signal intensities are fitted as a function of the relaxation delay. Water-selective 90° -flipback pulses were applied to avoid extensive amide proton exchange saturation transfer from water protons. Both pulse-programs included a temperature compensation scheme that kept overall pulsing equal to keep an even amount of sample heating during the experiment.

^{15}N-R$_1$ was determined employing a modified scheme of the classical inversion-recovery experiment (Fig. 3.2 **A**). After an initial INEPT pulse train, magnetization is converted to the z-dimension for the relaxation period, during which the protons are saturated to remove other relaxation pathways. After the evolution time, magnetization is reverted to protons by a reverse INEPT block, followed by ^{15}N decoupling and detection.

The ^{15}N-R$_2$ experiment repeats the basic INEPT building blocks of the ^{15}N-R$_1$ experiment, but employs a Carl-Purcell-Meiboom-Gill (CPMG) pulse train during transverse ^{15}N magnetization in the relaxation period (Fig. 3.2 **B**). The CPMG sequence consists of ^{15}N 180° refocusing pulses that are separated by a constant delay and thus increase in number with longer relaxation times (Fig. 3.2 **C**). Due to coherence loss between spins, the overall signal intensity is reduced with increasing relaxation times. However, the delay between the pulses has to be sufficiently short to minimize the effects of relaxation by the ^{15}N-^{1}H antiphase component.

The heteronuclear nuclear Overhauser effect (hetNOE) between a proton and the directly bonded ^{15}N-heteronucleus dominates the relaxation of the backbone amide ^{15}N and is dependent on the dynamics of the respective bond vector. Like the conventional homonuclear NOE, the effect results from through-space magnetization transfer *via* dipolar coupling. As a result, hetNOEs can report on the local flexibility of the protein backbone as a complementary site-specific observable which is measured by determining the loss in signal intensity caused by small amplitude bond fluctuations. The HSQC-based pulse-program alternates between an amide proton-saturated experiment prior to the initial INEPT sequence and a reference experiment with a corresponding delay and no saturation (Fig. 3.2 **D**). The hetNOE is obtained by taking the ratio of the signal intensities in the presence and absence of dipolar coupling and ranges from -4 to 1 for amides.

All relaxation and hetNOE experiments were measured on 100 µM uniformly ^{15}N-labelled protein. The ^{15}N-R$_2$ and ^{15}N-R$_1$ were carried out using a ^{1}H-^{15}N HSQC-based

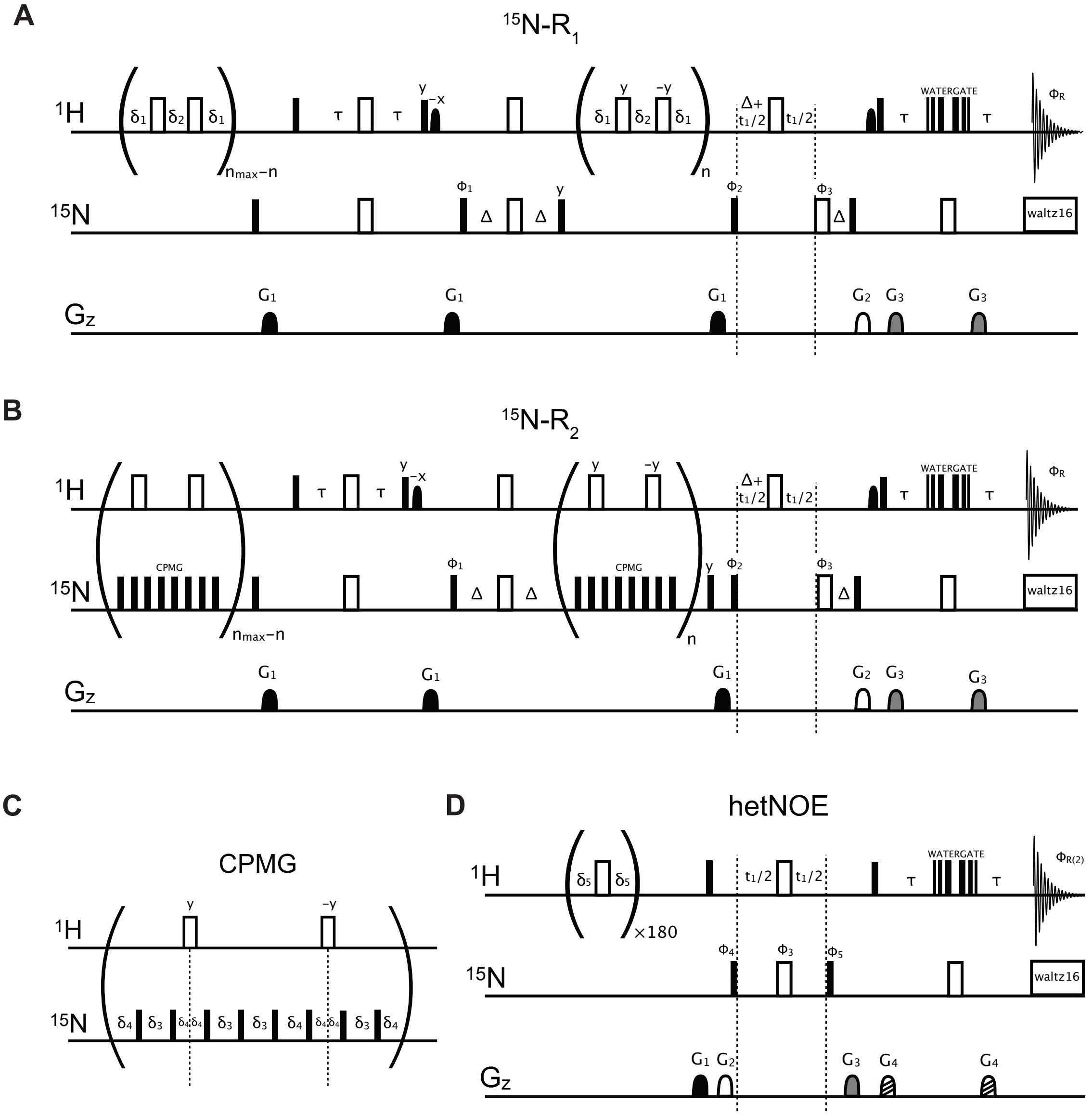

Figure 3.2 **R_1 and R_2 relaxation and hetNOE A** and **B** Schematic representation of the ^{15}N-R_1 and ^{15}N-R_2 pulse sequence, respectively. Black and round pulses are selective water-flipback pulses. Gradients G_z have a sinus shape and a duration of 1 ms. ϕ_1 = x, -x; ϕ_2 = y, y, -y, -y; ϕ_3 = 4x, 4y, 4(-x), 4(-y); ϕ_R = x, -x, -x, x, -x, x, x, -x. Delay $\delta_1 = \delta_2/2 = 2.5$ ms. Bracketed blocks are repeated as indicated. The first block in each experiment acts as a temperature compensation. Image adapted and modified from [185]. **C** CPMG sequence with $\delta_3 = \delta_4/2 = 1$ ms (total of 8 ms per CPMG block). **D** In the hetNOE pulse sequence, saturation is repeated 180 times with the transmitter on the amide protons and $\delta_5 = 11$ ms. In the reference experiment, the saturation is replaced by a delay of equal time. ϕ_4 = y, -y; ϕ_5 = x, x, -x, -x

experiment, recorded as a pseudo 3D with single-FID interleaving and WALTZ-16 ^{15}N-decoupling during acquisition periods. Each 2D plane was comprised of 512 x 128 complex data points in the ^{1}H (direct, F_2) and ^{15}N (indirect, F_1), corresponding to 51 ms and 55 ms of acquisition time, respectively. For the ^{15}N-R_2 experiment, a relaxation-compensated Carr-Purcell-Meiboom-Gill (CPMG) scheme at an effective CPMG frequency of 550 Hz was applied and relaxation delays were set to 16, 32, 48, 80, 112, 144, 200 ms with 16, 80 and 144 ms recorded twice within one experiment. In the ^{15}N-R_1 experiments the relaxation delays were measured with 80 (2x), 240, 400 (2x), 640, 880 (2x), 1280 and 1600 ms as set delays. ^{15}N-R_2 and ^{15}N-R_1 experiments were acquired with 16 scans. All experiments employed an interscan delay of 1.3 s resulting in a total measurement time of 17.5 h for the ^{15}N-R_2 and 23.5 h for the ^{15}N-R_1 experiment. For analysis, the cross-peaks in the 2D spectra were picked manually and the peak intensity was fitted to an exponential function with CCPN Analysis. ^{1}H-^{15}N hetNOE values were determined by analysing the ratios of peak intensities in paired NMR spectra with and without 3 s of proton saturation in 64 scans.

3.5.3 Relaxation and interaction

In recent years, a variety of relaxation-based NMR experiments have been used to study dynamic protein interactions in large molecular complexes [102, 35, 34]. Specifically, quantification of line broadening and exchange-induced chemical shifts together with CPMG relaxation dispersion spectroscopy can provide detailed information on the residue-specific dynamics and structure of the free and bound states.

CPMG relaxation dispersion experiments exploit the observation that chemical exchange can directly affect relaxation (Fig. 3.3 **A**) [186, 187]. Given a conformational exchange between two states on the ms to µs time scale, fluctuations in chemical shift can cause an increase of transverse relaxation rates R_2 by R_{ex} leading to peak broadening (see chapter 1.2.2). In the above-described ^{15}N-R_2 experiment this relaxation due to exchange is quenched by the trains of refocusing pulses of the CPMG sequence. In the intermediate exchange regime, low pulse repetition rates increase the effect of R_{ex} on the overall R_2^{eff} since refocusing will be less efficient due to an increased probability of exchange between the pulses. The CPMG frequency is defined as $\nu_{CPMG} = 1/(2\tau)$, where τ is the delay between successive refocusing pulses. In a relaxation dispersion experiment ν_{CPMG} is sampled over the relevant frequency regime, while the overall relaxation delay is kept constant. R_2^{eff} values are calculated based on the respective peak intensity and plotted as a function of the CPMG frequency. The resulting relaxation dispersion profile is dependent on chemical shift differences between the free and bound states and their respective exchange rates, which can be used for a quantitative analysis of the underlying protein dynamics.

The essential building blocks of the relaxation dispersion pulse scheme are similar to the ^{15}N-R$_2$ experiment, employing an INEPT and a reverse INEPT block followed by proton detection and ^{15}N decoupling (Fig. 3.3 **B**). A temperature compensation block is implemented to control for pulse-induced sample heating. As described above, the CPMG sequence is modulated in frequency ν_{CPMG} for each experiment rather than overall relaxation time length T_{relax}. However, the rate constants for in-phase and antiphase coherences are averaged during the CPMG sequence, thus compensating for evolution during the spin-echo pulse train between in-phase and antiphase transverse coherences [188].

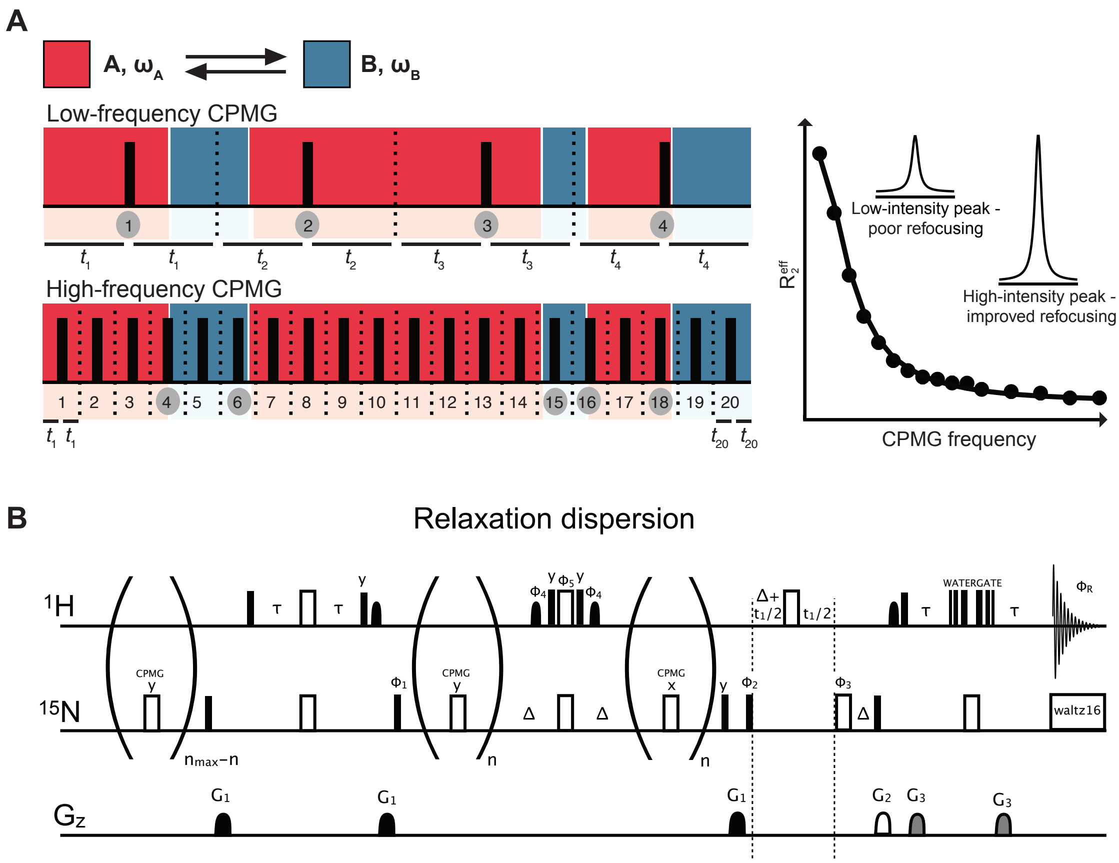

Figure 3.3 **Relaxation dispersion. A** Stochastic interconversion between two conformational states (A, red and B, blue) with two different chemical shifts (ω_A and ω_B). With increasing CPMG frequencies refocusing is more efficient leading to lower R$_2^{eff}$ with reduced R$_{ex}$ contribution. The plot reflects a typical relaxation dispersion profile of a two state exchange in the intermediate regime. Image adapted and modified from [187]. **B** Schematic representation of the relaxation dispersion pulse sequence. Gradients G_z have a sinus shape and a duration of 1 ms. ϕ_1 = x, -x; ϕ_2 = y, y, -y, -y; ϕ_3 = 4x, 4y, 4(-x), 4(-y); ϕ_R = x, -x, -x, x, -x, x, x, -x.

Protein interaction was further evaluated by calculating the difference in ^{15}N-R$_2$ relaxation rates of the free and the bound states ($\Delta R_2 = R_2^{bound} - R_2^{free}$) and the intensity ratio of NMR signals originating from the respective states (I_{bound}/I_{free}). Intensity ratios were calculated based on BEST-type HNCA spectra recorded on 150 µM uniformly ^{15}N-^{13}C-labelled samples of CC1ΔC223 and CC1ΔC223YYAA in the absence and the presence of 100 µM microtubules. Each experiment was acquired with 16 scans and 512 x 36 x 44 complex data points, corresponding to an acquisition time of 51 ms in F$_3$ (^{1}H), 22 ms in F$_2$ (^{15}N) and 11 ms in F$_1$ (^{13}C), respectively. The total measurement time of each experiment was 20 h. In crowding experiments, HSCQ spectra of 100 µM CC1ΔC223 were measured in the absence and presence of 200 g/l Ficoll70 or BSA and intensity ratios were determined, respectively. For relaxation-based interaction studies, experiments were recorded on 100 µM uniformly ^{15}N-labelled CC1ΔC223 before and after adding 25 µM of microtubules or tubulin. CPMG relaxation dispersion measurements were carried out using a ^{1}H-^{15}N HSQC-based experiment recorded as a pseudo 3D with single-FID interleaving and WALTZ-16 ^{15}N-decoupling during acquisition periods. Experiments were measured at CPMG frequencies ν_{CPMG} of 80, 160, 240, 320, 400 (2x), 640, 800, 1000 Hz, which were applied for a constant relaxation delay T_{relax} of 100 ms for each CPMG field. The experiments were recorded with 64 scans resulting in a total measurement time of 26 h. ^{15}N-R$_2^{eff}$ values were determined as following:

$$R_2^{eff} = \frac{-1}{T_{relax} ln \frac{I}{I_0}} \tag{3.6}$$

where I is the peak intensity in the spectrum and I_0 is the reference peak intensity of a spectrum recorded without the relaxation delay T_{relax}.

3.5.4 Peptide binding and assignment

Saturation transfer difference (STD) spectroscopy is a robust ligand-based technique to study receptor-ligand interactions in solution [189]. STD NMR can be used to study weak ligand binding (K$_D$ in the micromolar to millimolar regime) to a high molecular weight receptor (Fig. 3.4 **A**). Magnetization is transferred from the receptor to its bound ligand, where it is detected directly by only analysing ligand-derived signals. The experiment benefits from a low receptor concentration with a high excess of ligand and transfer is enhanced with a high molecular weight receptor. Selective proton saturation is achieved by irradiating only the spectral regions containing resonances of the receptor with a cascade of Gaussian shaped pulses (Fig. 3.4 **B**). Due the effective spin diffusion of high molecular weight receptors, saturation is spread rapidly to the whole molecule and is transferred to the protons of the

bound ligand *via* cross relaxation, which is most efficient in the regions closest to the receptor. These regions receive an attenuation of the signals in the proton spectrum. The effect is typically presented in the form of a difference spectrum between the saturated (on-resonance) and the reference (off-resonance) spectrum. Moreover, STD-NMR experiments can be employed to distinguish between competitive and non-competitive ligand binding.
The relevant resonances of the unlabelled peptides were assigned using 2D ^{1}H-^{13}C HMQC spectra and further validated with the help of ^{1}H-^{1}H TOCSY and ^{1}H-^{1}H NOESY experiments.

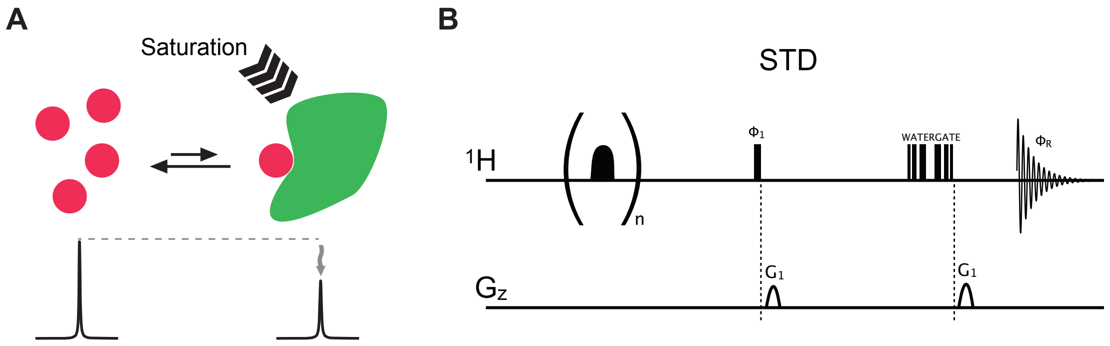

Figure 3.4 **Saturation transfer difference.** **A** Cartoon of the general principles of STD-NMR. The ligand (red) is bound to the receptor (green). After saturation of the receptor, the ligand signals from regions that made close contact to the receptor are selectively attenuated. **B** Schematic representation of the STD pulse sequence. The initial gaussian G4 saturation pulse is repeated *n* times either on- or off-resonance. G_z have a sinus shape and a duration of 1 ms. The pulse sequence uses a WATERGATE block for water suppression. ϕ_1 = x, -x; ϕ_R = x, x, -x, -x.

Saturation-transfer difference NMR spectra were recorded using a series of equally spaced 20 ms G4 Gaussian pulse cascades [190] for a total saturation time of 2 s and an interscan delay of 5 s. On- and off-resonance frequencies were set to - 0.5 ppm and 60 ppm, respectively. The measurements were performed on samples containing 1 mM CC1-peptide and 25 µM microtubules in the above mentioned buffer ratio. Control STD experiments were conducted in the absence of microtubules to check for residual STD from other sources.
The 2D ^{1}H-^{13}C HMQC were recorded with 1024 x 128 complex data points, corresponding to an acquisition time of 69 ms in the ^{1}H (direct, F_2) and 14 ms in the ^{13}C (indirect, F_1) dimension. Applying an interscan delay of 1.3 s and 256 scans, the experiment's duration was 25 h. ^{1}H-^{1}H TOCSY and ^{1}H-^{1}H NOESY experiments were acquired with 512 x 128 complex data points and each 32 scans resulting in a total experiment time of 3 h, respectively. TOCSY experiments employed DIPSI2 mixing for improved polarization transfer [191].

Chapter 4

Results

4.1 CC1 sequence analysis and phylogeny

Members of the CC-protein family have been proposed to be present in all of the sequenced higher plant genomes [163]. Phylogenetic analysis of popular model plants reveal the presence of at least two CC1 homologues for every species (Fig. 4.1). In Arabidopsis, CC2 represents the closest CC1 homologue, while the other gene family members CC3 and CC4 are more distant homologues and have been shown to not compensate CC1/CC2 function under salt stress [163]. However, species like poplar carry multiple CC-protein family members that show close sequence homology to CC1 and CC2 and possibly share similar cellular function. Outside the plant kingdom, CC proteins do not share any significant sequence homology with other proteins and thus represent a plant-specific protein family.

The domain architecture of CC1 contains a cytosolic N-terminus, a transmembrane domain and an apoplastic C-terminus (Fig. 4.2 **A**). As described in chapter 2.2.4, both termini adopt distinct roles within the cell: while the C-terminus CC1ΔN120 was proposed to aid with restoring defects related to cellulose inhibition, the cytosolic N-terminus CC1ΔC223 was observed to engage directly with microtubules and was sufficient to restore salt-related growth defects [163]. Within the plant kingdom, sequence homology search yielded no significant matches for proteins of known function for CC1ΔC223, while CC1ΔN120 shares some sequence similarity with the Late Embryogenesis Abundant (LEA) protein family. These chaperone-like proteins protect against protein aggregation under cell-stress conditions like dehydration, low temperatures and salt stress [192]. At the subcellular level, these proteins are usually found in the cytosol, the nucleoplasm or the chloroplast [193].

A sequence analysis by the structural algorithm JPRED4 predicted strong structural differences between the termini potentially reflecting their respective roles in cellular function (Fig. 4.2 **B**). The C-terminus was predicted to contain a large number of β-strand secondary

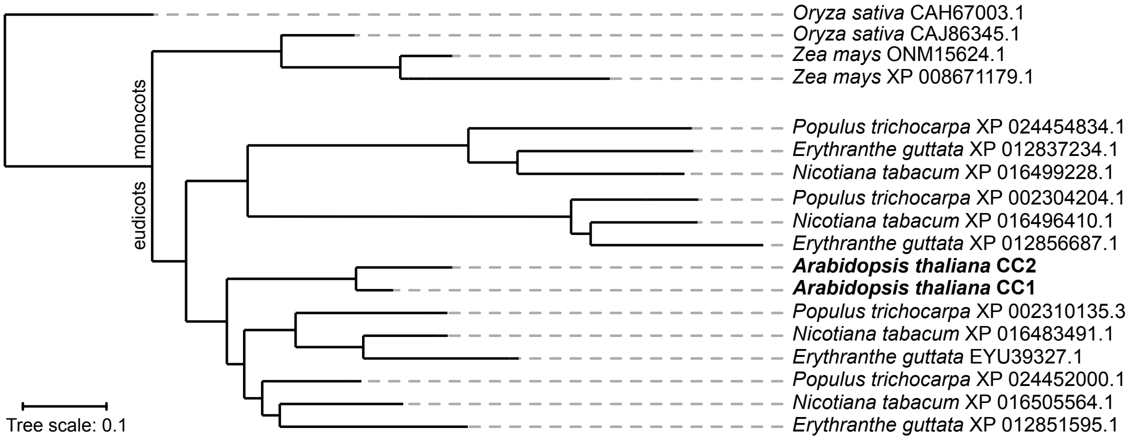

Figure 4.1 **Phylogenetic tree of CC1 and CC2.** CC-protein members are shown for the monocotyle plant model organisms *Oryza sativa* (rice), *Zea mays* (corn). Besides *Arabidopsis thaliana*, the eudicotyl plants *Populus trichocarpa* (poplar), *Nicotiana tabacum* (tobacco) and *Erythranthe guttata* (monkeyflower) were included in the phylogenetic analysis. Branch length indicate evolutionary distances and NCBI reference IDs are given for each sequence.

structure only interspersed with stretches of disorder. The region CC1(250-288) represents the longest continuous stretch of disorder in the C-terminus, containing a high proportion of proline residues and a short lysine repeat. The transmembrane helix is predicted to stretch from residue A133 to A152. The cytosolic part of the protein is predicted to be almost fully unstructured with the exception of two β-strand regions comprising Y26-Q29 and R127-L132, only the first being included in the CC1ΔC223 construct. Analysis of CC1ΔC223 with several disorder prediction algorithms (VSL2, VL3, P-FIT) reports an overall disordered protein structure, but with no predicted structure in the β-strand region mentioned above (Fig. 4.2 **C**). Indeed, the overall sequence composition of CC1ΔC223 shows a high abundance of serine, proline and arginine residues when compared to the average composition of the Arabidopsis proteome (Fig. 4.2 **C**) [194]. CC1ΔC223 is deficient in hydrophobic amino-acids like leucine, isoleucine, tryptophan, tyrosine and phenylalanine. This is characteristic of IDPs that have a compositional bias to hydrophilic amino acids, while hydrophobic amino acids facilitate the formation of the hydrophobic core in folded proteins.

4.2 Initial biochemical characterization of CC1ΔC223

After successful expression and purification of CC1ΔC223 (Fig. 4.3 **A**), the protein's structural features were studied. The heat stability of His-CC1ΔC223 was assessed by subjecting

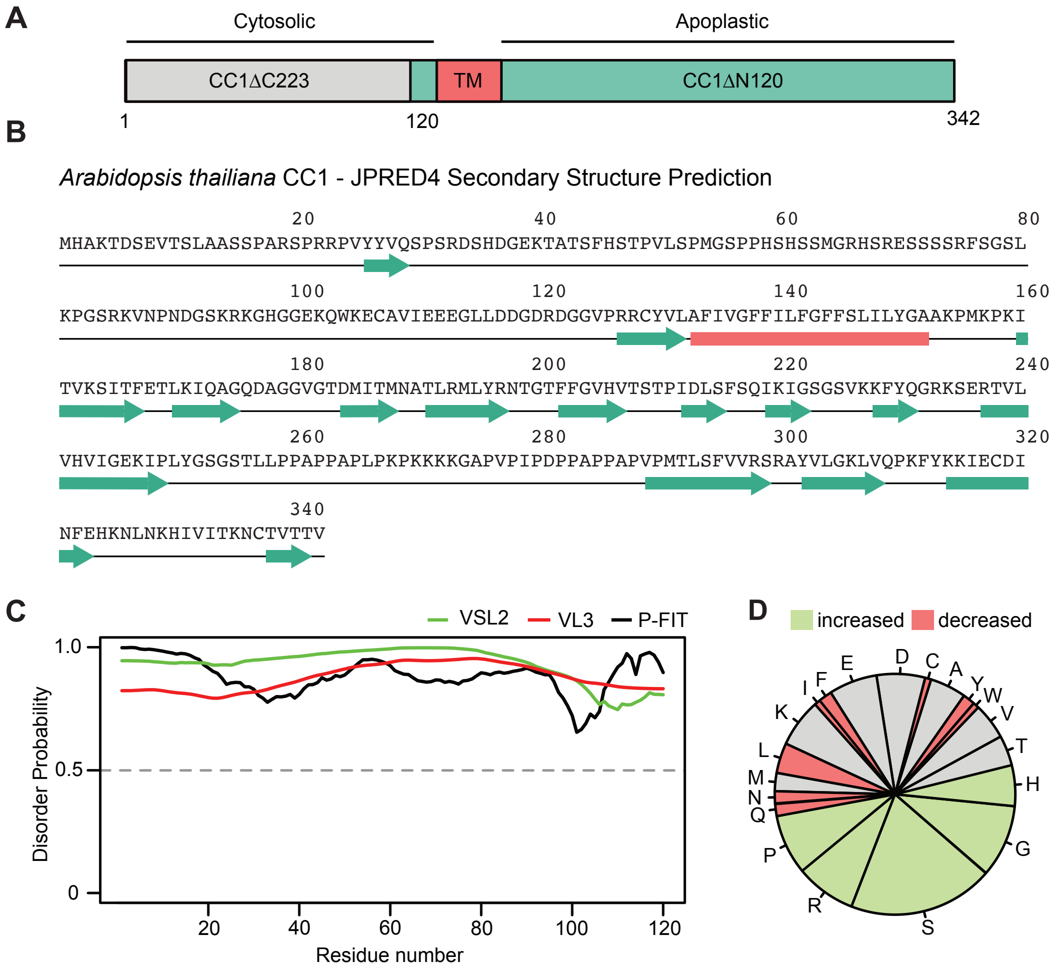

Figure 4.2 **CC1 structure prediction.** **A** The domain architecture of CC1 with cytosolic N-terminus CC1ΔC223 highlighted in green. **B** JPRED4 secondary structure prediction for CC1. β-strand secondary structure is marked with a green arrow, α-helices with a red barrel and random coil with a horizontal black line. **C** Prediction of the degree of disorder of CC1ΔC223 with the algorithms VSL2 (green), VL3 (red) and P-FIT (black). Regions with a disorder probability above 0.5 are considered disordered. **D** Amino acid composition of CC1ΔC223. When compared to the average amino acid frequency of the Arabidopsis proteome, under- and over-represented amino acids are coloured in red and green, respectively.

the cell lysate to a temperature of 95 °C for increasing durations and subsequent centrifugation to remove insoluble aggregates. While most of the proteins in the lysate aggregate after 5 min of heat application, a significant proportion of CC1ΔC223 remains soluble even after 2 h at 95 °C (Fig. 4.3 **B**). As predicted by the sequence analysis algorithms, the CD measurement of CC1ΔC223 in solution yielded spectra that showed the typical characteristics of proteins in the disordered state, with low ellipticity above 210 nm and negative bands near 195 nm (Fig. 4.3 **C**). AUC analysis revealed only monomeric forms of the protein in solution (Fig. 4.3 **D**). The frictional coefficient of 1.7 is indicative of highly elongated protein shapes.

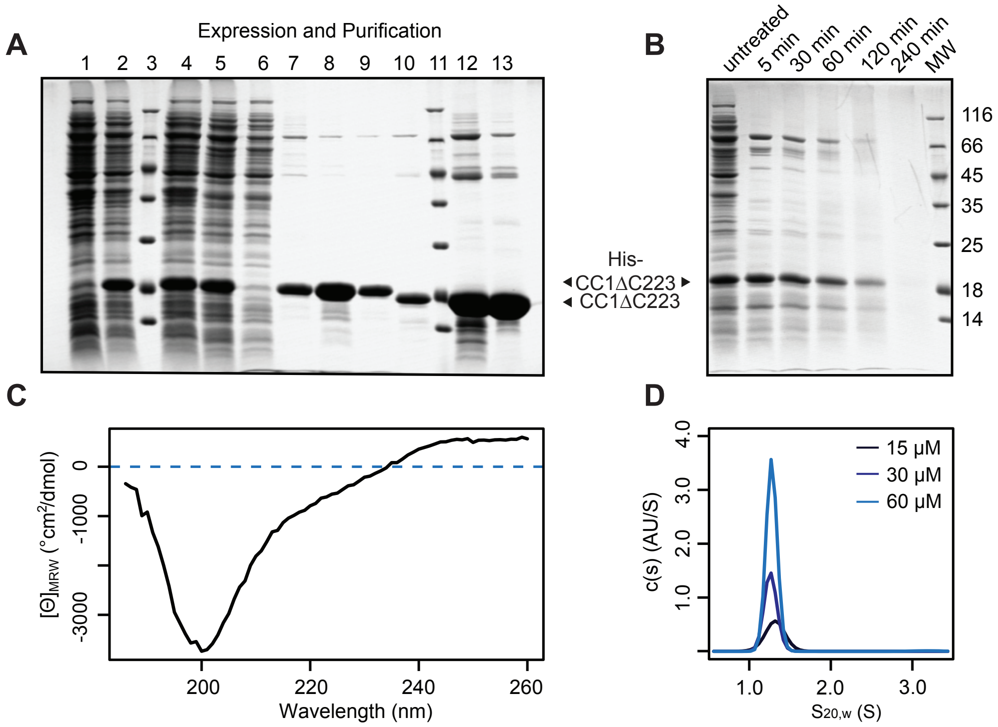

Figure 4.3 **CC1ΔC223 expression and purification.** **A** Expression and purification of CC1ΔC223: **L1** BL21(DE3)star pBAD-σ32 (I54N) uninduced, **L2** BL21(DE3)star pBAD-σ32 (I54N) pETM11-His-CC1ΔC223 induced, **L3** MW Marker from bottom to top 14; 18; 25; 35; 45; 66; 116 kDa, **L4** Lysate, **L5** Supernatant, **L6** Flow through metal chelating column (MCC), **L7** MCC Elution Fraction 8, **L8** MCC Elution Fraction 9, **L9** Elution Pool MCC Fr. 8 to 10, **L10** Cleavage with 3C/Prescission Protease, **L11** Marker like L3 **L12** Before gel filtration, **L13** Final product CC1ΔC223 after gel filtration. Molecular size of His-CC1ΔC223 and CC1ΔC223 are indicated by arrows. **B** Heat stability His-CC1ΔC223 at 95 °C in lysate, supernatants after 30 min centrifugation at 20,000 x g. **C** Circular dichroism (CD) spectrum of 6xHis-CC1ΔC223 in solution indicating lack of α-helix or β-strand secondary structure. **D** Analytical ultracentrifugation at three different CC1ΔC223 concentrations shows a single size population at the approximate molecular weight of monomeric CC1ΔC223.

4.3 Backbone assignment of CC1ΔC223

For further structural characterization, a uniformly ^{13}C-^{15}N-labelled CC1ΔC223 sample was prepared for study by solution-state NMR. The 2D ^{1}H-^{15}N-HSQC spectrum of CC1ΔC223 showed narrow signals and poor chemical shift dispersion in the ^{1}H dimension. This strong spectral crowding in the random-coil region (between 8.5 and 7.8 ppm) is characteristic of intrinsically disordered proteins (IDPs). The slow Brownian tumbling of large folded proteins in solution leads to fast spin relaxation and broad signals in NMR. In contrast, the fast internal motions of proteins with low intrinsic structure like CC1ΔC223 result in favourable relaxation properties but inherently low signal dispersion due to a more uniform chemical environment of the spins. Signal overlap can become particularly severe in proteins with highly repetitive sequence stretches and general low sequence complexity. Hence, NMR experiments for IDP studies often rely on multidimensional correlation spectra to reduce signal overlap and take advantage of slow relaxation processes. Like in many IDPs, the carbonyl chemical shifts are comparably well-dispersed in CC1ΔC223 and thus provide valuable information for the assignment.

For the sequence-specific backbone assignment, a combination of three-dimensional and four-dimensional experiments with non-uniform sampling was employed. As described above, the sequence of CC1ΔC223 is overly rich in serine and proline residues, which complicated conventional assignment strategies based on 3D spectra only. However, as widely reported in the literature, the available reconstruction methods of non-uniformly sampled data can introduce artefacts to the spectra that can complicate the identification and assignment of real peaks. Although the overall sampling size was reasonably high (22 %), the reconstruction of the 4D spectra produced some minor spectral artefacts that had to be cross-checked with the uniformly-sampled 3D spectra, which also allowed for easy navigation in the 4D space. Each amino acid is expected to produce only one strong peak in the 4D spectra making the reliable distinction between real peaks and artefacts more feasible.

In the presented assignment strategy, the spectra were evaluated to yield the assignment of backbone resonances N, H, CA, CB and CO for each amino acid. In the 3D HNCACB spectrum, the CA and CB resonances belonging to a specific NH_i pair are determined. The CA, N and H resonances are then used to determine CO resonances in the 4D HNCACO spectrum. The 3D HN(CO)CACB and 4D HNCOCA yield the CA, CB and CO resonances of the preceding residue and by navigating to these resonances in the spectra, the NH_{i-1} pair from the preceding residue can be found. With this procedure the resonances of two consecutive spin-systems can be unambiguously connected and assigned. As shown in Figure 4.4 **A**, overlapping signals could be resolved with adding the carbonyl as a fourth dimension in the 4D HNCACO/HNCOCA spectra.

The overall backbone assignment of CC1ΔC223 was completed with 84 % of the resonances assigned (Fig. 4.4 **B** and **C**; see Appendix A for full chemical shift table). Of the missing 16 %, unassigned serine residues made up a substantial part of the missing amino acid types with 6 %. The lack of serine assignment was due to a severe overlap of the signals caused by the high frequency of HS and SS repeats. Figure 4.4 **D** shows a region in the 3D HNCACB spectrum that shows massive crowding of signals stemming from typical CA and CB resonances of serine residues. Since these spin systems cannot be accounted

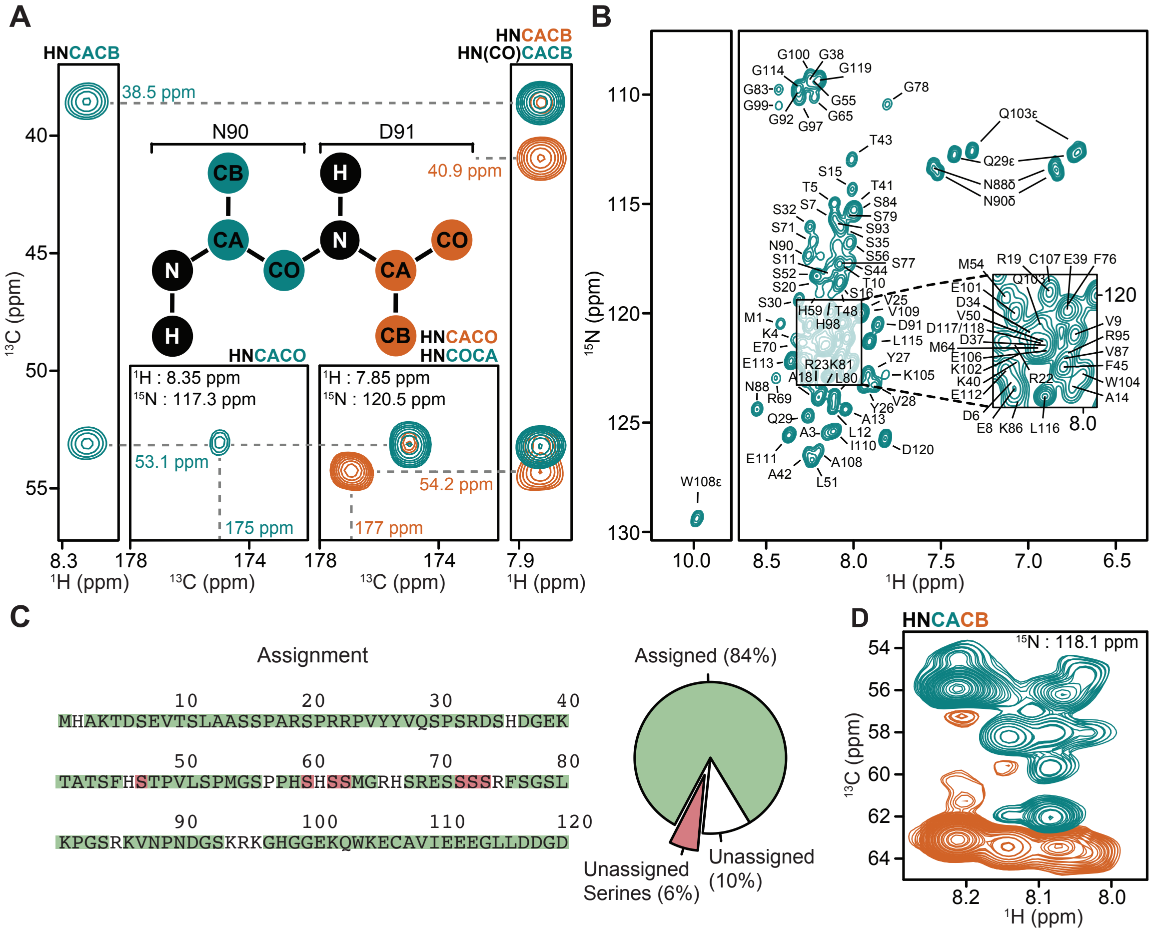

Figure 4.4 **Resonance assignment of CC1ΔC223. A** Assignment procedure based on two 3D and two 4D correlation spectra. The NH pair of D91 is correlated with its intra-residual CA, CB and CO resonances in the 3D HNCACB and 4D HNCACO spectra (orange) and with CA, CB and CO resonances of the preceding N90 residue in the 3D HN(CO)CACB and 4D HNCOCA spectra (teal). **B** Assigned ^{1}H-^{15}N HSQC spectrum of CC1ΔC223 in solution. **C** Sequence-overview of the backbone assignment with highlighted assigned (green), unassigned (white) and unassigned serine (red) residues.**C** 2D plane from a 3D HNCACB spectrum (CA = teal, CB = orange) of a crowded region containing many overlapping signals from serine residues.

for, loss of signals from chemical exchange effects can also not be excluded as a possible explanation. Between amino acids, there are large differences in the peak intensities, which remain consistent over the different spectra. This indicates that the observed differences stem from the individual relaxation properties of the amino acids rather than spectroscopic particularities. Some residues preceding prolines display a second set of amide peaks with low signal intensity in addition to the principal peaks, presumably due to *cis-trans* isomerization.

4.4 Secondary structure propensity and dynamics

Based on the assigned backbone resonances, the CC1ΔC223 secondary structure propensity was estimated by calculating secondary chemical shift values $\Delta\delta$ (Fig. 4.5 **A**-**D**). For this purpose, experimental CA, CB and CO chemical shifts were subtracted from the respective neighbour-corrected random coil values for each amino acid type. Propensity scores of 1 and -1 report on fully formed α- or β-structure, respectively. The resulting secondary chemical shifts revealed few and rather scattered deviations from random coil values. $\Delta\delta$CA values did not exceed ± 1.5 ppm, indicating the absence of any rigid secondary structures. However, the propensity plot revealed short residue stretches that could adopt helical and β-structure-like organizations. In particular the C-terminal region from A108-G119 shows increasing propensity for additional β-strand structure, with a maximum score close to -0.5, indicating that 50 % of the conformers adopt β-strand structure at that position. Although with significantly lower score values of about -0.2, the region ^{25}VYYVQS^{30} also represents a prominent stretch of secondary β-structure propensity. Interestingly, this stretch was also the sole CC1ΔC223 region predicted to adopt β-strand structure in the JPRED4 secondary structure prediction (Fig. 4.2 **B**).
The relaxation parameters and heteronuclear NOE (nuclear Overhauser effect) of CC1ΔC223 indicated fast and uniform dynamics, consistent with a lack of stable structural elements and supporting the notion that the protein is not folded in solution (Fig. 4.5 **E**-**G**).

4.5 CC1ΔC223-microtubule interaction

To study CC1ΔC223-microtubule interactions in a residue-specific manner, ^{1}H-^{15}N HSQC NMR spectra of [u-^{15}N]-labelled protein in the presence of Taxol-stabilized microtubules were recorded. This experiment resulted in line broadening and vanishing of individual cross-peaks upon microtubule addition, which indicated faster relaxation of the signals. At a ratio of 4:1 CC1ΔC223:microtubule all peaks were still detectable and, thus, the increased relaxation rates of CC1ΔC223 upon microtubule addition were quantifiable by determining

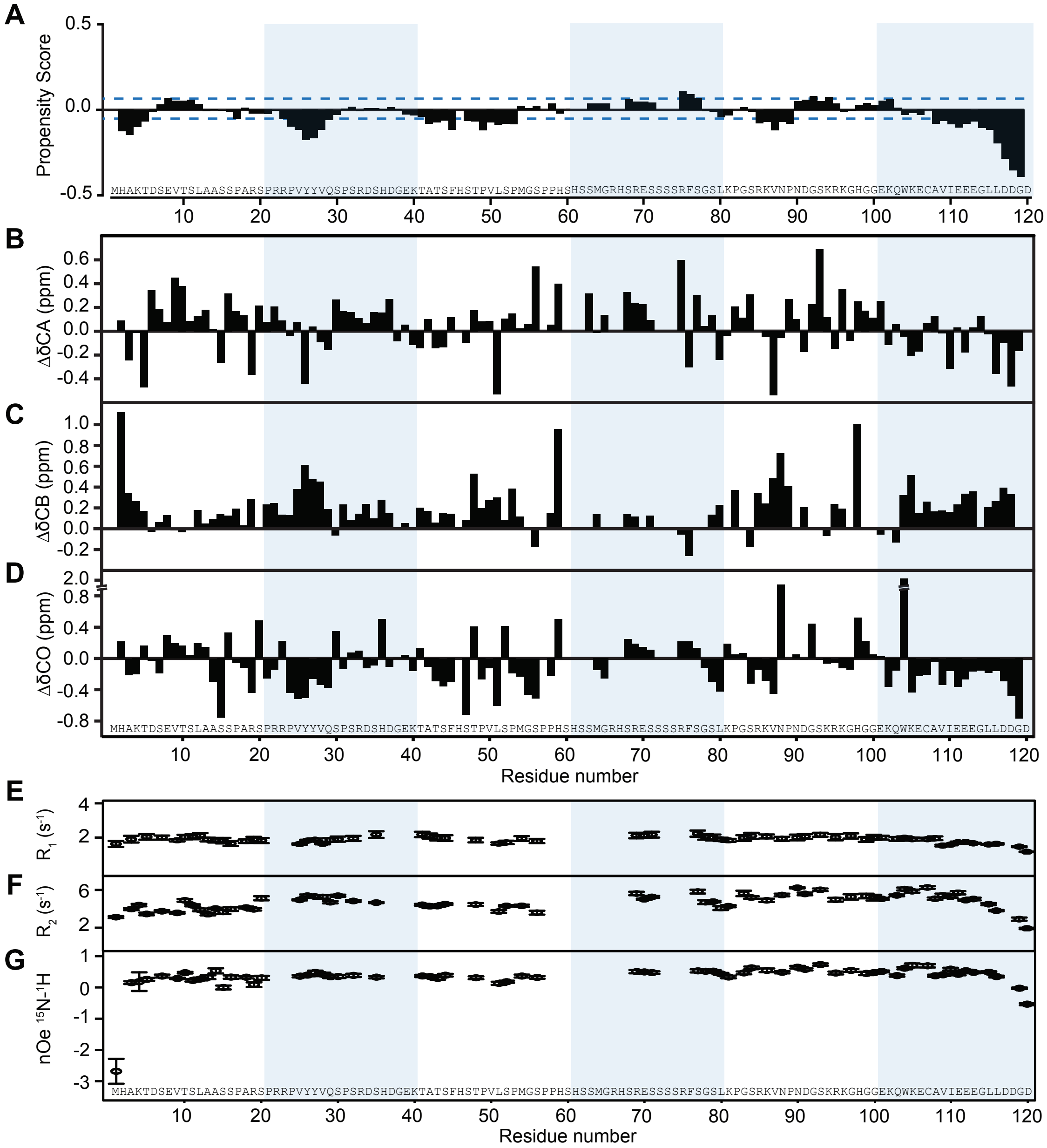

Figure 4.5 **Secondary structure propensity and dynamics. A** Structural propensity plot of CC1ΔC223 calculated by ncSPC [182]. **B - C** ΔδCA, ΔδCB and ΔδCO secondary chemical shifts values for CC1ΔC223 according to Tamiola et al. [181]. **E** and **F** Residue-resolved ^{15}N longitudinal (R_1) and transverse (R_2) relaxation rates of CC1ΔC223, respectively. **G** ^{15}N–^{1}H hetero-nuclear Overhauser effect data of CC1ΔC223.

the transverse relaxation rate ^{15}N-R$_2$ (Fig. 4.6 **A**, **B** and **C**). After the microtubule array disintegrated during storage at room temperature for 22 days, the CC1ΔC223 relaxation properties returned to the values similar to the microtubule-free sample (Fig. 4.6 **D** and **E**). Hence, the changes in the transverse relaxation rate of CC1ΔC223 signals are reversible and directly depend on the presence of microtubules. Furthermore, the effects of the microtubules on the transverse relaxation rate (ΔR$_2$) are not uniform but rather residue-specific and follow a gradual pattern along the sequence (Fig. 4.6 **F**). The determination of ΔR$_2$ on 600 MHz and 750 MHz NMR spectrometers revealed its independence of the magnetic field strength (Fig. 4.6 **G**). The addition of microtubules induced minor chemical shift changes (maximum of ^{15}N-$\Delta\delta$ of 0.4 Hz) to the CC1ΔC223 spectrum (Fig. 4.7 **A**), which did not correlate with the changes in the transverse relaxation rate ΔR$_2$ (Fig. 4.7 **B**). Relaxation dispersion experiments showed no contribution of intermediate exchange suggesting exchange slower than the millisecond regime (Fig. 4.7 **C**).

As described in chapter 1.2.1, line broadening can stem from two different sources: lifetime line broadening due to fast transverse relaxation rates in the bound state and chemical exchange broadening that arises from differences in chemical shifts between the free and bound states. Based on the data described above, the interaction between CC1ΔC223 and microtubules meets the requirements of slow exchange since addition of microtubules results in signals with almost identical chemical shift but substantial and field-independent differences in ^{15}N-R$_2$ values. Hence, the primary mechanism for the detected line broadening is the association of the free NMR-visible CC1ΔC223 to the microtubule, where it experiences fast transverse relaxation due to the long rotational correlation time of the complex. Therefore, the maximum observed increase in ^{15}N-R$_2$ is equal to the apparent first-order association rate constants k_{on}^{app} under the measurement conditions (^{15}N-ΔR_2^{max} = 3.95 $\pm$ 0.35 s^{-1} for V25). Altogether, these data indicate that the observed signal broadening is a direct result of CC1ΔC223-microtubule complex formation and can be further taken as a proxy for the efficacy and stability of the interaction.

As the broadening effect increased with higher microtubule concentrations, at a ratio of 1:1 CC1ΔC223:microtubule, signals of several residues were broadened beyond detection, while others retained most of their intensity (Fig. 4.8 **A** and **B**). Figure 4.8 **C** shows the intensity ratio of cross-peaks taken from 3D HNCA spectra of [u-^{13}C, ^{15}N]-labelled CC1ΔC223 in the presence and the absence of microtubules (I_{bound}/I_{free}) for each assigned residue. The 3D spectrum was chosen to reduce signal overlap to a minimum, but retain a short enough measurement time to ensure the stability of the microtubules.

Resulting from the broadening effect described above, small intensity ratios are the result of strong signal broadening due to the interaction of the corresponding region with microtubules.

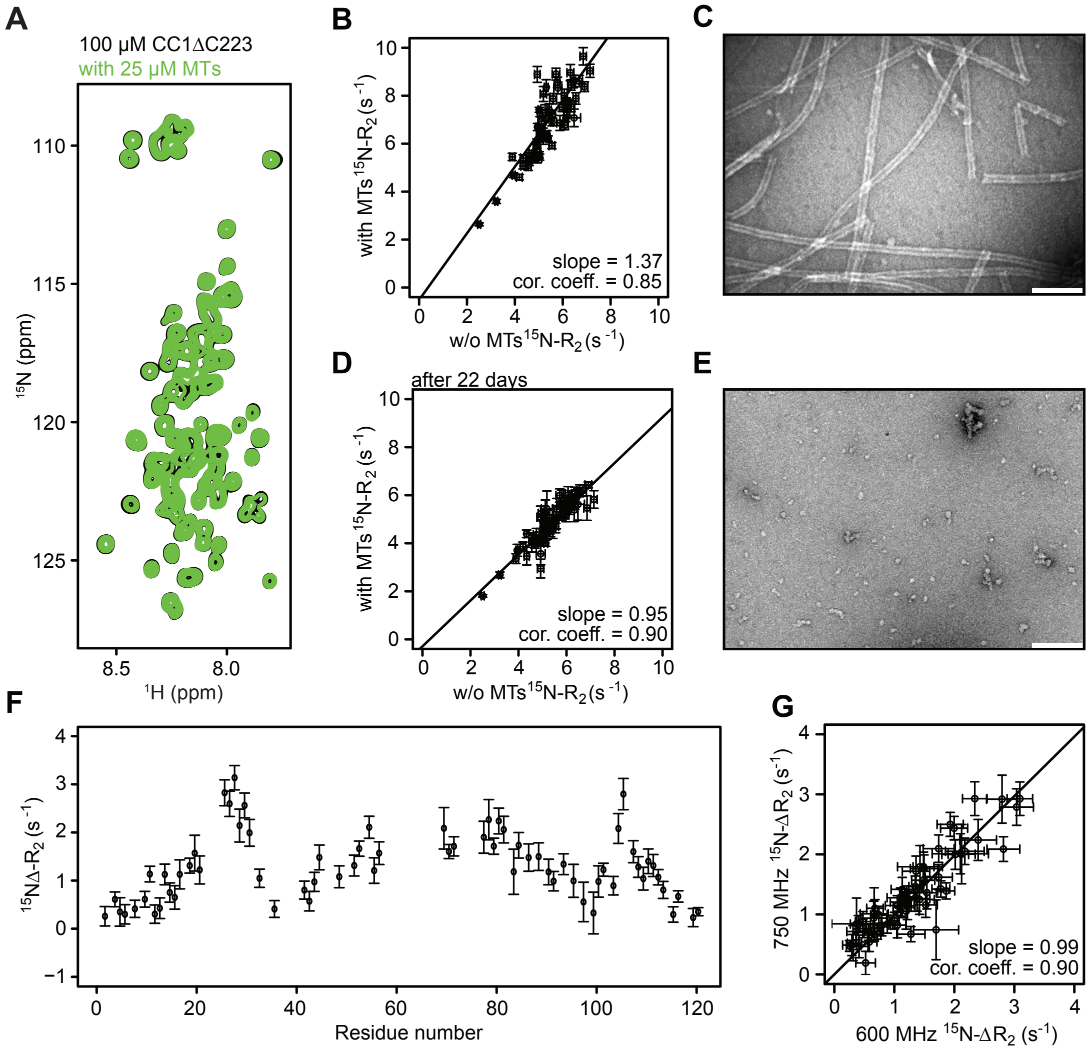

Figure 4.6 **Effect of microtubule binding on CC1ΔC223 relaxation properties. A** ^{1}H-^{15}N HSQC spectrum of free 100 μM CC1ΔC223 (black) and in the presence of 25 μM Taxol-stabilized microtubules (green). **B** CC1ΔC223 ^{15}N-R$_2$ relaxation rates before and after complexation with microtubules. EM micrograph of sample shown in **C**. Scale bar = 100 nm. **D** Comparison of the ^{15}N-R$_2$ relaxation of the free form and after the microtubules disintegrated. Insoluble protein aggregates were observed at the bottom of the NMR tube. EM micrograph of soluble sample shown in **E**. Scale bar = 100 nm. **F** Residue-specific changes in relaxation rates ^{15}N-ΔR$_2$ after addition of microtubules. **G** Correlation of ^{15}N-ΔR$_2$ values recorded at spectrometer frequencies of 600 and 750 MHz.

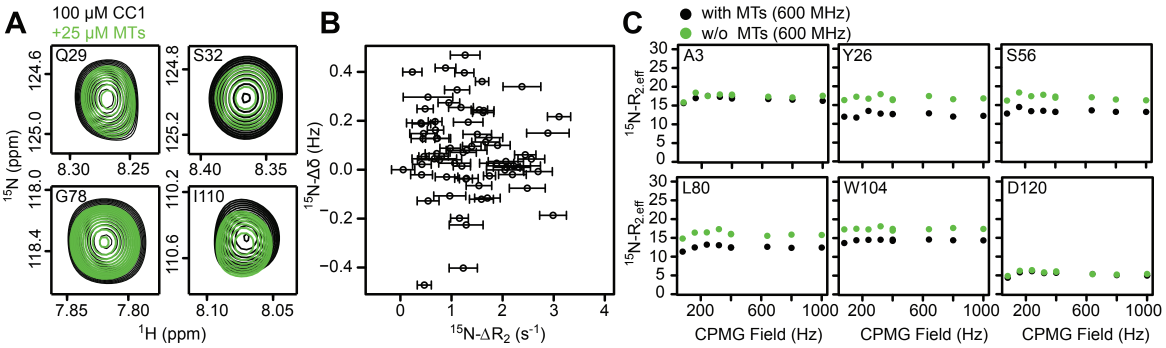

Figure 4.7 **Induced shifts and relaxation dispersion upon microtubule binding. A** Selection of peaks of the ^{1}H-^{15}N HSQC spectra of 100 µM CC1ΔC223 in the absence (black) and the presence (green) of 25 µM microtubules. **B** ^{15}N-ΔR$_2$ do not correlate with ^{15}N chemical shift changes that occur upon complex formation. **C** Examples of ^{15}N CPMG relaxation dispersion curves for free CC1ΔC223 (black) and in the presence of microtubules (green) at 600 MHz.

Overall, a significant decrease of intensities in four linear motifs of the sequence, comprising residues ^{23}RPVYYVQS^{30}, ^{45}FHSTPVLSPM^{54}, ^{74}FSGSLKPG^{83} and ^{103}QWKECAVI^{110}, was observed. Due to signal overlap resulting in incomplete assignments, the region between residues 60 and 80 is not well covered, but the sparse data indicates some involvement in the binding. Residues with severely overlapped signals in the HNCA spectrum were not included in the analysis.

The N-terminal region ^{23}RPVYYVQS^{30} received the strongest signal reduction and is broadened almost beyond detection. The most C-terminal region ^{103}QWKECAVI^{110} was broadened to a lesser extent and retained ∼ 20 % of its signal intensity. There is a clear correlation between the NMR-based microtubule-interaction profile and the hydrophobicity pattern of CC1ΔC223, highlighting the importance of hydrophobic interactions for the formation of the complex (Fig. 4.8 **D**).

The binding motifs are separated by stretches of residues that show gradually less signal broadening with distance from the minima of the motifs. It is likely that those residues also retain a higher degree of flexibility in the complex and might act as linker regions facilitating a highly dynamic interaction with microtubules. Moreover, the interaction motifs coincide with patches of higher overall sequence conservation, while the region representing the longest linker region CC1(83-103) shows high sequence variability.

The binding of CC1ΔC223 to unpolymerized tubulin was monitored using ^{1}H-^{15}N HSQC experiments before and after the polymerization (Fig. 4.9 **A**). The residue-resolved intensity ratio between tubulin-bound and microtubule-bound CC1ΔC223 does not show significant differences in the binding pattern as the same set of residues are affected and thus indicates

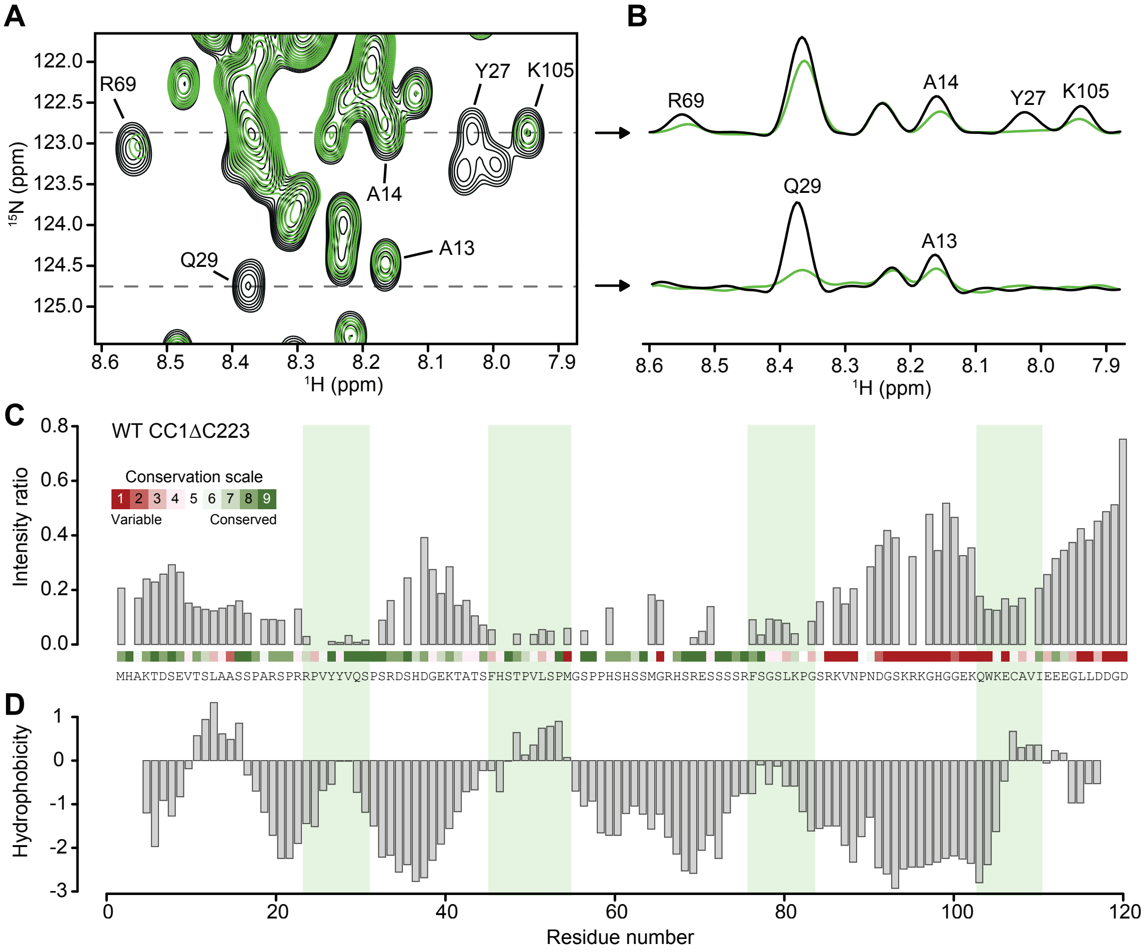

Figure 4.8 **CC1ΔC223 binding to microtubules. A** ^{1}H-^{15}N HSQC spectrum of CC1ΔC223 both free (black) and in the presence of equimolar Taxol-stabilized microtubules (green). Selected residues are labelled. **B** F_2-cross sections showing ^{1}H-signals taken along dotted lines in **A** at ^{15}N frequencies 122.9 and 124.7 ppm. **C** Intensity ratio of free CC1ΔC223 HNCA signals and in complex with microtubules. Minima are highlighted with green bars. Site-specific evolutionary conservation calculated by CONSURF is plotted above the sequence in a color code (green = conserved, red = unconserved). **D** Hydrophobicity scores of CC1ΔC223 according to the Kyte-Doolittle scale and calculated in a 5-amino-acid window.

that the overall binding features are similar. However, the possibility cannot be excluded that microtubule precursors like protofilaments or tubulin rings were induced by CC1ΔC223 upon addition of tubulin as CC1ΔC223 has been shown to promote microtubule formation in the presence of GTP [163].

To further characterize the dynamic properties of CC1ΔC223, peak intensity changes were measured in artificially crowded solutions containing Ficoll and BSA. In the microtubule interaction signal attenuations affected the previously described hydrophobic motifs, whereas the crowding agents did not recapitulate these line broadening effects. BSA-crowding led to an overall uniform signal reduction, consistent with a viscosity-driven reduction in overall protein mobility. However, the residues of the N-terminus displayed more severe attenuation of their signal intensities (Fig. 4.9 **B**). The biological inert crowding agent Ficoll caused some broadening around the N-terminal ^{16}SPARS^{20} region, but overall signal reduction did not show any significant pattern (Fig. 4.9 **C**). Under both crowding conditions the ^{23}RPVYYVQS^{30} regions retain almost all of their signal intensity indicating high flexibility.

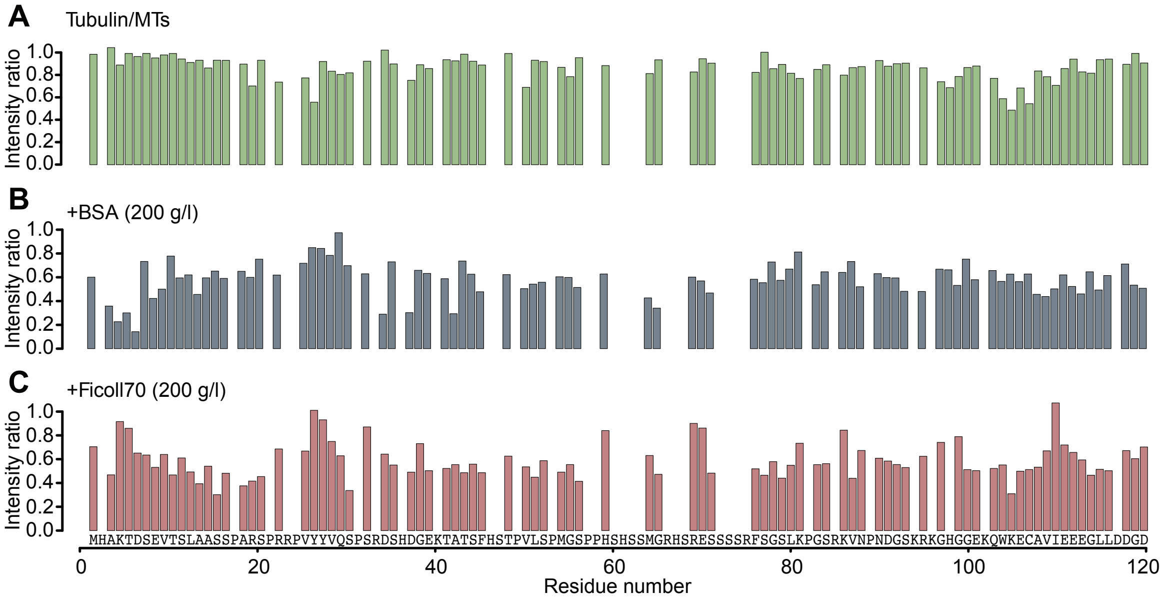

Figure 4.9 **CC1ΔC223 binding to tubulin and under crowding conditions.** **A** Signal intensity ratio of CC1ΔC223 in the presence of tubulin and after microtubule polymerization (I_{tub}/I_{MT}). **B** and **C** Signal intensity ratio of CC1ΔC223 under BSA and Ficoll70 crowding, respectively ($I_{crowded}/I_{free}$). All intensity ratio determinations were based on 2D ^{1}H-^{15}N HSQC experiments.

4.6 Microtubule interaction of CC1-derived peptides

To investigate the binding motifs individually and identify the amino acids that are major contributors to microtubule binding, Saturation Transfer Difference (STD) NMR measurements were performed on peptides that each contained one of the four microtubule-binding regions (Fig. 4.10 **A**). As STD NMR only yields a visible effect when the exchange from the bound to the free state is sufficiently fast, the binding of the targeted peptides to microtubules are required to be relatively weak. Since the overall K_D of CC1ΔC223 is in the micro-molar range, STD NMR was identified as a suitable method to study binding of individual binding motifs.

A positive control employing Tau(211-242) displayed significant STD intensities in the amide region as has been described in [38] (Fig. 4.10 **B**). The CC1-peptides CC1(41-64) and CC1(65-85) yielded strong STD intensities in the amide and aromatic regions of the ^{1}H spectrum (Fig. 4.10 **C** and **D**). The STD signals were assigned, using ^{1}H-^{13}C HMQC, to the aromatic side chains of histidine and phenylalanine residues, indicating strong contributions of these residues to the binding. In CC1(41-64), residues H46, H59 and H61 showed STD intensities from HE and HD2 protons and residue F45 from HD, HE and HZ protons. In CC1(65-85), HE and HD2 protons from residue H65 and HD, HE and HZ protons from residue F76 produced detectable STD signals.

No significant STD effects were observed for a negative control peptide CC1(83-103), which contains the third poorly conserved linker region (Fig. 4.10 **F**). The peptide carrying the most C-terminal region CC1(100-114) also showed no detectable STD intensities under the applied conditions (Fig. 4.10 **E**). However, the region also exhibited the weakest interaction properties of all binding-motifs in the relaxation-based binding studies.

The peptide CC1(16-38) showed the most efficient transfer of magnetization when irradiating microtubules, indicative of strong binding of the peptide (Fig. 4.10 **G**), which is in line with the strong effect of that region observed in the relaxation experiments. Strikingly, the HE/HD tyrosine ring protons of ^{26}YY^{27} displayed significant STD intensities, suggesting a direct involvement of at least one of the aromatic rings in the interaction.

As CC1ΔC223 is known to promote microtubule polymerization *in vitro* [163], microtubule turbidity assays were performed with CC1 peptides to investigate if a similar activity is also detectable for individual fragments of the protein. The assay is based on the light-scattering properties of microtubules and monitors changes in absorption at an OD of 340 nm. While the addition of the positive controls CC1ΔC223 and Taxol to the tubulin clearly promoted microtubule formation, none of the CC1 fragment peptides showed any similar activity (Fig. 4.10 **H**). This result indicates that the above-described peptide binding alone is not sufficient to induce microtubule polymerization *in vitro*.

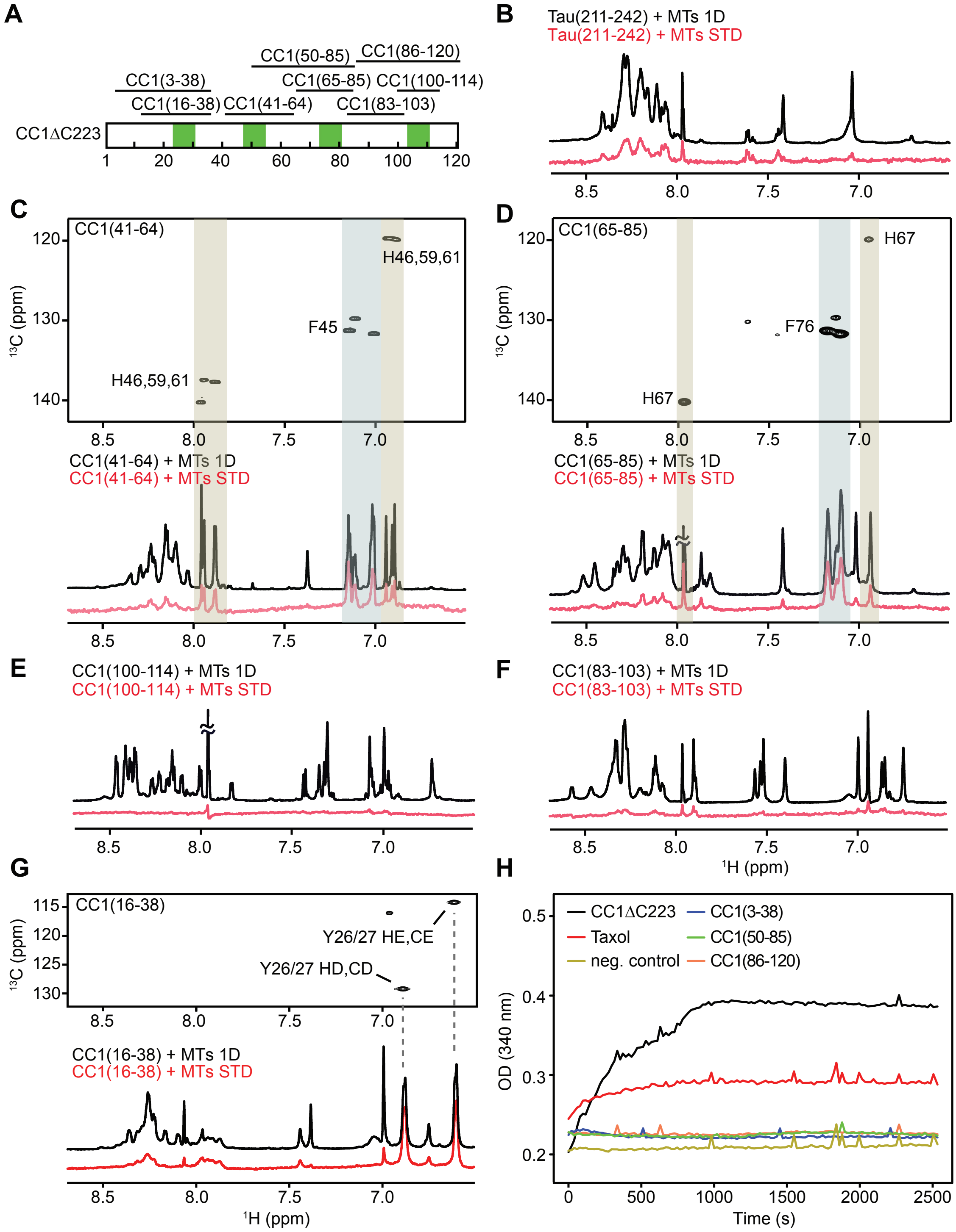

Figure 4.10 **CC1-derived peptides binding to microtubules.** **A** In the cartoon-overview of CC1ΔC223 the location of the microtubule-binding regions is highlighted in green and the peptides used for STD-NMR are indicated. **B** to **G**. Comparison of one-dimensional ^{1}H spectra (black) and STD difference spectra (red) of Tau(211-242), CC1(41-64), CC1(65-85), CC1(100-114), CC1(83-103) and CC1(16-38). The data of CC1(41-64), CC1(65-85) and CC1(16-38) are shown in combination with two-dimensional ^{1}H-^{13}C HMQC spectra for assignment. **H** In the turbidity assay, tubulin was incubated with buffer (negative control), Taxol, CC1ΔC223 and the respective CC1 peptides.

4.7 Microtubule bundling and diffusion activity of CC1ΔC223

To further investigate the molecular details of the CC1ΔC223-microtubule interaction and its effect on microtubule organization, additional *in vitro* experiments were conducted by members of Staffan Persson's lab at the University of Melbourne. Their results are presented here for the sake of completeness.

Semi-quantitative TEM image analysis showed that microtubule co-polymerization with increasing amounts of CC1ΔC223 promotes wall-to-wall microtubule bundling *in vitro* (Fig. 4.11 **A** and **B**). Using 5 nm gold-conjugates that recognize 6xHis-tagged CC1ΔC223, the microtubule binding pattern was visualized *via* TEM (Fig. 4.11 **C**). Intriguingly, gold-labelling only occurred between closely aligned microtubules with very small inter-microtubule distances. The gold particles were evenly distributed as straight rows along interfaces of the two neighbouring microtubules and typically did not shift between neighbouring protofilaments on the same microtubule. Multiple gold-labelled rows were also visible on a single microtubule if it was found in close proximity to several microtubules. The distances between successive intensity minima were quantified by mapping the light intensity minima along transects at the gold-labelled rows. The data indicated that CC1ΔC223 binds to neighbouring microtubules in rows of particles with an average spacing of 10 nm (± 2.4 nm) (Fig. 4.11 **D**).

As the TEM experiments only provide static information on the interaction between CC1ΔC223 and microtubules, CC1ΔC223 was labelled with the green fluorescent dye CF488A-maleimide to perform rhodamine-labelled microtubule interaction assays using total internal reflection fluorescence (TIRF) microscopy. In channels with fixed rhodamine labelled microtubules CF488A-labelled CC1ΔC223 diffused bidirectionally and freely along the microtubule-lattices with diffusion coefficient of $0.076 \pm 0.005\ \mu m^2/s$ (Fig. 4.11 **E** and **F**). Consistent with the co-occurrence of gold-labelled CC1ΔC223 with microtubule bundles, CF488A-labelled foci occupied bundled microtubules more stably than single microtubules (Fig. 4.11 **G**).

To determine the binding interface on the microtubules, 6xHis-tagged CC1ΔC223 was incubated with α-β-tubulin dimers and the complex was cross-linked using 1-ethyl-3-(3-dimethylaminopropyl) carbodiimide hydrochloride (EDC), an efficient zero-length covalent cross-linker. LC/MS/MS analysis of the cross-link reaction lysate and of cross-linked bands revealed five well-defined covalent bonds between CC1ΔC223 and α-β-tubulin. Here, four CC1ΔC223 residues were consistently detected to be cross-linked to β-tubulin (K40 to E111, K94 to E111, K96 to E111 and K96 to E158; amino acids in the protein sequence of CC1ΔC223 and β-tubulin, respectively; Fig. 4.11 **H**). On α-tubulin, CC1ΔC223 cross-linked to a single residue (K40 to D327), which is close to the hydrophobic interface between tubulin heterodimers.

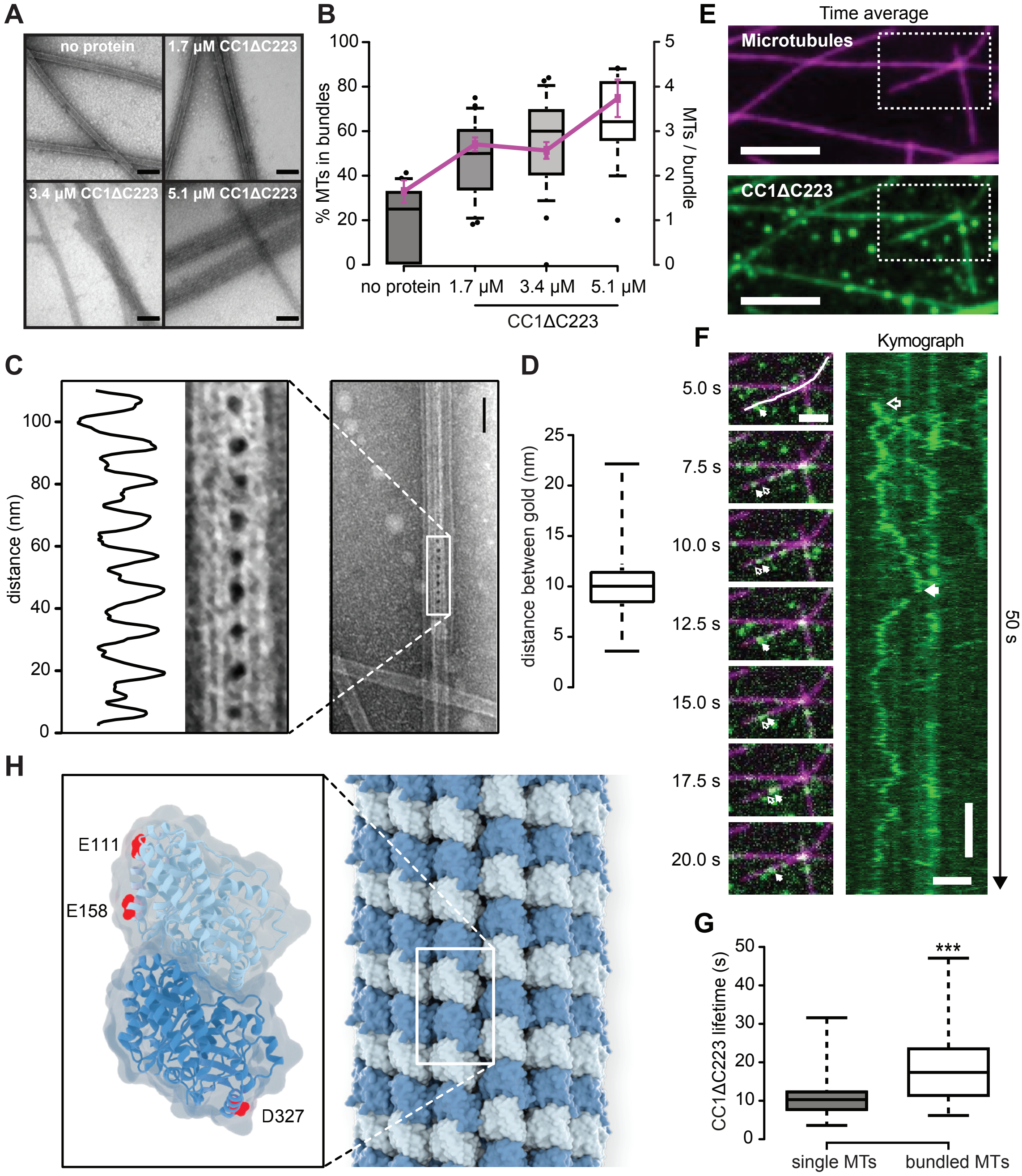

Figure 4.11 **CC1ΔC223 microtubule-binding and bundling properties.** **A** TEM images of negatively-stained taxol-stabilized microtubules after addition of increasing levels of 6xHis-CC1ΔC223. Scale bars = 100 nm. **B** Quantification of the proportion of microtubules in bundles (left y-axis, box plots) and number of microtubules per bundle (left y-axis, magenta line) with increasing concentration of 6xHis-CC1ΔC223. **C** Representative TEM image of CC1ΔC223 distribution along negatively-stained microtubules. **D** Quantification of the distance between individual gold particles. **E** CF488A-labelled 6xHis-CC1ΔC223 proteins (green) associated with surface-bound microtubules (magenta). Scale bar = 5 µm. **F** Time-series images (left panel) of CF488-labelled 6xHis-CC1ΔC223 diffusing along microtubules. Filled arrow = position in current frame, empty arrow = position in previous frame. Kymograph (right panel) along solid line in left panel (top) showing diffusion of 6xHis-CC1ΔC223 foci. Scale bars = 2 µm. **G** 6xHis-CC1ΔC223 lifetime on single versus bundled microtubules. **H** Projection of detected cross-links onto α- (dark) and β-tubulin (light).

4.8 CC1YYAAΔC223-microtubule interaction

The well-conserved residues ^{26}YY^{27} of the CC1ΔC223 N-terminal binding site showed strong binding in the relaxation-based and the STD-NMR experiments. Targeting this binding motif, the exchange of ^{26}YY^{27} to alanines was designed to investigate if mutation would lead to the disruption of microtubule binding. Indeed, the CC1YYAA(16-38) peptide showed a substantially reduced STD profile, corroborating a contribution of the tyrosine aromatic rings to the interaction (Fig. 4.12 **A**). The same mutation in the full N-terminal domain, CC1YYAAΔC223, was expressed, purified, isotopically labelled and assigned using 3D HNCACB and HN(CO)CACB NMR spectra. Beyond the mutation's effect on the immediate sequential environment, the resonances of CC1YYAAΔC223 closely resembled the ones assigned for CC1ΔC223 with no detectable long range effects (Fig. 4.12 **B**). The interaction with microtubules of [u-^{13}C, ^{15}N]-labelled CC1YYAAΔC223 resulted in significantly reduced signal broadening of residues in the N-terminal region, while the intensity ratios for the C-terminal part remained similar to the wild-type protein: the ^{23}RPVAAVQS^{30} region and its surrounding loop regions were affected most and the effect on the following ^{45}FHSTPVLSPM^{54} binding motif was not pronounced (Fig. 4.12 **C** and **D**). From residue 70 on, only minor effects were visible. However, the mutated site still represents a minor minimum in the intensity ratio profile indicating that the mutated motif retains some residual binding ability.

While the mutations did not abolish binding to microtubules, they weakened the interaction by reducing the contribution of the first microtubule binding site. This was corroborated with microtubule spin down assays, performed by Christopher Kesten, in which CC1YYAAΔC223 still bound to microtubules albeit with a lowered affinity compared to the wild-type CC1ΔC223 as per K_D estimates (Fig. 4.12 **E** and **F**). Overall, these results highlight the importance of the two tyrosine residues in microtubule binding and further indicate that the binding motifs function independently but cooperatively when interacting with microtubules.

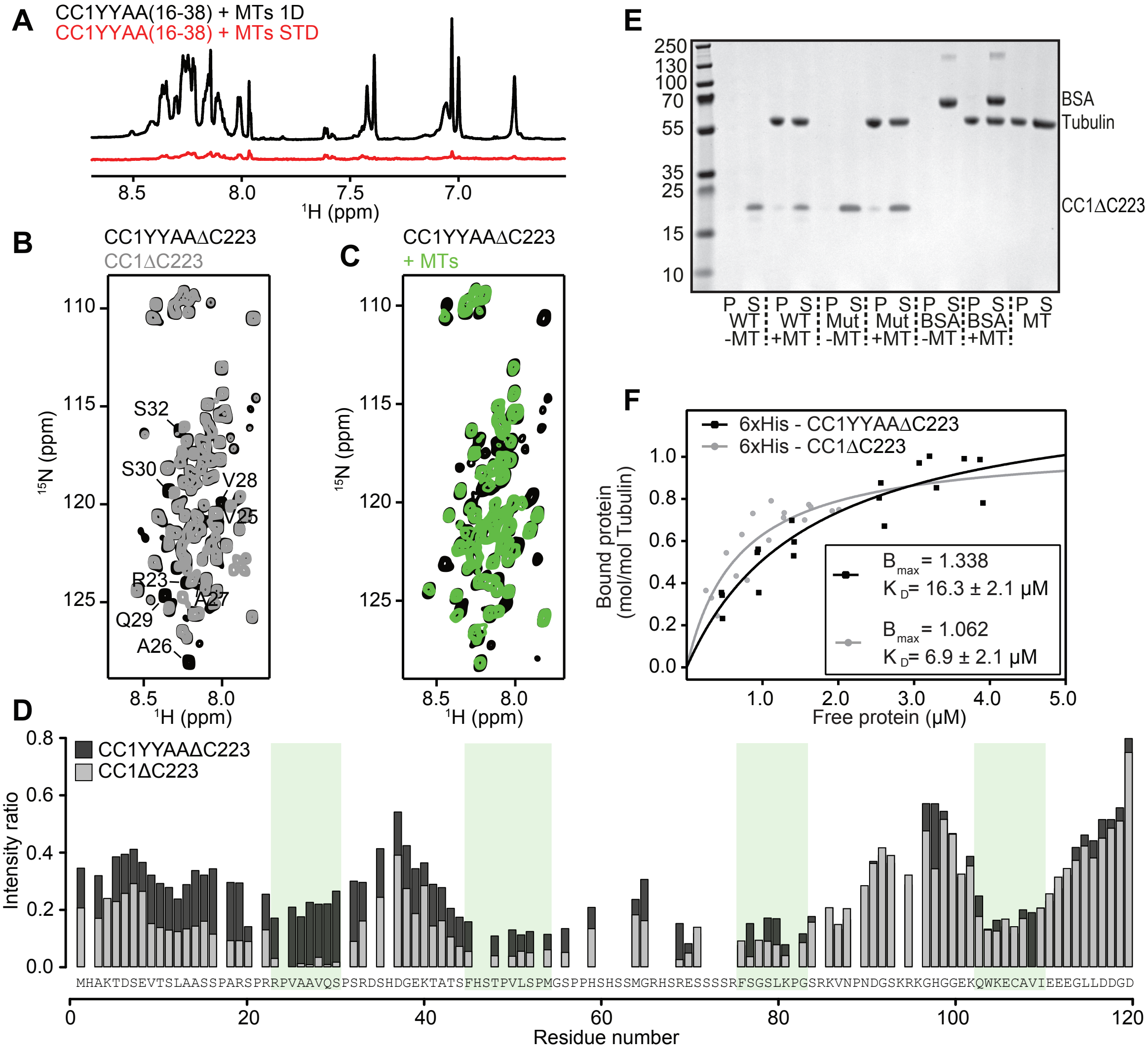

Figure 4.12 **CC1YYAAΔC223 microtubule binding.** **A** 1D NMR spectrum and STD profile for the mutated CC1YYAA(16-38) peptide in the presence of microtubules. **B** Overlay of the mutated CC1YYAAΔC223 and the CC1ΔC223 HSQC spectra with mutated residues, and residues in their proximity, assigned. **C** HSQC spectrum of CC1YYAAΔC223 before and after adding microtubules. **D** Intensity ratio of free CC1YYAAΔC223 HNCA signals, and in complex with microtubules, compared with the non-mutated profile. Colours and details are as those in Fig. 4.8. **E** Microtubule co-sedimentation assay of 6xHis-CC1ΔC223 (WT) and 6xHis-CC1YYAAΔC223 (Mut). The target protein was enriched in the pellet fraction after centrifugation when Taxol-stabilized microtubules were present. BSA was used as a negative control. **F** The microtubule binding constants of 6xHis-CC1ΔC223 (6.9 ± 2.1 μM) and 6xHis-CC1YYAAΔC223 (16.3 ± 4.1 μM) were determined by estimation of binding of the respective protein when microtubule levels were constant.

4.9 CC1YYAA mutation in Arabidopsis

To determine how the two microtubule-interacting tyrosine residues impact the function of CC1 *in vivo*, the wild-type and tyrosine mutated (^{26}YY^{27} to ^{26}AA^{27}; referred to as CC1YYAA) full-length versions of CC1 were transformed into *Arabidopsis thaliana cc1cc2* mutant plants. The respective proteins were N-terminally fused to GFP to track the proteins inside living plant cells. All *in vivo* experiments were conducted by members of Staffan Persson's lab at the University of Melbourne.

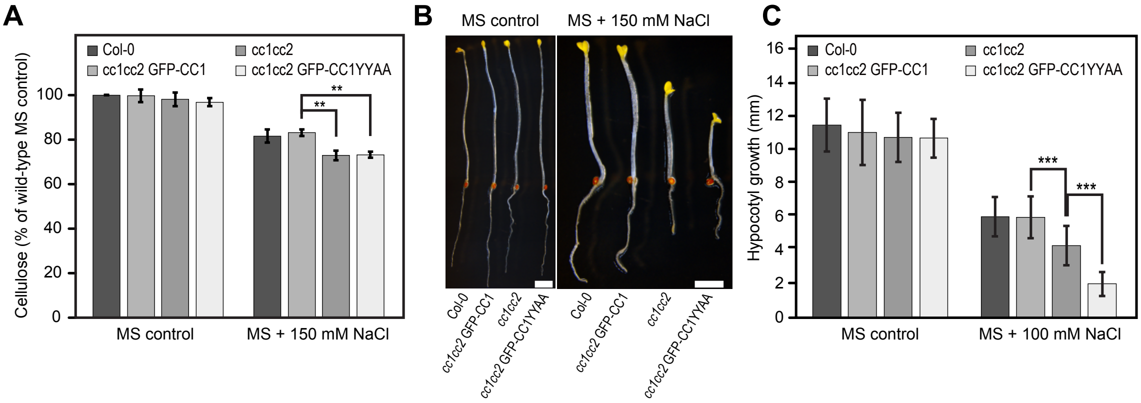

Figure 4.13 **Growth and cellulose synthesis of CC1YYAAΔC223 plant mutants under salt stress.** **A** Cellulose levels in seedlings grown as in (B). Values are means +/- SD expressed as % cellulose of wild-type seedlings grown on MS control media. Unpaired t-test; ** p-value 0.01. **B** Seedlings germinated and grown for two days on MS plates and then transferred to either MS control plates or MS plates supplemented with 150 mM NaCl and grown for additional 5 days. Scale bar = 2 mm. **B** Quantification of hypocotyl elongation of seedlings grown on MS plates for three days and then transferred to either MS control plates or MS plates supplemented with 100 mM NaCl and grown for additional 4 days. Unpaired t-test; *** p-value 0.001.

To study the salt-tolerance of the plants, seedlings were germinated and grown for three days on MS media and then transferred to salt-containing MS plates (100 mM NaCl). As reported in [163], the *cc1cc2* mutant seedlings display reduced growth and crystalline cellulose content on salt-containing media, which was fully restored in the CC1-GFP wild-type lines. However, these defects were not restored in *cc1cc2* GFP-CC1YYAA seedlings when grown on salt-containing media and displayed an even more pronounced growth defect than the *cc1cc2* seedlings (Fig. 4.13 **A** to **C**). Spinning-disc confocal microscopy was employed to study protein localization in dark-grown Arabidopsis hypocotyl cells.

Notably, GFP-CC1YYAA also co-migrated with the CSC (tdTomato(tdT)-CesA6) at the plasma membrane like the wild-type, but unlike GFP-CC1, the migration of GFP-CC1YYAA

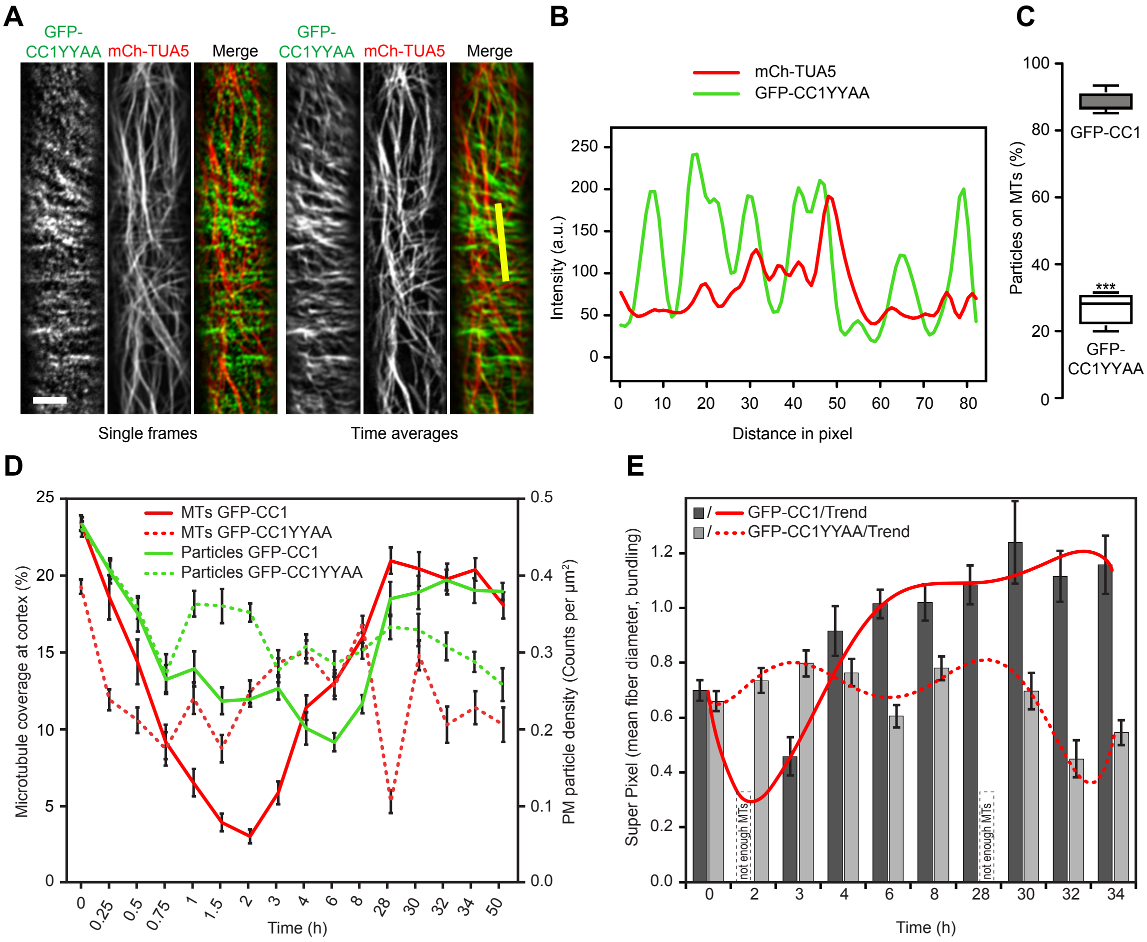

Figure 4.14 **Microtubule regulation and coverage of CC1YYAAΔC223 plant mutants under salt stress. A** GFP-CC1YYAA and mCh-TUA5 in dual-labelled three-day-old *cc1cc2* etiolated hypocotyls (left panels; single frame, right panels; time average projections). Scale bars = 5 µm. **B** Fluorescence intensity plot of GFP-CC1YYAA and tdT-CESA6 from transect in **D** along the depicted yellow line. **C** Quantification of GFP-CC1 and GFP-CC1YYAA fluorescent foci on cortical microtubules. Unpaired t-test; *** p-value 0.001. **D** Quantification of microtubule and GFP-CC (GFP-CC1 or GFP-CC1YYAA) coverage at the cell cortex and plasma membrane, respectively, after exposure of *cc1cc2* seedlings to 200 mM NaCl. **E** Quantification of microtubule bundling after exposure of *cc1cc2* GFP-CC1 /GFP-CC1YYAA seedlings to 200 mM NaCl.

was largely independent of cortical microtubules (mCherry (mCh)-TUA5) (Fig. 4.14 **A** to **C**). This indicates that reduced microtubule binding of GFP-CC1YYAA either directly affects the ability of CSCs to engage with microtubules, or that the microtubule array is mis-regulated to an extent that renders it unable to fulfil its guiding function.

In order to assess how the microtubules and CesAs behave in response to salt in the cc1cc2 GFP-CC1YYAA seedlings, time-lapse imaging was performed on the cells at multiple time points after exposure to salt. Since the GFP-CC1YYAA signal co-localized and migrated together with CesAs, its signal was used as proxy for the behaviour of the CSCs. While the CSCs in the *cc1cc2* mutant did not re-populate the plasma membrane after salt exposure, a distinct GFP-CC1YYAA-signal was visible at the plasma membrane after 2 h of salt stress. Exposed to 200 mM NaCl, the microtubule (mCh-TUA5) cell coverage of *cc1cc2* GFP-CC1YYAA-complemented seedlings revealed the inability of the mutant to establish the salt-tolerant microtubule array and to restore cellulose synthesis during the course of the experiment (Fig. 4.14 **D**). Furthermore, the salt-adjusted microtubule array of the GFP-CC1YYAA cell lines displayed no increase in bundling and deviated in the overall microtubule dynamics when compared to GFP-CC1 cells (Fig. 4.14 **E**).

4.10 Heparin interaction of CC1ΔC223

MAPs with biophysical properties similar to CC1ΔC223 have been reported to bind the highly negatively charged polymer heparin, which displaces the proteins from their microtubule-bound state [195, 196]. NMR experiments were conducted to investigate if this interaction is also observed with the microtubule-binding N-terminus of CC1.

Adding an equimolar amount of heparin to [u-^{15}N]-labelled CC1ΔC223 induced significant chemical shift changes and signal broadening to the signals in the ^{1}H-^{15}N HSQC spectrum (Fig. 4.15 **A**). Performing titrations showed that these changes were concentration-dependent and allowed for plotting chemical shift changes as a function of the heparin concentration (Fig. 4.15 **B** and **C**). The CC1ΔC223 signals affected by the interaction with heparin are in the fast exchange limit, as they exhibit a gradual frequency shift with increasing heparin concentration. Exchange in the slow exchange regime, resulting in distinct doubling of cross-peaks, was not observed. The application of a simple one site/one ligand model to the titration curves yielded apparent K_D values that displayed some variance in the heparin affinity between the regions. However, exchange-induced line broadening hindered more detailed descriptions of the binding curve and the presence of multiple interaction sites precluded a more rigorous evaluation since a more complex interaction model would have been required.

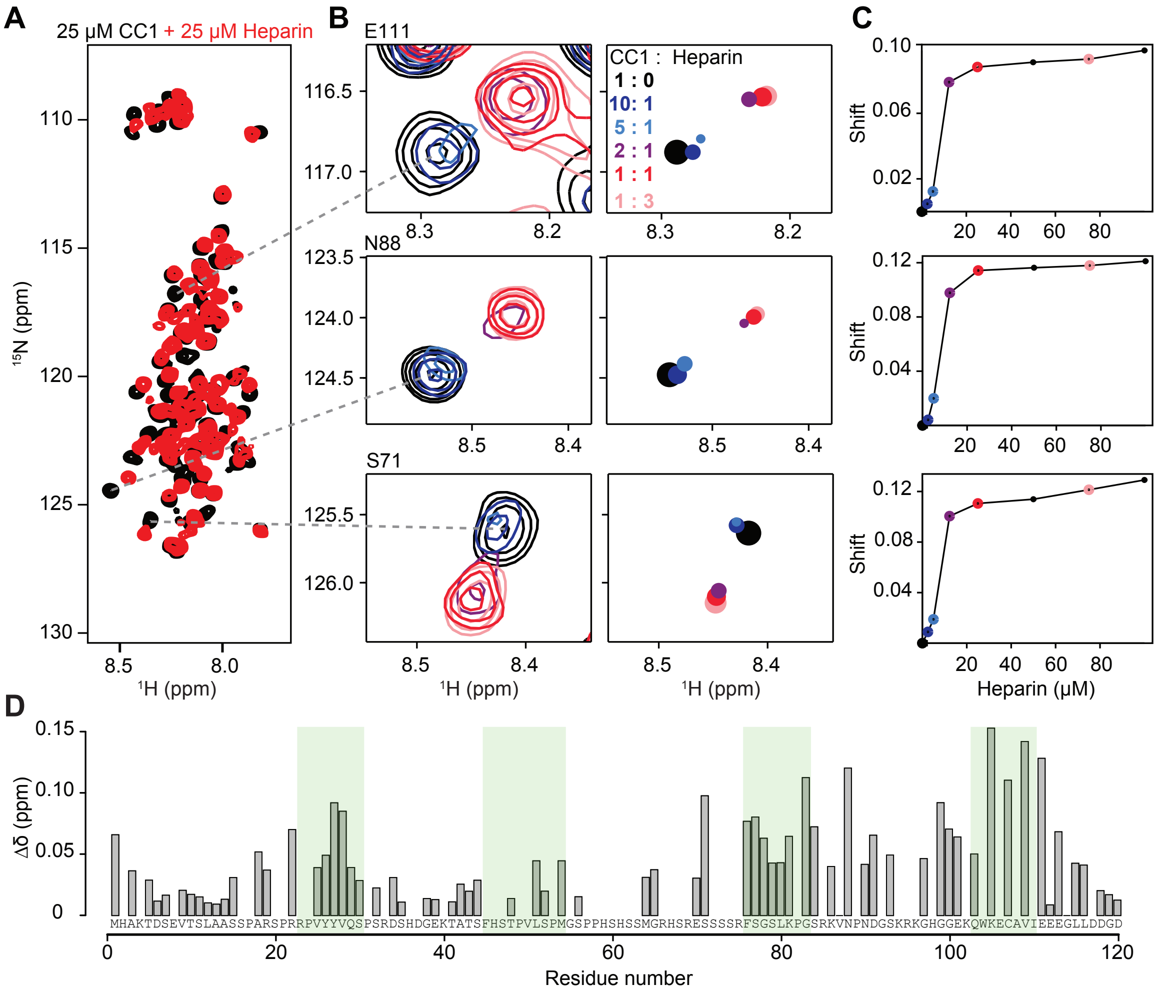

Figure 4.15 **CC1ΔC223 binding to heparin. A** ^{1}H-^{15}N HSQC spectrum of free CC1ΔC223 (black) and in the presence of equimolar heparin (red). **B** Titration of increasing concentrations of heparin to CC1ΔC223. Shifting and broadened peaks are represented by colored circles in the right panel. The size and and positioning of the circles correspond to the peak intensity and position, respectively. **C** Titration curves of CC1ΔC223 residues in **B** with heparin. **D** Residue-specific shift of CC1ΔC223 in the presence of equimolar heparin. Microtubule binding motifs are highlighted with green bars.

Although signal overlap and broadening prevented the determination of accurate dissociation constants for many signals, significant chemical changes were observed for resonances of residues covering different regions of the CC1ΔC223 sequence. When plotted for the residues of the protein, the changes follow a rather gradual pattern along the sequence, similar to the relaxation-based data of the microtubule interaction. Figure 4.15 **D** shows the weighted chemical shifts changes $\Delta\delta$ for each assigned residue of CC1ΔC223 when incubated with an equimolar concentration of heparin. Interestingly, residues that receive a significant change in chemical shift also cluster around the motifs that bind microtubules. In particular residues K105 and V109, located near the most C-terminal motif, show strong changes in chemical shift when in complex with heparin. Y27 and V28 of the N-terminal microtubule-binding motif represent a local maximum of chemical shift perturbation indicating that they potentially contribute to the heparin binding. While the signals stemming from ^{45}FHSTPVLSPM^{54} are rather unaffected by the heparin interaction, the motif ^{74}FSGSLKPG^{83} represents another site of strong interaction, although less well-defined due to missing assignments. The lack of any positively charged arginine and lysine residues in the non-interacting regions suggests that electrostatics might dominate the interaction between positively charged side chains of CC1 and the negative charges on the heparin polymer.

Since the heparin interaction sites seem to cluster close to the microtubule-binding sites of CC1ΔC223, NMR experiments were conducted to examine the effects of the presence of heparin on the microtubule binding. For this, [u-^{15}N]-labelled CC1ΔC223 was first incubated with an equimolar amount of microtubules and then heparin was added in equal amounts monitoring the changes in the ^{1}H-^{15}N HSQC spectrum (Fig. 4.16 **A** and **B**). Comparing the spectrum of CC1ΔC223 with both heparin and microtubules present to the peak positions of the free form and the spectrum with only heparin present shows that many chemical shifts resemble CC1ΔC223 in the heparin-bound state (Fig. 4.16 **C**). Moreover, some signals that were broadened beyond detection when bound to microtubules, reappear after heparin addition (e.g. ^{26}YY^{27}). These results indicate that CC1ΔC223-binding to heparin seems to directly compete with its microtubule-binding capability and heparin might displace CC1ΔC223 from microtubules.

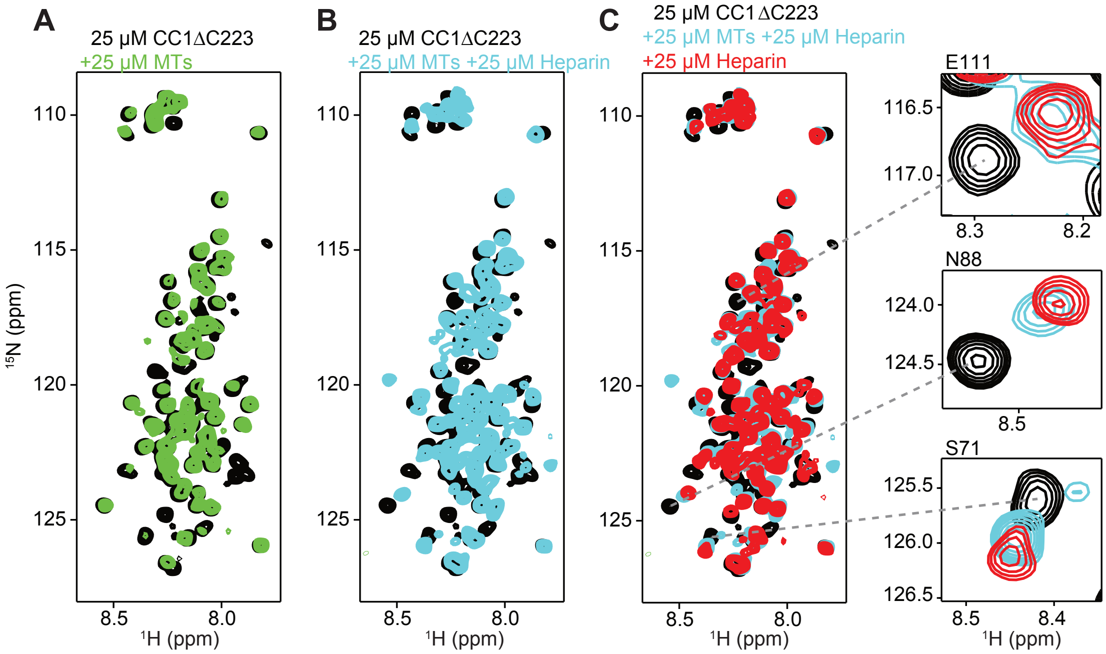

Figure 4.16 **CC1ΔC223 microtubule-binding in the presence of heparin.** **A** ^{1}H-^{15}N HSQC spectrum of free CC1ΔC223 (black) and in the presence of equimolar Taxol-stabilized microtubules (green). **B** ^{1}H-^{15}N HSQC spectrum of free CC1ΔC223 (black) and in the presence of equimolar Taxol-stabilized microtubules and heparin (blue). **C** ^{1}H-^{15}N HSQC spectrum of free CC1ΔC223 (black), in the presence of equimolar Taxol-stabilized microtubules and heparin (blue) and only in the presence of heparin (red). Blow-ups of selected peaks are shown to the right.

4.11 CC1 binding to AtSH3P1

In co-immunoprecipitation (Co-IP) pull-down experiments of GFP-CC1 with Arabidopsis cell extracts, 27 proteins were identified as putative interactors of CC1 [197]. One of these was the *Arabidopsis thaliana* Src homology 3 (SH3) domain containing protein (AtSH3P1; At1g31440) was enriched in the CC1 pull-down. AtSH3P1 has been shown to localize to the plasma membrane, where it colocalized with clathrin and was proposed to perform regulatory or scaffolding function in the fission and uncoating of clathrin-coated vesicles [198]. Since bulk endocytosis is upregulated by salt stress in plants, it is thus plausible that a potential CC1-AtSH3P1 interaction plays a role in the plant's reaction to saline conditions. AtSH3P1 has also been proposed to interact with the 65-kDa microtubule-associated protein 1 (MAP65), which was shown to bundle and stabilize adjacent microtubules [198, 154, 153]. Indeed, the sequence of CC1 contains multiple regions that match the typical PXXP (X is any amino acid and P is proline) motif, which was reported to be critical for SH3-domain binding [199]. After successful expression and purification of AtSH3, initial ^{1}H-^{15}N HSQC experiments showed a favourable peak dispersion in the proton dimension, indicating that the protein is folded (Fig. 4.17 **A**). The backbone assignment was realized employing 3D HNCACB an HN(CO)CACB experiments and nearly all resonances could be assigned (see Appendix A for full chemical shift table). The chemical shift indices matched the typical SH3 fold with five β-strands that form two tightly packed anti-parallel β-sheets in the structure (Fig. 4.17 **B**).

Binding experiments were performed using the peptides CC1(16-38) from the cytosolic N-terminus and CC1(258-291) from the apoplastic C-terminus. While CC1(16-38) includes only one matching motif (^{21}PRRP^{24}), CC1(258-291) is a proline-rich region that contains multiple motifs that repeat and partially overlap (e.g. ^{260}PAPP^{263}, ^{282}PAPP^{285}). The CC1(16-38) titration resulted in no clear chemical shift perturbations in the AtSH3 spectrum and thus there is no evidence for binding even at high peptide:AtSH3 ratios. In the titration with CC1(258-291), residues W40, Q17 and A18 of AtSH3 showed minor but significant chemical shift changes upon addition of the peptide (Fig. 4.17 **C**). As the structure of AtSH3 has not been solved, a three-dimensional AtSH3 model was calculated with Swiss Modeller using the X-ray structure of the C-terminal SH3 of the human Tuba protein (PDB code: 4CC7) as template, which shares 41 % identity with AtSH3. Mapping the shifting residues to the homology model of AtSH3 domain revealed their location close the classical core binding site of the protein (Fig. 4.17 **D**). Although the results indicate weak but consistent *in vitro* binding behaviour of CC1(258-291) to AtSH3, the physiological relevance of this interaction has yet to be determined.

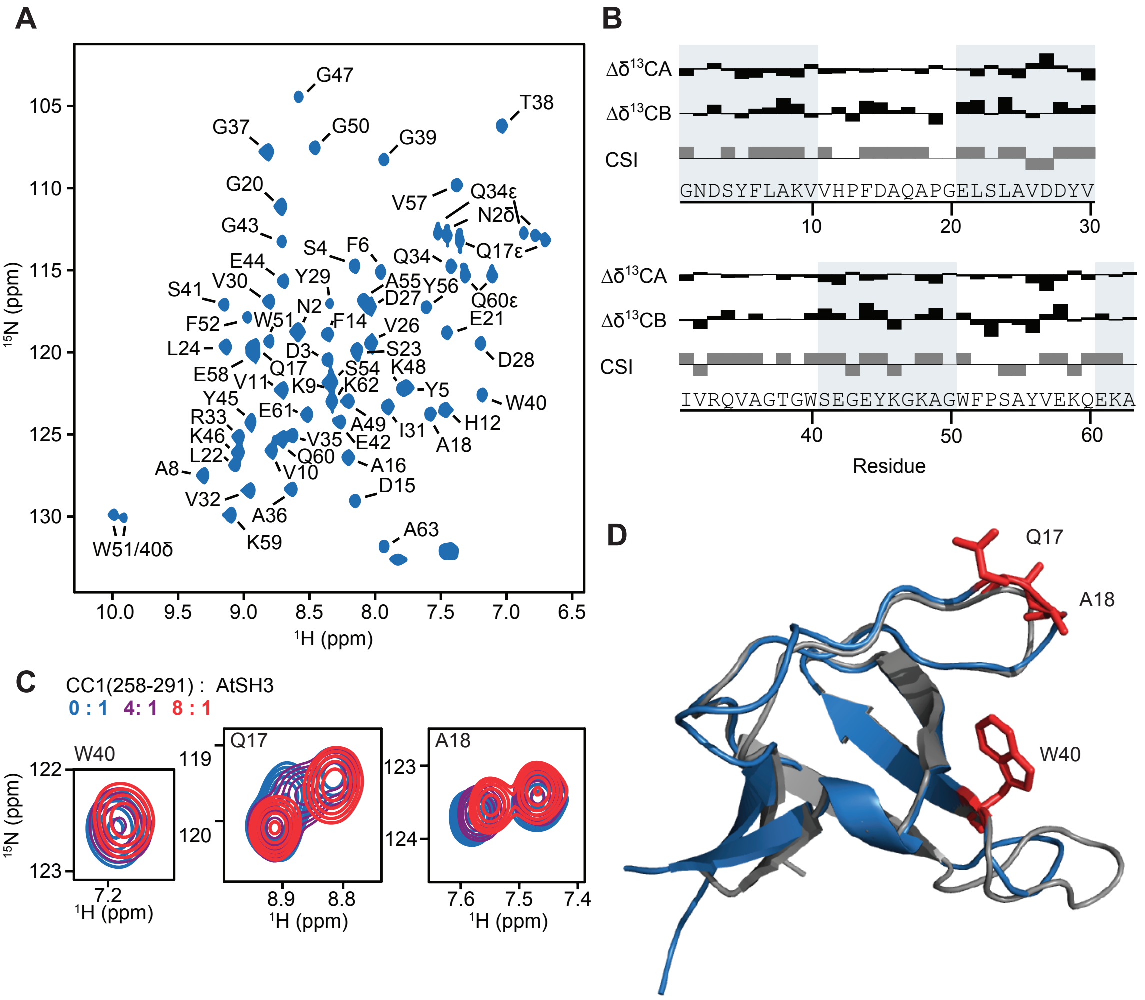

Figure 4.17 **AtSH3 binding to CC1-derived peptides. A** Assigned ^{1}H-^{15}N HSQC spectrum of AtSH3. **B** CSI of AtSH3 ($\Delta\delta$CA, $\Delta\delta$CB) according to Wishart and Sykes [200]. Positive, negative and neutral values represent β-strand, α-helical and random coil structure or propensity, respectively. **C** Detail from HSQC spectra of AtSH3 in titrations with peptide CC1(258-291). **D** Homology model AtSH3 (blue) and template structure from the human dynamin-binding protein Tuba (grey) [201]. Highlighted in red are the residues W40, Q17 and A18, which are located at the binding site of AtSH3.

Chapter 5

Discussion

5.1 CC1 engages transiently with microtubules via linear hydrophobic motifs

Abiotic stress caused by high soil salinity has detrimental effects on plant growth that severely impact global agricultural productivity [202, 203]. Understanding the molecular mechanisms that underpin salt-tolerance in plants is therefore of critical importance. A comprehensive investigation from Endler et al. introduced the CC-proteins as key molecular players in the plant's response to salt-induced stress: the experiments revealed an essential contribution to the formation of a stable stress-tolerant array and provided strong evidence of a direct interaction between CC1 and microtubules [163]. However, the molecular details of this interaction and its effect on the organization and structure of the microtubule array under salt stress conditions remained largely unknown. This work outlines a mechanism for how the cytosolic domain of CC1 can transiently interact with tubulin heterodimers and microtubules promoting polymerization and bundling of microtubules and ultimately the formation of a stress-stable microtubule array which sustains cellulose synthesis when plants are exposed to salt.

As described in chapter 2.1.3, many important cellular events are orchestrated by a collection of different MAPs, which control the structure, organization and dynamics of the microtubule array. Although MAPs contribute important functions to microtubule-related processes, knowledge concerning the involved molecular mechanisms is sparse, especially in plant biology. In previous studies, solution-state NMR spectroscopy has been successfully employed to gain new insights into the microtubule-binding mechanism of multiple MAPs [102, 204, 205]. Since NMR is capable of atomic resolution, it can provide highly-detailed structural information on the location and size of binding sites and the dynamics of the interaction. In the case of the neuronal protein Tau, NMR was utilized to gain structural information and to identify microtubule-interacting regions [36, 102, 106]. Because of the high molecular weight of the Tau-microtubule complex, these experiments mainly relied on line broadening effects observed in the HSQC spectrum of MT-bound Tau. Further attempts were made to resolve the complex structure of MT-bound Tau by applying transferred NOE methods to isolated Tau fragments [38]. Other members of the structural MAP family such as MAP2 and MAP4 were also intensively studied by NMR, employing similar methodology [206, 39].

The application of solution-state NMR techniques to the microtubule binding domain of CC1 revealed that CC1ΔC223 is intrinsically disordered and thus adopts highly dynamic conformations. Upon complexation with microtubules, the line broadening observed in the CC1ΔC223 spectrum due to the chemical exchange between bound and free proteins was used to identify the regions involved in binding. The interaction with tubulin and microtubules is mediated by four highly localized, conserved and hydrophobic binding motifs that are interconnected by flexible linker regions. Control experiments showed no contribution from intermediate exchange broadening, suggesting that the detected relaxation is mainly due to relatively stable binding of the individual binding sites to the high molecular weight microtubules. STD-NMR showed that most fragments of the isolated binding sites are still able to bind microtubules but cannot promote microtubule formation when incubated with tubulin.

These results suggest that the binding-motifs on CC1ΔC223 likely bind independently and cooperatively to microtubules. This binding behaviour enables the protein to bind to either multiple individual free tubulin dimers or to those within the microtubule lattice, plausibly either leading to polymerization by increasing the local tubulin concentration or bundling of microtubules. Indeed, CC1ΔC223 enhanced microtubule-bundling *in vitro* and cross-linking mass-spectrometry identified complexes in which one CC1ΔC223 molecule was bound to multiple tubulin dimers. Interestingly, two sequentially distant residues of CC1ΔC223 were linked to the same residue on β-tubulin, suggesting that two regions on CC1ΔC223 might bind similar sites on two distinct β-tubulin molecules. The cross-linked position on the α-tubulin is close to the hydrophobic interface between tubulin heterodimers, a site that is frequently occupied by agents such as vinblastine and the stathmin-like domain (SLD) of RB3 that directly regulate microtubule formation [207, 208]. However, since the interacting peptides alone cannot promote polymerization, the binding itself does not seem to have a direct impact on the stability of the microtubule.

Gold-labelling TEM experiments revealed that the microtubules were linked through evenly spaced CC1ΔC223 proteins (approximately 10 nm apart) that aligned in straight rows. While the reason for this distribution remains unclear, it could indicate that CC1ΔC223 is able to span beyond a single tubulin dimer that is 8 nm in length. In the light of the cross-linking results, it is therefore tempting to hypothesize that CC1 increases protofilament stability by linking consecutive tubulin dimers longitudinally.

The bidirectional diffusion of CF488A-maleimide-labelled CC1ΔC223 on rhodamine-labelled microtubules agrees well with the transient and dynamic mode of interaction observed in the NMR experiments. Moreover, it shows that the static arrangement of the protein in the proximity of bundled microtubules in the gold-labelling experiments might represent the most stable but not the only conformation in which CC1 can engage with microtubules.

5.2 Mutation in CC1 disrupts microtubule binding and impairs salt-tolerance

Mutation of two tyrosine residues (^{26}YY^{27}) to alanines in the N-terminal binding motif of CC1 disrupted the microtubule-binding of the peptide carrying the isolated motif. In the full-length protein, the mutation affected only the binding of the mutated region and its neighbouring residues, which further supports the conclusion that the binding sites operate in a relatively independent manner. With the other binding sites still intact, binding was reduced but not fully abolished. Notably, the mutated N-terminal binding motif contained the longest stretch of β-strand secondary structure propensity, which was in line with the predicted secondary structure by the JPRED4 algorithm. It is therefore conceivable that the mutation disrupts the formation of a specific conformation, represented by this local structure, which is necessary for the binding.

In the cell, CC1 is a transmembrane protein that is located in close proximity to the CSC. Although the cytosolic CC1ΔC223-GFP construct alone is sufficient to recover the salt sensitive phenotype of *cc1cc2* mutants, the localization within the membrane of the full-length CC1 might influence its microtubule-binding ability by altering the conformational properties of the protein [163]. Interestingly, the hydrophobic nature of the interactions in the CC1-microtubule complex likely permits a more robust binding under conditions of high ionic strength, corroborating the importance of the protein's function during salt stress. Investigation of this effect in the cellular context was done through mutation of the binding motif closest to the N-terminus, the most distal and presumably the most exposed binding region, so as to minimize any possible effects of the membrane association on the microtubule interaction.

The introduction of YYAA-mutated CC1 into Arabidopsis *cc1cc2* mutants revealed that the

N-terminal microtubule-binding region of CC1 is functionally essential for the protein to interact properly with microtubules *in vivo*. The mutations disrupted microtubule-guided CSC movement and led to failure in the generation of a stress-tolerant microtubule array in seedlings. Previous studies have shown that two other proteins, CSI1/POM2 and the Cellulose Microtubule Uncoupling (CMU) proteins, impact the alignment of CSC trajectories and cortical microtubules [209–211]. Considering that the *cc1cc2* knockout mutation does not disrupt the alignment, it is likely that the YYAA-mutation does not directly interfere with the CSC-microtubule association but rather causes a severe mis-organization of the microtubule array leading to the loss of its CSC steering capacity. This finding will allow for a more detailed analysis of the parameters governing the functional and structural requirements of microtubule arrays that facilitate CSC tracking.

The observation that salt-tolerance is severely impaired in the mutant plants corroborates the *in vitro* experimental approach and highlights the importance of the N-terminal microtubule-binding region for the *in vivo* function of CC1. Unexpectedly, the impact on the hypocotyl growth is even more severe than in the *cc1cc2* mutant, possibly indicating that the altered CC1-microtubule interaction together with the mis-regulated microtubule array and the loss of CSC tracking might render the mutant plants especially sensitive to salt stress. Intriguingly, bundling and dynamic properties of the array upon salt exposure were altered when compared to the wild-type. This illustrates how minor mutations can introduce major defects to a seemingly robust mechanism that relies on multiple interaction sites. The underlying processes are plausibly highly conserved and require tight regulation to sustain the fragile balance that couples microtubule array organization and cellulose synthesis in the cell.

5.3 CC1 confers salt tolerance through a Tau-like mechanism in plants

Intriguingly, the structural features of CC1ΔC223 and its interaction with microtubules are remarkably similar to Tau (Fig. 5.1 **A** and **B**). Both Tau and CC1ΔC223 are intrinsically disordered proteins that contain multiple hydrophobic linear motifs that interact with microtubules and do not fold into a single rigid structure upon binding [102]. In both proteins the binding of the individual sites is rather transient, with strong contributions from the amino acids Valine and Tyrosine. Although rigid secondary structure is not present in either protein, secondary chemical shifts were observed at or near binding motifs indicative of a propensity to adopt β-strand structure [102]. The linear binding motifs are distributed similarly along the protein sequences and are interspersed with hydrophilic linker regions. Both proteins interact with unpolymerized tubulin and microtubules in a comparable manner [38]. As in CC1ΔC223, site-specific mutations in Tau can lead to local impairment of microtubule binding without having any long-range effect on the other interacting regions, indicating the independent nature of the linear motif binding [212]. This modular interaction mode is consistent with the observation that Tau isoforms can show varying overall microtubule binding affinities when carrying different numbers of repeats and thus microtubule-binding sites [213].

While Tau bundles microtubules with a spacing of 25 to 41 nm *in vitro* [110], CC1ΔC223 links microtubules very tightly. Tau regulates this distance *via* its N-terminal projection domain, and truncations of this domain changed the microtubule spacing both *in vitro* and *in vivo* [109, 110]. The Tau fragment TauF4, which encompasses only the four NMR-derived microtubule binding regions (from the proline-rich and microtubule binding domain ranging from S208 to S324), binds to and polymerizes microtubules *in vitro* and thus recapitulates two important characteristics of the interaction of full-length Tau with tubulin heterodimers [214]. Intriguingly, TauF4 produced wall-to-wall microtubule bundles similar to what was observed with CC1ΔC223 [214]. In-depth NMR studies on TauF4 and cryo-EM studies on full-length Tau concluded that Tau spans multiple tubulin heterodimers along the microtubule principal axis when bound to microtubules [215, 104]. This suggests that Tau contributes to protofilament stability by connecting tubulin heterodimers longitudinally, which aligns well with the above-presented interpretation of the CC1ΔC223 gold-labelling and cross-linking experiments.

Interestingly, a recent study showed that multiple lysine residues of Tau also cross-link to α-tubulin residues in the inter-dimer interface, which are in immediate vicinity of the detected CC1ΔC223 cross-link position to α-tubulin (Fig. 5.1 **C**) [38]. While undecagold-labelled Tau was proposed to bind along individual protofilaments by bridging tubulin interfaces, it has also been shown to diffuse bidirectionally along the microtubule lattice with a speed comparable to CC1ΔC223 [216, 107]. Furthermore, similar to the tyrosine to alanine mutations in CC1, disease-related mutations in Tau cause distinct defects in microtubule organization [111]. Notably, both Tau and CC1 are relevant for the organism to function during conditions of stress: CC1 is important to promote cellulose synthesis during salt stress, whereas Tau has only recently emerged as a key regulator of stress-induced brain pathology in mice and oxidative stress in cultured fibroblasts [217, 218].

Remarkably, whereas CC1 appears to function analogously to Tau, sequence alignments show that the two proteins appear to do so without clear overall sequence similarity. However, comparing the sequence of the NMR-derived binding regions reveals a surprisingly high

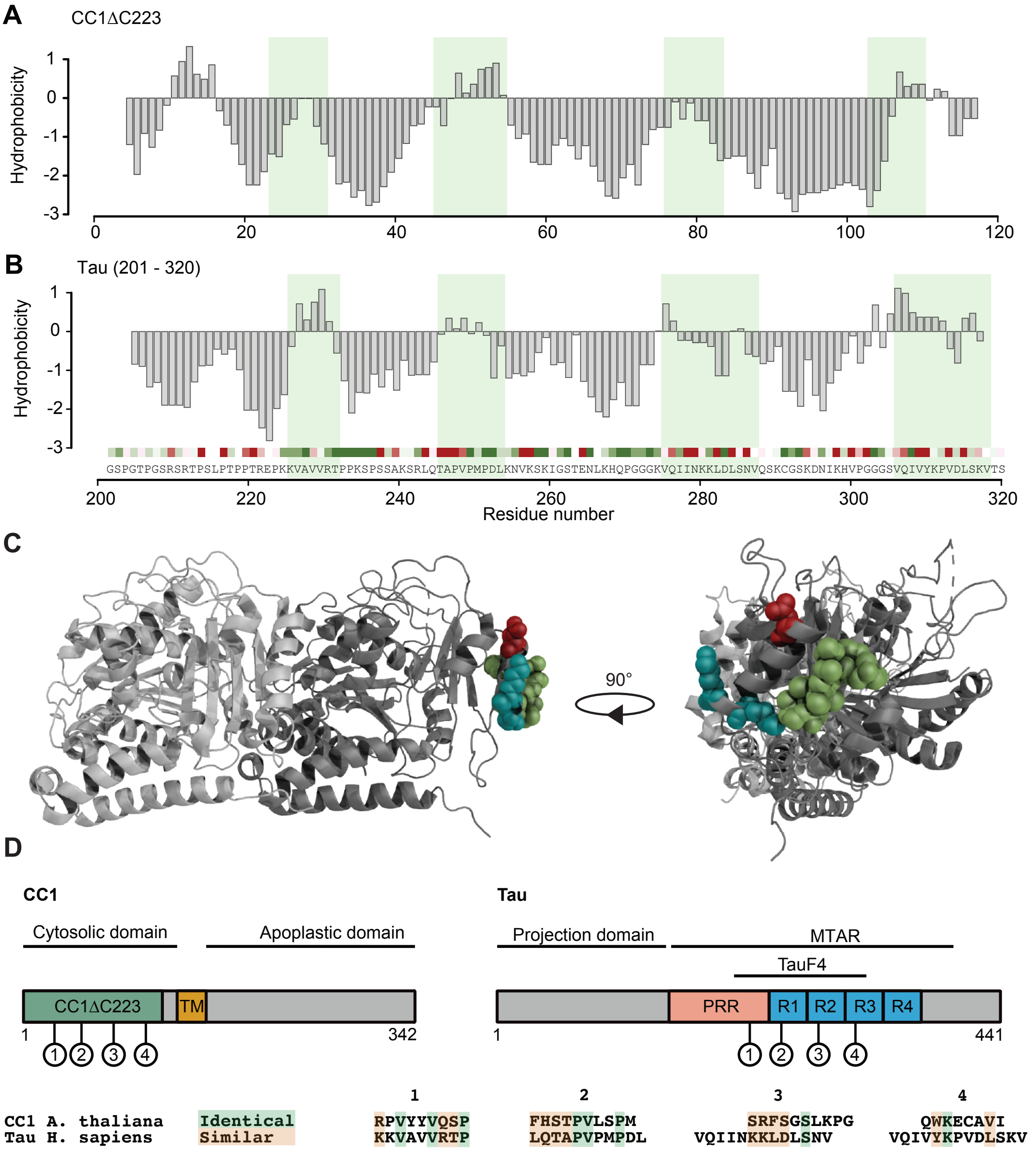

Figure 5.1 **Structural features of CC1 and Tau.** **A** and **B** Hydrophobicity scores of CC1ΔC223 and Tau according to the Kyte-Doolittle scale, respectively. NMR-derived microtubule-binding motifs are highlighted with green bars. Site-specific evolutionary conservation of Tau was calculated by CONSURF and is plotted above the sequence in a color code (green = conserved, red = unconserved). **C** Comparison of CC1ΔC223 cross-link position (red) with Tau cross-links (cyan) at the α-tubulin dimer interface (dark grey). The cross-link position is in close vicinity to the Vinblastine (green) binding site (PDB code: 4EB6). **D** Protein topology of CC1 and 4R-Tau with numbered microtubule-binding motifs. 4R-Tau contains a proline-rich region (PRR) and four imperfect repeats (R1-R4) in the microtubule assembly region (MTAR). The amino-acid sequence alignments below compare the motifs of *Arabidopsis thaliana* CC1 and human Tau. Identical (green) and similar (orange; score of 0 in BLOSUM62) amino acids are highlighted.

number of identical or similar residues (Fig. 5.1 **D**), implying evolutionary convergence of the microtubule-binding mechanism. Despite these similarities, the overall protein architectures differ strongly between Tau and CC1. The latter lacks the typical PGGG-containing imperfect repeats of the Tau microtubule binding domain (R1-R4 in Fig. 5.1 **D**). Moreover, while CC1 contains a putative transmembrane domain and is closely connected to the CSC, Tau is a purely cytoplasmic protein, albeit showing some association with membrane surfaces [219]. Naturally, the localization in these different cellular contexts will influence their modes of operation.

Notably, the microtubule arrays of animal and plant cells realize distinctive organizations: the microtubules in animal cells typically radiate from the centrosomes in the cell centre towards the periphery, while growing plant cells form cortical microtubule arrays, with evenly distributed microtubules along the cell cortex (described in chapter 2.2). Plausibly, these differences in the microtubule array organization are reflected in the domain architecture and localization of CC1 and Tau. Tau is mainly found in the cytosol of neuronal cells where it directly contributes to the stabilization of microtubules driving neurite outgrowth. As part of the CSC, CC1 is primarily localized on cortical microtubule bundles, which guide its movement in plant interphase cells (Fig. 5.2 **A**) [131]. Thus, CC1 is well situated to modulate microtubule dynamics and bundling to optimize cellulose synthesis under different environmental conditions.

Like Tau, CC1ΔC223 also binds to the polyanion polymer heparin that displaces the proteins from the microtubule surface *in vitro* [220]. While heparin does not play a role in plant organisms, other cellular polyanions such as actin, tubulin, ribosomes and DNA do. Many polyanion-binding proteins (PABPs) are intrinsically disordered, carry unique charge distributions and are involved in a variety of cellular protein-protein interaction networks [196]. Aside from being another common feature of the structural MAPs like Tau, it might help identifying functionally meaningful interactions with other polyanionic surfaces in the cell. Moreover, these shared biophysical properties possibly extend to recently discovered Tau functions like its ability to participate in liquid-liquid phase separation (LLPS) or to cross-link actin and microtubules [106, 221]. PABPs and structural MAPs are typically negatively regulated by phosphorylation. In the case of Tau, phosphorylation of key residues significantly impairs the binding to microtubules. Considering the similar biophysical determinants of CC1's interaction with microtubules, the biologically-relevant mechanisms of CC1 regulation will likely be similar.

Phosphorylation also negatively regulates Tau interactions with SH3 domains of several kinases [222]. The interaction of CC1-derived peptides with the ATSH3P1 SH3 domain was weak and potentially unspecific. Moreover, it is currently unclear if the regions from CC1's

C-terminal apoplastic domain can be localized to the cytoplasmic side of the membrane, where AtSH3P1 is situated or vice versa. However, since it is known that residues flanking the binding motif can have a large impact on the interaction with SH3 domains, it is possible that the region is directly regulated by phosphorylation and thus binding might be downregulated and not detectable in the unphosphorylated state.

Thus far, no clear homologs of the Tau/MAP2/MAP4 family have been identified in plants [223, 224]. Searching the Arabidopsis genome *via* BLAST does not reveal any proteins with obvious similarity to human Tau. Early research revealed that specific Tau antibodies can bind to proteins in maize plant extracts [225, 226]. Although some of these proteins promoted microtubule polymerization and bundling and co-localized to plant and mammalian microtubules, their functional and mechanistic relationship to Tau was not further investigated. Vice versa, studies on fava bean epidermal cells suggested that microtubule-binding sites are conserved between animal and plant MAPs since mammalian MAP4 microtubule-binding domain-GFP fusion proteins colocalize to plant microtubules *in vivo* [227]. Strikingly, while a sequence-based comparison failed to discover the CC1-Tau similarities, only a detailed functional analysis was able to resolve the shared features (Fig. 5.2 **B** and **C**). Because the full scope of Tau's biological role remains elusive, identification of Tau-related proteins outside the animal kingdom like the plant CC-proteins may help to better understand how this class of MAPs functions.

In summary, the presented results provide a comprehensive molecular understanding of how the CC1 proteins bind to microtubules and how this binding contributes to microtubule organization and cellulose synthase behaviour. The functional similarity of CC1 and Tau unveils related microtubule-regulating mechanisms in plants and neurons, and opens up exciting possibilities to explore evolutionary convergence of microtubule-related processes across evolutionary distant organisms.

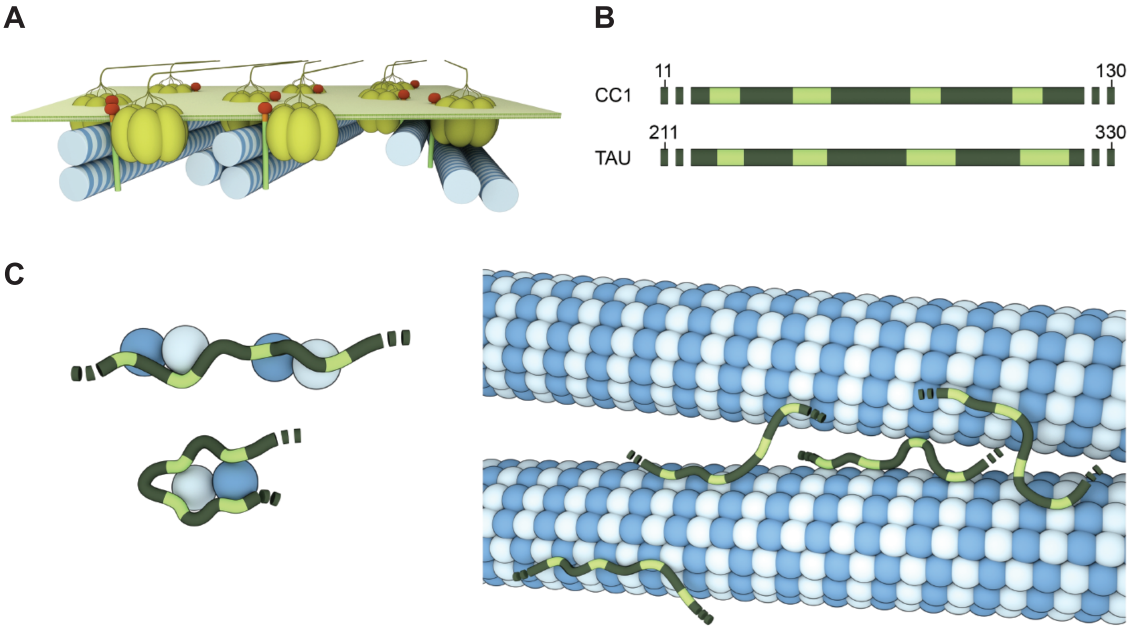

Figure 5.2 **Cartoon overview of the CC1 and Tau microtubule interaction A** CC1 localization in its cellular context as part of the CSC. CC1 interacts with microtubules while the CSC migrates on cortical microtubules during cellulose production. **B** Microtubule interacting CC1 N-terminus and the corresponding domain of Tau. Both microtubule binding domains show remarkable similarities: four similarly spaced, hydrophobic microtubule binding motifs (highlighted in green) that are spaced by flexible, hydrophilic linker regions. **C** The dynamic nature of the CC1ΔC223 and Tau binding behaviour suggests that both might be able to bind multiple distinct tubulin dimers *via* their individual binding motifs, thereby increasing the local tubulin concentration, connecting and stabilizing protofilaments or bundling microtubules. Image by Barth van Rossum.

Chapter 6

Signalosomes, NOD2 and RIP2

6.1 Pattern recognition in the innate immune response

The mammalian immune system consists of two major branches: the innate and the adaptive immune system. Adaptive immunity is especially important in the elimination of pathogens in the late stage of infection. It establishes the immunological memory by creating a collection of lymphocytes with antigen-specific receptors *via* gene rearrangement and clonal selection [228]. In contrast to adaptive immunity, innate immunity can respond rapidly to invading pathogens but relies on a limited repertoire of receptors for detection [229]. Representing an evolutionarily ancient immunity component, the innate immune system is the first line of defence against pathogens. It is mediated by haematopoietic cell types like macrophages, dendritic cells (DCs), natural killer (NK) and mast cells, but also by cells of non-haematopoietic origin, like the epithelial cells of gastrointestinal or respiratory tracts [228].

Invading microorganisms are recognized by various germline-encoded pattern-recognition receptors (PRRs) targeting conserved microbial components, known as pathogen-associated molecular patterns (PAMPs), that are broadly shared by groups of pathogens. PAMPs are usually important for the viability of the microorganism and are therefore not easily evaded by alteration [230]. The PRRs are broadly and constitutively expressed, independent of immunologic memory and react with specific PAMPs. Upon pathogen recognition they activate distinct signalling pathways triggering specific antipathogen responses including the subsequent activation of the adaptive immune response [231]. Thus, overall host defence is accomplished through tight integration between adaptive and innate immunity.

Based on protein domain homology, most PRRs can be classified into one of five families: C-type lectin receptors (CLRs), RIG-I- like receptors (RLRs), AIM2-like receptors (ALRs), Toll-like receptors (TLRs) and NOD-like receptors (NLRs) [232]. While TLRs and CLRs are membrane-bound receptors that can be found on the cell-surface or on endocytic compartments, NLRs, RLRs and ALRs are intracellular receptors located in the cytosol. The location of a receptor restricts the type of ligand that a PRR will be exposed to and therefore may give important parameters for a meaningful response. This receptor compartmentalization is one of the key mechanisms to prevent the activation of autoimmune-responses as some ligands, like nucleic acids, are also inherent to the host [233]. When activated, the PRR-induced immune response transcriptionally results in the production of proinflammatory interferons (IFN) and cytokines. Moreover, non-transcriptional processes like autophagy, phagocytosis and cell death can also be directly promoted [234, 235]. Within this signalling scheme, PRRs themselves do not function as signalling molecules, but rather recruit adaptor molecules to transmit the signal. The selective recruitment of these adaptor proteins mediates the differential activation of distinct signalling pathways depending on the respective ligand bound [229].

6.1.1 NOD-like receptors

In contrast to membrane-bound TLRs that are typically located on the cell surface or intracellular compartments like endosomes, the family of intracellular NOD-like receptors detects pathogens that have invaded the cytosol of the host (Fig. 6.1). Among the large NLR family with 23 NLR genes in the human genome, NOD1 and NOD2 are the best-studied members [236, 237]. Common to these receptors are the C-terminal leucine-rich repeat (LRR) motif that can detect conserved PAMPs and directly mediates receptor activity [238]. NOD1 and 2 have distinct target ligands as NOD1 detects the dipeptide bacterial γ-D-glutamyl-meso-diaminopimelic acid (iE-DAP) and NOD2 recognizes muramyl dipeptide (MDP), a component of the bacterial cell wall peptidoglycan [239, 240]. Although lacking defined localization domains, both proteins' signalling has been shown to occur in proximity to endosomal membranes [241, 242]. The endo-lysosomal peptide transporters SLC15A3 and SLC15A4 mediate the transport of pathogen-derived components for detection in the cytoplasm [241]. Since this is the site of signal transduction, the recruitment may directly regulate its activity, which is indicated by increased cytokine production [242]. After ligand recognition, NOD1 and NOD2 oligomerize and subsequently recruit the serine-threonine kinase RIP2 as an adaptor protein [243, 244]. After RIP2 auto-phosphorylation and ubiquitination, downstream effectors like ubiquitin E3-ligases are activated, ultimately triggering an inflammatory response through NF-κB activation [245, 246]. In addition, the MAP kinases p38, ERK, and JNK are activated by NOD1 and NOD2 stimulation [247–249]. The CARD-containing adaptor protein CARD9 mediates the activation of p38 and JNK, but not NF-κB [250]. Independently, autophagy and the production of anti-bacterial peptides is

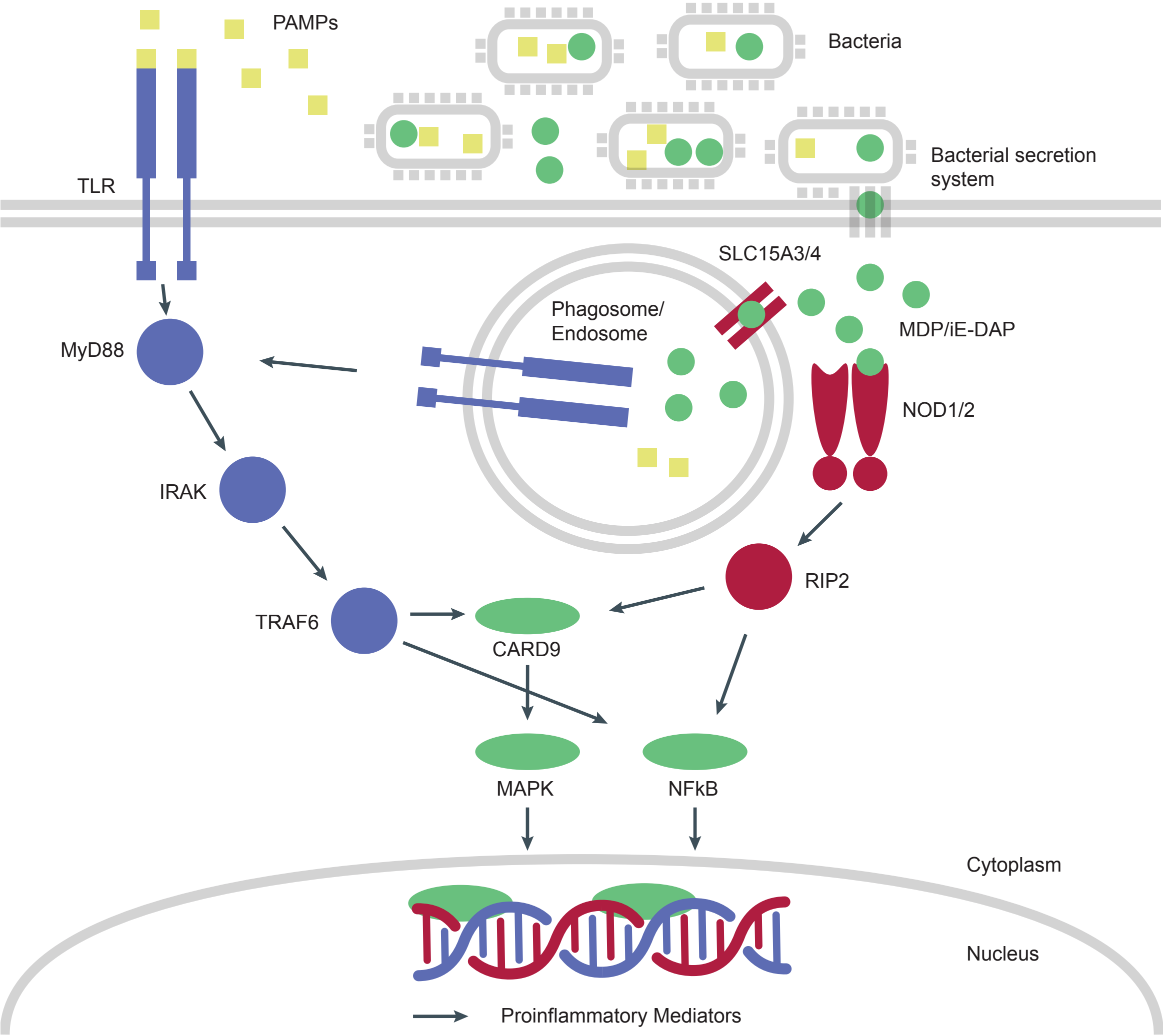

Figure 6.1 **TLR and NLR signalling in the innate immune system.** Extracellular PAMPs from bacteria are recognized by transmembrane TLRs, which signal through MyD88, IRAK and TRAF proteins to activate NF-κB and MAP kinases, which subsequently upregulates the expression of proinflammatory mediators. NOD1 and NOD2 recognize intracellular iE-DAP and MDP and signal through RIP2 and CARD9, ultimately activating NF-κB and MAP kinases. MDP can be translocated to the cytoplasm by bacterial secretion systems from the cell's exterior and from peptide transporters like SLC15A3 and SLC15A4 from the endosome. Image adapted and modified from [236].

induced, protecting gut epithelial cells from pathogen invasion [251, 252]. The upregulated production of proinflammatory molecules stimulates both the innate and adaptive immune response [248]. Further, NOD1 has been suggested to directly contribute to the activation of the adaptive immune response by priming antigen-specific T cell immunity *in vivo* [253]. *In vitro*, the NOD1 and NOD2 pathways have been indicated in the infection of a number of bacteria strains such as *Listeria monocytogenes*, *Chlamydophila pneumoniae* and *Mycobacterium tuberculosis* [236]. Studies on mice illustrated a clear *in vivo* relevance of NOD1 and NOD2 for bacterial infections from *Listeria monocytogenes* and *Helicobacter pylori*. Many bacterial strains are additionally recognized by other PRRs, such as TLRs, resulting in overlapping signalling pathways that increase the sensitivity for pathogen detection and enhance the inflammatory response [229].

6.2 Higher-order assemblies in innate immunity signalling

Early studies on signal transmission in G-protein-coupled receptors (GPCRs) and receptor tyrosine kinase (RTK) receptor systems led to a generalized perception of signalling processes as a chain reaction with successive steps of signalling protein activation. However, more recent work on multiple innate immune signalling pathways has shown that higher-order assemblies play a significant role in signal transduction (Fig. 6.2 **A**) [254, 255]. The formation of these so-called signalosomes is typically mediated by adaptor proteins that connect the initial activation of the receptor to the enzymatic downstream reaction [256]. While the ligand-binding receptor forms a defined oligomeric state upon activation, the downstream adaptor proteins can assemble to a potentially infinite and linear supramolecular complex. This polymerization of the adaptor proteins is an intrinsically cooperative process, since the addition of a subunit enhances the chances of an additional association event. Hence, it was proposed that the response curve of such a highly cooperative system exhibits a sharp sigmoidal dose-dependent transition upon ligand stimulation (Fig. 6.2 **B**) [6]. This all-or-nothing threshold response introduces a temporal delay in the signalling that could filter out biological noise. However, the response itself follows fully and swiftly upon reaching the threshold, leading to signal-amplification, as has been shown in apoptosis induced by the Fas death receptor and NF-κB activation by the tumour necrosis factor (TNF) [257, 258]. Due to their large size and decreased diffusion properties, the formation of supramolecular assemblies may allow for spatial control of signalling by transiently restricting spatial organization of the complexes [6].

6.2.1 Death domains

In the innate immune system, the helical polymerization of adaptor proteins to higher-order structures *via* death fold domains (DD) has been found to be relevant for multiple TLR and NLR signalling pathways (Fig. 6.2 **C**) [259]. The DD superfamily consists of four subfamilies: DD, Pyrin domain (PYD), death effector domain (DED) and caspase recruitment domain (CARD) [260]. The proteins are widely conserved and the human genome alone contains 32 DDs, 7 DEDs, 19 PYDs and 28 CARDs [260]. Most DD domains typically adopt a six-helical bundle structural fold with some variation in the length and direction of the helices [259]. However, due to the low sequence homology among the different DD classes, the surface features of the structures vary strongly between them. Among the DD fold super family, the CARD structure carries some unique features in helix H1, which is typically separated in two H1a and H1b helices in close proximity [259]. Furthermore, the CARD protein surfaces are strongly polarized with basic and acidic patches, which facilitate protein-protein interactions.

6.2.2 Helical assemblies and signalosomes

Examples of DD-mediated signalosome systems are the ASC-mediated caspase-1 inflammasome pathway [261, 23], RIG-I-mediated anti-viral MAVS pathway [15, 262] and the CARMA1– BCL10–MALT1 complex of the T- and B-cell signalosome [263]. In the past few years, many high-resolution structures of helical assemblies were solved by cryo-EM and solid-state NMR. Although all adopt a helical symmetry, their overall architectures can differ in the translational rise, rotational twist, the diameter or the number of strands of the assembly [19]. Typically, each protomer is in contact with six other protomers forming three interfaces commonly named Ia/Ib, IIa/IIb and IIIa/IIIb. These interfaces can be mediated by polar, charged or hydrophobic interactions, depending on the DD domain (Fig. 6.2 **G**) [259]. The structure of the MAVS CARD filament was independently solved by cryo-EM and ssNMR revealing a left-handed, 1-start helical assembly with no inner pore, a twist of 101°, a rise of 5.1 Å and a diameter of 82 Å (Fig. 6.2 **D-F**) [262, 15]. The overall architecture closely resembles the near-atomic structure of the BCL10 CARD filament solved by cryo-EM, which adopts a left-handed rotation of 100.8° and rise of 5.00 Å per subunit [263]. Cryo-EM and ssNMR studies on the human and mouse ASC PYD showed that it forms a hollow filament with inner and outer diameters of $\sim$ 20 and $\sim$ 90 Å, respectively (Fig. 6.2 **H**) [261, 23]. In contrast to the above-presented CARD assemblies, ASC PYD filaments adopt a 53° right-handed rotation and a 14 Å axial rise per subunit, but the inter-protomer interactions still rely on the classical type I-III interfaces.

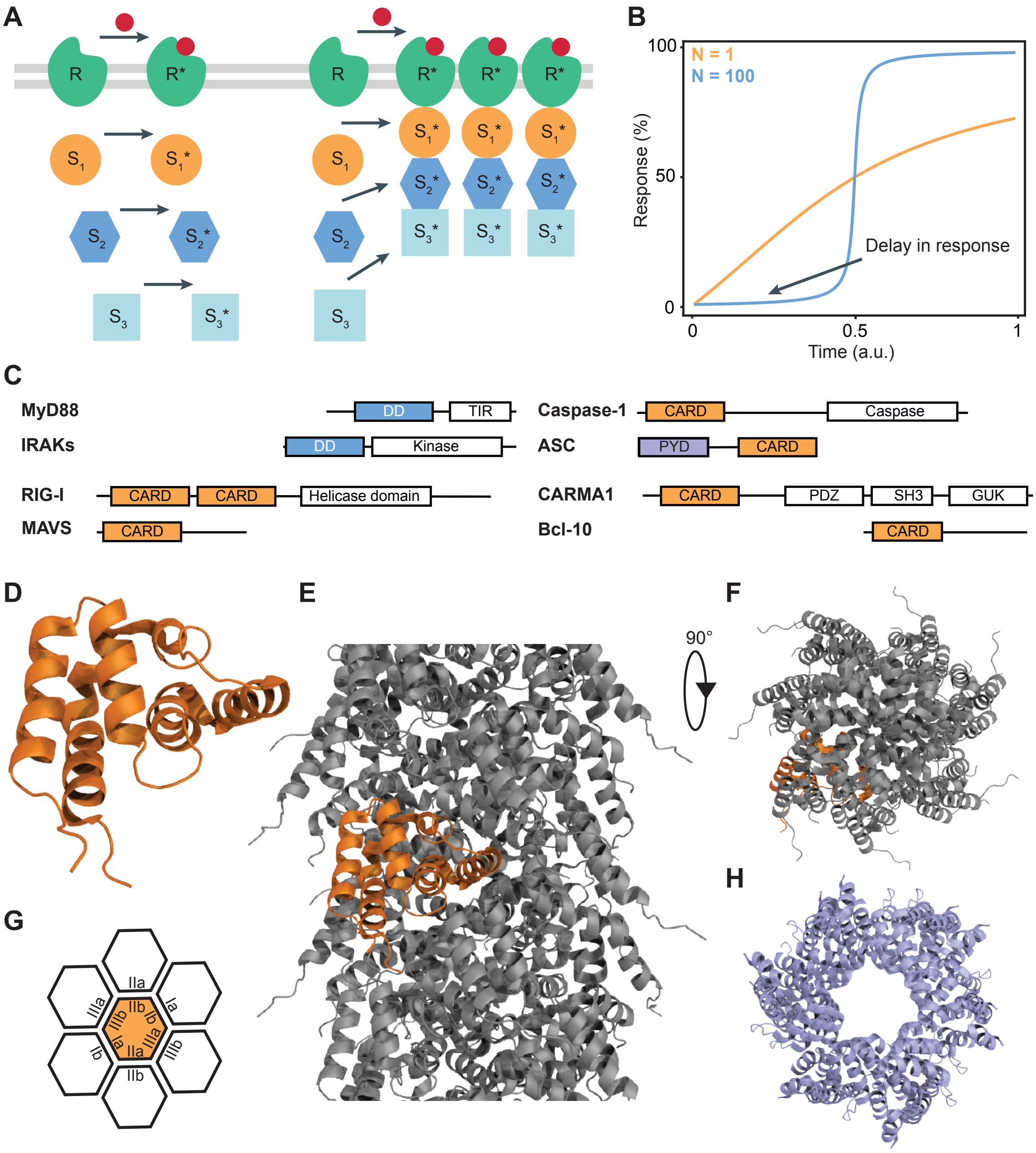

Figure 6.2 **Death domains and helical assemly signalosomes. A** Cartoon of the classical model of receptor (R) signal transduction involving successive steps of activation (left) and the receptor signal transduction *via* formation of higher-order oligomeric signalosomes (right). Intracellular signalling proteins are denoted as S1 to S3 with activated states marked by asterisks. Image adapted and modified from [6]. **B** Response curves as a function of time in arbitrary units (a.u.) according to the Hill equation with N being the Hill coefficient. In a highly cooperative process, the labelled delay may act as a noise filter. **C** Domain architecture of selected proteins containing death domains (Abbreviations: GUK, guanylate kinase-like; TIR, Toll/interleukin-1 receptor). Image adapted and modified from [259]. **D-F** Solid-state NMR structure of MAVS CARD domain (PDB code: 2MS7) alone (**D**) and embedded in the helical assembly (**E**) and a 90° rotated top view on the filament (**F**) [15]. **G** Relative orientations of the type I, type II and type III interfaces typical for DD helical filaments. **H** Top view on the hollow ASC PYD filament (PDB code: 2N1F) determined by combined NMR spectroscopy and cryo-EM [23].

As suggested by confocal imaging on BCL10 CARD, filament elongation is unidirectional with growth at one end only, which is corroborated by the observation that one-sided RIG-I tandem CARD binding can directly nucleate MAVS CARD filament formation [263, 262]. Furthermore, it has been shown that AIM2 promotes formation of ASC PYD filaments by binding to one end of the filaments *in vitro* [261]. Mutation of the interface I in ASC PYD prevented the induction of cell death and IL-1β secretion in immortalized mouse macrophages and the human THP-1 cell line [261, 23]. Once the complex is formed, signalling may have to be terminated by active processes like autophagy as has been indicated for the regulation of BCL10 [264].

Mutations leading to malfunctions in the assembly of signalosome complexes are associated with several genetic and non-genetic diseases. For example, defects in NLR signalling have been connected to Crohn's disease, psoriasis, type II diabetes and Alzheimer's disease [265, 266]. Disease-related mutations in NLRs have been proposed to directly disrupt either DD autoinhibition or interaction surfaces interfering with proper signal transduction [267]. Interestingly, the importance of signalosomes in the immune response is underscored by the microbial evolution of inhibitors that counteract signalosome activity [268]. These include viral PYD proteins that directly inhibit caspase-1 activation and thus suppress the host immune response [269].

6.2.3 Structural aspects of the RIP2-NOD2 signalling pathway

As described above, the adaptor protein RIP2, also known as RICK, is activated by the cytosolic PRR NOD2, which senses bacterial infection by detecting the peptidoglycan breakdown product MDP. As a member of the NLR family, NOD2 contains a LRR domain, an ATP-binding NOD domain and two CARD domains as N-terminal effector death domains (Fig. 6.3 **A**) [270]. The downstream adaptor protein RIP2 is comprised of an N- terminal kinase domain, a C-terminal CARD domain and a connecting intermediate domain [252]. Upon activation of NOD2 through ligand binding, the receptor oligomerizes and recruits RIP2 through CARD-CARD interactions, ultimately triggering an inflammatory response *via* NF-κB and MAPK activation [271–273].

The crystal structure of rabbit NOD2 in the ADP-bound state was determined recently revealing a hook-shaped structure built from the NOD domain and the LRR domain (Fig. 6.3 **B**) [273]. The latter consist of ten LRR units forming a typical horseshoe-like structure in a single curvature. The concave surface of the LRR contains the potential ligand-binding site. NOD2 is auto-inhibited *via* ADP-dependent inner domain interactions at the centre of the NOD domain. However, the structure lacks the two NOD2CARD domains that are essential for RIP2 activation.

The structure of the RIP2CARD domain was solved by solution-state NMR adopting the typical CARD fold forming a Greek key helical bundle with the N- and C-termini oriented in the same direction and two H1a and H1b helices (Fig. 6.3 **C**) [274]. Unlike other CARD domains, the domain forms a long disordered loop at the C-terminus containing putative phosphorylation sites instead of the common H6. Structurally, the CARD domain of the known RIP2 interactor NOD1 is the most similar structure to RIP2CARD sharing a similar arrangement of α-helices [274].
Aberrant signalling of the NOD/RIP2 pathway was linked to the pathogenesis of inflammatory diseases. Many single-nucleotide polymorphisms (SNPs) were identified in the NOD2 gene, which were reported to be associated with diseases like Blau syndrome, early-onset sarcoidosis and Crohn's disease [275]. While loss-of-function mutations leading to an inability to activate NOD2 result in impaired epithelial mucosal barrier function in Crohn's disease, gain-of-function mutations can cause the systematic granulomatous inflammatory diseases Blau syndrome and early-onset sarcoidosis increasing the basal activity of NF-κB [276–278]. As suggested by animal models and association studies, overactive NOD/RIP2 signalling might also be implicated in other diseases like arthritis, asthma and multiple sclerosis [279].

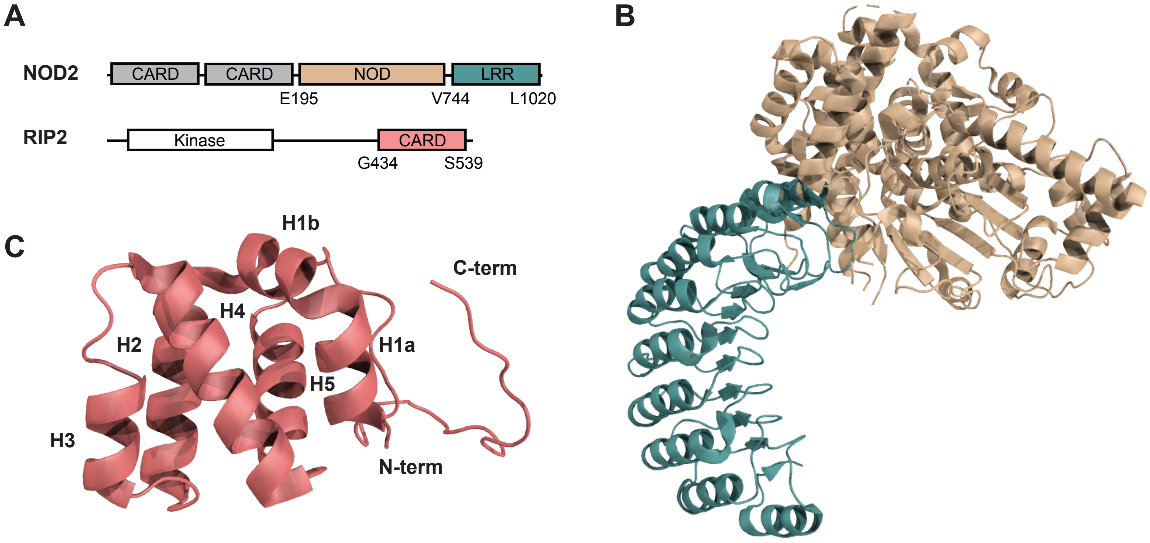

Figure 6.3 **Structural details of RIP2-NOD2 signalling. A** Domain architecture of NOD2 and RIP2. Image adapted and modified from [259]. **B** Crystal structure of NOD2 in the ADP-bound state with the NOD domain and the LRR domain coloured in brown and green, respectively (PDB code: 5IRN) [273]. **C** Solution-state NMR structure of RIP2CARD with the helices and termini labelled (PDB code: 2N7Z) [274].

6.3 Aim and scope of this project

In the innate immune response to bacteria, activation of the innate immune PRR NOD2 by MDP triggers recruitment of the downstream adaptor kinase RIP2, ultimately leading to NF-κB activation and proinflammatory cytokine production [280]. Despite the importance of the NOD2 signalling pathway in health and disease, the molecular basis of this activation is still not fully understood. As both proteins carry CARD DDs, ligand-induced NOD2 oligomerization might promote the polymerization of the adaptor protein through DD-interaction as seen in other intracellular innate immune signalling pathways [261–263]. Previous studies investigated the interaction between the NOD2CARDs and RIP2CARD but it remained unknown whether this hetero-CARD interaction also leads to the formation of a higher-order signalosome [272, 274].

The aim of this project was to characterize the atomic structure of the RIP2CARD filament. For this, a highly cooperative and integrated structural approach using solution- and solid-state NMR, X-ray crystallography and high-resolution cryo-EM was employed. In this thesis three main biological questions are addressed: How does the monomeric RIP2CARD subunit structure compare with the protein's filamentous form? In particular, is the disorder of the C-terminus retained upon filament formation? More broadly, can the NMR-derived chemical shift data of RIP2CARD be effectively integrated with the cryo-EM and X-ray results?

Identifying the intermolecular determinants that stabilize the assembly and disrupting these contacts by mutation could give insights into the relevance of RIP2 polymerization for overall signalling. Revealing the structural details of the mechanism by which NOD2 induces RIP2 activation could give new impulses to the development of new pharmacological strategies to treat inflammatory diseases characterized by aberrant NOD2 signalling. In particular, mapping disease-related mutations onto the CARD filament structure might help to identify functional links to symptoms and characteristics of the underlying disorder.

Chapter 7

Material and Methods

7.1 Materials

The main chemicals, equipment and software used in this project are listed in the respective tables of chapter 3.1. Project-specific information on buffer composition, equipment and chemicals are directly indicated in the sections below. Further customary chemicals not mentioned in the tables or the text were provided by the vendors Roth, Merck or Sigma-Aldrich.

7.2 Sample preparation

Cloning, expression and purification of RIP2CARD were performed by Dr. Anne Diehl and Kristina Rehbein at the FMP. Electron Microscopy was performed at the FMP core facility for Transmission Electron Microscopy (TEM), grid preparation and image acquisition were carried out by Martina Ringling and Svea Hohensee.

7.2.1 Isotope labelling schemes

The dense proton dipolar coupling network leads to strong proton-proton interactions within biomolecules. The average strength of dipolar interactions can be reduced by deuteration or high MAS rates to decrease the otherwise large proton linewidth in proton-detected solid-state NMR. Conversely, by using smaller diameter rotors with faster maximum MAS rates, the need for proton dilution by deuteration decreases. Thus, spectral resolution can be traded for overall sensitivity by increasing the proton back-exchange percentage. At spinning rates of 40 kHz and beyond, high-resolution spectra can be recorded with full reprotonation of the exchangeable sites of otherwise perdeuterated proteins. Due to the improved coil design for these fast-spinning probes and the higher content of exchanged protons, the loss of signal-to-noise caused by the smaller sample size is counterbalanced. The determined optimal relative effectiveness of 1.9 and 1.3 mm probes spinning samples at 40 and 60 kHz MAS was determined to be at proton back-exchange rates of 80 and 100 %, respectively [281]. Since RIP2CARD is not an overly large protein and thus signal overlap was not a major concern, the protein was back-exchanged to 100 % to gain sensitivity at 60 kHz MAS while retaining sufficiently narrow linewidths at 40 kHz MAS.

Spectral crowding often complicates the analysis of carbon-detected solid-state NMR spectra due to the reduced dimensionality and broader lines of the carbon-carbon correlations. Hence, in addition to a uniform labelling scheme, selective carbon labelling techniques were applied to simplify the spectra and reduce signal overlap. Moreover, sparse carbon labelling also produces narrower lines by reducing ^{13}C-^{13}C J-coupling and any spurious homonuclear dipolar coupling not spun out by the applied MAS. For RIP2CARD an [1,3-^{13}C]- and [2-^{13}C]-glycerol labelling scheme was employed that uses glycerol that is either labelled on 1,3- or the 2-position as the sole carbon source during protein expression. Depending on the respective amino acid metabolism, this leads to distinct labelling patterns of the amino-acid types (Fig. 7.1). Glycolytic and pentose phosphate pathway-derived amino acids (Gly, Ala, Ser, Cys, Tyr, Phe, His, Trp, Leu, Val) have all sites either completely ^{13}C or ^{12}C-labelled, while the remaining precursor-derived amino acids from the citric acid pathway (Arg, Gln, Glu, Pro, Asn, Asp, Thr, Met, Ile, Lys) produce non-random mixtures of isotopomers. As a result, there are amino acids with only one isotopomer and amino acids with multiple isotopomers. The differences in labelling result in characteristic NMR cross-peak patterns, which can be exploited for chemical shift assignment or collection of distance restraints for structure determination.

7.2.2 Expression of RIP2CARD

For heterologous protein production of RIP2CARD, pETM40-MBP-RIP2(435–540) (KanaR) were transformed into the *Escherichia coli* strain BL21(DE3) star. To repress the lac operon, all LB precultures contained 2 % glucose. NMR-specific labels were introduced by expression at 22 °C overnight in 1.5-fold M9 medium following the 2-fold concentration method in which the cells are first grown in unlabelled rich medium (OD600 of 0.8) and then transferred into labelled medium at high cell density [283]. Uniform ^{13}C- and ^{15}N-labelling ([u-^{13}C/^{15}N]) was achieved by supplementing M9 medium with 0.7 g/l ^{15}N NH_4Cl and 2.5 g/l ^{13}C-glucose. [2-^{13}C]- or [1,3-^{13}C]-glycerol (Eurisotop) was used for sparse ^{13}C labelling following the protocol described in [284]. Deuteration was achieved by using D_2O instead of H_2O in all media. The cells were grown for 40 min at 37 °C and 2 min at 20 °C, followed by

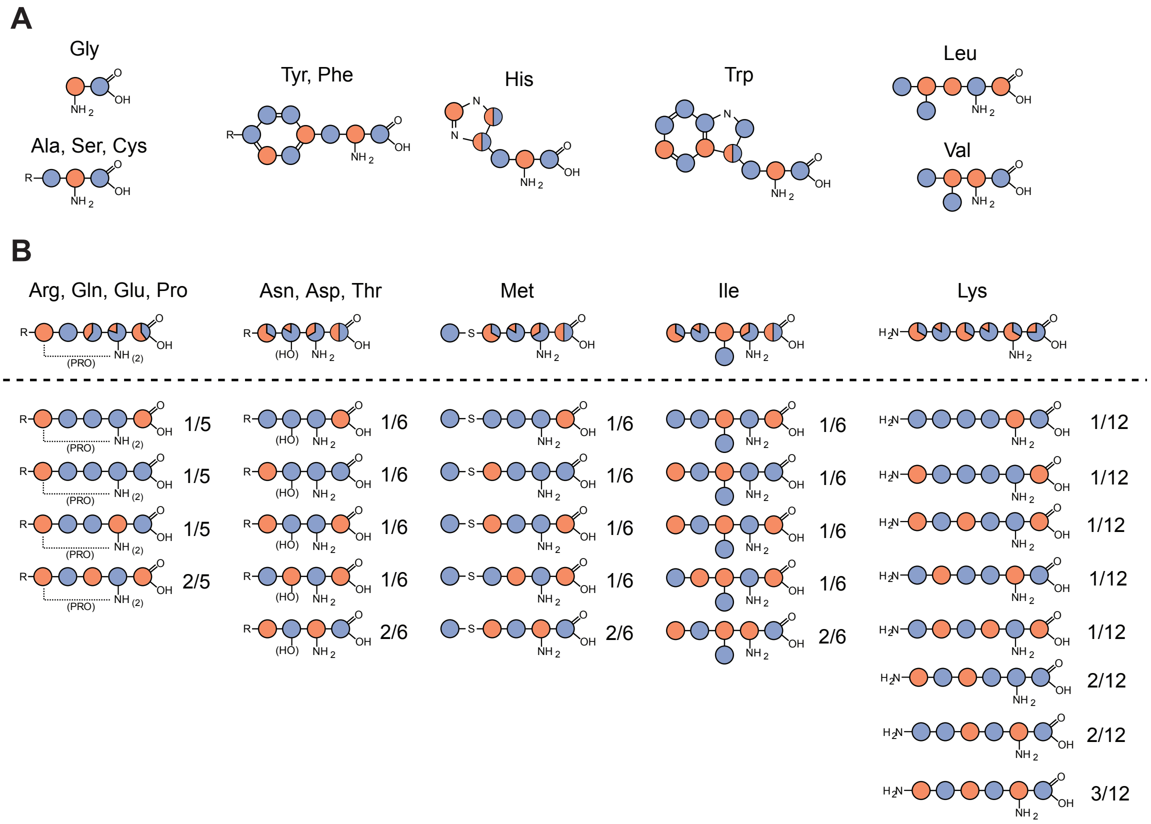

Figure 7.1 **[1,3-^{13}C]- and [2-^{13}C]-glycerol labelling pattern. A** 'All-or-nothing' labelled amino-acids with a single isotopomer **B** 'Mixed' labelled amino-acids with multiple isotopomers. [1,3-^{13}C]-glycerol-labelled sites are shown in blue and [2-^{13}C]-glycerol-labelled sites are shown in red. In cases of mixed labelling, the percentage of labelling is represented using relative blue/red colouring. The labelling percentage of the tryptophan CG and histidine CD and CE sites are not determined. The depiction was adapted and modified from [282].

Table 7.1 Sample labelling

Sample	Labelling	Application
1	[u-^{2}H, ^{13}C, ^{15}N], 100 % back-exchanged protons	Proton detection, 40 and 60 kHz MAS, 1.9 and 1.3 mm
2	[u-^{13}C, ^{15}N], fully protonated	Carbon detection, 13 and 15 kHz MAS, 3.2 mm
3	[1,3-^{13}C]-glycerol, [u-^{15}N], fully protonated	Carbon detection, 13 and 15 kHz MAS, 3.2 mm
4	[2-^{13}C]-glycerol, [u-^{15}N], fully protonated	Carbon detection, 13 and 15 kHz MAS, 3.2 mm

induction with 0.3 mM IPTG at 22 °C. After overnight expression, the cells were harvested by centrifugation and stored at -80 °C for later purification.

7.2.3 Purification of RIP2CARD and filament formation

Purification was performed in the presence of 2 M urea to prevent protein aggregation or premature filament formation as has been previously reported for RIP2CARD [152]. The harvested cell pellets from 1.2 l culture were resuspended in 20 mM Tris pH 8, 20 mM NaCl, 2 M urea, 2 mM 2-Mercaptoethanol, 1 mM Pefabloc (Sigma), 5 mM $MgCl_2$ and 15 µl Benzonase (Merck) and lysed using a shear fluid homogenizer in 5 cycles at 13,000 psi. After centrifugation at 22,000 x g for 1 h at 4 °C to remove the cellular debris, the supernatant was filtered (0.45 µm) and incubated with about 12 ml 50 % amylose resin (New England Biolabs) at 15 °C on a rotator for 3 h. After a washing step, MBP-RIP2CARD was eluted using 10 mM maltose in 20 mM Tris pH 8, 20 mM NaCl, 2 M urea, 2 mM 2-Mercaptoethanol. Concentrated at $\sim$ 1 mg/ml, the fusion protein was cleaved by TEV protease overnight at 22 °C. Next, the sample was dialysed overnight against 20 mM Tris pH 8, 20 mM NaCl, 2 mM 2-Mercaptoethanol at 8 °C. Removing the urea immediately initiated RIP2CARD filament formation. The sample was further incubated for 48 h at 20 °C to allow for full polymerization. The final filamentous product was collected by ultracentrifugation at 35,000 x g for 1 h and was packed into the respective rotor by ultracentrifugation at 100,000 x g for 1 h using a custom-made filling device.

7.2.4 Electron microscopy

Negative-stain electron microscopy was employed to check for proper assembly and stability of the RIP2CARD filaments. RIP2CARD filaments were applied to 0.3 % formvar-coated copper grids and incubated for 30 s, washed once with dH_2O, stained with 1 % aqueous uranyl acetate solution, rinsed with dH_2O again and dried. The samples were examined on a Zeiss 900 transmission electron microscope.

7.3 NMR spectroscopy

For the assignment of RIP2CARD, two sets of carbon- and proton-detected experiments were recorded on appropriately-labelled samples (Table 7.1). All proton-detected experiments were recorded on a wide-bore 800 MHz and 900 MHz spectrometer equipped with 1.3 mm and 1.9 mm triple-resonance MAS probes, respectively. The ^{13}C-^{13}C DARR correlation spectra were recorded on wide-bore 600 and 700 MHz spectrometers equipped with 3.2 mm triple-resonance MAS probes. Temperature and chemical shift calibration was achieved on 4,4-dimethyl-4-silapentane-1-sulfonic acid (DSS) added directly to the sample. The raw NMR data was collected with TopSpin and processing of the raw data was performed by either NMRPipe or TopSpin. All spectra were acquired and processed using the States-TPPI method and the processed data was further analysed with the CCPN Analysis v.2.4.2 package. A summary of the solid-state MAS NMR experiments employed is given below.

7.3.1 Proton-detected NMR experiments

As the technology for proton-detected solid-state NMR improved rapidly in recent years, it became more widely used for protein assignment and structure determination in the field of structural biology. In solids, the sample's strong proton-proton dipolar coupling can be reduced to a minimum by dilution of the proton content *via* deuteration and/or fast MAS sample spinning. Under these conditions, ^{13}C and ^{15}N nuclei yield long coherence lifetimes with only low power proton decoupling applied allowing for elaborate magnetization transfer schemes. Furthermore, scalar coupling interactions become available for efficient homonuclear ^{13}C transfer and carbonyl or aliphatic-specific H-C cross-polarization (CP) conditions can be utilized. Hence, similar to the standard solution NMR acquisition and analysis protocols described in chapter 3.5.1, proton-detected MAS NMR can employ analogous strategies for sequential assignment using triple-resonance pulse schemes correlating backbone ^{1}H, ^{13}C and ^{15}N resonances.

For the backbone assignment of RIP2CARD, three types of experiments were recorded for

Table 7.2 Experiment acquisition

Experiment	NS	^{1}H TD (AQ)	^{15}N TD (AQ)	^{13}C TD (AQ)
(H)CANH	16	4096 (41 ms)	92 (12 ms)	128 (9 ms)
(H)CO(CA)NH	24	4096 (41 ms)	112 (15 ms)	80 (10 ms)
(H)(CA)CB(CA)NH	24	4096 (41 ms)	80 (11 ms)	224 (8 ms)
(H)(CO)CA(CO)NH	32	4096 (41 ms)	92 (12 ms)	128 (10 ms)
(H)CONH	16	4096 (41 ms)	112 (15 ms)	80 (11 ms)
(H)(CA)CB(CA)(CO)NH	32	4096 (41 ms)	80 (11 ms)	224 (8 ms)

both the intra-residual and the connecting inter-residual resonances. The intra-residual set consisted of the (H)CANH, (H)CO(CA)NH and (H)(CA)CB(CA)NH experiment and correlates each backbone ^{1}H-^{15}N pair to the CA, CO and CB resonances of the same residue (*i*), respectively (Fig. 7.2). The inter-residual set includes the (H)CONH, (H)(CO)CA(CO)NH and (H)(CA)CB(CA)(CO)NH experiment and correlates the ^{1}H-^{15}N pairs to the CO, CA and CB frequencies of the preceding residue ($i-1$), respectively (Fig. 7.3). As described in chapter 3.5.1, a sequential connection can be established by matching the carbon-resonances from the intra-residual set to the ones of the inter-residual set. CA and CB chemical shifts can give information about the type of amino-acid providing valuable information for linking the connected stretches of spin systems to the corresponding amino acid sequence.

The used pulse sequences employ scalar-based homonuclear carbon–carbon coherence transfers and were developed by Barbet-Massin et al. [285]. Since the evolution of scalar coupling requires sufficiently long delays, long ^{13}C coherence lifetimes and, thus, MAS rates of 60 kHz and more are needed for the experiments. Common to all experiments is the initial CP transfer of magnetization from protons to carbon, where either chemical shift evolution is directly recorded ((H)CANH, (H)CONH, (H)CO(CA)NH) or magnetization is further transferred to other carbon nuclei *via* scalar coupling ((H)(CA)CB(CA)NH, (H)(CO)CA(CO)NH, (H)(CA)CB(CA)(CO)NH). In the latter experiments, so-called out-and-back transfer schemes are used to optimize the relaxation properties of the magnetization pathway. By storing transverse magnetization on slower relaxing nuclei during τ delays, the overall sensitivity of the experiment is increased. After carbon evolution, the magnetization is transferred back to nitrogen through another CP step, where it is evolved. Following MISSISSIPPI water suppression without homospoil gradients, magnetization is transferred to the attached amide proton *via* CP, where the signal is finally detected under ^{13}C and ^{15}N decoupling.

In contrast to the classical solution-state NMR HNCACB/HNCOCACB experiments, the use of a CP-based carbon-nitrogen transfer results in the absence of any inter-residual $i-1$ resonances in the intra-residual set of experiments.

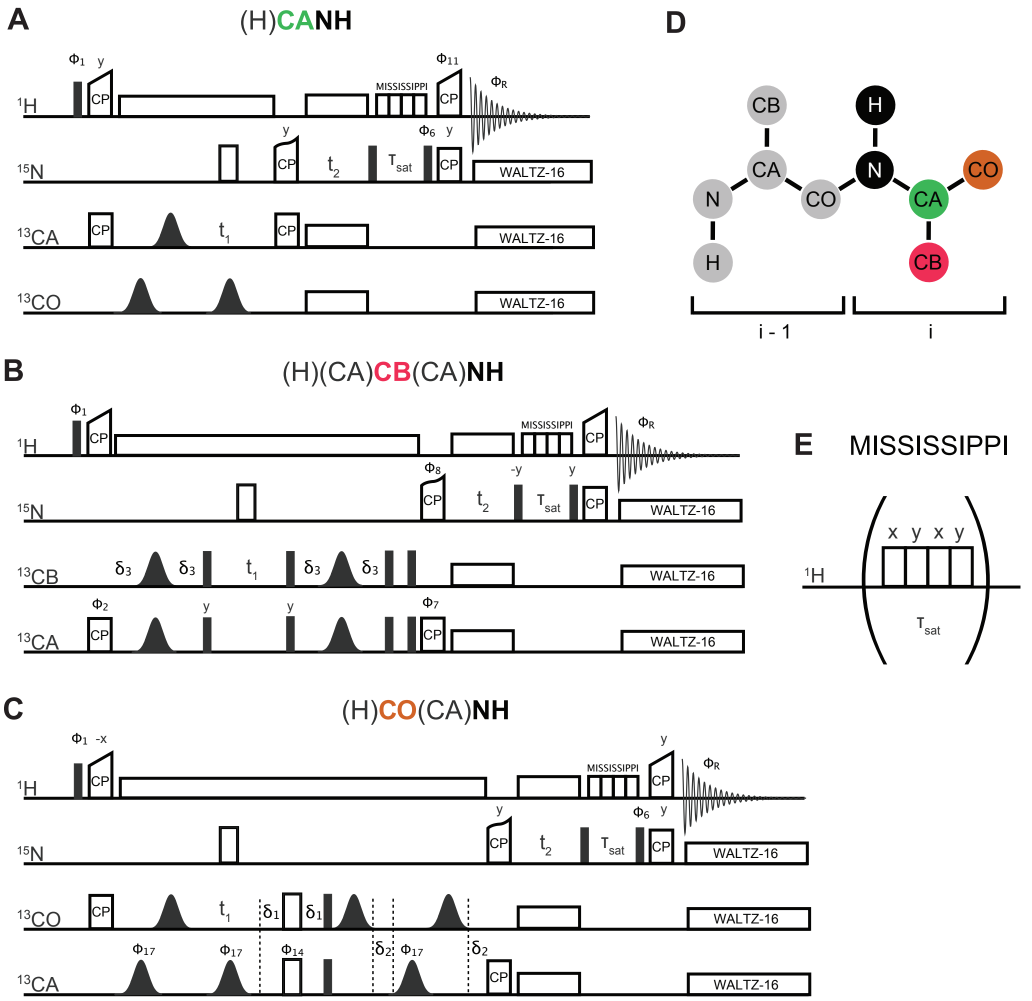

Figure 7.2 **Intra-residual backbone correlation.** Schematic representation of (H)CANH (**A**), (H)(CA)CB(CA)NH (**B**) and (H)CO(CA)NH (**C**) triple-resonance 3D pulse sequences. Filled and open pulse symbols indicate 90° and 180° RF pulses, respectively. Gaussian shapes indicate band selective 180° pulses and extended white rectangles represent decoupling. Cross polarization steps are marked with CP. All carbon-carbon transfers are scalar-based. Pulses are x-direction if not labelled otherwise. (**A**) ϕ_1 = x, -x; ϕ_6 = x, x, -x, -x; ϕ_{11} = 4y, 4(-y); ϕ_R = y, -y, -y, y, -y, y, y, -y. (**B**) ϕ_1 = y, -y; ϕ_2 = y, y, -y, -y; ϕ_7 = 4y, 4(-y); ϕ_8 = 8x, 8(-x); ϕ_R = x, -x, -x, x, -x, x, x, -x, -x, x, x, -x, x, -x, -x , x. (**C**) ϕ_1 = x, -x; ϕ_6 = x, x, -x, -x; ϕ_{14} = 4x, 4y; ϕ_{17} = 8x, 8y; ϕ_R = -y, y, y, -y, y, -y, y, -y, -y, y, y, -y, -y, y, -y, y, y, -y. Pulse sequences by Barbet-Massin et al. [285] and depiction adapted and modified from [282]. **D** Cartoon representation of the chemical shift information gained from the respective pulse programs. Colours mark the evolved nuclei. **E** MISSISSIPPI pulse sequence for water suppression employed in the pulse programs **A**-**C**.

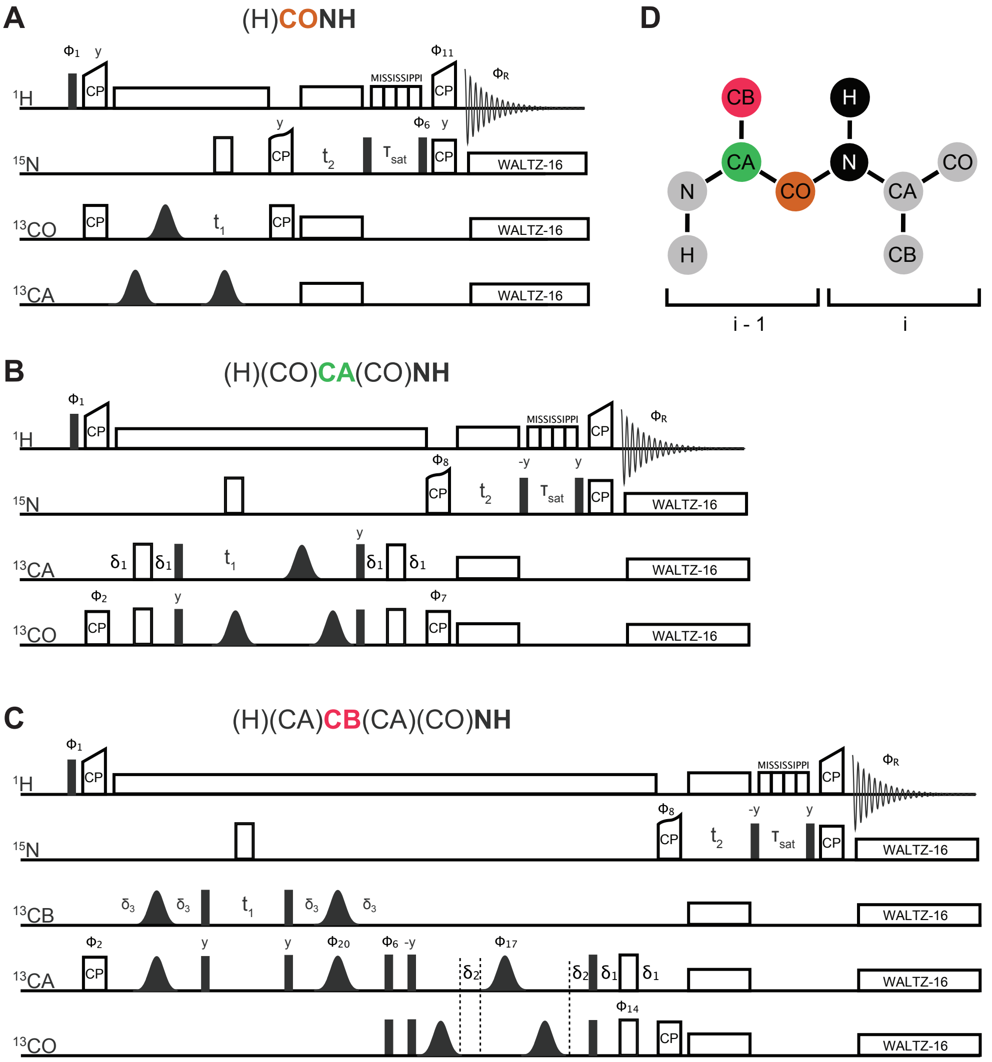

Figure 7.3 **Inter-residual backbone correlation.** Schematic representation of (H)CONH (**A**), (H)(CO)CANH (**B**) and (H)(CA)CB(CA)(CO)NH (**C**) triple-resonance 3D pulse sequences. Filled and open pulse symbols indicate 90° and 180° RF pulses, respectively. Gaussian shapes indicate band selective 180° pulses and extended white rectangles represent decoupling. All pulse sequences use a MISSISSIPPI block for water suppression. Cross polarization steps are marked with CP. All carbon-carbon transfers are scalar-based. Pulses are x-direction if not labelled otherwise. (**A**) ϕ_1 = x, -x; ϕ_6 = x, x, -x, -x; ϕ_{11} = 4y, 4(-y); ϕ_R = y, -y, -y, y, -y, y, y, -y. (**B**) ϕ_1 = y, -y; ϕ_2 = y, y, -y, -y; ϕ_7 = 4y, 4(-y); ϕ_8 = 8x, 8(-x); ϕ_R = x, -x, -x, x, -x, x, x, -x, -x, x, x, -x, x, -x, -x , x. (**C**) ϕ_1 = y, -y; ϕ_2 = y, y, -y, -y; ϕ_6 = 16x, 16(-x); ϕ_{14} = 8x, 8y; ϕ_{17} = 4x, 4y; ϕ_R = x, -x, -x, x, -x, x, x, -x, -x, x, x, -x, x, -x, -x, x, -x, x, x, -x, x, -x, -x, x, x, -x, -x, x, -x, x, x, -x. Pulse sequences by Barbet-Massin et al. [285] and depiction adapted and modified from [282]. **D** Cartoon representation of the chemical shift information gained from the respective pulse programs. Colours mark the evolved nuclei.

For the backbone assignment, a standard set of experiments was recorded on $\sim$ 1 mg of [u-^{2}H, ^{13}C, ^{15}N]-labelled and 100 % back-exchanged RIP2CARD filaments. Spinning at a MAS frequency of 60 kHz, the sample temperature was kept at approximately 295 K. Typical $\pi/2$-pulse lengths were 2.5 µs for ^{1}H, 5 µs for ^{13}C and 7 µs for ^{15}N. H-CA and H-CO CP transfers employed a contact time of 3 and 5 ms, respectively. The contact time of the CO-N, CA-N and N-H CP transfers was 11, 16 ms and 1.5 ms, respectively. Selective carbon pulses employed an Rsnob symmetric soft pulse shape and CP transfers a tangent-modulated amplitude spin lock. Half echo delays δ_3 were 4.7 ms and 7.2 ms for CA-CO and CA-CB scalar transfers, respectively. During proton detection, a WALTZ-16 scheme was used for ^{13}C and ^{15}N decoupling. All experiments employed an interscan delay of 1 s. The number of scans per point (NS), time domain (TD) data and acquisition time (AQ) used for each nucleus of the six 3D experiments are noted in table 7.2. The spectra were recorded in blocks with 8 scans and then processed employing shifted sine-bell and Lorentzian-to-Gaussian apodization functions, manually drift-corrected and added with NMRPipe.

7.3.2 Carbon-detected NMR experiments

Carbon detection has been applied to a wide range of biological systems with MAS NMR. Albeit having a lower gyromagnetic ratio γ than protons and hence a lower NMR sensitivity, carbons have a much larger chemical shift dispersion than protons. Moreover, the network of directly connected carbons form the framework of organic molecules and therefore can provide detailed structural information without requiring high spinning speeds.

The Dipolar Assisted Rotational Resonance (DARR) experiment makes use of a densely coupled proton network to allow for effective spin diffusion among low γ-nuclei like ^{13}C (Fig. 7.4). After an initial H-C CP transfer, the spins evolve while protons are decoupled. This is followed by a $\pi/2$-pulse pulse storing the carbon magnetization along the z-axis and the DARR mixing time during which magnetization is transferred through-space between carbon nuclei in proximity *via* spin diffusion. During the mixing time, the proton decoupling is replaced by a weak recoupling field matching the rotational resonance condition (in which the RF field strength equals the MAS frequency) that enhances the spin diffusion by allowing selective dipolar coupling between carbons and protons. Depending on the employed DARR mixing time (typically 10 - 500 ms), the experiment is applicable for the investigation of intra residual, as well as long distance correlations. After mixing, a second $\pi/2$-pulse converts the carbon magnetization back to the transverse plane and the signal is detected under proton decoupling.

For the DARR-experiments, typical $\pi/2$-pulse lengths were 3.1 µs for ^{1}H and 5 µs for ^{13}C. All 2D spectra were recorded at either 13333 (600 MHz) or 15555 Hz (700 MHz) MAS

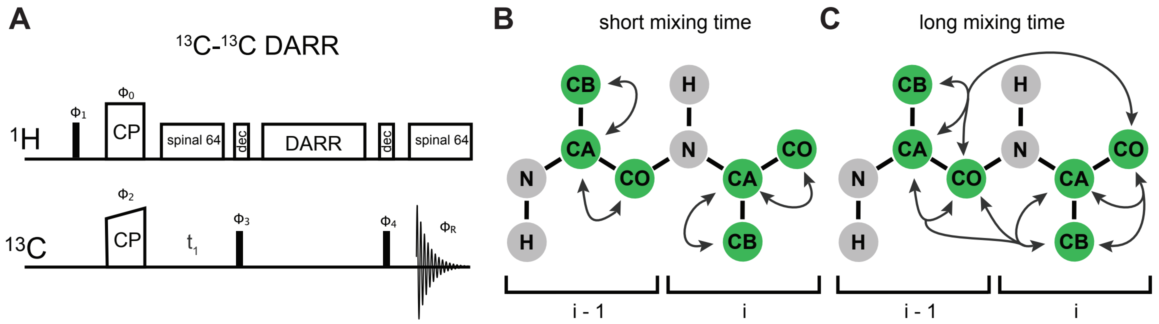

Figure 7.4 **^{13}C-^{13}C DARR. A** Schematic representation of the 2D ^{13}C-^{13}C DARR correlation pulse sequence. Filled symbols indicate 90° RF pulses. Pulses are x-direction if not labelled otherwise. ϕ_1 = y, -y; ϕ_2 = 8x, 8(-x) ; ϕ_3 = y, y, -y, -y; ϕ_4 = y, y, -x, -x, -y, -y, x, x; ϕ_R = -x, x, y, -y, x, -x,-y, y, x, -x,-y, y, -x, x, y, -y. **B** Magnetization transfer of ^{13}C-^{13}C DARR with short mixing time (e.g. 10 ms). Magnetization transfer will only occur between nuclei within the same residue. **C** Magnetization transfer of ^{13}C-^{13}C DARR with long mixing time (e.g. 100 ms). Long range correlations between neighbouring residues can be observed.

frequency at a sample temperature of approximately 285 K. H-C CP contact time was 1 ms using a carbon lock-field ramped (80 %) linearly around the n=1 Hartmann-Hahn matching condition. Various mixing times, with durations of 10, 50, 150, 300 and 500 ms were used for the [2-^{13}C]-glycerol and [1,3-^{13}C]-glycerol-labelled RIP2CARD samples, whereas DARR mixing times of 10 and 50 ms were used for the [u-^{13}C]-labelled sample. The time domain data matrix of the experiments recorded on [1,3-^{13}C]-glycerol and [2-^{13}C]-glycerol-labelled samples were 692 (indirect, F_1) x 1536 (direct, F_2) complex points, corresponding to 15 ms and 32 ms of acquisition time, respectively. The number of scans per point ranged from 16 to 120 depending on the employed DARR mixing time and the overall signal sensitivity of the sample. The experiments recorded on the [u-^{13}C]-labelled sample employed a 384 (indirect, F_1) x 1024 (direct, F_2) complex point data matrix, corresponding to 10 ms and 26 ms of acquisition time, respectively. These experiments were acquired with 32 scans each. All experiments employed an interscan delay of 2 s. During acquisition and indirect chemical shift evolution a SPINAL64 decoupling scheme with a RF strength of 90 kHz was applied to the proton spins. The data were processed applying shifted sine-bell and Lorentzian-to-Gaussian apodization functions and zero filled to 2048 (indirect, F_1) x 4096 (direct, F_2) points.

Chapter 8

Results and Discussion

8.1 RIP2CARD expression, purification and filament formation

After successful expression and purification of MBP-RIP2CARD (Fig. 8.1 **A**) and subsequent MBP-tag cleavage *via* TEV protease (Fig. 8.1 **B**), the incubation of the final protein product resulted in the formation of large protein complexes that were sedimented using ultracentrifugation. Negative-stain micrographs revealed that RIP2CARD forms filaments with a diameter of approximately 10 nm, variable length (0.1 - 1 µm) and a tendency for side-by-side aggregation. The filaments organized in larger aggregates of variable size (Fig. 8.1 **C**). Unlike full-length RIP2 filament structures, RIP2CARD polymerization was independent of the presence of magnesium and adenosine nucleotides [286].
For initial characterization, a uniformly ^{15}N-labelled RIP2CARD sample was prepared and studied by solution-state NMR. As expected, the 2D ^{1}H-^{15}N SOFAST-HMQC spectrum of RIP2CARD showed only few broad signals, stemming either from low-molecular-weight RIP2CARD oligomers or flexible residues of the macro-molecular assembly complex (Fig. 8.2 **A** and **B**). Denaturing RIP2CARD by lowering the sample pH to 3 lead to the appearance of a set of narrow signals with poor chemical shift dispersion in the proton dimension and the disintegration of the filamentous form (Fig. 8.2 **C** and **D**). After readjusting the pH back to the physiological range, these signals remained but weakened in intensity, while an additional set of rather narrow signals appeared, which had a proton chemical shift dispersion typical for folded proteins (Fig. 8.2 **E**). Many of these signals matched the reported resonances of RIP2CARD in solution (BMRB entry: 25828) [274]. However, after only a few minutes these signals disappeared again and negative-stain micrographs revealed a reformation of filamentous RIP2CARD (Fig. 8.2 **F**). Hence, similar to other DD filaments, RIP2CARD

filaments can be reversibly disassembled and reassembled into filaments by changing buffer pH [23, 15].

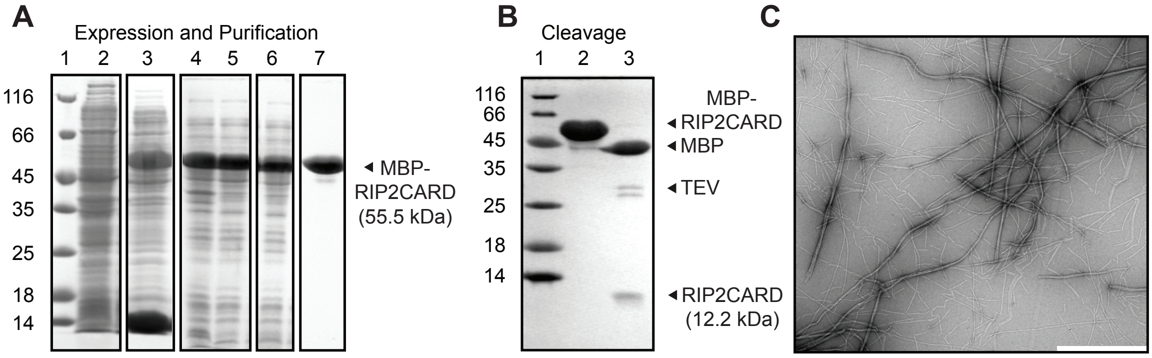

Figure 8.1 **RIP2CARD expression and purification.** **A** Expression and purification of MBP-RIP2CARD: **L1** MW Marker, **L2** BL21(DE3)star uninduced, **L3** BL21(DE3)star pETM40-MBP-RIP2(435–540) induced, **L4** Lysate, **L5** Supernatant, **L6** Flow through Amylose Column (AC), **L7** AC Elution fraction. Molecular size of MBP-RIP2CARD is indicated by an arrow. **B** Cleavage of MBP-RIP2CARD: **L1** MW Marker, **L2** Concentrated MBP-RIP2CARD **L3** After cleavage with TEV Protease. Molecular size of the TEV protease and RIP2CARD are indicated by arrows. **B** TEM micrograph of final product after dialysis and incubation period for filament formation. Scale bar = 500 nm.

8.2 NMR assignment of RIP2CARD

To study the structure of RIP2CARD within filaments, proton- and carbon-detected solid-state NMR were employed. For the backbone resonance assignments, proton-detected (H)CANH, (H)(CO)CA(CO)NH, (H)(CA)CB(CA)NH, (H)(CA)CB(CA)(CO)NH, (H)CONH and (H)CO(CA)NH spectra were recorded on [u-^{2}H, ^{13}C, ^{15}N]-labelled and 100% back-exchanged RIP2CARD samples at 60 kHz MAS (Fig. 8.3 **A**). The 2D ^{1}H-^{15}N projection of the (H)CANH spectrum showed relatively narrow linewidths and good peak dispersion in the proton dimension, indicating that the protein is well-folded within the filament (Fig. 8.3 **B**). With proton T_2 times of 2.6 ms and carbon T_2 times of 12 ms (selectively labelled) and 4 ms (uniformly labelled), the relaxation properties of the protein were favourable, yielding good linewidths and enabling the application of experiments with long transfer schemes. As NMR is highly sensitive to even small variations in the molecular conformation, these favourable spectroscopic properties suggested a high degree of order with only low heterogeneity within the NMR samples. Moreover, observing only a single set of resonances also indicated that the RIP2CARD monomers in the filament are all symmetry-equivalent.

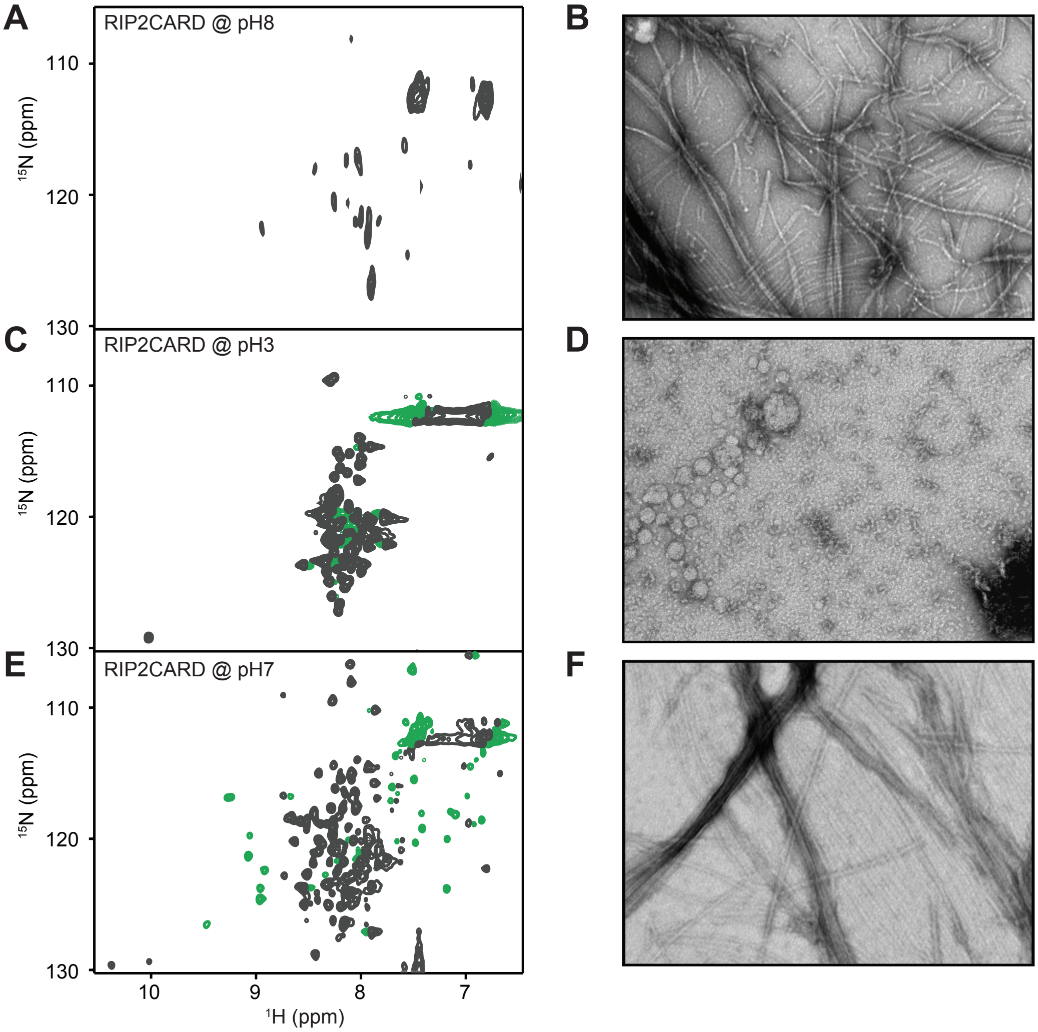

Figure 8.2 **RIP2CARD filament formation. A** ^{1}H-^{15}N SOFAST-HMQC of RIP2CARD at pH 8. EM micrograph of sample shown in **B**. **C** ^{1}H-^{15}N SOFAST-HMQC of RIP2CARD after changing the pH to 3. EM micrograph of sample shown in **D**. **E** ^{1}H-^{15}N SOFAST-HMQC of RIP2CARD after changing the pH back to 7. EM micrograph of sample shown in **F**.

Using the classical backbone-walk assignment strategy described in chapter 3.5.1, the spectra were evaluated to yield the assignment of backbone resonances N, H, CA, CB and CO for each amino acid. Except for the residues 448 – 451 and 497, the analysis of the proton-detected data yielded the sequence-specific assignment for residues Q441 to Q507 (Fig. 8.3 **C**). Projected onto the solution-state NMR structure of RIP2CARD, the missing residues are within or close to disordered loop regions between the helices, suggesting that local structural heterogeneity or flexibility of these regions are the reason for their absence in the spectra. Likewise, no assignment of any cross-peaks was made to the C-terminal 29 residues (N512 - M540) that were disordered in the structure of the monomer. The assigned set of residues correspond to 57 % of the full RIP2CARD sequence and 78 % of residues that are in the folded region of the solution-state NMR structure.

Interestingly, the (H)CANH spectrum measured at 40 kHz MAS on a 1.9 mm rotor yielded additional peaks that could not be assigned unambiguously. However, relying on chemical shift-based amino acid-typing and similarities to characteristic and unique chemical shifts values from the solution-state NMR resonances, these cross-peaks likely stem from the N-terminal region A434-I440, which includes the first helix H1a. Thus, the corresponding residues might exhibit a higher flexibility under 60 kHz MAS, since the increased frictional heating also raises the sample temperature.

The proton-detected data was evaluated together with carbon-detected ^{13}C-^{13}C DARR correlations on protonated samples that were either uniformly ^{13}C-labelled or selectively-labelled using [2-^{13}C]- or [1,3-^{13}C]-glycerol as the sole carbon source during protein expression. For this, the ^{13}C shifts assigned with the proton-detected experiments were used to identify CA-CB or CA-CO cross peaks in the 2D ^{13}C-^{13}C correlation spectra. Subsequently, the side-chain resonances of the identified residue were assigned by analysing spectra with longer mixing times and exploiting the characteristic peak patterns of amino acids in the selectively labelled samples. As the ^{13}C chemical shifts can change depending on protonation/deuteration levels, the analysis had to account for the occurrence of this nucleus-dependent deuterium isotope shift. Hence, by combining data from the proton- and carbon-detected spectra, side-chain chemical shifts were added to the assignment (see Appendix A for chemical shift tables).

In the proton-detected data, amino-acid typing of incomplete spin systems was challenging since the most sensitive experiments (H)CANH and (H)CONH provided only limited information on the amino acid type. In the carbon-detected experiments, however, the most sensitive DARRs with short mixing times provide multiple characteristic carbon-correlations that allow for accurate peak accounting. Thus, the carbon-detected spectra were inspected to determine if signals of residues from the C-terminal region are detectable in the slower spin-

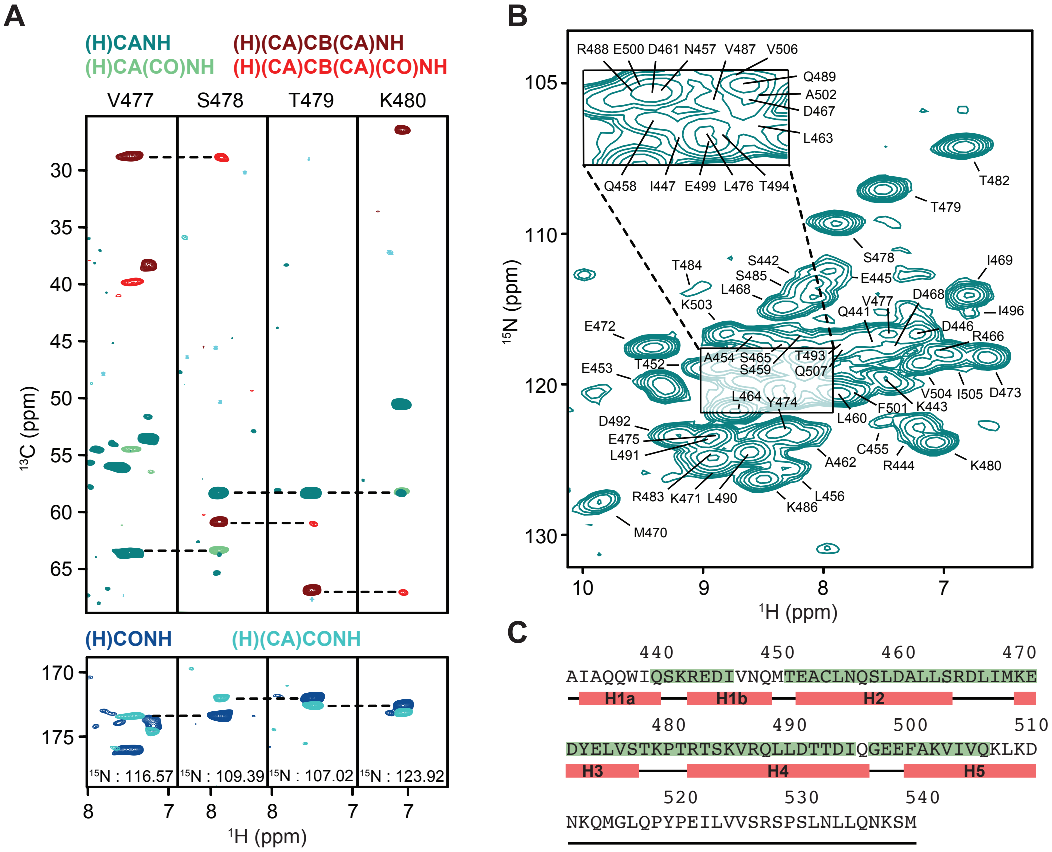

Figure 8.3 **Resonance assignment of proton-detected spectra.** **A** Assignment procedure based on six 3D triple-resonance correlation spectra. The NH pair is correlated with its intra-residual CA, CB and CO resonances in the (H)CANH, (H)(CA)CB(CA)NH and H(CA)CONH spectra and with the respective carbon resonances of the preceding residue in the (H)CA(CO)NH, (H)(CA)CB(CA)(CO)NH and HCONH spectra. **B** Assigned ^{1}H-^{15}N projection of the HNCA spectrum of RIP2CARD. **C** Sequence-overview of the backbone assignment with highlighted assigned (green) unassigned (white) residues. α-helices positioning derived from the solution-state NMR structure are indicated with red lines.

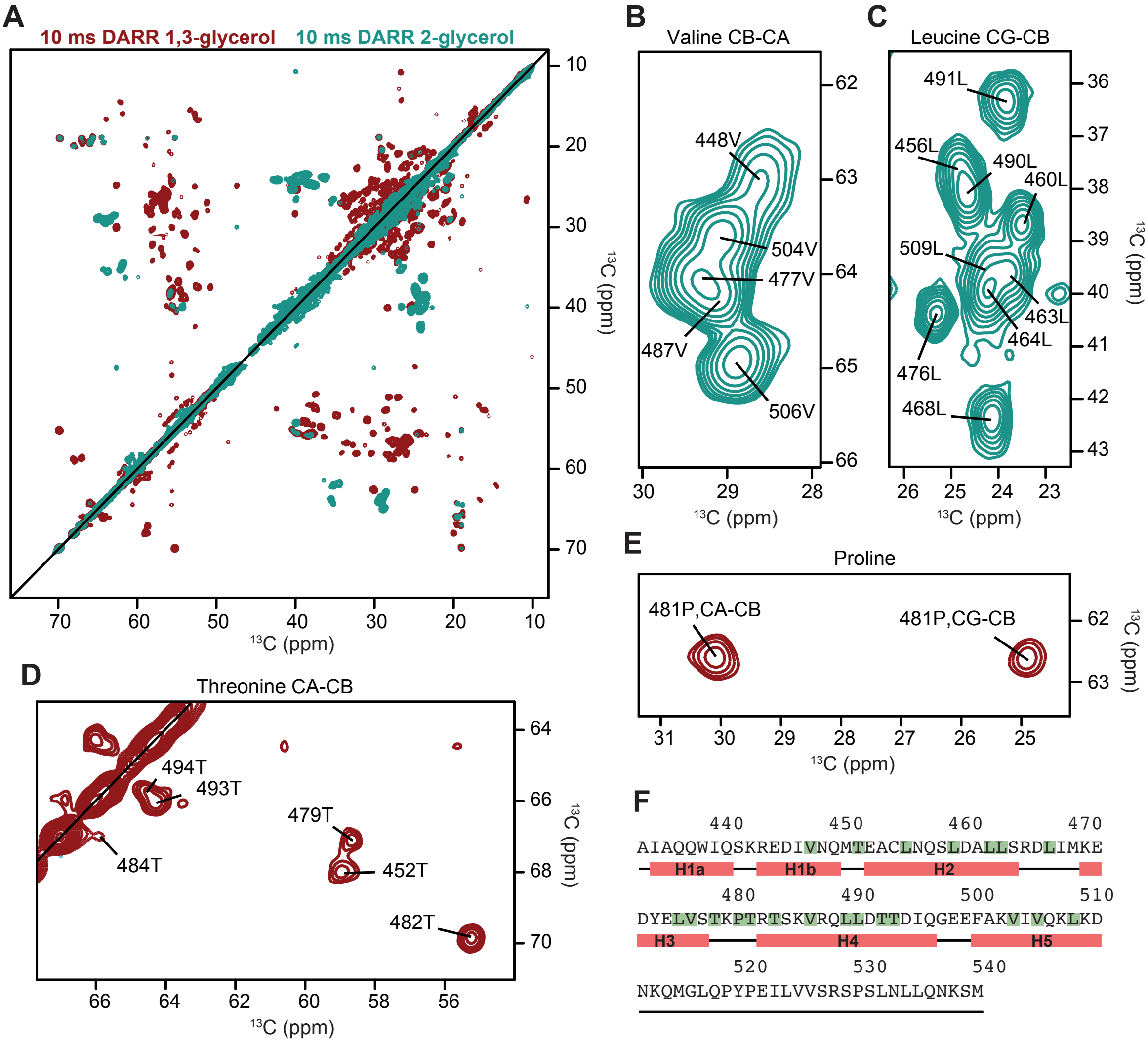

Figure 8.4 **Resonance assignment of carbon-detected spectra. A** Superposition of 10 ms DARR spectra of [1,3-^{13}C]- (green) and [2-^{13}C]-glycerol-labelled (red) RIP2CARD. **B-E** Sections of the spectra in **A**, highlighting the regions that include the characteristic cross peak patterns of valine (**B**) leucine (**C**), threonine (**D**) and proline (**E**) residues. Sequence-specific assignments are indicated. **F** Sequence of RIP2CARD with residues highlighted green that show assigned cross-peaks in the carbon-detected NMR spectra.

ning regime. In the samples with a [1,3-^{13}C]- or [2-^{13}C]-glycerol labelling scheme, Leu, Pro, Thr and Val amino acids produced characteristic cross-peak patterns in ^{13}C-^{13}C correlation spectra with 10 ms DARR mixing time (Fig. 8.4 **A**). The detected signals corresponded to 9 of 14 leucine residues, 6 of 6 Thr, 5 of 7 Val and only 1 of 4 proline residues (Fig. 8.4 **B**-**E**). Relying on the distribution of the respective amino acid types in the sequence, this suggested that the signals from residues in the N512-M540 C-terminal segment were also missing in the spectra. Especially the absence of three proline signal sets, only one being detected, indicated strong structural heterogeneity or mobility in C-terminal region where they cluster (Fig. 8.4 **F**). Furthermore, the number of missing Leu and Val signal sets corresponded to the number present in the C-terminus and thus corroborated the lack of an ordered structure, indicating that H6 is likely also absent in filamentous RIP2CARD.

8.3 RIP2CARD subunit structure

To aid structural analysis of the RIP2CARD filaments, the X-ray crystal structure of RIP2CARD was determined by Erika Pellegrini in Stephen Cusacks lab at the EMBL Grenoble [286]. The structure was solved by molecular replacement and refined at 3.3 Å resolution. Confirming the previously reported solution NMR structure, RIP2CARD adopts the typical CARD fold comprising a Greek key helical bundle with the N- and C-termini oriented in the same direction and with two short helices H1a and H1b instead of a single long helix H1 (Fig. 8.5 **A**-**B**). With a 0.95 Å root-mean-square deviation (RMSD) of all CA positions, the two structures are virtually identical. Both in the crystal and NMR structures, H6 is absent and replaced by a long C-terminal loop.

Since chemical shifts are highly sensitive to the local chemical environment, they provide valuable information on the structural features and can serve as a proxy for the similarity of proteins. Hence, secondary chemical shifts for the solid- and solution-state NMR data were determined by subtracting experimental CA and CB chemical shifts from the respective random coil values for each assigned amino acid ($\Delta\delta$CA, $\Delta\delta$CB) [200]. As shown in Figure 8.5 **C**, the chemical shifts of the assigned residues of filamentous RIP2CARD closely match the chemical shifts of monomeric RIP2CARD in solution. This observation suggests that the overall conformation of the RIP2CARD subunit is maintained upon filament formation. Hence, RIP2CARD monomers assemble into filaments by a rigid-body docking mechanism and do not undergo major structural rearrangement upon polymerization.

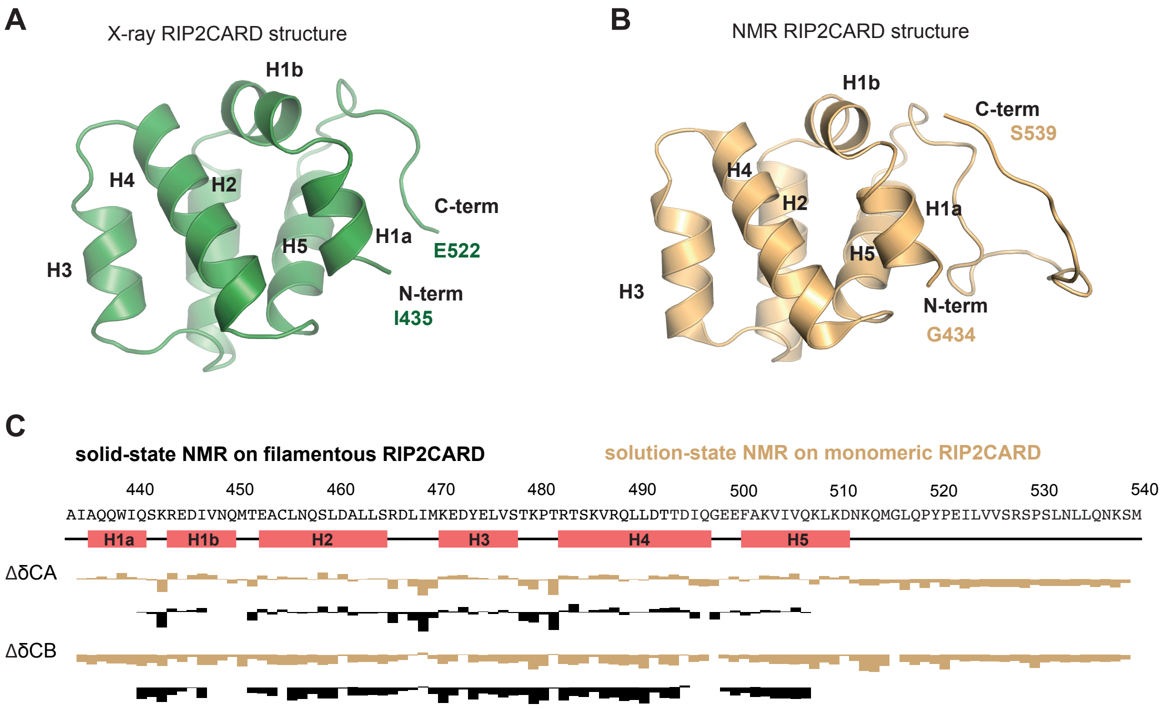

Figure 8.5 **Structure of RIP2CARD within the filament.** **A** Crystal structure of RIP2CARD with the helices and termini labelled (PDB code: 6GFJ) [286] **B** Solution-state NMR structure of RIP2CARD with the helices and termini labelled (PDB code: 2N7Z) [274]. **C** Comparison of secondary chemical shifts of monomeric RIP2CARD in solution (yellow; BMRB entry: 25828) and in the filament, determined by proton-detected solid-state NMR (black).

8.4 RIP2CARD filament structure

Using co-purification and immuno-gold labelling, collaborators from Stephen Cusack's lab showed that NOD2CARDs are preferentially bound to one end of the RIP2CARD filament, supporting the hypothesis that activated NOD2 can nucleate RIP2 filament formation for down-stream signalling [286]. As RIP2CARD filaments with associated NOD2CARDs are shorter, straighter and have a lower tendency to aggregate than RIP2CARD filaments without NOD2, the hetero-CARD filaments were chosen for cryo-EM data collection and analysis. The recorded data yielded a cryo-EM map at 3.94 Å resolution revealing a helical filament with an outer diameter of $\sim$ 75 Å and a central solvent channel with a $\sim$ 25 Å diameter. A final atomic model was built by fitting the crystal structure of RIP2CARD into the cryo-EM density followed by real space refinement. Consistent with the solid-state NMR results, the presumed flexible C-terminus was not observed in the cryo-EM map. The model comprises RIP2CARD residues P433 to Q518 with both N- and C-terminal ends orientated towards the outside of the filament (Fig. 8.6 **A**).

Following the established convention introduced in chapter 6.2.2, helical DD assemblies can be described through interactions of the type I, type II and type III asymmetric interfaces (Fig. 8.6 **B**-**F**). In the RIP2CARD filament, the type I interaction is mainly electrostatic in nature involving several charged residues forming polar contacts between helices H1 and H4 of one subunit (type Ia) with H2 and H3 of a second subunit (type Ib) (Fig. 8.6 **D**). At its centre, residues R444 and R448 from H1 and H4 (type Ia) interact with D461 and N457 from H3 (type Ib). Furthermore, the type I interface consists of additional charged and polar residues such as D492, D495, Q441, E445 and Q489 (type Ia) and D467, K471 (type IIb). The type II interface is formed between the H4-H5 and H2-H3 loops (type IIa) and the H1-H2 loop, the N-terminal of H2 and part of the RIP2CARD C-terminus (type IIb) (Fig. 8.6 **E**). This interface is structurally mediated by van der Waals interactions between M470 (type IIa) and C455 (type IIb) and further reinforced by polar interactions between N512 and Q458. The type III interface is mainly mediated by H3 (type IIIa) and the H3-H4 loop and N-terminal of H4 (type IIIb) (Fig. 8.6 **F**). Hydrophobic interactions between P481, T482 (type IIIa) and L476 (type IIIb) and potential salt-bridges between E472, E475 (type IIIa) and R488, R483 (type IIIb).

To identify residues that become buried in the filamentous core, the CA and CB chemical shift changes between RIP2CARD in solution and within the filament were analysed. These chemical shift differences report on changes in the chemical environment and potential minor local conformational changes due to the filament packing. Figure 8.6 **G** shows that the most significant chemical shift differences are localized in the subunit interfaces described above and therefore independently confirm the overall architecture of the cryo-EM-based

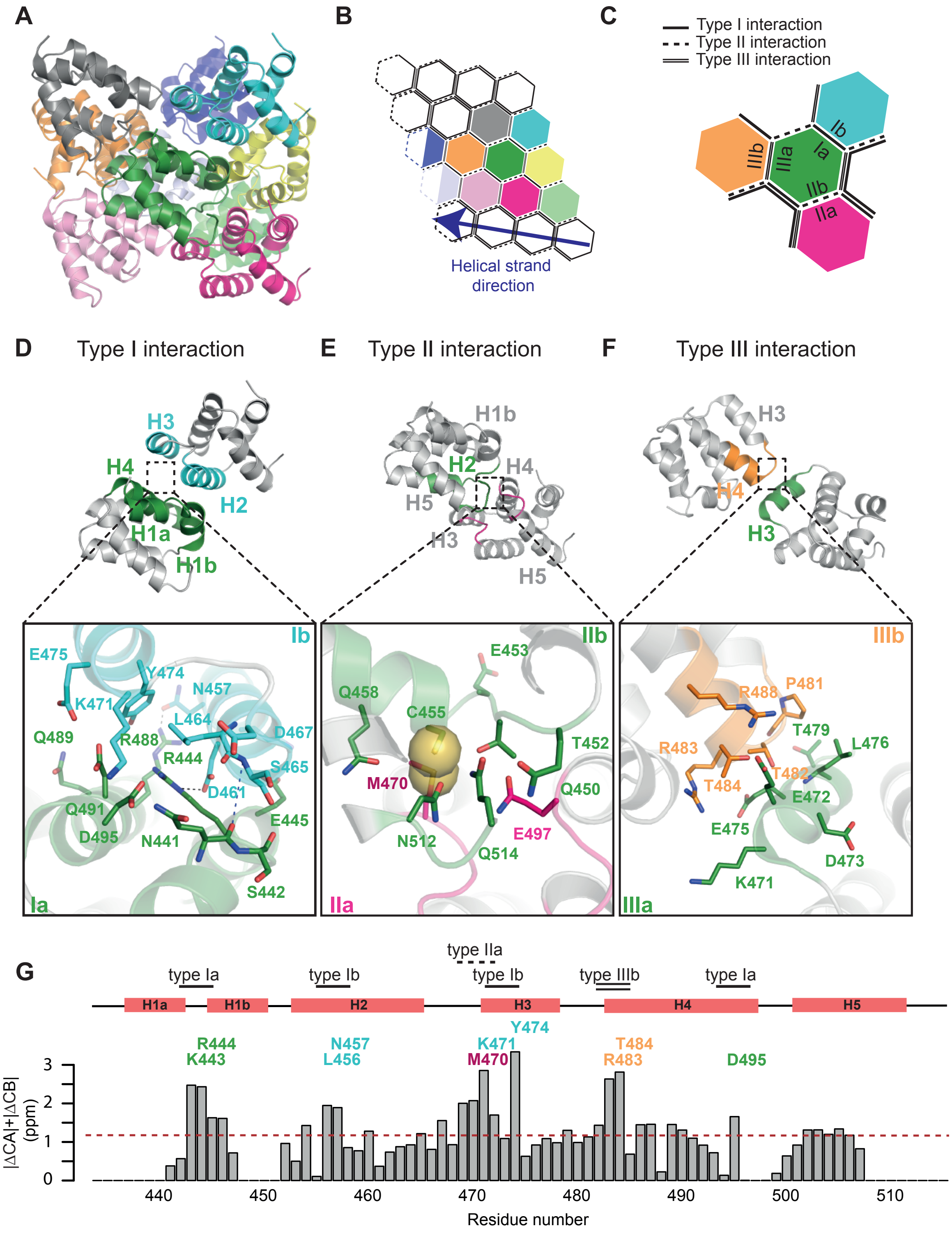

Figure 8.6 **RIP2CARD filament structure.** **A**-**C** Structure of the RIP2CARD filament (**A**) with a schematic diagram of the helical filament (**B**) and relative orientations of type I, type II and type III interfaces (**C**). Each subunit is represented as a hexagon with the same colour code as in **A**. Type I, II, III interfaces are represented as a single line, single-dashed line or double line, respectively. **D**–**F** Structure of RIP2CARD dimers interacting through type I (**D**), type II (**E**) and type III (**F**) interfaces. H-bonds and backbone contacts are represented by black and blue dashed lines, respectively. **G** Sum of ^{13}CA and ^{13}CB chemical shift differences between RIP2CARD in the solution and the solid-state for each assigned amino acid. Residues that show a strong variation from the mean (1.2 ppm; dotted red line) are labelled.

model. Notably, residues close to the type I interface, such as K443, R444, D495, L457, L456, K471 and Y474 undergo significant chemical shift changes in the filament with Y474 showing the largest effect. In ^{13}C-^{13}C correlations employing long mixing times, the Y474 CG resonance displays multiple contacts to residues from other subunits indicating tight packing of Y474 within the filament. Additional residues from the type IIa (M470) and type IIIb (R483, T484) interfaces also exhibit significant chemical shift changes stemming from a change in chemical environment of these residues. Hence, these results can be taken as an independent confirmation of the three characteristic asymmetric interfaces of the filament assembly.

Based on the structural model of the filament, mutational studies were performed on the RIP2CARD type II interface by members of the Cusack lab at EMBL. The introduced mutations aimed to disrupt the RIP2CARD filament assembly while leaving the RIP2-NOD2 hetero-CARD interaction intact to study the effect of inhibited polymerization on signalling. After using negative-stain EM to test the ability of each construct to polymerize *in vitro*, the effect of the mutations on the NOD2 activation of transcription factor NF-κB were investigated *via* a luciferase reporter assay in HEK293T cells [286]. Although EM micrographs revealed that many mutants were still able to polymerize, the filament quality was dramatically reduced. The type IIa/b surface mutants T452K, E453K, C455S and M470K formed irregular and aggregated structures or displayed a total absence of filaments. The T452K mutation both decreased the interaction with NOD2 and led to aberrant filament formation. Transfected into cells, all above-mentioned mutants were also unable to transmit the signal from NOD2 to NF-κB, as the luciferase readout was equal or lower than an empty control vector. Hence, these results illustrate the direct functional relationship between NOD2-dependent NF-κB signalling and RIP2 filament formation.

8.5 Discussion and proposed mechanism

Recent studies have shown that the formation of filamentous structures upon upstream activation by DD-containing PRRs are common in innate cellular immune signalling [6, 256]. These higher-order filamentous assemblies called signalosomes often adopt helical symmetries that share a striking similarity among different signalling pathways. For example, previous studies have identified such higher-order complexes in the MyD88-mediated TLR signalling pathway, the ASC-mediated inflammasome complex and the MAVS-mediated RLR pathway [261, 255, 262]. Despite previous efforts to unravel the mechanism of RIP2 activation by NOD2, the structural basis for RIP2 function remained poorly understood [271, 287, 288]. Since NOD2 and RIP2 both carry CARD DDs that were proposed to mediate their interaction, it was hypothesized that they form a signalosome assembly complex for signal transduction. A previous study had shown that RIP2 kinase dimerization with auto-phosphorylation of the activation loop leads to stable activation of RIP2 [245]. Thus, CARD polymerization into a helical complex might promote kinase dimerization by increasing the local RIP2 concentration.

In previous years, solid-state NMR was successfully applied to study a variety of different assembly complexes. Due to their high molecular weight and the absence of any long-range order, helical assemblies are challenging targets for traditional atomic-resolution techniques like X-ray diffraction and solution-state NMR. However, structure determination of filamentous proteins *via* solid-state NMR is not a trivial endeavour as it requires an unambiguous set of intra- and inter-protomer restraints combined with a highly specialized structure calculation methodology, in order to determine the correct subunit fold and filament symmetry [15]. More recently, an integrated strategy using data from solid-state NMR and cryo-EM has emerged as a powerful alternative to study the structure of protein assemblies. Making use of the complementary information provided by the techniques, this approach was used to gain comprehensive structural insights into a large variety of proteins [21–23].

Applying a highly integrated structural approach employing solid- and solution-state NMR data in combination with X-ray crystallography and cryo-EM facilitated a detailed analysis of the structural features of RIP2CARD and its activation by NOD2. The structural and functional analysis presented here show that RIP2 can form NOD2-nucleated helical filaments through its CARD domain and that this filament formation is necessary for proper NOD2-activated signalling. Beyond the gained biological insights into RIP2 signalling, this joint strategy represents a promising example of an emerging approach of conducting structural studies on assembly complexes.

The sequence-specific assignment of filamentous RIP2CARD was achieved by using a combined approach of proton- and carbon-detected solid-state MAS NMR. The chemical shift analysis of filamentous RIP2CARD validated the previously solved solution-state NMR and X-ray crystallography structure of monomeric RIP2CARD and confirmed the absence of an ordered structure for the C-terminal segment within the filament. Performing cryo-EM imaging and data analysis on co-purified RIP2CARD and NOD2CARDs successfully yielded an EM density map at 3.94 Å resolution, into which the RIP2CARD X-ray structure could be unambiguously fitted. The resulting model revealed that RIP2CARD assembles into a left-handed helical filament with 3.56 subunits per turn, -101.12° rotation per subunit, an axial rise of 4.848 Å per subunit and a 75 Å outer and 25 Å inner diameter.

Only recently, a study by Gong et al. also solved the structure of the RIP2CARD filament complex by cryo-EM at 4.1 Å resolution [289]. With a helical rise of 4.936 Å and a helical rotation of -101.37°, the RIP2CARD filament structure is virtually identical to the structure determined by the Pellegrini et al. presented here (Fig. 8.7). The two independently determined X-ray crystal structures that were fit into the respective cryo-EM density maps are structurally equivalent with a CA position RMSD of 0.853 Å. In contrast to the structure presented here, the structure by Gong et al. was not based on RIP2CARD filaments that were co-purified with NOD2CARDs. Hence, there is no indication that NOD2-nucleated RIP2CARD filaments differ from the self-assembled form.

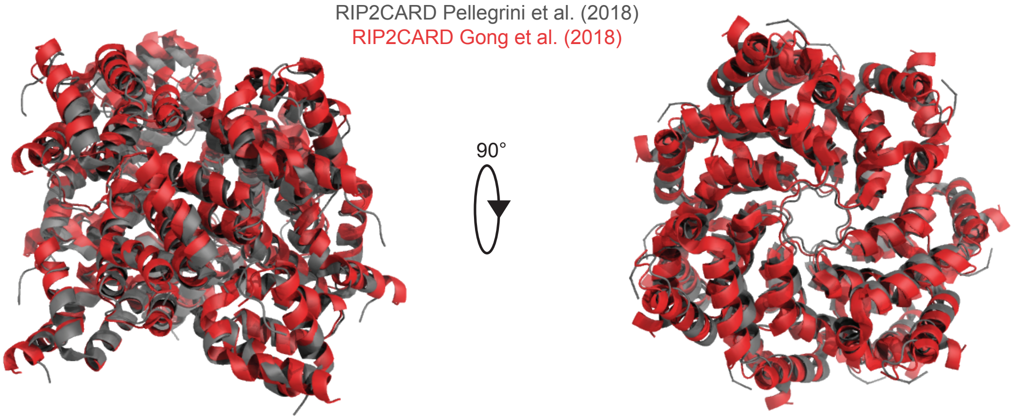

Figure 8.7 **RIP2CARD filament comparison.** Overlay of RIP2CARD filament models from the presented Pellegrini et al. (grey; PDB code: 6GGS) and Gong et al. (red; PDB code: 5YRN) [286, 289].

In contrast to RIP2, RIP1 and RIP3 polymerize through their RIP homotopic interaction motif (RHIM) domain into amyloid fibrils [290]. However, the structural parameters of the RIP2CARD filament closely resemble parameters from other innate immune signalosomes like MAVS and Caspase-1, which also have a helical rise of $\sim$ 5 Å and a helical rotation of $\sim$ 101° [262, 291]. It is therefore tempting to hypothesize that these similarities may enable structural crosstalk between the different innate immune pathways.

In agreement with other reported DD helical assemblies, the RIP2CARD filament structure is based on the conventional type I–III interfaces. Consistent with the cryo-EM-derived structure, significant chemical shift differences between the solution- and solid-state NMR data map to the residues involved in these interfaces. Y474 received the highest chemical shift change and is observed deeply buried in the type I interface of the filament. Indeed, a mutation to phenylalanine and arginine has been shown to disrupt RIP2 activity and the effect was attributed to the abolishment of tyrosine auto-phosphorylation [292, 289]. Receiving a strong chemical shift change, R444 was shown to be also involved in the type I interaction and previous work had already proposed its importance for stabilizing the RIP2 oligomeric state [288]. Similarly, the involvement of R483 in the type III interface was also corroborated by chemical shift analysis. This is also supported by an earlier and the recent Gong et al. study showing that mutation of this residue disrupts RIP2 signalling [288, 289].

Targeting the RIP2 type II surface by mutagenesis to selectively inhibit homo-CARD interaction provided supporting information on the validity of the structural model and allowed for a detailed analysis of the biological significance of the filament formation for signalling. In the type II interface, the cryo-EM structure revealed a more hydrophobic interface with the RIP2-specific residue M470 that also received significant chemical shift change. Mutations of M470 (M470A, M470K) did not affect the interaction with NOD2 but had a disruptive effect on the quality of RIP2 *in vitro* polymerization and abolished *in vivo* signalling plausibly by weakening the hydrophobic interaction at the type II interface. The charge reversal mutation E453K inhibited RIP2 polymerization, presumably by affecting the inner filament electrostatics, as has been seen in similar type II interface mutations in MAVS CARD filament formation [293]. By designing charge-reversal RIP2CARD double mutants, Gong et al. showed that the replacement of elastic interaction with stronger charge–charge pairs (e.g. N449D, D495R in the type II interface) can lead to an increase in signalling activity compared to the WT protein [289]. This further demonstrates how altering RIP2 filament formation directly affects its cellular role and highlights the importance of a finely tuned polymerization mechanism for proper signalling.

Overall, the results indicate that RIP2 filament formation is required for NOD2-dependent NF-κB signalling. A summary of the proposed mechanism based on other published work and the obtained results is depicted in Figure 8.8. After NOD2 activation triggers the receptor to oligomerize, it recruits RIP2 *via* a hetero-CARD interaction. This event nucleates RIP2CARD filament formation and elongation, which stabilizes the active RIP2 kinase dimer. The active RIP2CARD recruits E3 ubiquitin ligases like XIAP and becomes K63-ubiquitinated facilitating further downstream effector activation [294].

The presented work not only gives important structural insights into the NOD2-RIP2 signalling mechanism, but also paves the way for future research on the structural aspects of the interaction. For example, the obtained chemical shift assignments can be used to map the NOD2CARDs-RIP2CARD interface, which until now has only been studied using homology models, docking and mutational analysis [289, 286]. Moreover, since many essential details on the regulation of the signalling pathway are still unknown, the identification of potential RIP2CARD cofactors and post-translational modifications could benefit the understanding of its role within the cell. As many phosphorylation sites are predicted to be situated at the flexible RIP2CARD C-terminus, NMR represents a well-suited tool for studying the kinetics of the reaction and the effects on local structure, plausibly enabling novel protein interactions.

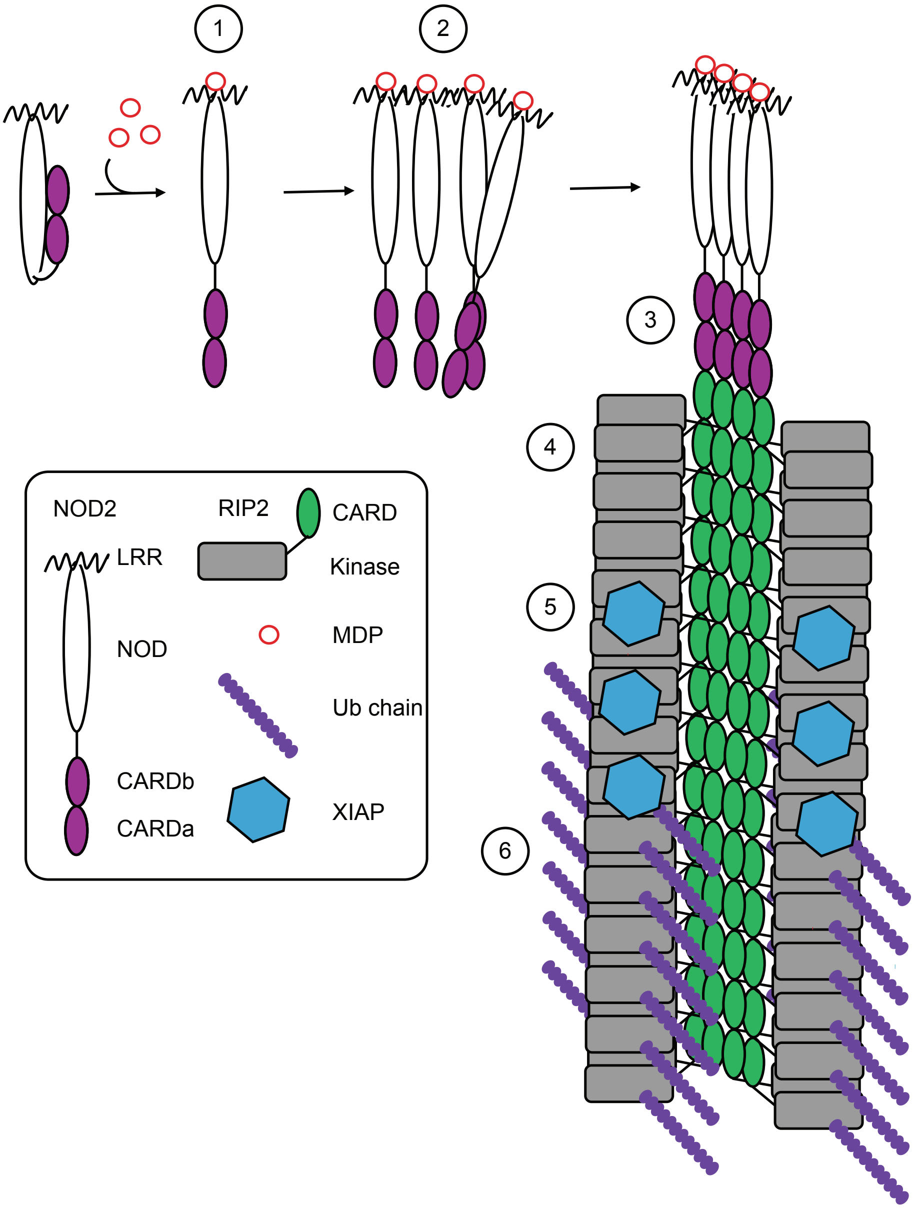

Figure 8.8 **Model of NOD2-RIP2 signalling.** (1) MDP binding to the NOD2 LRR domain activates the receptor *via* derepression of the CARD domains. (2) NOD2 oligomerizes with its NOD and CARD domains and (3) recruits RIP2 *via* its CARD domain. (4) The hetero-CARD complex promotes filament elongation resulting in the RIP2CARD helical assembly and stabilizes the active dimeric form of RIP2K. (5) E3 ligases, such as XIAP, bind the active from of RIP2K and, subsequently, (6) RIP2 is K63-ubiquitinated enabling downstream effector recruitment.

References

[1] Joseph A. Marsh and Sarah A. Teichmann. Structure, Dynamics, Assembly, and Evolution of Protein Complexes. *Annual Review of Biochemistry*, 84(1):551–575, 2015.

[2] Joseph A. Marsh, Helena Hernández, Zoe Hall, Sebastian E. Ahnert, Tina Perica, Carol V. Robinson, and Sarah A. Teichmann. Protein complexes are under evolutionary selection to assemble via ordered pathways. *Cell*, 153(2):461–470, 2013.

[3] Anthony W.P. Fitzpatrick, Benjamin Falcon, Shaoda He, Alexey G. Murzin, Garib Murshudov, Holly J. Garringer, R. Anthony Crowther, Bernardino Ghetti, Michel Goedert, and Sjors H.W. Scheres. Cryo-EM structures of tau filaments from Alzheimer's disease. *Nature*, 547(7662):185–190, 2017.

[4] Marcus D. Tuttle, Gemma Comellas, Andrew J. Nieuwkoop, Dustin J. Covell, Deborah A. Berthold, Kathryn D. Kloepper, Joseph M. Courtney, Jae K. Kim, Alexander M. Barclay, Amy Kendall, William Wan, Gerald Stubbs, Charles D. Schwieters, Virginia M.Y. Lee, Julia M. George, and Chad M. Rienstra. Solid-state NMR structure of a pathogenic fibril of full-length human α-synuclein. *Nature Structural and Molecular Biology*, 23(5):409–415, 2016.

[5] Dror Tobi and Ivet Bahar. Structural changes involved in protein binding correlate with intrinsic motions of proteins in the unbound state. *Proceedings of the National Academy of Sciences*, 102(52):18908–18913, 2005.

[6] Hao Wu. Higher-order assemblies in a new paradigm of signal transduction. *Cell*, 153(2):287–292, 2013.

[7] Daniel A. Fletcher and R. Dyche Mullins. Cell mechanics and the cytoskeleton. *Nature*, 463(7280):485–492, 2010.

[8] Patrick C.A. van der Wel. New applications of solid-state NMR in structural biology. *Emerging Topics in Life Sciences*, 2(1):57–67, 2018.

[9] Lucio Frydman. High magnetic field science and its application in the United States: A magnetic resonance perspective. *Journal of Magnetic Resonance*, 242:256–264, 2014.

[10] Aany Sofia Lilly Thankamony, Johannes J. Wittmann, Monu Kaushik, and Björn Corzilius. Dynamic nuclear polarization for sensitivity enhancement in modern solid-state NMR. *Progress in Nuclear Magnetic Resonance Spectroscopy*, 102-103:120–195, 2017.

[11] Loren B. Andreas, Kristaps Jaudzems, Jan Stanek, Daniela Lalli, Andrea Bertarello, Tanguy Le Marchand, Diane Cala-De Paepe, Svetlana Kotelovica, Inara Akopjana, Benno Knott, Sebastian Wegner, Frank Engelke, Anne Lesage, Lyndon Emsley, Kaspars Tars, Torsten Herrmann, and Guido Pintacuda. Structure of fully protonated proteins by proton-detected magic-angle spinning NMR. *Proceedings of the National Academy of Sciences*, 113(33):9187–9192, 2016.

[12] Joren S. Retel, Andrew J. Nieuwkoop, Matthias Hiller, Victoria A. Higman, Emeline Barbet-Massin, Jan Stanek, Loren B. Andreas, W. Trent Franks, Barth Jan Van Rossum, Kutti R. Vinothkumar, Lieselotte Handel, Gregorio Giuseppe De Palma, Benjamin Bardiaux, Guido Pintacuda, Lyndon Emsley, Werner Kühlbrandt, and Hartmut Oschkinat. Structure of outer membrane protein G in lipid bilayers. *Nature Communications*, 8(1), 2017.

[13] Ivano Bertini, Claudio Luchinat, Giacomo Parigi, Enrico Ravera, Bernd Reif, and Paola Turano. Solid-state NMR of proteins sedimented by ultracentrifugation. *Proceedings of the National Academy of Sciences*, 108(26):10396–10399, 2011.

[14] W. Ying Chow, Rakesh Rajan, Karin H. Muller, David G. Reid, Jeremy N. Skepper, Wai Ching Wong, Roger A. Brooks, Maggie Green, Dominique Bihan, Richard W. Farndale, David A. Slatter, Catherine M. Shanahan, and Melinda J. Duer. NMR spectroscopy of native and in vitro tissues implicates polyADP ribose in biomineralization. *Science*, 344(6185):742–746, 2014.

[15] Lichun He, Benjamin Bardiaux, Mumdooh Ahmed, Johannes Spehr, Renate König, Heinrich Lünsdorf, Ulfert Rand, Thorsten Lührs, and Christiane Ritter. Structure determination of helical filaments by solid-state NMR spectroscopy. *Proceedings of the National Academy of Sciences*, 113(3):272–281, 2016.

[16] Christian Wasmer, Adam Lange, Hélène Van Melckebeke, Ansgar B. Siemer, Roland Riek, and Beat H. Meier. Amyloid fibrils of the HET-s(218-289) prion form a β solenoid with a triangular hydrophobic core. *Science*, 319(5869):1523–1526, 2008.

[17] Antoine Loquet, Nikolaos G. Sgourakis, Rashmi Gupta, Karin Giller, Dietmar Riedel, Christian Goosmann, Christian Griesinger, Michael Kolbe, David Baker, Stefan Becker, and Adam Lange. Atomic model of the type III secretion system needle. *Nature*, 486(7402):276–279, 2012.

[18] Yun Han, Jinwoo Ahn, Jason Concel, In Ja L. Byeon, Angela M. Gronenborn, Jun Yang, and Tatyana Polenova. Solid-state NMR studies of HIV-1 capsid protein assemblies. *Journal of the American Chemical Society*, 132(6):1976–1987, 2010.

[19] Edward H. Egelman. Reconstruction of helical filaments and tubes. *Methods in Enzymology*, 482(C):167–183, 2010.

[20] Werner Kühlbrandt. The Resolution Revolution. *Science*, 343(6178):1443–1444, 2014.

[21] Lothar Gremer, Daniel Schölzel, Carla Schenk, Elke Reinartz, Jörg Labahn, Raimond B.G. Ravelli, Markus Tusche, Carmen Lopez-Iglesias, Wolfgang Hoyer, Henrike Heise, Dieter Willbold, and Gunnar F. Schröder. Fibril structure of amyloid-β(1–42) by cryo–electron microscopy. *Science*, 358(6359):116–119, 2017.

[22] Jean Philippe Demers, Birgit Habenstein, Antoine Loquet, Suresh Kumar Vasa, Karin Giller, Stefan Becker, David Baker, Adam Lange, and Nikolaos G. Sgourakis. High-resolution structure of the Shigella type-III secretion needle by solid-state NMR and cryo-electron microscopy. *Nature Communications*, 5, 2014.

[23] Lorenzo Sborgi, Francesco Ravotti, Venkata P Dandey, Mathias S Dick, Adam Mazur, Sina Reckel, Mohamed Chami, Sebastian Scherer, Matthias Huber, Anja Böckmann, Edward H Egelman, Henning Stahlberg, Petr Broz, Beat H Meier, and Sebastian Hiller. Structure and assembly of the mouse ASC inflammasome by combined NMR spectroscopy and cryo-electron microscopy. *Proceedings of the National Academy of Sciences*, 112(43):13237–13242, 2015.

[24] Konstantin Pervushin, Roland Riek, Gerhard Wider, and Kurt Wüthrich. Attenuated T2 relaxation by mutual cancellation of dipole-dipole coupling and chemical shift anisotropy indicates an avenue to NMR structures of very large biological macromolecules in solution. *Proceedings of the National Academy of Sciences*, 94(23):12366–12371, 1997.

[25] Roland Riek, Jocelyne Fiaux, Eric B. Bertelsen, Arthur L. Horwich, and Kurt Wüthrich. Solution NMR techniques for large molecular and supramolecular structures. *Journal of the American Chemical Society*, 124(41):12144–12153, 2002.

[26] Jocelyne Fiaux, Eric B. Bertelsen, Arthur L. Horwich, and Kurt Wüthrich. NMR analysis of a 900K GroEL-GroES complex. *Nature*, 418(6894):207–211, 2002.

[27] Kevin H. Gardner and Lewis E. Kay. The use of 2H, 13C, 15N multidimensional NMR to study the structure and dynamics of proteins. *Annual Review of Biophysics and Biomolecular Structure*, 27(1):357–406, 1998.

[28] Rina Rosenzweig, Shoeib Moradi, Arash Zarrine-Afsar, John R. Glover, and Lewis E. Kay. Unraveling the mechanism of protein disaggregation through a ClpB-DnaK interaction. *Science*, 339(6123):1080–1083, 2013.

[29] Vitali Tugarinov and Lewis E. Kay. An isotope labeling strategy for methyl TROSY spectroscopy. *Journal of Biomolecular NMR*, 28(2):165–172, 2004.

[30] Remco Sprangers and Lewis E. Kay. Quantitative dynamics and binding studies of the 20S proteasome by NMR. *Nature*, 445(7128):618–622, 2007.

[31] H. Jane Dyson and Peter E. Wright. Unfolded proteins and protein folding studied by NMR. *Chemical Reviews*, 104(8):3607–3622, 2004.

[32] Malene Ringkjøbing Jensen, Rob W H Ruigrok, and Martin Blackledge. Describing intrinsically disordered proteins at atomic resolution by NMR. *Current Opinion in Structural Biology*, 23(3):426–435, 2013.

[33] Francois-Xavier Theillet, Andres Binolfi, Beata Bekei, Andrea Martorana, Honor May Rose, Marchel Stuiver, Silvia Verzini, Dorothea Lorenz, Marleen van Rossum, Daniella Goldfarb, and Philipp Selenko. Structural disorder of monomeric α-synuclein persists in mammalian cells. *Nature*, 530(7588):45–50, 2016.

[34] Nicolas L. Fawzi, Jinfa Ying, Rodolfo Ghirlando, Dennis a. Torchia, and G. Marius Clore. Atomic-resolution dynamics on the surface of amyloid-β protofibrils probed by solution NMR. *Nature*, 480(7376):268–272, 2011.

[35] David S. Libich, Nicolas L. Fawzi, Jinfa Ying, and G. Marius Clore. Probing the transient dark state of substrate binding to GroEL by relaxation-based solution NMR. *Proceedings of the National Academy of Sciences*, 110(28):11361–11366, 2013.

[36] Alain Sillen, Pascale Barbier, Isabelle Landrieu, Sylvie Lefebvre, Jean Michel Wieruszeski, Arnaud Leroy, Vincent Peyrot, and Guy Lippens. NMR investigation of the interaction between the neuronal protein Tau and the microtubules. *Biochemistry*, 46:3055–3064, 2007.

[37] Harindranath Kadavath, Mariusz Jaremko, Jukasz Jaremko, Jacek Biernat, Eckhard Mandelkow, and Markus Zweckstetter. Folding of the Tau Protein on Microtubules. *Angewandte Chemie - International Edition*, 54(35):10347–10351, 2015.

[38] Harindranath Kadavath, Romina V. Hofele, Jacek Biernat, Satish Kumar, Katharina Tepper, Henning Urlaub, Eckhard Mandelkow, and Markus Zweckstetter. Tau stabilizes microtubules by binding at the interface between tubulin heterodimers. *Proceedings of the National Academy of Sciences*, 112(24):7501–7506, 2015.

[39] Yurika Hashi, Gota Kawai, and Susumu Kotani. Microtubule-associated protein (MAP) 4 interacts with microtubules in an intrinsically disordered manner. *Bioscience, Biotechnology, and Biochemistry*, 78(11):1864–1870, 2014.

[40] Teppei Kanaba, Ryoko Maesaki, Tomoyuki Mori, Yutaka Ito, Toshio Hakoshima, and Masaki Mishima. Microtubule-binding sites of the CH domain of EB1 and its autoinhibition revealed by NMR. *Biochimica et Biophysica Acta - Proteins and Proteomics*, 1834(2):499–507, 2013.

[41] Maximilian Zinke, Pascal Fricke, Camille Samson, Songhwan Hwang, Joseph S. Wall, Sascha Lange, Sophie Zinn-Justin, and Adam Lange. Bacteriophage Tail-Tube Assembly Studied by Proton-Detected 4D Solid-State NMR. *Angewandte Chemie - International Edition*, 56(32):9497–9501, 2017.

[42] Bill Wickstead and Keith Gull. The evolution of the cytoskeleton. *Journal of Cell Biology*, 194(4):513–525, 2011.

[43] Gabor Forgacs, Soon Hyung Yook, Paul A Janmey, Hawoong Jeong, and Christopher G Burd. Role of the cytoskeleton in signaling networks. *Journal of Cell Science*, 117(13):2769–2775, 2004.

[44] Paul A. Janmey and Christopher A. McCulloch. Cell Mechanics: Integrating Cell Responses to Mechanical Stimuli. *Annual Review of Biomedical Engineering*, 9(1):1–34, 2007.

[45] Harold P. Erickson. FtsZ, a tubulin homologue in prokaryote cell division. *Trends in Cell Biology*, 7(9):362–367, 1997.

[46] Frederick Gittes, Brian Mickey, Jilda Nettleton, and Jonathon Howard. Flexural rigidity of microtubules and actin filaments measured from thermal fluctuations in shape. *Journal of Cell Biology*, 120(4):923–934, 1993.

[47] Eva Nogales, Michael Whittaker, Ronald A. Milligan, and Kenneth H. Downing. High-resolution model of the microtubule. *Cell*, 96(1):79–88, 1999.

[48] David Sept, Nathan A. Baker, and J. Andrew McCammon. The physical basis of microtubule structure and stability. *Protein Science*, 12(10):2257–2261, 2009.

[49] Joseph Atherton, Melissa Stouffer, Fiona Francis, and Carolyn A. Moores. Microtubule architecture in vitro and in cells revealed by cryo-electron tomography. *Acta Crystallographica Section D: Structural Biology*, 74(6):572–584, 2018.

[50] Arshad Desai and Timothy J. Mitchison. Microtubule Polymerization Dynamics. *Annual Review of Cell and Developmental Biology*, 13(1):83–117, 1997.

[51] Eva Nogales, Sharon G. Wolf, and Kenneth H. Downing. Structure of the $\alpha\beta$ tubulin dimer by electron crystallography. *Nature*, 391(6663):199–203, 1998.

[52] Justin M. Kollman, Andreas Merdes, Lionel Mourey, and David A. Agard. Microtubule nucleation by γ-tubulin complexes. *Nature Reviews Molecular Cell Biology*, 12(11):709–721, 2011.

[53] E. M. Mandelkow, E. Mandelkow, and R. A. Milligan. Microtubule dynamics and microtubule caps: A time-resolved cryo-electron microscopy study. *Journal of Cell Biology*, 114(5):977–991, 1991.

[54] Gregory M. Alushin, Gabriel C. Lander, Elizabeth H. Kellogg, Rui Zhang, David Baker, and Eva Nogales. High-Resolution microtubule structures reveal the structural transitions in $\alpha\beta$-tubulin upon GTP hydrolysis. *Cell*, 157(5):1117–1129, 2014.

[55] Tim Mitchison and Marc Kirschner. Dynamic instability of microtubules. *Nature*, 312:237–242, 1984.

[56] Anna Akhmanova and Michel O. Steinmetz. Control of microtubule organization and dynamics: Two ends in the limelight. *Nature Reviews Molecular Cell Biology*, 16(12):711–726, 2015.

[57] Eckhard Mandelkow and Eva Maria Mandelkow. Microtubules and microtubule-associated proteins. *Current Opinion in Cell Biology*, 7(1):72–81, 1995.

[58] Clare M. Waterman-Storer and E.D. Salmon. Microtubule dynamics: Treadmilling comes around again. *Current Biology*, 7(6):369–372, 1997.

[59] Hélder Maiato, Paula Sampaio, and Claudio E. Sunkel. Microtubule-associated proteins and their essential roles during mitosis. *International Review of Cytology*, 241(SPEC.ISS.):53–153, 2004.

[60] David J. Stephens. Functional coupling of microtubules to membranes – implications for membrane structure and dynamics. *Journal of Cell Science*, 125(12):2795–2804, 2012.

[61] Nobutaka Hirokawa. Kinesin and dynein superfamily proteins and the mechanism of organelle transport. *Science*, 279(5350):519–526, 1998.

[62] Harvey Lodish, Arnold Berk, S Lawrence Zipursky, Paul Matsudaira, David Baltimore, and James Darnell. *Microtubule Dynamics and Motor Protein during Mitosis*. 2000.

[63] Arshad Desai, Suzie Verma, Timothy J. Mitchison, and Claire E. Walczak. Kin I kinesins are microtubule-destabilizing enzymes. *Cell*, 96(1):69–78, 1999.

[64] Ana B. Asenjo, Chandrima Chatterjee, Dongyan Tan, Vania DePaoli, William J. Rice, Ruben Diaz-Avalos, Mariena Silvestry, and Hernando Sosa. Structural model for tubulin recognition and deformation by kinesin-13 microtubule depolymerases. *Cell Reports*, 3(3):759–768, 2013.

[65] Anna Akhmanova and Casper C. Hoogenraad. Microtubule plus-end-tracking proteins: Mechanisms and functions. *Current Opinion in Cell Biology*, 17(1):47–54, 2005.

[66] Gary J. Brouhard, Jeffrey H. Stear, Tim L. Noetzel, Jawdat Al-Bassam, Kazuhisa Kinoshita, Stephen C. Harrison, Jonathon Howard, and Anthony A. Hyman. XMAP215 Is a Processive Microtubule Polymerase. *Cell*, 132(1):79–88, 2008.

[67] Yulia Komarova, Christian O. De Groot, Ilya Grigoriev, Susana Montenegro Gouveia, E. Laura Munteanu, Joseph M. Schober, Srinivas Honnappa, Rubén M. Buey, Casper C. Hoogenraad, Marileen Dogterom, Gary G. Borisy, Michel O. Steinmetz, and Anna Akhmanova. Mammalian end binding proteins control persistent microtubule growth. *Journal of Cell Biology*, 184(5):691–706, 2009.

[68] Linda Sandblad, Karl Emanuel Busch, Peter Tittmann, Heinz Gross, Damian Brunner, and Andreas Hoenger. The Schizosaccharomyces pombe EB1 homolog Mal3p binds and stabilizes the microtubule lattice seam. *Cell*, 127(7):1415–1424, 2006.

[69] Jawdat Al-Bassam, Hwajin Kim, Gary Brouhard, Antoine van Oijen, Stephen C. Harrison, and Fred Chang. CLASP promotes microtubule rescue by recruiting tubulin dimers to the microtubule. *Developmental Cell*, 19(2):245–258, 2010.

[70] Yulia A. Komarova, Anna S. Akhmanova, Shin Ichiro Kojima, Niels Galjart, and Gary G. Borisy. Cytoplasmic linker proteins promote microtubule rescue in vivo. *Journal of Cell Biology*, 159(4):589–599, 2002.

[71] Philippe Pierre, Jochen Scheel, Janet E. Rickard, and Thomas E. Kreis. CLIP-170 links endocytic vesicles to microtubules. *Cell*, 70(6):887–900, 1992.

[72] Jacob E. Lazarus, Armen J. Moughamian, Mariko K. Tokito, and Erika L.F. Holzbaur. Dynactin Subunit p150GluedIs a Neuron-Specific Anti-Catastrophe Factor. *PLoS Biology*, 11(7), 2013.

[73] Sabine Petry, Aaron C. Groen, Keisuke Ishihara, Timothy J. Mitchison, and Ronald D. Vale. Branching microtubule nucleation in xenopus egg extracts mediated by augmin and TPX2. *Cell*, 152(4):768–777, 2013.

[74] Sarah S. Goodwin and Ronald D. Vale. Patronin Regulates the Microtubule Network by Protecting Microtubule Minus Ends. *Cell*, 143(2):263–274, 2010.

[75] Kai Jiang, Shasha Hua, Renu Mohan, Ilya Grigoriev, Kah Wai Yau, Qingyang Liu, Eugene A. Katrukha, A. F.Maarten Altelaar, Albert J.R. Heck, Casper C. Hoogenraad, and Anna Akhmanova. Microtubule Minus-End Stabilization by Polymerization-Driven CAMSAP Deposition. *Developmental Cell*, 28(3):295–309, 2014.

[76] Melissa C. Hendershott and Ronald D. Vale. Regulation of microtubule minus-end dynamics by CAMSAPs and Patronin. *Proceedings of the National Academy of Sciences*, 111(16):5860–5865, 2014.

[77] Francis J. McNally and Ronald D. Vale. Identification of katanin, an ATPase that severs and disassembles stable microtubules. *Cell*, 75(3):419–429, 1993.

[78] Elena Zehr, Agnieszka Szyk, Grzegorz Piszczek, Ewa Szczesna, Xiaobing Zuo, and Antonina Roll-Mecak. Katanin spiral and ring structures shed light on power stroke for microtubule severing. *Nature Structural and Molecular Biology*, 24(9):717–725, 2017.

[79] Ivan Luptovčiak, George Komis, Tomáš Takáč, Miroslav Ovečka, and Jozef Šamaj. Katanin: A Sword Cutting Microtubules for Cellular, Developmental, and Physiological Purposes. *Frontiers in Plant Science*, 8, 2017.

[80] Jelmer J. Lindeboom, Masayoshi Nakamura, Anneke Hibbel, Kostya Shundyak, Ryan Gutierrez, Tijs Ketelaar, Anne Mie C. Emons, Bela M. Mulder, Viktor Kirik, and David W. Ehrhardt. A mechanism for reorientation of cortical microtubule arrays driven by microtubule severing. *Science*, 342(6163), 2013.

[81] Thomas A. Schoenfeld and Robert A. Obar. Diverse Distribution and Function of Fibrous Microtubule-Associated Proteins in the Nervous System. *International Review of Cytology*, 151(C):67–137, 1994.

[82] Leif Dehmelt and Shelley Halpain. The MAP2/Tau family of microtubule-associated proteins. *Genome Biology*, 6(1), 2005.

[83] Shelley Halpain and Leif Dehmelt. The MAP1 family of microtubule-associated proteins. *Genome Biology*, 7(6), 2006.

[84] Gerard Drewes, Andreas Ebneth, and Eva Maria Mandelkow. MAPs, MARKs and microtubule dynamics. *Trends in Biochemical Sciences*, 23(8):307–311, 1998.

[85] Gerard Drewes, Bernhard Trinczek, Susanne Illenberger, Jacek Biernat, Gerold Schmitt-Ulms, Helmut E. Meyer, Eva-Maria Mandelkow, and Eckhard Mandelkow. Microtubule-associated protein/microtubule affinity-regulating kinase (p110mark). *Journal of Biological Chemistry*, 270(13):7679–7688, 1995.

[86] Susanne Illenberger, Gerard Drewes, Bernhard Trinczek, Jacek Biernat, Helmut E. Meyer, Joanna B. Olmsted, Eva Maria Mandelkow, and Eckhard Mandelkow. Phosphorylation of microtubule-associated proteins MAP2 and MAP4 by the protein kinase p110mark: Phosphorylation sites and regulation of microtubule dynamics. *Journal of Biological Chemistry*, 271(18):10834–10843, 1996.

[87] Martin Schwalbe, Harindranath Kadavath, Jacek Biernat, Valery Ozenne, Martin Blackledge, Eckhard Mandelkow, and Markus Zweckstetter. Structural Impact of Tau Phosphorylation at Threonine 231. *Structure*, 23(8):1448–1458, 2015.

[88] Gerard Drewes, Andreas Ebneth, Ute Preuss, Eva Maria Mandelkow, and Eckhard Mandelkow. MARK, a novel family of protein kinases that phosphorylate microtubule-associated proteins and trigger microtubule disruption. *Cell*, 89(2):297–308, 1997.

[89] Ram Dixit, Jennifer L. Ross, Yale E. Goldman, and Erika L.F. Holzbaur. Differential regulation of dynein and kinesin motor proteins by tau. *Science*, 319(5866):1086–1089, 2008.

[90] James W. Mandell and Gary A. Banker. Microtubule-associated proteins, phosphorylation gradients, and the establishment of neuronal polarity. *Perspect Dev Neurobiol*, 4(2):125–135, 1996.

[91] O. Goransson. Regulation of the polarity kinases PAR-1/MARK by 14-3-3 interaction and phosphorylation. *Journal of Cell Science*, 2006.

[92] Bernardino Ghetti, Adrian L. Oblak, Bradley F. Boeve, Keith A. Johnson, Bradford C. Dickerson, and Michel Goedert. Invited review: Frontotemporal dementia caused by microtubule-associated protein tau gene (MAPT) mutations: A chameleon for neuropathology and neuroimaging. *Neuropathology and Applied Neurobiology*, 41(1):24–46, 2015.

[93] Lester I. Binder, Anthony Frankfurter, and Lionel I. Rebhun. The distribution of tau in the mammalian central nervous central nervous. *Journal of Cell Biology*, 101(4):1371–1378, 1985.

[94] David G. Drubin, Stuart C. Feinstein, Eric M. Shooter, and Marc W. Kirschner. Nerve growth factor-induced neurite outgrowth in PC12 cells involves the coordinate induction of microtubule assembly and assembly-promoting factors. *Journal of Cell Biology*, 101(5):1799–1807, 1985.

[95] Jesus Avila, Jose Lucas, Mar Perez, and Felix Hernandez. Role of Tau Protein in Both Physiological and Pathological Conditions. *Physiological Reviews*, 84(2):361–384, 2004.

[96] Tariq Ahmed, Ann Van der Jeugd, David Blum, Marie Christine Galas, Rudi D'Hooge, Luc Buee, and Detlef Balschun. Cognition and hippocampal synaptic plasticity in mice with a homozygous tau deletion. *Neurobiology of Aging*, 35(11):2474–2478, 2014.

[97] Elka R. Georgieva, Shifeng Xiao, Peter P. Borbat, Jack H. Freed, and David Eliezer. Tau binds to lipid membrane surfaces via short amphipathic helices located in its microtubule-binding repeats. *Biophysical Journal*, 107(6):1441–1452, 2014.

[98] Yoann Sottejeau, Alexis Bretteville, François Xavier Cantrelle, Nicolas Malmanche, Florie Demiaute, Tiago Mendes, Charlotte Delay, Harmony Alves Dos Alves, Amandine Flaig, Peter Davies, Pierre Dourlen, Bart Dermaut, Jocelyn Laporte, Philippe Amouyel, Guy Lippens, Julien Chapuis, Isabelle Landrieu, and Jean Charles Lambert.

Tau phosphorylation regulates the interaction between BIN1's SH3 domain and Tau's proline-rich domain. *Acta neuropathologica communications*, 3:58, 2015.

[99] Isabel Correas, Rodolfo Padilla, and Jesus Avila. The tubulin-binding sequence of brain microtubule-associated proteins, tau and MAP-2, is also involved in actin binding. *Biochemical Journal*, 269(1):61, 1990.

[100] M. Goedert, M. G. Spillantini, R. Jakes, D. Rutherford, and R. A. Crowther. Multiple isoforms of human microtubule-associated protein tau: sequences and localization in neurofibrillary tangles of Alzheimer's disease. *Neuron*, 3(4):519–526, 1989.

[101] Cecilia Conde and Alfredo Cáceres. Microtubule assembly, organization and dynamics in axons and dendrites. *Nature Reviews Neuroscience*, 10(5):319–332, 2009.

[102] Marco D. Mukrasch, Stefan Bibow, Jegannath Korukottu, Sadasivam Jeganathan, Jacek Biernat, Christian Griesinger, Eckhard Mandelkow, and Markus Zweckstetter. Structural polymorphism of 441-residue Tau at single residue resolution. *PLoS Biology*, 7(2):0399–0414, 2009.

[103] Karen A. Butner and Marc W. Kirschner. Tau protein binds to microtubules through a flexible array of distributed weak sites. *Journal of Cell Biology*, 115(3):717–730, 1991.

[104] Elizabeth H. Kellogg, Nisreen M.A. Hejab, Simon Poepsel, Kenneth H. Downing, Frank DiMaio, and Eva Nogales. Near-atomic model of microtubule-tau interactions. *Science*, 1780:1–8, 2018.

[105] Amayra Hernández-Vega, Marcus Braun, Lara Scharrel, Marcus Jahnel, Susanne Wegmann, Bradley T. Hyman, Simon Alberti, Stefan Diez, and Anthony A. Hyman. Local Nucleation of Microtubule Bundles through Tubulin Concentration into a Condensed Tau Phase. *Cell Reports*, 20(10):2304–2312, 2017.

[106] Susmitha Ambadipudi, Jacek Biernat, Dietmar Riedel, Eckhard Mandelkow, and Markus Zweckstetter. Liquid-liquid phase separation of the microtubule-binding repeats of the Alzheimer-related protein Tau. *Nature Communications*, 8(1), 2017.

[107] Maike H. Hinrichs, Avesta Jalal, Bernhard Brenner, Eckhard Mandelkow, Satish Kumar, and Tim Scholz. Tau protein diffuses along the microtubule lattice. *Journal of Biological Chemistry*, 287(46):38559–38568, 2012.

[108] Don W. Cleveland, Shu Ying Hwo, and Marc W. Kirschner. Physical and chemical properties of purified tau factor and the role of tau in microtubule assembly. *Journal of Molecular Biology*, 116(2):227–247, 1977.

[109] J. Chen, Y. Kanai, N. J. Cowan, and N. Hirokawa. Projection domains of MAP2 and tau determine spacings between microtubules in dendrites and axons. *Nature*, 360(6405):674–677, 1992.

[110] Peter J. Chung, Chaeyeon Song, Joanna Deek, Herbert P. Miller, Youli Li, Myung Chul Choi, Leslie Wilson, Stuart C. Feinstein, and Cyrus R. Safinya. Tau mediates microtubule bundle architectures mimicking fascicles of microtubules found in the axon initial segment. *Nature Communications*, 7, 2016.

[111] Elea Prezel, Auréliane Elie, Julie Delaroche, Virginie Stoppin-Mellet, Christophe Bosc, Laurence Serre, Anne Fourest-Lieuvin, Annie Andrieux, Marylin Vantard, and Isabelle Arnal. Tau can switch microtubule network organizations: from random networks to dynamic and stable bundles. *Molecular Biology of the Cell*, 29(2):154–165, 2018.

[112] Gloria Lee and Susan L. Rook. Expression of tau protein in non-neuronal cells: microtubule binding and stabilization. *Journal of Cell Science*, 102(2):227–237, 1992.

[113] Alfredo Caceres and Kenneth S. Kosik. Inhibition of neurite polarity by tau antisense oligonucleotides in primary cerebellar neurons. *Nature*, 343(6257):461–463, 1990.

[114] Yazi D. Ke, Alexandra K. Suchowerska, Julia Van Der Hoven, Dineeka M. De Silva, Christopher W. Wu, Janet Van Eersel, Arne Ittner, and Lars M. Ittner. Lessons from Tau-deficient mice. *International Journal of Alzheimer's Disease*, 2012, 2012.

[115] A. Harada, K. Oguchi, S. Okabe, J. Kuno, S. Terada, T. Ohshima, R. Sato-Yoshitake, Y. Takei, T. Noda, and N. Hirokawa. Altered microtubule organization in small-calibre axons of mice lacking tau protein. *Nature*, 369(6480):488–491, 1994.

[116] Sofia Lopes, João Vaz-Silva, Vitor Pinto, Christina Dalla, Nikolaos Kokras, Benedikt Bedenk, Natalie Mack, Michael Czisch, Osborne F. X. Almeida, Nuno Sousa, and Ioannis Sotiropoulos. Tau protein is essential for stress-induced brain pathology. *Proceedings of the National Academy of Sciences*, 113(26):3755–3763, 2016.

[117] Siddhartha Mondragón-Rodríguez, George Perry, Xiongwei Zhu, Paula I. Moreira, Mariana C. Acevedo-Aquino, and Sylvain Williams. Phosphorylation of tau protein as the link between oxidative stress, mitochondrial dysfunction, and connectivity failure: Implications for Alzheimer's disease. *Oxidative Medicine and Cellular Longevity*, 940603, 2013.

[118] Michael Kidd. Paired helical filaments in electron microscopy of Alzheimer's Disease. *Nature*, 197(4863):192–193, 1963.

[119] Richard A. Crowther. Straight and paired helical filaments in Alzheimer disease have a common structural unit. *Proceedings of the National Academy of Sciences*, 88(6):2288–2292, 1991.

[120] Niki Nanavaty, Lauren Lin, Samantha H. Hinckley, and Jeff Kuret. Detection and quantification methods for fibrillar products of in vitro tau aggregation assays. *Methods in Molecular Biology*, 1523:101–111, 2017.

[121] Yann Fichou, Michael Vigers, Andrew K. Goring, Neil A. Eschmann, and Songi Han. Heparin-induced tau filaments are structurally heterogeneous and differ from Alzheimer's disease filaments. *Chemical Communications*, 54(36):4573–4576, 2018.

[122] Benjamin Falcon, Wenjuan Zhang, Alexey G. Murzin, Garib Murshudov, Holly J. Garringer, Ruben Vidal, R. Anthony Crowther, Bernardino Ghetti, Sjors H.W. Scheres, and Michel Goedert. Structures of filaments from Pick's disease reveal a novel tau protein fold. *Nature*, 561(7721):137–140, 2018.

[123] Takashi Hashimoto. Microtubules in Plants. *The Arabidopsis Book*, 13:e0179, 2015.

[124] Diego Breviario, Silvia Gianì, and Laura Morello. Multiple tubulins: Evolutionary aspects and biological implications. *Plant Journal*, 75(2):202–218, 2013.

[125] Sidney L. Shaw, Roheena Kamyar, and David W. Ehrhardt. Sustained microtubule treadmilling in Arabidopsis cortical arrays. *Science*, 300(5626):1715–1718, 2003.

[126] Masayoshi Nakamura, David W. Ehrhardt, and Takashi Hashimoto. Microtubule and katanin-dependent dynamics of microtubule nucleation complexes in the acentrosomal Arabidopsis cortical array. *Nature Cell Biology*, 12(11):1064–1070, 2010.

[127] Satoshi Fujita, Jaromir Pytela, Takashi Hotta, Takehide Kato, Takahiro Hamada, Rie Akamatsu, Yasumasa Ishida, Natsumaro Kutsuna, Seiichiro Hasezawa, Yuko Nomura, Hirofumi Nakagami, and Takashi Hashimoto. An atypical tubulin kinase mediates stress-induced microtubule depolymerization in arabidopsis. *Current Biology*, 23(20):1969–1978, 2013.

[128] J. Christian Ambrose and Richard Cyr. Mitotic spindle organization by the preprophase band. *Molecular Plant*, 1(6):950–960, 2008.

[129] Laurie G. Smith. Plant cell division: Building walls in the right places. *Nature Reviews Molecular Cell Biology*, 2(1):33–39, 2001.

[130] M. C. Ledbetter and K. R. Porter. A "microtubule" in plant cell fine structure. *Journal of Cell Biology*, 19(1):239–250, 1963.

[131] Alexander R. Paredez, Christopher R. Somerville, and David W. Ehrhardt. Visualization of cellulose synthase demonstrates functional association with microtubules. *Science*, 312(5779):1491–1495, 2006.

[132] Heather E. McFarlane, Anett Döring, and Staffan Persson. The Cell Biology of Cellulose Synthesis. *Annual Review of Plant Biology*, 65(1):69–94, 2014.

[133] Anne Endler and Staffan Persson. Cellulose synthases and synthesis in Arabidopsis. *Molecular Plant*, 4(2):199–211, 2011.

[134] Ying Gu, Nick Kaplinsky, Martin Bringmann, Alex Cobb, Andrew Carroll, Arun Sampathkumar, Tobias I. Baskin, Staffan Persson, and Chris R. Somerville. Identification of a cellulose synthase-associated protein required for cellulose biosynthesis. *Proceedings of the National Academy of Sciences*, 107(29):12866–12871, 2010.

[135] Clara Sanchez-Rodriguez, Stefan Bauer, Kian Hematy, Friederike Saxe, Ana B. Ibanez, Vera Vodermaier, Cornelia Konlechner, Arun Sampathkumar, Markus Ruggeberg, Ernst Aichinger, Lutz Neumetzler, Ingo Burgert, Chris Somerville, Marie-Theres Hauser, and Staffan Persson. Chitinase-like1/POM-POM1 and Its Homolog CTL2 Are Glucan-Interacting Proteins Important for Cellulose Biosynthesis in Arabidopsis. *the Plant Cell Online*, 24(2):589–607, 2012.

[136] Martin Bringmann, Eryang Li, Arun Sampathkumar, Tomas Kocabek, Marie-Theres Hauser, and Staffan Persson. POM-POM2/CELLULOSE SYNTHASE INTERACTING1 Is Essential for the Functional Association of Cellulose Synthase and Microtubules in Arabidopsis. *The Plant Cell*, 24(1):163–177, 2012.

[137] Paul B. Green. Mechanism for plant cellular morphogenesis. *Science*, 138(3548):1404–1405, 1962.

[138] Laura Vineyard, Andrew Elliott, Sonia Dhingra, Jessica R. Lucas, and Sidney L. Shaw. Progressive Transverse Microtubule Array Organization in Hormone-Induced Arabidopsis Hypocotyl Cells. *The Plant Cell*, 25(2):662–676, 2013.

[139] Chris Somerville, Stefan Bauer, Ginger Brininstool, Michelle Facette, Thorsten Hamann, Jennifer Milne, Erin Osborne, Alex Paredez, Staffan Persson, Ted Raab, Sonja Vorwerk, and Heather Youngs. Toward a systems approach to understanding plant cell walls. *Science*, 306(5705):2206–2211, 2004.

[140] Daniel J. Cosgrove. Growth of the plant cell wall. *Nature Reviews Molecular Cell Biology*, 6(11):850–861, 2005.

[141] Sang Jin Kim and Federica Brandizzi. The plant secretory pathway: An essential factory for building the plant cell wall. *Plant and Cell Physiology*, 55(4):687–693, 2014.

[142] Cécile Albenne, Hervé Canut, Georges Boudart, Yu Zhang, Hélne San Clemente, Rafael Pont-Lezica, and Elisabeth Jamet. Plant cell wall proteomics: Mass spectrometry data, a trove for research on protein structure/function relationships. *Molecular Plant*, 2(5):977–989, 2009.

[143] Yoshihisa Oda. Cortical microtubule rearrangements and cell wall patterning. *Frontiers in Plant Science*, 6(April):1–7, 2015.

[144] Takahiro Hamada. Microtubule-associated proteins in higher plants. *Journal of Plant Research*, 120(1):79–98, 2007.

[145] Jana Krtková, Martina Benáková, and Kateřina Schwarzerová. Multifunctional Microtubule-Associated Proteins in Plants. *Frontiers in Plant Science*, 7(April):474, 2016.

[146] Edouard Pesquet, Andrey V. Korolev, Grant Calder, and Clive W. Lloyd. The Microtubule-Associated Protein AtMAP70-5 Regulates Secondary Wall Patterning in Arabidopsis Wood Cells. *Current Biology*, 20(8):744–749, 2010.

[147] Keiji Nakajima, Ikuyo Furutani, Hideki Tachimoto, Hiroshige Matsubara, and Takashi Hashimoto. SPIRAL1 encodes a plant-specific microtubule-localized protein required for directional control of rapidly expanding Arabidopsis cells. *The Plant cell*, 16(5):1178–1190, 2004.

[148] Maki Yao, Yoshinori Wakamatsu, Tomohiko J. Itoh, Tsubasa Shoji, and Takashi Hashimoto. Arabidopsis SPIRAL2 promotes uninterrupted microtubule growth by suppressing the pause state of microtubule dynamics. *Journal of Cell Science*, 121(14):2372–2381, 2008.

[149] Juan Li, Yunyuan Xu, and Kang Chong. The novel functions of kinesin motor proteins in plants. *Protoplasma*, 249(SUPPL.2):95–100, 2012.

[150] Moé Yamada, Yohko Tanaka-Takiguchi, Masahito Hayashi, Momoko Nishina, and Gohta Goshima. Multiple kinesin-14 family members drive microtubule minus end-directed transport in plant cells. *Journal of Cell Biology*, 216(6):1705–1714, 2017.

[151] Ivan Luptovčiak, George Komis, Tomáš Takáč, Miroslav Ovečka, and Jozef Šamaj. Katanin: A Sword Cutting Microtubules for Cellular, Developmental, and Physiological Purposes. *Frontiers in Plant Science*, 8(November), 2017.

[152] Deshu Lin, Lingyan Cao, Zhenzhen Zhou, Lei Zhu, David Ehrhardt, Zhenbiao Yang, and Ying Fu. Rho GTPase signaling activates microtubule severing to promote microtubule ordering in arabidopsis. *Current Biology*, 23(4):290–297, 2013.

[153] Jordi Chan, Cynthia G Jensen, Lawrence C Jensen, Max Bush, and Clive W Lloyd. The 65-kDa carrot microtubule-associated protein forms regularly arranged filamentous cross-bridges between microtubules. *Proceedings of the National Academy of Sciences*, 96(26):14931–14936, 1999.

[154] Andrei P Smertenko, Hsin-yu Chang, Vera Wagner, Despina Kaloriti, Stepan Fenyk, Seiji Sonobe, Clive Lloyd, Marie-Theres Hauser, and Patrick J Hussey. The Arabidopsis microtubule-associated protein AtMAP65-1: molecular analysis of its microtubule bundling activity. *The Plant cell*, 16(8):2035–2047, 2004.

[155] Chin-Min K. Ho, Yuh-Ru J. Lee, Lindsay D. Kiyama, Savithramma P. Dinesh-Kumar, and Bo Liu. Arabidopsis Microtubule-Associated Protein MAP65-3 Cross-Links Antiparallel Microtubules toward Their Plus Ends in the Phragmoplast via Its Distinct C-Terminal Microtubule Binding Domain. *The Plant Cell*, 24(5):2071–2085, 2012.

[156] Rana Munns and Mark Tester. Mechanisms of Salinity Tolerance. *Annual Review of Plant Biology*, 59(1):651–681, 2008.

[157] Pooja Shrivastava and Rajesh Kumar. Soil salinity: A serious environmental issue and plant growth promoting bacteria as one of the tools for its alleviation. *Saudi Journal of Biological Sciences*, 22(2):123–131, 2015.

[158] Elizabeth F. Crowell, Volker Bischoff, Thierry Desprez, Aurelia Rolland, York-Dieter Stierhof, Karin Schumacher, Martine Gonneau, Herman Hofte, and Samantha Vernhettes. Pausing of Golgi Bodies on Microtubules Regulates Secretion of Cellulose Synthase Complexes in Arabidopsis. *The Plant cell*, 21(4):1141–1154, 2009.

[159] Ryan Gutierrez, Jelmer J. Lindeboom, Alex R. Paredez, A. M C Emons, and David W. Ehrhardt. Arabidopsis cortical microtubules position cellulose synthase delivery to the plasma membrane and interact with cellulose synthase trafficking compartments. *Nature Cell Biology*, 11(7):797–806, 2009.

[160] Abdelbagi M. Ismail and Tomoaki Horie. Genomics, Physiology, and Molecular Breeding Approaches for Improving Salt Tolerance. *Annual Review of Plant Biology*, 68(1):405–434, 2017.

[161] Che Wang, Jiejie Li, and Ming Yuan. Salt tolerance requires cortical microtubule reorganization in Arabidopsis. *Plant and Cell Physiology*, 48(11):1534–1547, 2007.

[162] Songhu Wang, Jasmina Kurepa, Takashi Hashimoto, and Jan A. Smalle. Salt Stress-Induced Disassembly of Arabidopsis Cortical Microtubule Arrays Involves 26S Proteasome-Dependent Degradation of SPIRAL1. *the Plant Cell Online*, 23(9):3412–3427, 2011.

[163] Anne Endler, Christopher Kesten, René Schneider, Yi Zhang, Alexander Ivakov, Anja Froehlich, Norma Funke, and Staffan Persson. A Mechanism for Sustained Cellulose Synthesis during Salt Stress. *Cell*, 162(6):1353–1364, 2015.

[164] Christopher B. Field, Michael J. Behrenfeld, James T. Randerson, and Paul Falkowski. Primary production of the biosphere: Integrating terrestrial and oceanic components. *Science*, 281(5374):237–240, 1998.

[165] Ting Wang, Heather E. McFarlane, and Staffan Persson. The impact of abiotic factors on cellulose synthesis. *Journal of Experimental Botany*, 67(2):543–552, 2016.

[166] Che Wang, Jiejie Li, and Ming Yuan. Salt tolerance requires cortical microtubule reorganization in Arabidopsis. *Plant and Cell Physiology*, 48(11):1534–1547, 2007.

[167] Elisabeth Gasteiger, Christine Hoogland, Alexandre Gattiker, Severine Duvaud, Marc R Wilkins, Ron D. Appel, and Amos Bairoch. Protein Identification and Analysis Tools on the ExPASy Server. In *The Proteomics Protocols Handbook*, pages 571–607. 2005.

[168] Mirco Castoldi and Andrei V. Popov. Purification of brain tubulin through two cycles of polymerization- depolymerization in a high-molarity buffer. *Protein Expression and Purification*, 32(1):83–88, 2003.

[169] Peter Schuck. Size-distribution analysis of macromolecules by sedimentation velocity ultracentrifugation and Lamm equation modeling. *Biophysical Journal*, 78(3):1606–1619, 2000.

[170] Bin Xue, Roland L. Dunbrack, Robert W. Williams, A. Keith Dunker, and Vladimir N. Uversky. PONDR-FIT: a meta-predictor of intrinsically disordered amino acids. *Biochim Biophys Acta*, 1804(4):996–1010, 2010.

[171] Peter Rice, Lan Longden, and Alan Bleasby. EMBOSS: The European Molecular Biology Open Software Suite. *Trends in Genetics*, 16(6):276–277, 2000.

[172] Stephen F. Altschul, Warren Gish, Webb Miller, Eugene W. Myers, and David J. Lipman. Basic local alignment search tool. *Journal of Molecular Biology*, 215(3):403–410, 1990.

[173] Jason S. Papadopoulos and Richa Agarwala. COBALT: Constraint-based alignment tool for multiple protein sequences. *Bioinformatics*, 23(9):1073–1079, 2007.

[174] Fabian Glaser, Tal Pupko, Inbal Paz, Rachel E. Bell, Dalit Bechor-Shental, Eric Martz, and Nir Ben-Tal. ConSurf: Identification of functional regions in proteins by surface-mapping of phylogenetic information. *Bioinformatics*, 19(1):163–164, 2003.

[175] Fabian Sievers, Andreas Wilm, David Dineen, Toby J. Gibson, Kevin Karplus, Weizhong Li, Rodrigo Lopez, Hamish McWilliam, Michael Remmert, Johannes Söding, Julie D. Thompson, and Desmond G. Higgins. Fast, scalable generation of high-quality protein multiple sequence alignments using Clustal Omega. *Molecular Systems Biology*, 7, 2011.

[176] Paul Schanda, Eriks Kupĉe, and Bernhard Brutscher. SOFAST-HMQC experiments for recording two-dimensional deteronuclear correlation spectra of proteins within a few seconds. *Journal of Biomolecular NMR*, 33(4):199–211, 2005.

[177] Ēriks Kupše and Ray Freeman. Wideband Excitation with Polychromatic Pulses. *Journal of Magnetic Resonance*, 108(2):268–273, 1994.

[178] Helen Geen and Ray Freeman. Band-selective radiofrequency pulses. *Journal of Magnetic Resonance*, 93(1):93–141, 1991.

[179] Paul Schanda, Hélène Van Melckebeke, and Bernhard Brutscher. Speeding up three-dimensional protein NMR experiments to a few minutes. *Journal of the American Chemical Society*, 128(28):9042–9043, 2006.

[180] Mehdi Mobli and Jeffrey C. Hoch. Nonuniform sampling and non-Fourier signal processing methods in multidimensional NMR. *Progress in Nuclear Magnetic Resonance Spectroscopy*, 83:21–41, 2014.

[181] Kamil Tamiola, Burçin Acar, and Frans A.A. Mulder. Sequence-specific random coil chemical shifts of intrinsically disordered proteins. *Journal of the American Chemical Society*, 132(51):18000–18003, 2010.

[182] Kamil Tamiola and Frans A.A. Mulder. Using NMR chemical shifts to calculate the propensity for structural order and disorder in proteins. *Biochemical Society Transactions*, 40(5):1014–1020, 2012.

[183] Joseph A. Marsh, Vinay K. Singh, Zongchao Jia, and Julie D. Forman-Kay. Sensitivity of secondary structure propensities to sequence differences between α- and γ-synuclein: Implications for fibrillation. *Protein Science*, 15(12):2795–2804, 2006.

[184] Ian R. Kleckner and Mark P. Foster. An introduction to NMR-based approaches for measuring protein dynamics. *Biochimica et biophysica acta*, 1814(8):942–68, aug 2011.

[185] Martin Ballaschk. *Kernmagnetresonanzspektroskopische Untersuchungen der Dynamik von HLA-B * 27*. PhD thesis, Free University Berlin, 2016.

[186] Philipp Neudecker, Patrik Lundström, and Lewis E. Kay. Relaxation dispersion NMR spectroscopy as a tool for detailed studies of protein folding. *Biophysical Journal*, 96(6):2045–2054, 2009.

[187] Andrew J. Baldwin and Lewis E. Kay. NMR spectroscopy brings invisible protein states into focus. *Nature Chemical Biology*, 5(11):808–814, 2009.

[188] J. Patrick Loria, Mark Rance, and Arthur G. Palmer. A relaxation-compensated Carr-Purcell-Meiboom-Gill sequence for characterizing chemical exchange by NMR spectroscopy [13]. *Journal of the American Chemical Society*, 121(10):2331–2332, 1999.

[189] Moriz Mayer and Bernd Meyer. Characterization of ligand binding by saturation transfer difference NMR spectroscopy. *Angewandte Chemie - International Edition*, 38(12):1784–1788, 1999.

[190] Lyndon Emsley and Geoffrey Bodenhausen. Gaussian pulse cascades: New analytical functions for rectangular selective inversion and in-phase excitation in NMR. *Chemical Physics Letters*, 165(6):469–476, 1989.

[191] Steven P. Rucker and A. J. Shaka. Broadband homonuclear cross polarization in 2D NMR using DIPSI-2. *Molecular Physics*, 68(2):509–517, 1989.

[192] Shao Hong-Bo, Liang Zong-Suo, and Shao Ming-An. LEA proteins in higher plants: Structure, function, gene expression and regulation. *Colloids and Surfaces: Biointerfaces*, 45(3-4):131–135, 2005.

[193] Johann Grelet, Abdelilah Benamar, Emeline Teyssier, Marie-Hélène Avelange-Macherel, Didier Grunwald, and David Macherel. Identification in Pea Seed Mitochondria of a Late-Embryogenesis Abundant Protein Able to Protect Enzymes from Drying. *Plant Physiology*, 137(1):157–167, 2005.

[194] Daniel Brüne, Miguel A. Andrade-Navarro, and Pablo Mier. Proteome-wide comparison between the amino acid composition of domains and linkers. *BMC Research Notes*, 11(1):1–6, 2018.

[195] Nathalie Sibille, Alain Sillen, Arnaud Leroy, Jean Michel Wieruszeski, Barbara Mulloy, Isabelle Landrieu, and Guy Lippens. Structural impact of heparin binding to full-length Tau as studied by NMR spectroscopy. *Biochemistry*, 45(41):12560–12572, 2006.

[196] Nazila Salamat-Miller, Jianwen Fang, Christopher W. Seidel, Yassen Assenov, Mario Albrecht, and C. Russell Middaugh. A network-based analysis of polyanion-binding proteins utilizing human protein arrays. *Journal of Biological Chemistry*, 282(14):10153–10163, 2007.

[197] Christopher Kesten. *Good companions: the Cellulose Synthase Complex and the CC proteins*. PhD thesis, University of Melbourne, 2016.

[198] Bernard C.-H. Lam, Tammy L. Sage, Fabrizio Bianchi, and Eduardo Blumwald. Role of SH3 domain-containing proteins in clathrin-mediated vesicle trafficking in Arabidopsis. *The Plant cell*, 13(11):2499–512, 2001.

[199] Sibo Feng, James K. Chen, Hongtao Yu, Julian A. Simon, and Stuart L. Schreiber. Two binding orientations for peptides to the Src SH3 domain: Development of a general model for SH3-ligand interactions. *Science*, 266(5188):1241–1247, 1994.

[200] David S. Wishart and Brian D. Sykes. The 13C Chemical-Shift Index: A simple method for the identification of protein secondary structure using 13C chemical-shift data. *Journal of Biomolecular NMR*, 4(2):171–180, 1994.

[201] Lilia Polle, Luciano A. Rigano, Rowan Julian, Keith Ireton, and Wolf Dieter Schubert. Structural details of human tuba recruitment by InlC of listeria monocytogenes elucidate bacterial cell-cell spreading. *Structure*, 22(2):304–314, 2014.

[202] Grant R. Cramer, Kaoru Urano, Serge Delrot, Mario Pezzotti, and Kazuo Shinozaki. Effects of abiotic stress on plants: A systems biology perspective. *BMC Plant Biology*, 11(163), 2011.

[203] Pooja Shrivastava and Rajesh Kumar. Soil salinity: A serious environmental issue and plant growth promoting bacteria as one of the tools for its alleviation. *Saudi Journal of Biological Sciences*, 22(2):123–131, 2015.

[204] Teppei Kanaba, Ryoko Maesaki, Tomoyuki Mori, Yutaka Ito, Toshio Hakoshima, and Masaki Mishima. Microtubule-binding sites of the CH domain of EB1 and its autoinhibition revealed by NMR. *Biochimica et Biophysica Acta - Proteins and Proteomics*, 1834(2):499–507, 2013.

[205] Mark A. Seeger, Yongbo Zhang, and Sarah E. Rice. Kinesin tail domains are intrinsically disordered. *Proteins: Structure, Function and Bioinformatics*, 80(10):2437–2446, 2012.

[206] Séverine Jansen, Katerina Melková, Zuzana Trosanová, Katerina Hanáková, Milan Zachrdla, Jirí Novácek, Erik Zupa, Zbynek Zdráhal, Jozef Hritz, and Lukás Zídek. Quantitative mapping of microtubule-associated protein 2c (MAP2c) phosphorylation and regulatory protein 14-3-3ζ-binding sites reveals key differences between MAP2c and its homolog Tau. *Journal of Biological Chemistry*, 292(16):6715–6727, 2017.

[207] Benoît Gigant, Chunguang Wang, Raimond B.G. Ravelli, Fanny Roussi, Michel O. Steinmetz, Patrick A. Curmi, André Sobel, and Marcel Knossow. Structural basis for the regulation of tubulin by vinblastine. *Nature*, 435(7041):519–522, 2005.

[208] Ralmond B.G. Ravelli, Benoit Gigant, Patrick A. Curmi, Isabelle Jourdain, Sylvie Lachkar, André Sobel, and Marcel Knossow. Insight into tubulin regulation from a complex with colchicine and a stathmin-like domain. *Nature*, 428(6979):198–202, 2004.

[209] Martin Bringmann, Benoit Landrein, Christian Schudoma, Olivier Hamant, Marie Theres Hauser, and Staffan Persson. Cracking the elusive alignment hypothesis: The microtubule-cellulose synthase nexus unraveled. *Trends in Plant Science*, 17(11):666–674, 2012.

[210] Shundai Li, Lei Lei, Chris R. Somerville, and Ying Gu. Cellulose synthase interactive protein 1 (CSI1) links microtubules and cellulose synthase complexes. *Proceedings of the National Academy of Sciences*, 109(1):185–190, 2012.

[211] Zengyu Liu, Rene Schneider, Christopher Kesten, Yi Zhang, Marc Somssich, Youjun Zhang, Alisdair R. Fernie, and Staffan Persson. Cellulose-Microtubule Uncoupling Proteins Prevent Lateral Displacement of Microtubules during Cellulose Synthesis in Arabidopsis. *Developmental Cell*, 38(3):305–315, 2016.

[212] Martin Schwalbe, Jacek Biernat, Stefan Bibow, Valéry Ozenne, Malene R. Jensen, Harindranath Kadavath, Martin Blackledge, Eckhard Mandelkow, and Markus Zweckstetter. Phosphorylation of human tau protein by microtubule affinity-regulating kinase 2. *Biochemistry*, 52(50):9068–9079, 2013.

[213] Bruce L. Goode, Miu Chau, Paul E. Denis, and Stuart C. Feinstein. Structural and functional differences between 3-repeat and 4-repeat tau isoforms: Implications for normal tau function and the onset of neurodegenerative disease. *Journal of Biological Chemistry*, 275(49):38182–38189, 2000.

[214] Caroline Fauquant, Virginie Redeker, Isabelle Landrieu, Jean Michel Wieruszeski, Dries Verdegem, Olivier Laprévote, Guy Lippens, Benoît Gigant, and Marcel Knossow. Systematic identification of tubulin-interacting fragments of the microtubule-associated protein Tau leads to a highly efficient promoter of microtubule assembly. *Journal of Biological Chemistry*, 286(38):33358–33368, 2011.

[215] Isabelle Landrieu, Caroline Fauquant, Pascale Barbier, Isabelle Huvent, Jean-michel Wieruszeski, Marcel Knossow, and Guy Lippens. Mechanism of Tau-Promoted Microtubule Assembly As Probed by NMR Spectroscopy. *Journal of the American Chemical Society*, 136(36):1261512623, 2014.

[216] Jawdat Al-Bassam, Rachel S. Ozer, Daniel Safer, Shelley Halpain, and Ronald A. Milligan. MAP2 and tau bind longitudinally along the outer ridges of microtubule protofilaments. *Journal of Cell Biology*, 157(7):1187–1196, 2002.

[217] Sofia Lopes, João Vaz-Silva, Vitor Pinto, Christina Dalla, Nikolaos Kokras, Benedikt Bedenk, Natalie Mack, Michael Czisch, Osborne F. X. Almeida, Nuno Sousa, and Ioannis Sotiropoulos. Tau protein is essential for stress-induced brain pathology. *Proceedings of the National Academy of Sciences*, 113(26):3755–3763, 2016.

[218] Alejandro Ibáñez-Salazar, Bernardo Bañuelos-Hernández, Ildefonso Rodríguez-Leyva, Erika Chi-Ahumada, Elizabeth Monreal-Escalante, María E. Jiménez-Capdeville, and Sergio Rosales-Mendoza. Oxidative stress modifies the levels and phosphorylation state of tau protein in human fibroblasts. *Frontiers in Neuroscience*, 11(SEP), 2017.

[219] Elka R. Georgieva, Shifeng Xiao, Peter P. Borbat, Jack H. Freed, and David Eliezer. Tau binds to lipid membrane surfaces via short amphipathic helices located in its microtubule-binding repeats. *Biophysical Journal*, 107(6):1441–1452, 2014.

[220] M. Goedert, R. Jakes, M. G. Spillantini, M. Hasegawa, M. J. Smith, and R. A. Crowther. Assembly of microtubule-associated protein tau into Alzheimer-like filaments induced by sulphated glycosaminoglycans. *Nature*, 383(6600):550–553, 1996.

[221] Yunior Cabrales Fontela, Harindranath Kadavath, Jacek Biernat, Dietmar Riedel, Eckhard Mandelkow, and Markus Zweckstetter. Multivalent cross-linking of actin filaments and microtubules through the microtubule-associated protein Tau. *Nature Communications*, 8(1), 2017.

[222] C. Hugh Reynolds, Claire J. Garwood, Selina Wray, Caroline Price, Stuart Kellie, Timothy Perera, Marketa Zvelebil, Alice Yang, Paul W. Sheppard, Ian M. Varndell, Diane P. Hanger, and Brian H. Anderton. Phosphorylation regulates tau interactions with Src homology 3 domains of phosphatidylinositol 3-kinase, phospholipase Cγ1, Grb2, and Src family kinases. *Journal of Biological Chemistry*, 283(26):18177–18186, 2008.

[223] John Gardiner. The evolution and diversification of plant microtubule-associated proteins. *Plant Journal*, 75(2):219–229, 2013.

[224] John Gardiner, Robyn Overall, and Jan Marc. Distant plant homologues: Don't throw out the baby. *Trends in Plant Science*, 17(3):126–128, 2012.

[225] Peter Nick, Anne-Marie -M Lambert, and Marylin Vantard. A microtubule-associated protein in maize is expressed during phytochrome-induced cell elongation. *The Plant Journal*, 8(6):835–844, 1995.

[226] Marylin Vantard, Paul Schellenbaum, Anne Marie Lambert, and Arlette Fellous. Characterization of Maize Microtubule-Associated Proteins, One of Which Is Immunologically Related to Tau. *Biochemistry*, 30(38):9334–9340, 1991.

[227] J. Marc, Cheryl L Granger, Jennifer Brincat, Deborah D Fisher, Teh-Hui Kao, Andrew G Mccubbin, and Richard J Cyr. A GFPMAP4 Reporter Gene for Visualizing Cortical Microtubule Rearrangements in Living Epidermal Cells. *the Plant Cell Online*, 10(11):1927–1940, 1998.

[228] Jacqueline Parkin and Bryony Cohen. An overview of the immune system. *Lancet - Immunology*, 357:1777–1789, 2001.

[229] Sky W. Brubaker, Kevin S. Bonham, Ivan Zanoni, and Jonathan C. Kagan. *Innate Immune Pattern Recognition: A Cell Biological Perspective*, volume 33. 2015.

[230] B. Brett Finlay and Grant McFadden. Anti-immunology: Evasion of the host immune system by bacterial and viral pathogens. *Cell*, 124(4):767–782, 2006.

[231] Rachael Clark and Thomas Kupper. Old meets new: The interaction between innate and adaptive immunity. *Journal of Investigative Dermatology*, 125(4):629–637, 2005.

[232] Shizuo Akira, Satoshi Uematsu, and Osamu Takeuchi. Pathogen recognition and innate immunity. *Cell*, 124(4):783–801, 2006.

[233] Roman Barbalat, Sarah E. Ewald, Maria L. Mouchess, and Gregory M. Barton. Nucleic Acid Recognition by the Innate Immune System. *Annual Review of Immunology*, 29(1):185–214, 2011.

[234] Vojo Deretic, Tatsuya Saitoh, and Shizuo Akira. Autophagy in infection, inflammation and immunity. *Nature Reviews Immunology*, 13(10):722–737, 2013.

[235] Rebecca A. Drummond and Gordon D. Brown. The role of Dectin-1 in the host defence against fungal infections. *Current Opinion in Microbiology*, 14(4):392–399, 2011.

[236] Thirumala Devi Kanneganti, Mohamed Lamkanfi, and Gabriel Núñez. Intracellular NOD-like Receptors in Host Defense and Disease. *Immunity*, 27(4):549–559, 2007.

[237] Jonathan A. Harton, Michael W. Linhoff, Jinghua Zhang, and Jenny P.-Y. Ting. Cutting Edge: CATERPILLER: A Large Family of Mammalian Genes Containing CARD, Pyrin, Nucleotide-Binding, and Leucine-Rich Repeat Domains. *The Journal of Immunology*, 169(8):4088–4093, 2002.

[238] Tsuyoshi Tanabe, Mathias Chamaillard, Yasunori Ogura, Li Zhu, Su Qiu, Junya Masumoto, Partho Ghosh, Anthony Moran, Martina M. Predergast, Gerard Tromp, Charlene J. Williams, Naohiro Inohara, and Gabriel Núñez. Regulatory regions and critical residues of NOD2 involved in muramyl dipeptide recognition. *EMBO Journal*, 23(7):1587–1597, 2004.

[239] Stephen E. Girardin, Ivo G. Boneca, Jérôme Viala, Mathias Chamaillard, Agnès Labigne, Gilles Thomas, Dana J. Philpott, and Philippe J. Sansonetti. Nod2 is a general sensor of peptidoglycan through muramyl dipeptide (MDP) detection. *Journal of Biological Chemistry*, 278(11):8869–8872, 2003.

[240] Stephen E. Girardin, Ivo G. Boneca, Leticia A.M. Carneiro, Aude Antignac, Muguette Jéhanno, Jérôme Viala, Karsten Tedin, Muhamed Kheir Taha, Agnès Labigne, Ulrich Zähringer, Anthony J. Coyle, Peter S. DiStefano, John Bertin, Philippe J. Sansonetti, and Dana J. Philpott. Nod1 detects a unique muropeptide from gram-negative bacterial peptidoglycan. *Science*, 300(5625):1584–1587, 2003.

[241] Norihiro Nakamura, Jennie R. Lill, Qui Phung, Zhaoshi Jiang, Corey Bakalarski, Ann De Mazière, Judith Klumperman, Megan Schlatter, Lélia Delamarre, and Ira Mellman. Endosomes are specialized platforms for bacterial sensing and NOD2 signalling. *Nature*, 509(7499):240–244, 2014.

[242] Aaron T. Irving, Hitomi Mimuro, Thomas A. Kufer, Camden Lo, Richard Wheeler, Lorinda J. Turner, Belinda J. Thomas, Christian Malosse, Michael P. Gantier, Linda N. Casillas, Bartholomew J. Votta, John Bertin, Ivo G. Boneca, Chihiro Sasakawa, Dana J. Philpott, Richard L. Ferrero, and Maria Kaparakis-Liaskos. The immune receptor NOD1 and kinase RIP2 interact with bacterial peptidoglycan on early endosomes to promote autophagy and inflammatory signaling. *Cell Host and Microbe*, 15(5):623–635, 2014.

[243] Naohiro Inohara, Takeyoshi Koseki, Luis Del Peso, Yuanming Hu, Christina Yee, Shu Chen, Roberto Carrio, Jesus Merino, Ding Liu, Jian Ni, and Gabriel Núñez. Nod1, an Apaf-1-like activator of caspase-9 and nuclear factor-κB. *Journal of Biological Chemistry*, 274(21):14560–14567, 1999.

[244] Yasunori Ogura, Naohiro Inohara, Adalberto Benito, Felicia F. Chen, Shoji Yamaoka, and Gabriel Núñez. Nod2, a Nod1/Apaf-1 Family Member That Is Restricted to Monocytes and Activates NF-κB. *Journal of Biological Chemistry*, 276(7):4812–4818, 2001.

[245] Erika Pellegrini, Luca Signor, Saurabh Singh, Elisabetta Boeri Erba, and Stephen Cusack. Structures of the inactive and active states of RIP2 kinase inform on the mechanism of activation. *PLoS ONE*, 12(5), 2017.

[246] Chiara Nembrini, Jan Kisielow, Abdijapar T. Shamshiev, Luigi Tortola, Anthony J. Coyle, Manfred Kopf, and Benjamin J. Marsland. The kinase-activity of Rip2 determines its stability and consequently Nod1 - and Nod2-mediated immune responses. *Journal of Biological Chemistry*, 284(29):19183–19188, 2009.

[247] Stephen E. Girardin, Régis Tournebize, Maria Mavris, Anne Laure Page, Xiaoxia Li, George R. Stark, John Bertin, Peter S. Distefano, Moshe Yaniv, Philippe J. Sansonetti, and Dana J. Philpott. CARD4/Nod1 mediates NF-B and JNK activation by invasive Shigella flexneri. *EMBO Reports*, 2(8):736–742, 2001.

[248] Koichi Kobayashi, Naohiro Inohara, Lorraine D. Hernandez, Jorge E. Galán, Gabriel Nüñez, Charles A. Janeway, Ruslan Medzhitov, and Richard A. Flavell. RICK/Rip2/CARDIAK mediates signalling for receptors of the innate and adaptive immune systems. *Nature*, 416(6877):194–199, 2002.

[249] Jong-Hwan Park, Yun-Gi Kim, Christine McDonald, Thirumala-Devi Kanneganti, Mizuho Hasegawa, Mathilde Body-Malapel, Naohiro Inohara, and Gabriel Nunez. RICK/RIP2 Mediates Innate Immune Responses Induced through Nod1 and Nod2 but Not TLRs. *The Journal of Immunology*, 178(4):2380–2386, 2007.

[250] Yen Michael S. Hsu, Yongliang Zhang, Yun You, Donghai Wang, Hongxiu Li, Omar Duramad, Xiao Feng Qin, Chen Dong, and Xin Lin. The adaptor protein CARD9 is required for innate immune responses to intracellular pathogens. *Nature Immunology*, 8(2):198–205, 2007.

[251] Craig R. Homer, Amrita Kabi, Noemí Marina-Garci, Arun Sreekumar, Alexey I. Nesvizhskii, Kourtney P. Nickerson, Arul M. Chinnaiyan, Gabriel Nuñez, and Christine McDonald. A dual role for receptor-interacting protein kinase 2 (RIP2) kinase activity in nucleotide-binding oligomerization domain 2 (NOD2)-dependent autophagy. *Journal of Biological Chemistry*, 287(30):25565–25576, 2012.

[252] F. Humphries, S. Yang, B. Wang, and P. N. Moynagh. RIP kinases: Key decision makers in cell death and innate immunity. *Cell Death and Differentiation*, 22(2):225–236, 2015.

[253] Jörg H. Fritz, Lionel Le Bourhis, Gernot Sellge, Joao Gamelas Magalhaes, Hafida Fsihi, Thomas A. Kufer, Cathy Collins, Jérôme Viala, Richard L. Ferrero, Stephen E. Girardin, and Dana J. Philpott. Nod1-Mediated Innate Immune Recognition of Peptidoglycan Contributes to the Onset of Adaptive Immunity. *Immunity*, 26(4):445–459, 2007.

[254] Hyun Ho Park, Emmanuelle Logette, Stefan Raunser, Solange Cuenin, Thomas Walz, Jurg Tschopp, and Hao Wu. Death Domain Assembly Mechanism Revealed by Crystal Structure of the Oligomeric PIDDosome Core Complex. *Cell*, 128(3):533–546, 2007.

[255] Su Chang Lin, Yu Chih Lo, and Hao Wu. Helical assembly in the MyD88-IRAK4-IRAK2 complex in TLR/IL-1R signalling. *Nature*, 465(7300):885–890, 2010.

[256] Hao Wu and Monika Fuxreiter. The Structure and Dynamics of Higher-Order Assemblies: Amyloids, Signalosomes, and Granules. *Cell*, 165(5):1055–1066, 2016.

[257] M. Bentele, I. Lavrik, M. Ulrich, S. Stößer, D. W. Heermann, H. Kalthoff, P. H. Krammer, and R. Eils. Mathematical modeling reveals threshold mechanism i n CD95-induced apoptosis. *Journal of Cell Biology*, 166(6):839–851, 2004.

[258] Ali Asghar Tehrani, Sirous Sadeghian, Javad Javanbakht, Abbas Imani, and Shabnam Sadeghzadeh. Studies of clinical and histopathological lesions resulting from Psoroptes cuniculli mange in domestic rabbits. *Biochemical and Cellular Archives*, 11(1):221–226, 2011.

[259] Hyun Ho Park, Yu-Chih Lo, Su-Chang Lin, Liwei Wang, Jin Kuk Yang, and Hao Wu. The Death Domain Superfamily in Intracellular Signaling of Apoptosis and Inflammation. *Annual Review of Immunology*, 25(1):561–586, 2007.

[260] John C. Reed, Kutbuddin S. Doctor, and Adam Godzik. The Domains of Apoptosis: A Genomics Perspective. *Science Signaling*, 2004(239):re9, 2004.

[261] Alvin Lu, Venkat Giri Magupalli, Jianbin Ruan, Qian Yin, Maninjay K. Atianand, Matthijn R. Vos, Gunnar F. Schröder, Katherine A. Fitzgerald, Hao Wu, and Edward H. Egelman. Unified polymerization mechanism for the assembly of ASC-dependent inflammasomes. *Cell*, 156(6):1193–1206, 2014.

[262] Hui Xu, Xiaojing He, Hui Zheng, Lily J. Huang, Fajian Hou, Zhiheng Yu, Michael Jason de la Cruz, Brian Borkowski, Xuewu Zhang, Zhijian J. Chen, and Qiu Xing Jiang. Structural basis for the prion-like MAVS filaments in antiviral innate immunity. *eLife*, 2014(3), 2014.

[263] Liron David, Yang Li, Jun Ma, Ethan Garner, Xinzheng Zhang, and Hao Wu. Assembly mechanism of the CARMA1–BCL10–MALT1–TRAF6 signalosome. *Proceedings of the National Academy of Sciences*, 115(7):201721967, 2018.

[264] Suman Paul, Anuj K. Kashyap, Wei Jia, You Wen He, and Brian C. Schaefer. Selective Autophagy of the Adaptor Protein Bcl10 Modulates T Cell Receptor Activation of NF-κB. *Immunity*, 36(6):947–958, 2012.

[265] Till Strowig, Jorge Henao-Mejia, Eran Elinav, and Richard Flavell. Inflammasomes in health and disease. *Nature*, 481(7381):278–286, 2012.

[266] Luigi Franchi, Raul Muñoz-Planillo, and Gabriel Núñez. Sensing and reacting to microbes through the inflammasomes. *Nature Immunology*, 13(4):325–332, 2012.

[267] Isabelle Touitou, Suzanne Lesage, Michael McDermott, Laurence Cuisset, Hal Hoffman, Catherine Dode, Nitza Shoham, Ebun Aganna, Jean Pierre Hugot, Carol Wise, Hans Waterham, Denis Pugnere, Jacques Demaille, and Cyril Sarrauste De Menthiere. Infevers: An evolving mutation database for auto-inflammatory syndromes. *Human Mutation*, 24(3):194–198, 2004.

[268] Hongnga T. Le and Jonathan A. Harton. Pyrin- and CARD-only proteins as regulators of NLR functions. *Frontiers in Immunology*, 4(SEP), 2013.

[269] James B. Johnston, John W. Barrett, Steven H. Nazarian, Megan Goodwin, Dan Ricuttio, Gen Wang, and Grant McFadden. A poxvirus-encoded pyrin domain protein interacts with ASC-1 to inhibit host inflammatory and apoptotic responses to infection. *Immunity*, 23(6):587–598, 2005.

[270] Jenny P.Y. Ting, Ruth C. Lovering, Emad S. Alnemri, John Bertin, Jeremy M. Boss, Beckley K. Davis, Richard A. Flavell, Stephen E. Girardin, Adam Godzik, Jonathan A. Harton, Hal M. Hoffman, Jean Pierre Hugot, Naohiro Inohara, Alex MacKenzie, Lois J. Maltais, Gabriel Nunez, Yasunori Ogura, Luc A. Otten, Dana Philpott, John C. Reed, Walter Reith, Stefan Schreiber, Viktor Steimle, and Peter A. Ward. The NLR Gene Family: A Standard Nomenclature. *Immunity*, 28(3):285–287, 2008.

[271] Veronica Fridh and Katrin Rittinger. The tandem cards of NOD2: Intramolecular interactions and recognition of RIP2. *PLoS ONE*, 7(3), 2012.

[272] Roland N. Wagner, Martina Proell, Thomas A. Kufer, and Robert Schwarzenbacher. Evaluation of Nod-like receptor (NLR) effector domain interactions. *PLoS ONE*, 4(4), 2009.

[273] Sakiko Maekawa, Umeharu Ohto, Takuma Shibata, Kensuke Miyake, and Toshiyuki Shimizu. Crystal structure of NOD2 and its implications in human disease. *Nature Communications*, 7, 2016.

[274] Zhi Lin, Jason Y. Tann, Eddy T.H. Goh, Claire Kelly, Kim Buay Lim, Jian Fang Gao, and Carlos F. Ibanez. Structural basis of death domain signaling in the p75 neurotrophin receptor. *eLife*, 4, 2015.

[275] Janice C. Jun, Fabio Cominelli, and Derek W. Abbott. RIP2 activity in inflammatory disease and implications for novel therapeutics. *Journal of Leukocyte Biology*, 94(5):927–932, 2013.

[276] Nobuo Kanazawa, Ikuo Okafuji, Naotomo Kambe, Ryuta Nishikomori, Mami Nakata-Hizume, Sonoko Nagai, Akihiko Fuji, Takenosuke Yuasa, Akira Manki, Yoshihiko Sakurai, Mitsuru Nakajima, Hiroko Kobayashi, Ikuma Fujiwara, Hiroyuki Tsutsumi, Atsushi Utani, Chikako Nishigori, Toshio Heike, Tatsutoshi Nakahata, and Yoshiki Miyachi. Early-onset sarcoidosis and CARD15 mutations with constitutive nuclear factor-κB activation: Common genetic etiology with Blau syndrome. *Blood*, 105(3):1195–1197, 2005.

[277] Corinne Miceli-Richard, Suzanne Lesage, Michel Rybojad, Anne Marie Prieur, Sylvie Manouvrier-Hanu, Renate Häfner, Mathias Chamaillard, Habib Zouali, Gilles Thomas, and Jean Pierre Hugot. CARD15 mutations in Blau syndrome. *Nature Genetics*, 29(1):19–20, 2001.

[278] Jean Pierre Hugot. CARD15/NOD2 mutations in Crohn's disease. *Annals of the New York Academy of Sciences*, 1072:9–18, 2006.

[279] Joseph P. Boyle, Rhiannon Parkhouse, and Tom P. Monie. Insights into the molecular basis of the NOD2 signalling pathway. *Open Biology*, 4(12):140178–140178, 2014.

[280] Joao G. Magalhaes, Jooeun Lee, Kaoru Geddes, Stephen Rubino, Dana J. Philpott, and Stephen E. Girardin. Essential role of Rip2 in the modulation of innate and adaptive immunity triggered by Nod1 and Nod2 ligands. *European Journal of Immunology*, 41(5):1445–1455, 2011.

[281] Andrew J. Nieuwkoop, W. Trent Franks, Kristina Rehbein, Anne Diehl, Ümit Akbey, Frank Engelke, Lyndon Emsley, Guido Pintacuda, and Hartmut Oschkinat. Sensitivity and resolution of proton detected spectra of a deuterated protein at 40 and 60 kHz magic-angle-spinning. *Journal of Biomolecular NMR*, 61(2):161–171, 2015.

[282] Joren Sebastian Retel. *Structure Determination of Outer Membrane Protein G in Native Lipids by Solid-State NMR Spectroscopy*. PhD thesis, Free University Berlin, 2016.

[283] Jonathan Marley, Min Lu, and Clay Bracken. A method for efficient isotopic labeling of recombinant proteins. *Journal of Biomolecular NMR*, 20(1):71–75, 2001.

[284] David M. LeMaster and Diana M. Kushlan. Dynamical mapping of E. coli thioredoxin via 13C NMR relaxation analysis. *Journal of the American Chemical Society*, 118(39):9255–9264, 1996.

[285] Emeline Barbet-Massin, Andrew J. Pell, Joren S. Retel, Loren B. Andreas, Kristaps Jaudzems, W. Trent Franks, Andrew J. Nieuwkoop, Matthias Hiller, Victoria Higman, Paul Guerry, Andrea Bertarello, Michael J. Knight, Michele Felletti, Tanguy Le Marchand, Svetlana Kotelovica, Inara Akopjana, Kaspars Tars, Monica Stoppini, Vittorio Bellotti, Martino Bolognesi, Stefano Ricagno, James J. Chou, Robert G. Griffin, Hartmut Oschkinat, Anne Lesage, Lyndon Emsley, Torsten Herrmann, and Guido Pintacuda. Rapid proton-detected NMR assignment for proteins with fast magic angle spinning. *Journal of the American Chemical Society*, 136(35):12489–12497, 2014.

[286] Erika Pellegrini, Ambroise Desfosses, Arndt Wallmann, Wiebke Manuela Schulze, Kristina Rehbein, Philippe Mas, Luca Signor, Stephanie Gaudon, Grasilda Zenkeviciute, Michael Hons, Helene Malet, Irina Gutsche, Carsten Sachse, Guy Schoehn, Hartmut Oschkinat, and Stephen Cusack. RIP2 filament formation is required for NOD2 dependent NF-κB signalling. *Nature Communications*, 9(1), 2018.

[287] Jitendra Maharana, Sukanta Kumar Pradhan, and Sachinandan De. NOD1CARDmight be using multiple interfaces for RIP2-mediated CARD-CARD interaction: Insights from molecular dynamics simulation. *PLoS ONE*, 12(1), 2017.

[288] Sophie Mayle, Joseph P. Boyle, Eiki Sekine, Birte Zurek, Thomas A. Kufer, and Tom P. Monie. Engagement of nucleotide-binding oligomerization domain-containing protein 1 (NOD1) by Receptor-interacting Protein 2 (RIP2) is insufficient for signal transduction. *Journal of Biological Chemistry*, 289(33):22900–22914, 2014.

[289] Qin Gong, Ziqi Long, Franklin L. Zhong, Daniel Eng Thiam Teo, Yibo Jin, Zhan Yin, Zhao Zhi Boo, Yaming Zhang, Jiawen Zhang, Renliang Yang, Shashi Bhushan, Bruno Reversade, Zongli Li, and Bin Wu. Structural basis of RIP2 activation and signaling. *Nature Communications*, 9(1), 2018.

[290] Jixi Li, Thomas McQuade, Ansgar B. Siemer, Johanna Napetschnig, Kenta Moriwaki, Yu Shan Hsiao, Ermelinda Damko, David Moquin, Thomas Walz, Ann McDermott, Francis Ka Ming Chan, and Hao Wu. The RIP1/RIP3 necrosome forms a functional amyloid signaling complex required for programmed necrosis. *Cell*, 150(2):339–350, 2012.

[291] Alvin Lu, Yang Li, Florian I. Schmidt, Qian Yin, Shuobing Chen, Tian Min Fu, Alexander B. Tong, Hidde L. Ploegh, Youdong Mao, and Hao Wu. Molecular basis of caspase-1 polymerization and its inhibition by a new capping mechanism. *Nature Structural and Molecular Biology*, 23(5):416–425, 2016.

[292] Justine T. Tigno-Aranjuez, John M. Asara, and Derek W. Abbott. Inhibition of RIP2's tyrosine kinase activity limits NOD2-driven cytokine responses. *Genes and Development*, 24(23):2666–2677, 2010.

[293] Bin Wu, Alys Peisley, David Tetrault, Zongli Li, Edward H. Egelman, Katharine E. Magor, Thomas Walz, Pawel A. Penczek, and Sun Hur. Molecular imprinting as a signal-activation mechanism of the viral RNA sensor RIG-I. *Molecular Cell*, 55(4):511–523, 2014.

[294] Tatiana Goncharov, Stefanie Hedayati, Melinda M. Mulvihill, Anita Izrael-Tomasevic, Kerry Zobel, Surinder Jeet, Anna V. Fedorova, Celine Eidenschenk, Jason DeVoss, Kebing Yu, Andrey S. Shaw, Donald S. Kirkpatrick, Wayne J. Fairbrother, Kurt Deshayes, and Domagoj Vucic. Disruption of XIAP-RIP2 Association Blocks NOD2-Mediated Inflammatory Signaling. *Molecular Cell*, 69(4):648–663, 2018.

Appendix A

Chemical Shifts

CC1ΔC223

		H	N	CO	CA	CB			
1	Met	8.43	120.47	175.81	55.34	32.45			
2	His	-	-	174.64	55.68	30.50			
3	Ala	8.17	125.51	177.44	52.06	19.16			
4	Lys	8.34	121.20	176.76	56.22	32.92			
5	Thr	8.12	114.93	174.32	61.34	69.73			
6	Asp	8.28	122.48	176.35	54.45	40.86			
7	Ser	8.12	115.63	174.60	58.54	63.50			
8	Glu	8.26	122.68	176.63	56.45	30.03			
9	Val	8.05	121.10	176.61	62.63	32.41			
10	Thr	8.09	117.77	174.61	62.01	69.49			
11	Ser	8.15	118.16	174.54	58.18	63.43			
12	Leu	8.13	124.32	177.29	55.14	42.04			
13	Ala	8.06	124.40	177.63	52.46	18.81			
14	Ala	8.06	122.69	177.70	52.41	18.93			
15	Ser	8.02	114.30	174.05	57.88	63.64			
16	Ser	8.08	118.46	172.57	56.18	63.10			
17	Pro	-	-	176.54	63.10	31.91			
18	Ala	8.21	123.93	177.63	52.27	18.81			
19	Arg	8.14	119.99	175.96	55.51	30.71			
20	Ser	8.20	118.49	172.61	55.96	63.09			
21	Pro	-	-	176.53	62.94	31.98			
22	Arg	8.25	121.38	176.01	55.84	30.62			
23	Arg	8.21	123.77	173.93	53.56	30.15			
24	Pro	-	-	176.18	62.74	31.99			
25	Val	7.97	119.98	175.36	62.08	32.71			
26	Tyr	7.94	123.27	174.72	57.03	39.02			
27	Tyr	7.92	122.85	174.72	57.12	39.07			
28	Val	7.88	123.29	175.24	61.70	32.94			
29	Gln	8.27	124.70	175.45	55.39	29.42	112.78:Ne2	6.74:He2a	7.42:He2b
30	Ser	8.32	119.43	172.56	56.10	62.99			
31	Pro	-	-	176.79	63.13	32.02			
32	Ser	8.26	116.03	174.65	58.06	63.53			
33	Arg	8.28	123.22	175.94	56.04	30.55			
34	Asp	8.22	121.11	176.13	54.06	41.16			
35	Ser	8.08	116.12	174.53	58.34	63.51			
36	His	-	-	174.88	55.96	29.71			
37	Asp	8.15	121.41	176.64	54.45	40.93			
38	Gly	8.26	109.39	174.20	45.15	-			
39	Glu	8.08	120.46	176.65	56.34	30.09			
40	Lys	8.24	122.03	176.70	56.13	32.68			
41	Thr	8.01	115.17	174.32	61.57	69.70			
42	Ala	8.27	126.42	177.85	52.50	19.07			

43	Thr	8.02	112.95	174.41	61.58	69.59			
44	Ser	8.04	117.68	173.85	57.90	63.65			
45	Phe	8.09	122.08	175.25	57.74	39.48			
47	Ser	-	-	173.93	57.98	63.63			
48	Thr	8.09	118.68	172.53	59.62	69.53			
49	Pro	-	-	176.48	62.97	32.03			
50	Val	8.16	121.46	176.00	62.05	32.53			
51	Leu	8.24	126.71	176.74	54.43	42.24			
52	Ser	8.22	118.28	172.67	55.90	63.07			
53	Pro	-	-	176.95	63.20	31.88			
54	Met	8.30	120.05	176.68	55.42	32.44			
55	Gly	8.24	109.50	173.56	44.95	-			
56	Ser	8.03	116.77	171.84	56.26	62.94			
58	Pro	-	-	176.60	62.79	31.90			
59	His	8.20	119.03	175.34	56.01	30.40			
63	Ser	-	-	-	58.54	-			
64	Met	8.18	121.46	176.67	55.52	32.46			
65	Gly	8.23	110.13	173.63	44.93	-			
68	Ser	-	-	174.62	58.27	63.64			
69	Arg	8.45	122.96	176.38	56.19	30.50			
70	Glu	8.31	121.37	176.55	56.54	30.07			
71	Ser	8.24	116.71	174.83	58.25	63.65			
75	Arg	-	-	176.02	56.38	30.29			
76	Phe	8.07	120.43	175.86	57.29	39.23			
77	Ser	8.11	117.63	174.70	58.27	63.62			
78	Gly	7.82	110.45	173.90	45.06	-			
79	Ser	8.04	115.46	174.32	58.08	63.63			
80	Leu	8.12	123.88	176.96	54.81	42.10			
81	Lys	8.19	123.55	174.43	53.82	32.13			
82	Pro	-	-	177.48	63.36	32.13			
83	Gly	8.44	109.79	174.17	45.00	-			
84	Ser	8.00	115.45	174.28	58.19	63.42			
85	Arg	-	-	176.03	55.89	30.69			
86	Lys	8.25	123.21	176.03	55.96	32.95			
87	Val	8.09	122.01	175.34	61.72	32.83			
88	Asn	8.56	124.34	173.71	50.61	38.73	113.34:Nd2	6.85:Hd2a	7.54:Hd2b
89	Pro	-	-	176.64	63.46	32.05			
90	Asn	8.27	117.31	174.99	53.04	38.49	113.55:Nd2	6.83:Hd2a	7.52:Hd2b
91	Asp	7.88	120.54	176.92	54.23	40.88			
92	Gly	8.33	109.89	174.66	45.38	-			
93	Ser	8.11	115.90	174.70	58.68	63.57			
94	Lys	-	-	176.40	56.21	32.53			
95	Arg	8.08	121.77	176.13	55.78	30.64			
96	Lys	-	-	176.85	56.58	32.86			
97	Gly	8.32	110.22	173.69	44.88	-			
98	His	8.15	119.04	175.88	56.00	30.51			
99	Gly	8.44	110.51	174.61	45.26	-			
100	Gly	8.27	109.12	174.18	45.06	-			
101	Glu	8.27	120.55	176.63	56.54	29.98			
102	Lys	8.24	121.85	176.27	56.15	32.60			
103	Gln	8.17	120.84	175.54	55.67	29.13	112.61:Ne2	6.71:He2a	7.32:He2b
104	Trp	8.02	122.29	175.85	57.22	29.45	129.38:Ne1	9.98:He1	
105	Lys	7.83	122.78	175.81	55.93	33.24			
106	Glu	8.15	121.59	176.17	56.50	29.89			
107	Cys	8.14	119.68	173.87	58.16	28.03			
108	Ala	8.21	126.28	177.29	52.29	19.11			
109	Val	7.97	119.95	175.94	62.14	32.59			
110	Ile	8.12	125.31	176.03	60.72	38.43			
111	Glu	8.38	125.53	176.21	56.30	30.20			
112	Glu	8.29	122.13	176.32	56.36	30.29			
113	Glu	8.37	122.14	176.93	56.63	30.25			
114	Gly	8.33	109.67	173.83	45.13	-			
115	Leu	7.92	121.29	177.24	54.83	42.15			
116	Leu	8.15	122.87	176.90	54.67	42.20			
117	Asp	8.18	121.40	175.72	54.00	41.21			
118	Asp	8.19	121.40	176.56	53.94	41.02			
119	Gly	8.21	109.38	173.05	45.05	-			

ATSH3

		H	N	CA	CB				
1	Gly	–	–	43.27	–				
2	Asn	8.59	118.73	53.19	38.44	112.90:Nd2	6.79:Hd2a	7.46:Hd2b	
3	Asp	8.36	120.44	54.60	40.86				
4	Ser	8.16	114.77	58.19	63.92				
5	Tyr	7.77	122.22	55.27	37.59				
6	Phe	7.97	114.94	55.49	41.08				
7	Leu	–	–	54.15	44.15				
8	Ala	9.29	127.57	50.60	23.80				
9	Lys	8.34	121.79	54.02	36.04				
10	Val	8.78	125.94	63.60	31.72				
11	Val	8.70	122.20	60.82	32.61				
12	His	7.47	123.44	52.02	30.93				
13	Pro	–	–	62.28	32.53				
14	Phe	8.35	118.86	57.06	43.46				
15	Asp	8.15	129.02	52.11	41.53				
16	Ala	8.21	126.38	52.84	20.24				
17	Gln	8.89	119.60	55.31	31.34	113.22:Ne2	6.71:He2a	7.36:He2b	33.67:Cg
18	Ala	7.56	123.66	49.48	19.29				
19	Pro	–	–	64.02	31.63				
20	Gly	8.71	111.12	45.13	–				
21	Glu	7.45	118.73	55.59	32.25				
22	Leu	9.06	126.85	53.27	46.40				
23	Ser	8.13	119.83	59.51	63.68				
24	Leu	9.12	119.58	53.63	47.19				
25	Ala	–	–	49.86	20.26				
26	Val	8.03	119.36	64.30	31.51				
27	Asp	8.04	117.20	57.39	38.45				
28	Asp	7.18	119.37	53.85	41.64				
29	Tyr	8.37	116.97	57.29	40.55				
30	Val	8.80	116.83	59.02	35.32				
31	Ile	7.91	123.32	59.82	38.52				
32	Val	8.94	128.46	63.26	30.20				
33	Arg	9.02	125.07	56.63	31.96				
34	Gln	7.43	114.78	55.11	32.22	112.69:Ne2	6.87:He2a	7.52:He2b	33.64:Cg
35	Val	8.62	125.05	61.77	32.90				
36	Ala	8.63	128.33	52.69	20.95				
37	Gly	8.81	107.79	45.62	–				
38	Thr	7.03	106.16	60.56	70.18				
39	Gly	7.93	108.23	44.89	–				
40	Trp	7.18	122.54	56.71	31.61				
41	Ser	9.14	117.08	56.51	67.25				
42	Glu	8.27	124.21	53.22	30.74				
43	Gly	8.69	113.13	46.11	–				
44	Glu	8.68	115.61	54.25	33.71				
45	Tyr	8.95	124.37	56.90	41.73				
46	Lys	9.02	126.05	57.03	30.35				
47	Gly	8.60	104.38	45.23	–				
48	Lys	7.80	122.21	54.77	34.72				
49	Ala	8.20	122.93	50.27	22.55				
50	Gly	8.45	107.56	45.66	–				
51	Trp	8.79	119.29	56.77	31.71				
52	Phe	8.96	117.88	54.86	38.20				
53	Pro	–	–	62.42	29.82				
54	Ser	8.33	121.76	61.70	63.14				
55	Ala	8.08	116.80	52.51	17.78				
56	Tyr	7.61	117.21	55.67	35.07				
57	Val	7.38	109.84	57.81	34.37				
58	Glu	8.92	120.06	54.20	33.34				
59	Lys	9.09	129.84	57.88	32.73				
60	Gln	8.70	125.25	54.62	30.07	115.29:Ne2	7.12:He2a	7.32:He2b	34.28:Cg
61	Glu	8.52	123.83	55.97	30.58				
62	Lys	8.34	123.01	56.10	33.04				
63	Ala	7.94	131.76	53.59	19.93				

RIP2CARD (proton detection)

		H	N	CO	CA	CB
440	Ile	-	-	173.88	-	-
441	Gln	7.58	117.10	175.76	56.01	24.91
442	Ser	8.07	113.32	172.39	57.96	60.35
443	Lys	7.46	119.72	173.10	50.53	27.41
444	Arg	7.20	122.69	173.26	57.73	27.87
445	Glu	8.06	112.45	174.23	56.43	27.27
446	Asp	7.21	116.65	174.59	53.58	38.23
447	Ile	8.49	120.31	174.81	63.27	34.72
451	Met	-	-	173.00	-	-
452	Thr	9.02	118.80	171.85	58.46	67.89
453	Glu	9.31	120.24	174.60	57.30	26.43
454	Ala	8.60	116.91	176.20	51.86	15.96
455	Cys	7.51	122.61	173.81	59.55	-
456	Leu	8.29	125.61	174.99	55.24	37.21
457	Asn	8.60	118.37	174.17	52.82	34.50
458	Gln	8.66	119.75	175.62	55.98	26.91
459	Ser	8.20	117.02	172.14	60.85	59.66
460	Leu	7.87	120.66	175.10	55.23	38.13
461	Asp	8.66	118.57	175.24	55.14	37.94
462	Ala	8.16	123.45	176.99	51.57	15.97
463	Leu	8.06	120.01	176.54	54.94	39.19
464	Leu	8.72	121.76	178.06	54.85	39.48
465	Ser	8.36	117.19	172.42	58.31	60.94
466	Arg	7.04	117.75	171.32	52.16	28.06
467	Asp	8.11	118.96	172.25	52.12	37.09
468	Leu	8.34	114.84	172.33	52.18	41.59
469	Ile	6.80	114.12	169.77	53.79	39.20
470	Met	9.86	127.86	174.96	53.24	30.43
471	Lys	8.92	125.45	175.29	57.41	26.87
472	Glu	9.39	117.53	174.58	56.32	25.65
473	Asp	6.66	118.12	175.75	54.98	37.66
474	Tyr	8.33	123.02	174.40	57.63	34.02
475	Glu	8.89	123.35	176.15	56.17	26.51
476	Leu	8.39	120.42	176.00	54.49	39.75
477	Val	7.44	116.70	173.40	63.45	28.80
478	Ser	7.88	109.32	172.00	58.27	60.95
479	Thr	7.50	107.11	172.58	58.26	66.98
480	Lys	7.07	123.88	173.14	50.56	26.44
481	Pro	-	-	174.05	62.04	29.59
482	Thr	6.83	104.25	170.07	54.76	69.71
483	Arg	8.91	124.65	174.57	57.18	25.62
484	Thr	9.06	113.77	172.25	65.27	66.64
485	Ser	8.08	114.26	175.54	58.45	60.30
486	Lys	8.48	126.21	175.06	57.51	31.50
487	Val	8.28	118.82	175.24	63.65	28.48
488	Arg	8.76	118.43	174.21	58.27	26.87
489	Gln	8.13	118.26	176.17	55.07	24.02
490	Leu	8.60	124.50	176.92	55.38	37.51
491	Leu	8.94	123.70	176.50	55.35	36.03
492	Asp	9.22	123.48	176.19	54.24	36.46
493	Thr	8.01	117.34	171.83	63.90	65.84
494	Thr	8.26	120.35	171.61	63.97	65.50
495	Asp	7.40	117.40	175.53	53.74	39.08
496	Ile	6.81	115.09	-	59.30	-
497	Gln	8.01	117.21	-	-	-
498	Gly	7.88	104.37	171.21	42.29	-
499	Glu	8.36	120.74	174.87	55.88	27.42
500	Glu	8.71	118.19	175.15	56.58	25.78
501	Phe	7.75	120.48	173.76	56.66	37.57
502	Ala	8.05	118.45	175.88	52.14	15.36
503	Lys	8.81	116.74	175.61	57.42	29.70
504	Val	7.19	118.53	174.10	63.07	28.48
505	Ile	6.96	118.30	174.61	61.56	34.52
506	Val	8.18	117.29	173.77	64.36	28.25
507	Gln	7.92	117.52	174.61	55.74	25.07

RIP2CARD (carbon detection)

```
              CO      CA     CB
439    Trp 174.64  60.11  24.19 109.37:Cg   127.85:Cd2  118.23:Ce3
440    Ile 175.29  64.25  35.24  12.97:Cd1
441    Gln 176.50  56.56  25.63  30.93:Cg
442    Ser 173.20  58.49  60.68
443    Lys 173.72  51.11  28.09  25.33:Cd
444    Arg 173.80  58.26  28.24  41.11:Cd   157.57:Cz
445    Glu 174.81  57.11  27.83
446    Asp 175.32  54.08  38.83
447    Ile 175.63  63.73  35.45  26.96:Cg1   16.63:Cg2   13.14:Cd1
448    Val      -  63.07  28.64
451    Met      -  55.08  28.36  29.03:Cg    14.34:Ce
452    Thr 172.77  58.81  68.00  19.94:Cg2
453    Glu 175.38  57.93  26.97  33.98:Cg   180.59:Cd
454    Ala 176.91  52.59  16.31
455    Cys 174.44  60.18      -
456    Leu 175.78  55.77  37.60  24.80:Cg    22.19:Cd1
457    Asn 174.87  53.33  34.80
458    Gln 176.24  56.60  27.53
459    Ser 172.90  61.46  60.02
460    Leu 175.79  55.80  38.63  23.49:Cg    20.78:Cd1   22.65:Cd2
461    Asp 175.86  55.74  38.37
462    Ala 177.73  52.27  16.68
463    Leu 177.23  55.79  39.70  23.76:Cg    20.13:Cd1   23.90:Cd2
464    Leu 178.71  55.49  40.02  24.22:Cg    20.81:Cd1   21.81:Cd2
465    Ser 173.21  58.84  61.22
466    Arg 172.12  52.58  28.48  24.91:Cg    40.93:Cd   156.87:Cz
467    Asp 173.23  52.40  37.39 178.86:Cg
468    Leu 173.03  52.58  42.36  24.13:Cg    20.50:Cd1   24.28:Cd2
469    Ile 170.52  54.22  39.86  26.62:Cg1   14.11:Cg2   10.72:Cd1
470    Met 175.78  53.91  30.89  30.82:Cg    15.19:Ce
471    Lys 176.15  58.06  27.25
472    Glu 175.37  56.90  26.09  32.65:Cg
473    Asp 176.37  55.61  38.28
474    Tyr 175.05  58.13  34.34 124.80:Cg
475    Glu 176.90  56.69  26.98
476    Leu 176.76  55.13  40.38  25.32:Cg    21.11:Cd1   22.12:Cd2
477    Val 174.20  64.08  29.31  18.88:Cg1   21.50:Cg2
478    Ser 172.75  58.95  61.19
479    Thr 173.29  58.61  67.03  19.00:Cg2
480    Lys 173.94  51.14  26.97  21.00:Cg
481    Pro 174.87  30.06  62.59  24.86:Cg    47.43:Cd
482    Thr 170.86  55.11  69.83  19.00:Cg2
483    Arg 175.20  57.97  26.08  22.57:Cg
484    Thr 173.17  65.88  66.94  19.53:Cg2
485    Ser 176.37  59.16  60.56
486    Lys 175.67  58.10  32.16  22.75:Cg    28.30:Cd    39.98:Ce
487    Val 175.92  64.21  29.04  20.26:Cg1   21.19:Cg2
488    Arg 174.81  58.79  27.84
489    Gln 176.85  55.54  24.38  30.11:Cg
490    Leu 177.70  55.85  38.11  24.63:Cg    20.64:Cd1   23.45:Cd2
491    Leu 176.96  55.93  36.34  23.82:Cg    18.31:Cd1   23.77:Cd2
492    Asp 176.84  54.80  36.75
493    Thr 172.51  64.21  65.99  19.49:Cg2
494    Thr 172.80  64.47  65.68  18.96:Cg2
496    Ile 174.70  61.77  34.50  27.02:Cg1   15.90:Cg2   11.31:Cd1
498    Gly 172.13  42.95      -
499    Glu 175.49  56.53  28.00
500    Glu 175.78  57.20  26.40
501    Phe 174.59  57.24  38.01 136.41:Cg
502    Ala 176.61  52.83  15.94
503    Lys 176.36  58.08  30.35  24.26:Cg    27.14:Cd    39.56:Ce
504    Val 174.58  63.60  29.05  19.72:Cg1   20.45:Cg2
505    Ile 175.25  62.03  35.10  26.60:Cg1   14.46:Cg2   12.36:Cd1
506    Val 174.62  64.83  28.85  19.18:Cg1   21.34:Cg2
507    Gln      -  56.27  25.79
509    Leu 175.32  55.58  39.63  24.31:Cg
```

Appendix B

Publications

Parts of this thesis have been published and can be found in the following publications:

Christopher Kesten*, Arndt Wallmann*, René Schneider, Heather E. McFarlane, Anne Diehl, Ghazanfar Abbas Khan, Barth-Jan van Rossum, Edwin R. Lampugnani, Witold G. Szymanski, Nils Cremer, Peter Schmieder, Kristina L. Ford, Florian Seiter, Joshua L. Heazlewood, Clara Sanchez-Rodriguez, Hartmut Oschkinat, and Staffan Persson. The Companion of Cellulose Synthase 1 confers salt tolerance through a Tau-like mechanism in plants. *Nature Communications*, 10(1):857, 2019.

Erika Pellegrini, Ambroise Desfosses, Arndt Wallmann, Wiebke Manuela Schulze, Kristina Rehbein, Philippe Mas, Luca Signor, Stephanie Gaudon, Grasilda Zenkeviciute, Michael Hons, Helene Malet, Irina Gutsche, Carsten Sachse, Guy Schoehn, Hartmut Oschkinat, and Stephen Cusack. RIP2 filament formation is required for NOD2 dependent NF-κB signalling. *Nature Communications*, 9(1):4043, 2018.

* These authors contributed equally

Acknowledgements

This thesis would not have been possible without our collaborators: Christopher Kesten and Staffan Persson, who first approached us with CC1 and have put up with many of the ups and downs of the project. I truly appreciated the discussions and the can-do spirit. Special thanks go out to Erika Pellegrini and Stephen Cusack, who had already done a ton of work on RIP2CARD before we even joined the effort.

I want to thank the members of the Oschkinat group for the support and in particular Anne and the whole wet-lab team for being the backbone of this group, Martina, Nils, Natalja & Kristina for providing proteins and the nice chats, Lisa for grinding pig brains with me, Peter, Andy & Monika for all the help at the spectrometer, Ying for putting up with me, Kelsey for proof-reading this thesis, Matthias for his rebellious attitude and his boyish charms, Johanna for organizing everything fun and important, Madhu, Trent & Shakeel for making our office the place to be, Daniel & Michel for sharing the PhD struggle and Andrea for always brightening up the day. I am especially indebted to Barth, who, from the first day on, was incredibly helpful and kind, always lending an ear for 'just five minutes' and always curious for everything scientific and everything else. One could not have asked for a better person to share an office with. I would also like to thank Hartmut Oschkinat for having me in his group and the resilience to let me pursue my own scientific ideas.

Apart from my colleagues, I would like to thank my family and friends, who have listened to my recent scientific progress with interest or at least a tired but patient smile on their faces.

Curriculum Vitae

For reasons of data protection, the curriculum vitae is not published in the online version.